FAR INFRARED TRANSMISSION SPECTROSCOPY OF BINARY SEMICONDUCTORS

by

Ahmad Kamil Wan Abdullah

A Thesis submitted for the internal Degree of Doctor of Philosophy in the Faculty of Science,

Royal Holloway and Bedford New College
University of London

May 1986

ABSTRACT

The far infrared optical properties of a selection of binary semiconductors have been studied by the technique of dispersive Fourier transform spectroscopy.

A commercial modular Michelson interferometer has been rebuilt in a single pass dispersive mode for this work. The performance of the instrument has been substantially improved by mounting the moving mirror on a pneumatically controlled precision linear slide to provide a smooth travel. The interferogram was sampled internally by monitoring the interference fringes derived from a secondary He-Ne laser channel. Precision alignment maximises the throughput signal enabling a relatively small specimen to be studied.

Direct measurements of the amplitude and phase transmission spectra of GaP, GaAs, InSb, InAs and ZnSe have been performed at room temperature and 100K for the first time. The single-pass configuration has enabled new optical constant data to be obtained accurately on either side of the reststrahlen band. In most cases, these are the first reported results at the two temperatures. In each case the absorption coefficient and the complex dielectric response functions have also been calculated. Prominent features in the spectra are assigned as phonon-combination bands with the aid of critical point phonon frequencies derived from a lattice dynamical model.

The magnitude of the imaginary part of the anharmonic self-energy function of the zone-centre transverse optical phonon required to account fully for the observed absorption has been estimated. The results give a clear indication of the range of validity of the anharmonic mechanism and the onset of lattice absorption due to non linear terms in the dipole moment expansion.

ACKNOWLEDGEMENTS

My sincerest thanks first go to Dr. T.J. Parker for supervising this research and for his consistent help and encouragement throughout the course of this work. I must also thank him for a critical reading of this thesis.

I would also like to thank all my fellow co-workers in the Solid State research group. Dr. K.A. Maslin should be especially thanked for making some of his experimental data available to me. I must also thank Dr. G.A. Gledhill, John Collins, Brendan King and Ahmed El Gohary for their kind cooperation. Thanks are also due to Dr. W.G. Chambers for a number of fruitful discussions.

It is a pleasure to thank the technical staff of the Physics Department for their help. Particular thanks are due to Mr. R. Elton for help with mechanical aspects of the project, Mr. T. Brooks for assisting with the electronics and Mr. C. Winterton for help with the technical drawings.

I would also like to acknowledge the financial assistance of the Government of Malaysia and Universiti Sains Malaysia which has enabled me to carry out this research work.

Finally, I must thank my wife, Rasheedah, for her understanding and support throughout this work.

CONTENTS

LIST OF FIGURES

LIST OF TABLES

Chapter 1

INTRODUCTION

The measurement of the optical and dielectric properties of crystalline solids is one of the most important branches of experimental solid state physics because the results provide valuable information about elementary excitations in solids. In order to obtain precise information about these properties and the underlying mechanisms powerful spectroscopic techniques are required so that unambiguous results can be obtained without the use of approximations. The purpose of this thesis is essentially two fold. Firstly, to describe the development of an experimental technique to determine the optical constants of transparent solids precisely and secondly, to study the optical and dielectric response of binary semiconductors in the far infrared.

The traditional approach adopted in the measurement of the optical properties of crystalline solids has been to use grating spectrometry. In the last twenty years, however, with the advent of fast and efficient computation, Fourier transform spectroscopy (FTS), using interferometers based on the Michelson interferometer, has become a competitive technique. The multiplex and throughput gains obtained from the technique have made FTS far superior to grating spectrometry particularly in the far infrared. The advantages of FTS and some of the more important

theoretical aspects of FTS are presented in the first part of chapter 2. The crux of the mathematical description of FTS is the pair of Fourier integrals which relate an interferogram with its spectrum. Other necessary elements of FTS will also be discussed.

However, in the determination of the optical constants, conventional or "power" FTS has one major disadvantage. The phase spectrum, which is required in the calculation of the complex refractive index (i.e. both n and k) over the required spectral region is not measured directly but must be determined indirectly from a technique such as a Kramers-Kronig analysis of a measured power reflection spectrum. This is because the specimen is placed in the exit port of the interferometer and the phase shift caused by the specimen is present in both beams and cannot be determined from the recorded interferograms. The analysis requires reflectivity measurements to be made over as wide a spectral range as possible, and usually an extrapolation of the measured spectrum is required to take account of the infinite limits in the integration. This means that the accuracy of the determination of the optical constants depends on the size of the measured spectral range.

However, when the specimen is inserted in one partial beam in the interferometer, its refractive index causes the measured fringe pattern to become asymmetric and shifted in path difference. This enables the complex reflectivity or transmissivity, that is both the amplitude and phase spectra, to be directly measured. Thus the optical constants can then be measured without using the

Kramers-Kronig analysis. This technique came to be known as dispersive Fourier transform spectrometry (DFTS). The asymmetry described above is the most important feature of the technique and leads to its sensitivity to the phase of the interaction between the electromagnetic field and the specimen. Several pioneering workers in DFTS include Chamberlain (1963), Gebbie [see for example Chamberlain et al (1963)] and Bell (1966). The earliest measurements at low temperatures were made by Parker and Chambers (1974). A comprehensive review of most aspects of the technique of DFTS has been written by Birch and Parker (1979).

Many measurements have been carried out in the past using the technique of reflection DFTS to obtain detailed information in the reststrahlen region of ionic crystals. However, as the phase response approaches zero on either side of the reststrahlen band large errors can occur in the value of k determined by the reflection method. Further away from the reststrahl region accurate measurements can only be carried out using the technique of transmission DFTS because the phase delay produced in transmission will be much larger.

Measurements of the optical constants below and above the reststrahlen band are the main concern of this thesis. Thus, in the second part of chapter 2 the theoretical basis for the determination of the optical constants by the technique of transmission DFTS is explained. There are two different interferometric configurations commonly used in transmission studies depending on the transparency and opacity of the specimen under investigation. A double pass

configuration allows the radiation to pass through the specimen twice while a single pass configuration permits the radiation to pass through the specimen only once. The discussion is specifically referred to transmission measurements on thick absorbing solids. Under such circumstances, the single pass transmission technique is the better choice because the square root advantage of amplitude spectroscopy can be fully exploited while avoiding the more difficult task of preparing thin samples with very well defined geometry. This also has the advantage of separating the different transmitted partial waves so that analytical difficulties associated with the interpretation of overlapping partial waves with thinner specimens are avoided.

Chapter 3 describes the interferometer system that has been developed. The interferometer works in a single pass dispersive mode for the reasons stated above. It was based on an NPL/Grubb Parsons modular interferometer. Originally the moving mirror was driven by a mechanical stepper motor. It was found, however, that the step driven interferometer had a number of serious limitations. To eliminate them many modifications were required. The main improvement was on the moving mirror assembly. A hydraulic piston has been constructed to drive the moving mirror which was mounted on a precision linear slide. Interferograms can then be sampled accurately using a laser-controlled sampling technique. A computer-controlled data acquisition system and the software associated with it have also been developed. With this system interferograms can be

co-averaged systematically so that the number of manual hours required to record the data has been substantially reduced. An experimental technique called the partial insertion technique has been introduced so that the gross phase shift associated with the shift of the interferogram can be measured very accurately. This technique can also be used in the process of co-adding noisy interferograms.

The far infrared properties of binary semiconductors are discussed in chapter 4. The dielectric response of a simple harmonic oscillator is first derived. The response function is then extended to include a frequency dependent anharmonic damping function $\Gamma(\nu)$. In the expression for $\Gamma(\nu)$ as given by Cowley (1963) it was assumed that non-linear contributions to the dipole moment can be neglected and that measured structure arises predominantly from anharmonic interactions due to the decay of the zone centre transverse optic phonon into combinations of phonons at other points in the Brillouin zone. However, the above assumption may not be valid in the case of zinc blende structure crystals where the contributions from the higher order dipole moment can be significant (Geick, 1965). Thus, the importance of non-linear dipole absorption is discussed in the chapter.

The optical constant data of a selection of binary semiconductors obtained at room temperature and 100K are presented in chapter 5. The detailed procedures that have been used to obtain the optical constant data from the measured amplitude and phase spectra are shown using the results of one of the specimens. In general, complementary

reflection data are required so as to compare the phase on one of the branches with values calculated from the refractive index determined from reflection measurements [Birch and Parker (1979)]. However, in the absence of reflection data at 100K a simple deduction has been found useful for determining the correct branching indices above the reststrahlen band so that the refractive index at 100K can still be obtained.

From the measured values of n and k the real and imaginary parts of the dielectric response and the power absorption coefficient of the materials are determined. Where possible, comparisons are made with other published results, and the significance of the contribution from the non linear dipole moment to the lattice absorption is assessed. Features observed in the spectra are interpreted as due to the combination of phonons at critical points. Selection rules provide information about the forbidden and allowed combinations. With the aid of a suitable lattice dynamical model such as the 11-parameter rigid ion model (Patel et al, 1984), critical point phonon frequencies can be obtained, and by making measurements at two different temperatures the spectral features can be classified into summation and difference bands.

It is anticipated that these measurements will also be useful in later work where precise values of the optical constants are required, such as in the study of low dimensional structures.

Finally, the most important results obtained from this work are summarised in chapter 6.

References to chapter 1

Bell E E; Infrared Phys. 6, 57 (1966).

Birch J R and Parker T J; "Infrared and Millimeter Waves", Vol. 2, Ed. Button K J, Academic Press, New York (1979).

Chamberlain J E, Gibbs J E, Gebbie H A; Nature (London) 198, 874 (1963).

Cowley R A; Advances in Physics 12, 421 (1963).

Geick R; Phys. Rev. 138, 1495 (1965).

Parker T J and Chambers W G; IEEE Trans MTT-22, 1032 (1974).

Patel C, Parker T J, Jamshidi H, Sherman W F; Phys. Stat. Sol. (b) 122, 461 (1984).

Chapter 2

FOURIER TRANSFORM SPECTROSCOPY

2.1 FUNDAMENTAL ASPECTS OF FOURIER TRANSFORM SPECTROSCOPY

In this section the fundamental principles and definitions of Fourier Transform Spectroscopy (FTS) are explained. The Fourier integrals which relate the interferogram and the spectrum are given. Situations which arise due to finite recording and discrete sampling of the interferogram are discussed briefly. At the end of the section several advantages of FTS are pointed out. Comprehensive accounts of FTS can be found in the book by Bell (1972) and the proceedings of the Aspen International Conference On Fourier Transform Spectroscopy (1970).

2.1.1 FOURIER TRANSFORM PAIR

Consider a Michelson interferometer as illustrated schematically in fig. 2.1. In principle the beam from the source is divided into two separate beams of equal amplitude which are recombined after travelling different paths. The interferogram is obtained by varying the optical path length in one arm and superimposing the two light beams after they return to the beam divider. The detector records the intensity as a function of distance travelled by the moving mirror.

The intensities of all spectral elements which are present in the bandwidth of observation are simultaneously

observed by the detector during the entire time of measurement. If the moving mirror is scanned continuously the interferometer modulates the intensity of all these spectral elements with cosine functions of different periodicities which are related very simply to the scan speed and the wavelengths of the spectral components. All spectral elements are in phase with respect to each other only at the position of zero optical path difference and each element interferes constructively at this mirror displacement to give the maximum value of the observed intensity. By Fourier inversion, the recorded interferogram signal is then decoded into a spectrum.

The intensity D(x) measured by the detector as a function of optical path difference x is expressed as

$$D(x) = \int_0^\infty B(\nu)[1 + \cos(2\pi\nu x)]\, d\nu \qquad (2.1)$$

where $B(\nu)$ is the source spectral energy density at wavenumber ν. In order to obtain a complete spectrum Eq. (2.1) must be integrated over the whole frequency spectrum. The interferogram function I(x) is obtained by eliminating the unmodulated term from Eq. (2.1), leaving :

$$I(x) = \int_0^\infty B(\nu)\cos(2\pi\nu x)\, d\nu \qquad (2.2)$$

The source intensity $B(\nu)$ can be obtained by applying an inverse cosine transformation to I(x). Thus, the equation for spectral recovery is expressed as

$$B(\nu) = \int_0^{\infty} I(x)\cos(2\pi\nu x)\, dx \qquad (2.3)$$

Eqs. (2.2) and (2.3) are called a Fourier transform pair.

If the interferogram is not symmetric, which can be due to either an imperfectly balanced optical system or because the interferometer is operating in a dispersive mode, a complex Fourier transform is used instead of a cosine transform. The complex form of the interferogram function $I_C(x)$ is given as

$$I_C(x) = \int_{-\infty}^{+\infty} B(\nu)e^{+i2\pi\nu x}\, d\nu \qquad (2.4)$$

and the spectrum

$$B(\nu) = \int_{-\infty}^{+\infty} I_C(x)e^{-i2\pi\nu x}\, dx \qquad (2.5)$$

The use of complex Fourier integrals in dispersive Fourier transform spectroscopy will be discussed in section 2.2. However, in order to illustrate how the instrument function and the resolution can be defined it is best to consider a simple monochromatic source. In this case, the most convenient mathematical representation of $B(\nu)$ is in the form of two Dirac δ-functions i.e.;

$$B(\nu) = [\delta(\nu-\nu_0) + \delta(\nu+\nu_0)] \qquad (2.6)$$

where ν_0 is the frequency of a monochromatic spectral line. Substituting Eq. (2.6) into Eq. (2.4), $I_C(x)$ reduces to

$$I_C(x) = 2\cos(2\pi\nu_0 x) \qquad (2.7)$$

which is an even function.

2.1.2 INSTRUMENT FUNCTION AND APODISATION

It is obvious that in a real measurement of an interferogram x must be a finite quantity. Thus, in recording a double sided interferogram the integral in Eq. (2.4) is truncated to within the range $-L \leq x \leq +L$ where L is the length of travel of the moving mirror. Therefore, substituting Eq. (2.7) into Eq. (2.5) the spectral recovery $B(\nu)$ of Eq. (2.5) becomes

$$B(\nu) = \int_{-L}^{+L} 2 \cos(2\pi\nu_0 x) \cos(2\pi\nu x)\, dx \qquad (2.8)$$

$$= 2L \operatorname{sinc}[2\pi(\nu-\nu_0)L] + 2L \operatorname{sinc}[2\pi(\nu+\nu_0)L] \qquad (2.9)$$

Since, in practice, it is nearly always true that $\nu_0 L \gg 1$, the second term in Eq.(2.9) can be safely ignored and therefore,

$$B(\nu) \approx 2L \operatorname{sinc}(y) \qquad (2.10)$$

where

$$y = [2\pi(\nu-\nu_0)L] \qquad (2.11)$$

This sinc function is shown in fig. 2.2(a). This shows that truncating an interferogram gives rise to an "instrument function" which is a sinc function instead of the original Dirac δ-function. The width of this instrument function varies according to the inverse of the maximum path difference L. The height of the undesirable side lobes is reduced by multiplying the interferogram function by a function which tapers smoothly to zero at $\pm L$. This technique is known as apodisation. In this work, the

apodising function A(x) used is a triangular type i.e.,

$$A(x) = 1 - |x/L| \tag{2.12}$$

Introducing A(x) into Eq. (2.8) gives

$$B(\nu) = L\ \mathrm{sinc}^2(y/2) \tag{2.13}$$

This sinc^2 function is illustrated in fig. 2.2(b). The line width is obviously broader than a sinc function but with much smaller side lobes.

2.1.3 SPECTRAL RESOLUTION

The resolution of the spectral recovery of a triangularly apodised interferogram may be obtained by using the Rayleigh criterion which states that two neighbouring resonances are resolved if they are separated such that the peak of one resonance falls on the first zero of the second resonance.

Therefore, when each resonance is a sinc^2 function as shown in fig. 2.2(b), according to the Rayleigh criterion they are resolved when their peaks are separated by 2π. In other words,

$$(y_0 - y') = 2\pi \tag{2.14}$$

where

$$y_0 = [2\pi(\nu - \nu_0)L] \tag{2.15}$$

and $$y' = [2\pi(\nu - \nu')L] \tag{2.16}$$

where L is the maximum optical path difference and the two resonant frequencies are ν_0 and ν' respectively. By substituting Eqs. (2.15) and (2.16) into Eq. (2.14), the resolution of a triangularly apodised interferogram can then be defined as

$$\Delta\nu = (\nu' - \nu_0) = 1/L \tag{2.17}$$

Using the above definition, the resolutions $\Delta\nu \approx 4,2$ and 1 cm^{-1} are obtained from the scan lengths L=8000s, 16000s and 32000s respectively, where s=0.3164μm. is the natural spacing of He-Ne laser interference fringes.

2.1.4 DISCRETE SAMPLING

In order to compute Eq.(2.5) it is necessary for the interferogram to be digitised and each discrete value is then fed into a computer for Fourier transformation. To do this, the sampling function $\text{Ш}(x/\Delta x)$ known as the shah "comb" function is used to sample the interferogram and is defined as (Loewenstein, 1970)

$$\text{Ш}(x/\Delta x) = \sum_{n=-\infty}^{\infty} \delta(x-n) \qquad (2.18)$$

which is a series of δ functions at the integers. The fact that the shah function is its own Fourier transform is of paramount importance in Fourier spectroscopy. What is of concern here is that the shah function is used not only as a sampling but also as a replicating function. Sampling is accomplished by multiplication

$$\text{Ш}(x/\Delta x) I_{C(x)} = \sum_{n=-\infty}^{\infty} I_C(n)\delta(x-n) \qquad (2.19)$$

and replication by convolution

$$\text{Ш}(x/\Delta x) * I_C(x) = \sum_{n=-\infty}^{\infty} I_C(n)\delta(x-n) \qquad (2.20)$$

The difference between these two processes is the sliding property of the convolution. This will be discussed below.

When sampling an interferogram, it is necessary to know what sampling interval is needed. The information is supplied by the sampling theorem. Assume that the spectrum

$B(\nu)$ extends from 0 to $\nu_{max.}$ as illustrated in fig. 2.3. The continuous interferogram $I_C(x)$ is sampled by using the shah function which then gives

$$I_S(x) = \text{Ш}(x/\Delta x) \cdot I_C(x) \qquad (2.21)$$

where $I_S(x)$ is the sampled interferogram. The spectrum $B_S(\nu)$ derived from the Fourier transform of $I_C(x)$ is

$$B_S(\nu) = (\Delta x)\,\text{Ш}(\nu/\Delta\nu) * B_C(\nu) \qquad (2.22)$$

where $B_C(\nu)$ is the complete (unsampled) spectrum and $\Delta\nu=1/\Delta x$. It is clear from fig. 2.3 that $\Delta\nu$ must be made large enough such that the maximum frequency contribution of the positive spectrum $+\nu_{max.}$ does not overlap with the aliased spectrum extending to $(\Delta\nu-\nu_{max.})$. This can be achieved by setting

$$\Delta x \leq 1/2\nu_{max.} \qquad (2.23)$$

This is the basic sampling theorem i.e., sampling must be carried out at a rate equal to the reciprocal of twice the highest frequency present in the spectrum in order to avoid aliasing.

Therefore, values of $\nu_{max}\approx$1975, 987 and 493 cm^{-1} will require the minimum discrete moving mirror increment of $\Delta x'=\Delta x/2=4s$, 8s and 16s respectively, where s is defined as before.

2.1.5 ADVANTAGES OF FOURIER SPECTROSCOPY

There are two well-known principal advantages of FTS compared with conventional grating spectroscopy, namely the multiplex and throughput advantages. The multiplex or Fellgett advantage is practically realised in FTS because all wavelengths present in an interferogram are observed

simultaneously whereas, in a grating instrument the wavelengths are observed sequentially. As a consequence, the signal-to-noise ratio of a spectrum of N elements achieved in an FTS instrument is superior to that of a grating instrument by a factor of $\sqrt{N}$. This is realised in far infrared spectroscopy because the noise usually comes from the detector and is independent of the amount of radiation falling on the detector. The Jacquinot or throughput advantage is achieved in FTS since the radiant throughput of an interferometer is larger than that of a grating spectrometer because of the absence of optical slits in FTS. This advantage becomes very important in the far infrared where the energy output from a black body source is small.

There are also two other advantages which will be stated here. Firstly, only one standard is enough to give a complete calibration of the wave number scale. This is achieved very precisely using a simultaneously recorded additional interferogram of a monochromatic source, i.e. a laser, whose wave number is already well-known, to act as a control signal (Guelachvili, 1981). The use of this technique will be discussed in chapter 3. Secondly, in a Michelson interferometer the two partial beams are spacially well separated. This advantage is fully exploited in dispersive FTS.

2.2 DISPERSIVE FOURIER TRANSFORM SPECTROSCOPY

The technique of dispersive Fourier transform spectroscopy (DFTS) provides a direct method for obtaining

the optical constants of a material.

In conventional FTS, the measured power reflection or transmission spectrum does not contain any phase information since the phase shift caused by the specimen is present in both beams. Therefore, the optical constants must be obtained indirectly by using a technique such as the Kramers-Kronig analysis of the power reflection spectrum. However, the Kramers-Kronig analysis involves approximations because the spectrum obtained does not extend over an infinite range of frequencies i.e., it is band-limited. Because of this inevitable limitation, the technique of DFTS has in recent years become a powerful alternative in obtaining the optical constants.

In DFTS, the specimen to be studied is placed in one partial beam in the interferometer instead of placing it in the output of the two beams as in the case of conventional FTS. This asymmetric configuration allows the amplitude attenuation and the phase shift of the specimen to be obtained simultaneously from the recorded interferograms. The three basic configurations are shown in fig. 2.4. The choice of configuration depends on the transparency or opacity of the specimen. (Birch and Parker, 1979). If the specimen is opaque in the spectral region to be investigated, a reflection measurement is required and if the specimen is transparent a double pass transmission measurement can be conveniently used. However, in the case where the specimen is highly absorbing and not highly reflecting, it may not be particularly well-suited for either of these techniques. In this case, a third

dispersive technique called the single pass transmission measurement can be used with advantage as discussed in the previous chapter. The construction of a suitable interferometer is described in chapter 3. The discussion in this section is specifically concerned with the determination of the optical constants of a thick specimen by transmission DFTS. A comprehensive review of DFTS of solids, liquids and gases has been given by Birch and Parker (1979).

2.2.1 COMPLEX INSERTION LOSS

The complex insertion loss is the quantity measured in DFTS. It is the complex factor by which the amplitude of a wave is changed when the symmetry of the interferometer is disturbed by either inserting a transparent specimen into the beam in the fixed arm or by inserting an opaque specimen as a replacement for a perfect reflector. It is defined as (Chamberlain, 1972):

$$\hat{L}(\nu) = L(\nu)e^{i\Phi_L(\nu)} \qquad (2.24)$$

When a specimen is placed in the fixed mirror arm, the electric field vector from this arm is modified because of the presence of $\hat{L}(\nu)$ in the electric field equation. From the resultant field amplitude of the two beams, it can be shown (Birch and Parker, 1979) that $\hat{L}(\nu)$ can be determined from the ratio of the two complex Fourier transforms

$$\hat{L}(\nu) = \frac{FT[I_S(x)]}{FT[I_O(x)]} \qquad (2.25)$$

where $I_S(x)$ and $I_O(x)$ are the interferogram functions of the sample and the background respectively. Eq. (2.25) can be rearranged in a more convenient form to give

$$L(\nu) = [p^2(\nu)+q^2(\nu)]^{1/2}/[p_o^2(\nu)+q_o^2(\nu)]^{1/2} \qquad (2.26)$$

and

$$\Phi_L(\nu) = \text{arc tan}[q(\nu)/p(\nu)] - \text{arc tan}[q_o(\nu)/p_o(\nu)] \qquad (2.27)$$

where $p(\nu)$ and $q(\nu)$ are the cosine and sine transforms of $I_s(x)$, and $p_o(\nu)$ and $q_o(\nu)$ are the cosine and sine transforms of $I_o(x)$, respectively.

The important results shown in Eqs.(2.25-27) will be used later on to determine the optical constants of a specimen.

2.2.2 COMPLEX REFRACTIVE INDEX

It is well-known from the electromagnetic theory of light (Born and Wolf, 1965) that when Maxwell's equations are solved for a wave propagating in a medium of conductivity σ, relative permeability μ and relative permittivity ϵ_r, the complex refractive index is given as

$$\hat{n} = c[\mu\mu_o(\epsilon_o\epsilon_r + i\sigma/\omega)]^{1/2} \qquad (2.28)$$

where μ_o and ϵ_o are the permeability and permittivity of free space respectively, and c is the speed of light. For non-magnetic materials, for which μ=1 and writing $c=(\mu_o\epsilon_o)^{-1/2}$ Eq. (2.28) can be written as

$$\hat{n} = [\epsilon_r + (i\sigma/\omega\epsilon_o)]^{1/2} \qquad (2.29)$$
$$= n + ik$$

where n and k are the real and imaginary parts of $\hat{n}$ respectively and are called the optical constants of the absorbing medium.

Eq. (2.29) may be written in the form

$$\hat{n} = (\hat{\epsilon})^{1/2} \qquad (2.30)$$

where $\hat{\epsilon}$ is the complex dielectric constant which may be

written as

$$\hat{\epsilon} = \epsilon' + i\epsilon'' \qquad (2.31)$$

The relationships for ϵ' and ϵ'' in terms of n and k are thus

$$\epsilon' = n^2 - k^2 \qquad (2.32)$$

and $$\epsilon'' = 2nk \qquad (2.33)$$

2.2.3 TRANSMISSION OF A PLANE PARALLEL SOLID

Fig. (2.5) shows the rays reflected from and transmitted through a plane parallel transparent solid in a medium. The complex refractive indices of the solid and medium are $\hat{n}_1$ and $\hat{n}_2$, respectively. The following discussion is aimed at showing how the single pass transmission coefficient of a specimen is obtained by using the Fresnel relations.

The complex transmission and reflection coefficients $\hat{T}_{12}$ and $\hat{R}_{12}$ are given as

$$\hat{T}_{12} = \hat{t}_{12}\hat{a}_2\hat{t}_{21} + \hat{t}_{12}\hat{a}_2^3\hat{r}_{21}^2\hat{t}_{21} + \ldots \qquad (2.34)$$

$$\hat{R}_{12} = \hat{r}_{12} + \hat{t}_{12}\hat{a}_2^2\hat{r}_{21}\hat{t}_{21} + \ldots \qquad (2.35)$$

where $\hat{a}_2$ is the complex propagation factor of the medium given by

$$\hat{a}_2 = e^{i2\pi\nu\hat{n}_2 d}\ , \qquad (2.36)$$

d is the thickness of the specimen,

and $$\hat{t}_{12} = 2\hat{n}_1/(\hat{n}_1+\hat{n}_2) \qquad (2.37)$$

$$\hat{t}_{21} = \hat{n}_2\hat{t}_{12}/\hat{n}_1 \qquad (2.38)$$

$$\hat{r}_{12} = (\hat{n}_1-\hat{n}_2)/(\hat{n}_1+\hat{n}_2) \qquad (2.39)$$

$$\hat{r}_{21} = -\hat{r}_{12} \qquad (2.40)$$

are the Fresnel transmission and reflection coefficients of the interfaces between the two media.

In DFTS the phase sensitivity of the interferometer resolves the contributions of each partial wave given in Eqs. (2.34) and (2.36) into separate interference signatures in the interferogram.

2.2.4 DETERMINATION OF THE OPTICAL CONSTANTS BY SINGLE PASS TRANSMISSION

Fig. (2.6) is a schematic illustration of a background interferogram and a specimen interferogram recorded from an instrument working in a single pass dispersive mode. Since the specimen is considered to be sufficiently thick, the signatures associated with the successive partial waves in Eq. (2.34) are well separated on the recorded specimen interferogram. It can be observed from the figure that the signatures are displaced in optical path lengths by amounts of approximately $(\bar{n}-1)d$, $(3\bar{n}-1)d$, $(5\bar{n}-1)d$ etc. from the background interferogram $I_0(x)$ where $\bar{n}$ is the mean value of the refractive index of the specimen over the measured spectral range and d is its thickness.

Since, in the work presented in this thesis, only the signature due to the first transmitted partial wave is recorded in the specimen interferogram, the relevant complex transmission coefficient of the specimen is fully described by the first term in Eq. (2.34). Consequently, the computation of the optical constants is much simpler because the higher order terms containing the reflection coefficients are excluded from the calculation. With the aid of Eqs. (2.36-38) and putting $\hat{n}_1(\nu)=1$ and $\hat{n}_2(\nu)=\hat{n}(\nu)$, the complex single pass transmission coefficient can be

written as

$$\hat{t}(\nu) = t(\nu)e^{i\Phi(\nu)}$$

$$= \frac{4\hat{n}(\nu)}{[1+\hat{n}(\nu)]^2} e^{i2\pi\nu\hat{n}(\nu)d} \qquad (2.41)$$

where $t(\nu)$ and $\Phi(\nu)$ refer implicitly to the entire specimen.

The complex ratio of the Fourier transforms of the two interferograms can be written as

$$\hat{L}'(\nu) = L'(\nu)e^{i\Phi'(\nu)} = \frac{FT[I_S(x)]}{FT[I_O(x)]} \qquad (2.42)$$

This is different from the complex insertion loss $\hat{L}(\nu)$ because it does not include the large phase shift $[2\pi\nu(\bar{n}-1)d]$ associated with the specimen, which causes a large displacement of the starting points of the two interferograms. With the inclusion of this phase shift, $\hat{L}(\nu)$ can be written in terms of experimentally measured quantities as

$$\hat{L}(\nu) = L'(\nu)e^{i[\Phi'(\nu)+4\pi\nu B]} \qquad (2.43)$$

where

$$2B \approx (\bar{n}-1)d \qquad (2.44)$$

The term $\Phi'(\nu)$ is the principal value of the phase difference between the two complex spectra. For a highly dispersive specimen, $\Phi'(\nu)$ must be replaced by

$$\Phi(\nu) = \Phi'(\nu) \pm 2m\pi \qquad (2.45)$$

where m=0,1,2, etc. The factor $\pm 2m\pi$ is used to ensure continuity in the true value of the phase difference when its computed value changes branches. Generally, additional information is required to assign a value of m to a particular branch. In some of the present transmission work, the optical constants are measured in the spectral

region below the reststrahlen band where particular values of m can be assigned by recognising that $\Phi'(\nu)$ approaches zero at low frequencies. To obtain $\Phi(\nu)$ above the spectral region where the crystal is opaque, the following expression is used in order to assign m correctly;

$$n(\nu) = 1 + \frac{2B}{d} + \frac{\Phi'(\nu) \pm 2m\pi}{2\pi\nu d} \qquad (2.46)$$

where $n(\nu)$ may be obtained by the technique of reflection DFTS over a small spectral band near the opaque region in which the signal-to-noise ratio obtained by the reflection and transmission methods is acceptable. Once the branch has been assigned correctly in this spectral band, then the remaining branches beyond this region can be assigned following the normal procedure. At the same time, this method also provides a test for spectral reproducibility.

The relationship between $\hat{L}(\nu)$ and the optical constants can be obtained by writing

$$\hat{L}(\nu) = \hat{t}(\nu)e^{-i2\pi\nu d}$$

$$= \frac{4\hat{n}(\nu)}{[1+\hat{n}(\nu)]^2} e^{i2\pi\nu(\hat{n}-1)d} \qquad (2.47)$$

The factor $e^{-i2\pi\nu d}$ arises because the length d of vacuum is replaced by the specimen.

Therefore, for $n(\nu) \gg k(\nu)$, the values of n and k can now be obtained separately by using Eqs. (2.43-47) and are expressed as

$$n(\nu) = 1 + \frac{[4\pi\nu B + \Phi'(\nu) \pm 2m\pi]}{2\pi\nu d} \qquad (2.48)$$

and

$$k(\nu) = \frac{1}{2\pi\nu d} \ln\left[\frac{4n(\nu)}{[1+n(\nu)]^2} \frac{1}{L(\nu)}\right] \qquad (2.49)$$

References to chapter 2

Bell R J; "Introductory Fourier transform spectroscopy", Academic Press, New York (1972).

Birch J R and Parker T J; "Infrared and Millimeter waves", Vol. 2, Ed. Button K J, Academic Press, New York (1979).

Born M and Wolf E; "Principles of Optics", 4th. Edition, Pergamon Press (1970).

Chamberlain J E; "The principles of interferometric spectroscopy", Wiley Publications, New York (1979).

Guelachvili G; "Spectrometric Techniques", Vol. 2, Ed. Vanasse G A, Academic Press (1981).

Loewenstein E V; Proc. Aspen Int. Conf. on Fourier Spectroscopy, Eds. Vanasse G A, Stair Jr A T and Baker D J, AFCRL special reports no. 114 (1970).

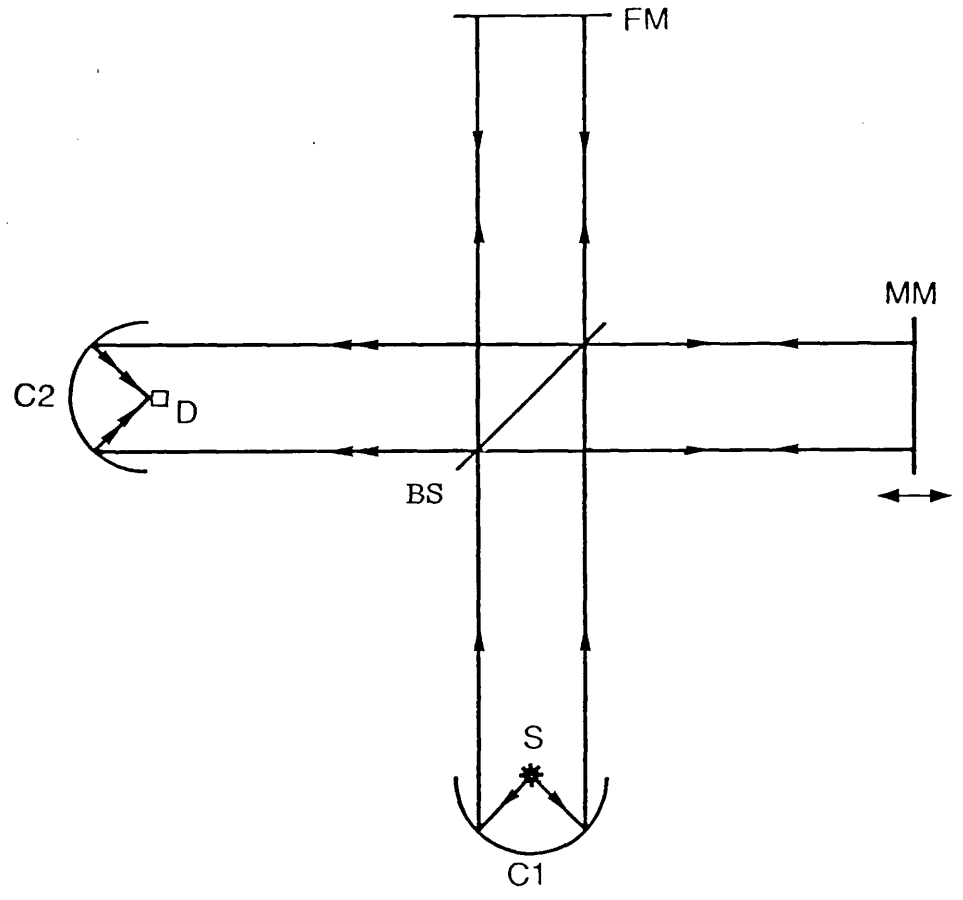

Figure 2.1 Schematic diagram of a Michelson Interferometer

Key: MM moving mirror, FM fixed mirror,
C1 and C2 collimators, BS beam splitter,
S source, D detector.

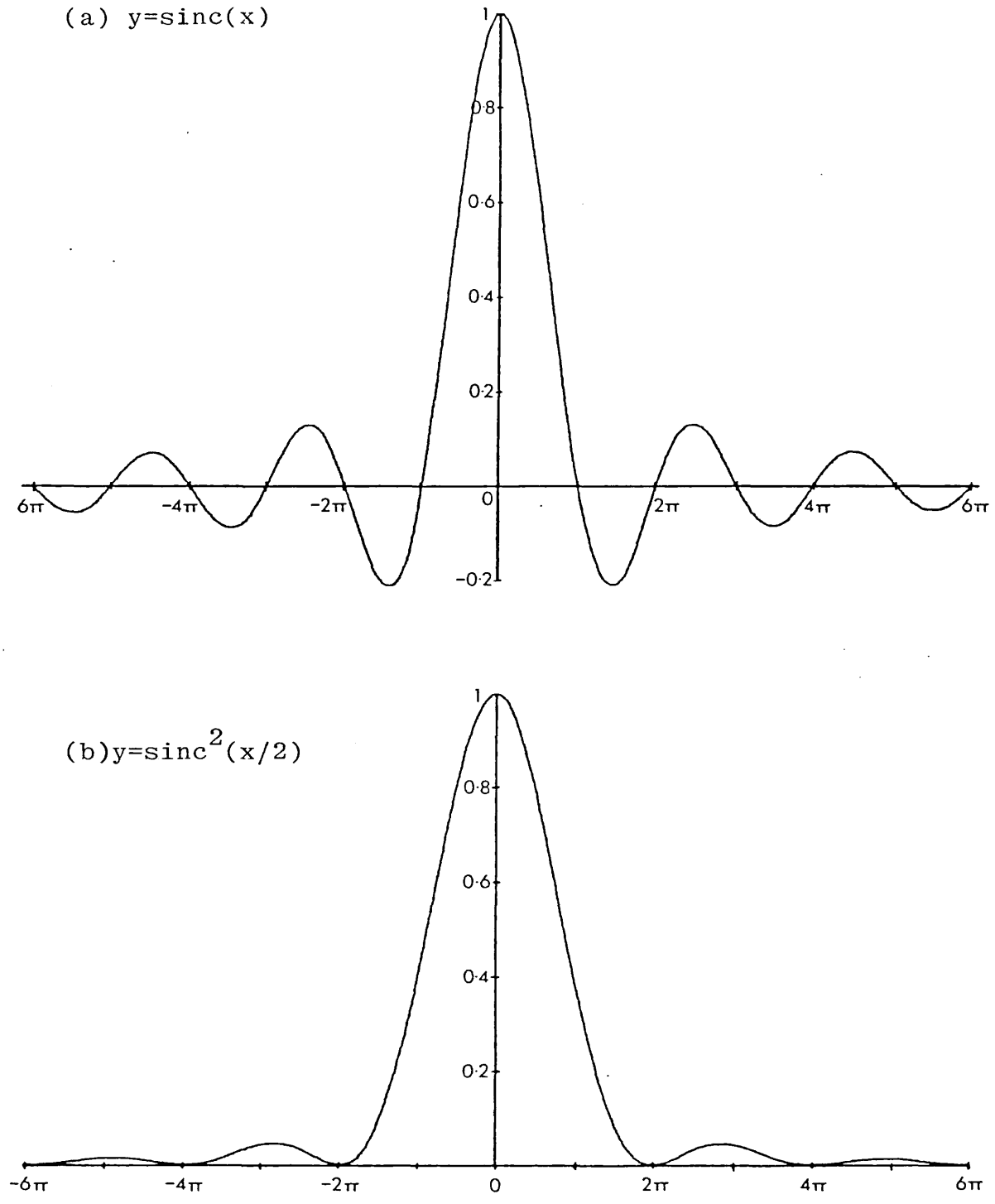

Figure 2.2 (a) Effect of truncating the interferogram on the spectrum of a monochromatic source.
(b) Effect of applying a triangular apodising function on the spectrum of (a).

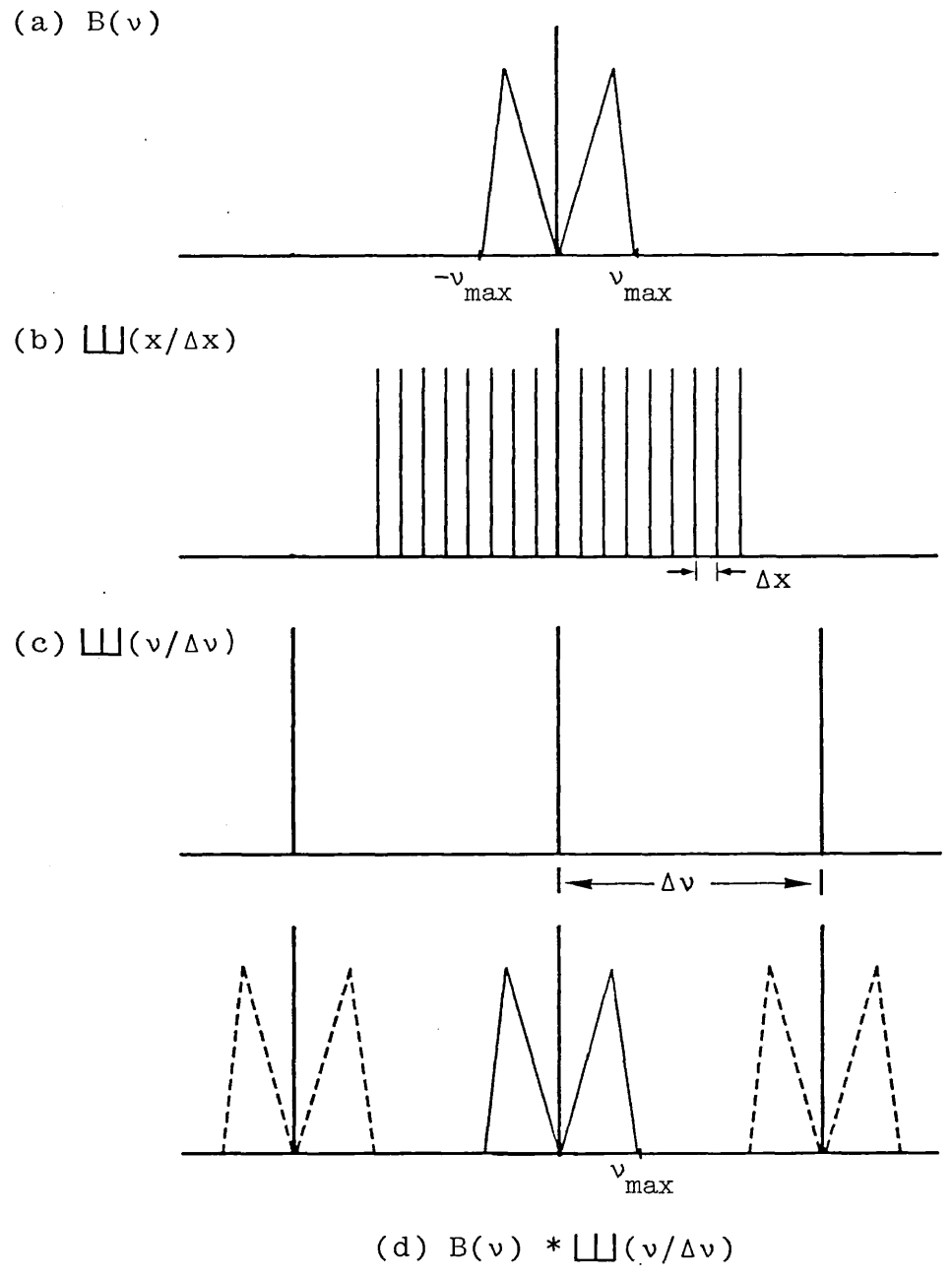

Figure 2.3 Illustrating the replication of the spectrum arising from the sampling of the interferogram. (d) is used to show that the sampling interval Δx must be $\leqslant 1/2\nu_{max}$ in order to avoid aliasing.

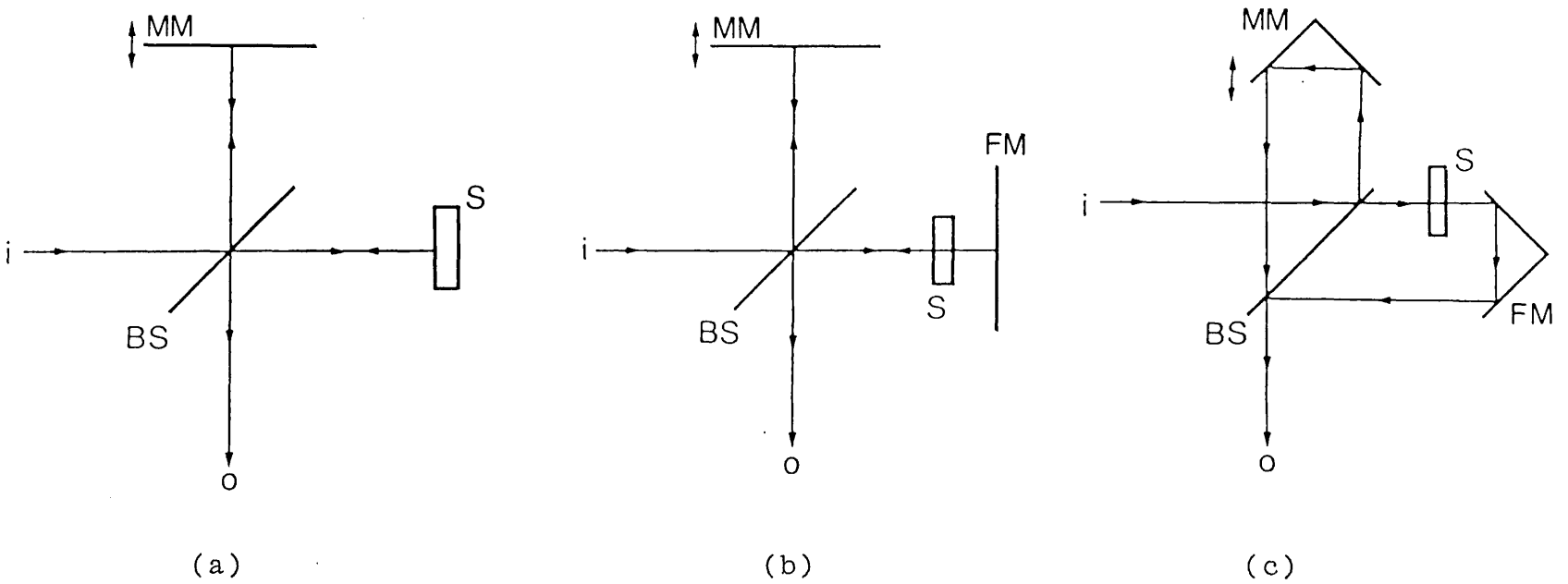

Figure 2.4 Three basic interferometer configurations used in DFTS
(a) reflection, (b) double pass transmission
(c) single pass transmission.
Key: MM moving mirror, FM fixed mirror, BS beam splitter,
S specimen, i input beam, o output beam.

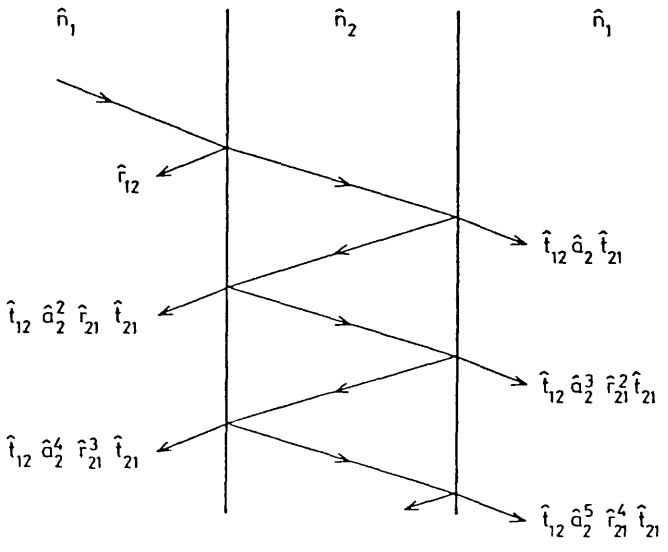

Figure 2.5 The rays reflected from, and transmitted through, a lamellar specimen of complex refractive index $\hat{n}_2$ immersed in a medium of complex refractive index $\hat{n}_1$.

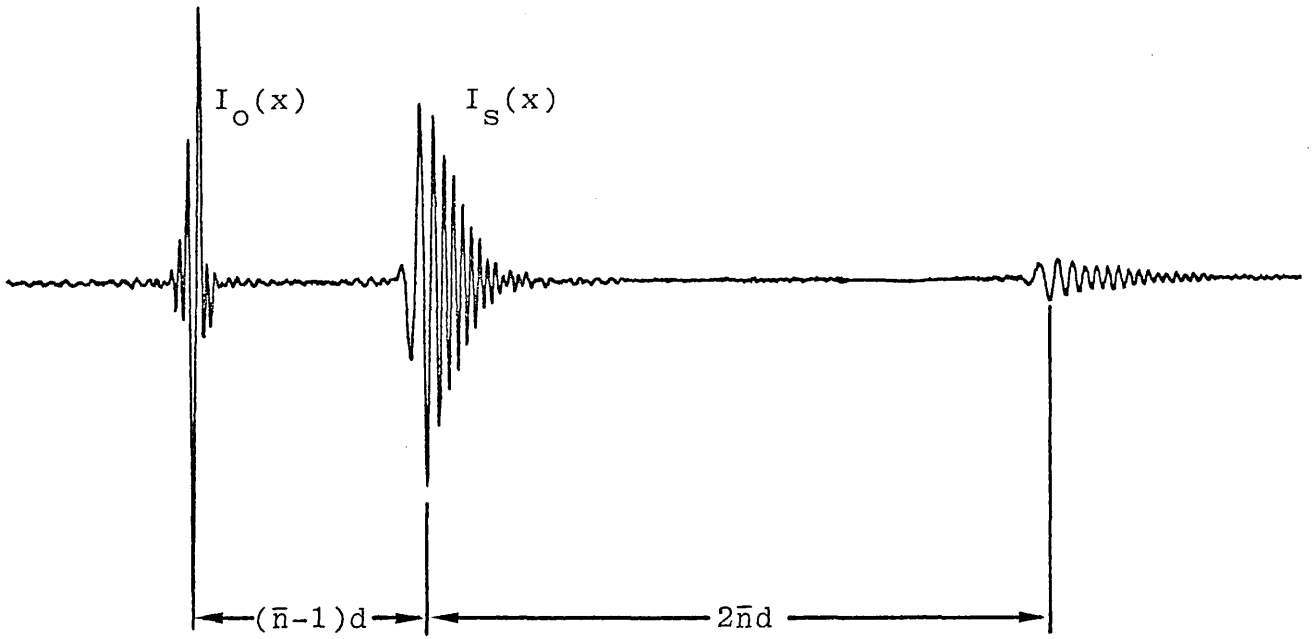

Figure 2.6 Illustration of a background interferogram $I_o(x)$ and a specimen interferogram $I_s(x)$ recorded from an instrument working in a single pass dispersive mode.

Chapter 3

INSTRUMENTATION AND EXPERIMENTAL METHODS

3.1 INTRODUCTION

In this chapter the apparatus and experimental techniques that have been developed on a Michelson interferometer are described.

The major work has been the reconstruction of an NPL/Grubb Parsons interferometer to work in a single pass dispersive mode. Modular components which are not available commercially have been designed to incorporate pneumatic technology and a laser-controlled sampling technique. Essentially, it is a Martin-Puplett type of interferometer (Martin and Puplett, 1970) and is illustrated schematically in figure 3.1.

The instrument allows measurements to be carried out at temperatures between room temperature and 100 K. The specimen can be inserted into the collimated beam without breaking the vacuum in the interferometer.

The computer-controlled data acquisition system employed in this work will be explained. The spectrometer operates in a multiple-scanning mode and the interferograms are co-added systematically by the software that has been developed.

A block diagram of the complete interferometer and data acquisition system described in this chapter is shown in figure 3.2.

3.2 SINGLE PASS TRANSMISSION INTERFEROMETER

A single pass transmission (SPT) interferometer has been developed in order to perform transmission measurements satisfactorily on specimens which are highly absorbing. It has been shown in the previous chapter that in this configuration the radiation in the fixed mirror arm only passes through the specimen once and therefore the transmission signal obtained will be enhanced because of the square root advantage of amplitude spectroscopy. The interferometer works in a continuous scanning mode and interferograms are sampled accurately by using a laser-controlled sampling technique. To improve the signal-to-noise (S/N) ratio, several interferograms are co-added systematically and in order to do this the interferometer is set to operate in a multiple scanning mode. This mode of operation is illustrated in figure 3.3.

In the past a Michelson interferometer was developed for SPT experiments at Westfield College. However, it was found that the step drive mechanism for the moving mirror produced serious random errors in the sampled interferograms. Simultaneously, other work in the laboratory resulted in the development of a high precision hydraulic drive for use in the moving mirror arm which, when used with laser sampling control was shown to eliminate these random errors. These techniques have been utilised to enable state-of-the-art sampling precisions to be achieved.

The limitations of the mechanical step drive are first described in the following section. Then the improvements

that have been made to the interferometer to eliminate these limitations are explained.

3.2.1 LIMITATIONS OF THE STEP DRIVEN INTERFEROMETER

In the conventional interferometer a stepper motor is used to drive the mirror in one of the arms. An externally triggered electronic circuit turns the micrometer that is attached to the mirror and after a short time delay the signal from the detector is received by the phase sensitive detector.

The periodic screw errors of the micrometer in motion give rise to ghostlines appearing around a sharp absorption line. It can be shown that the separation between the ghostlines and the absorption line is precisely 10 cm^{-1}, corresponding to a travel of 0.5 mm in one revolution of the micrometer. The intensities of the ghost lines are obviously larger the larger the deviations are from a linear movement. The relation between ghostline intensity and amplitude of periodic travel distortion has been discussed by Steeg et al.,1980.

Apart from the appearance of ghostlines in the spectrum, it can also be difficult to ensure the constancy of the step interval to within less than 1μm say, throughout a complete scan by using a mechanical stepper motor.If the signals are obtained at unequal increments of path difference, errors will be produced in the sampled interferogram (Zachor, 1977). This problem will become more serious especially in the higher wavenumber region as the sampled interferogram starts to lose its coherence.

When the error in the sampling interval gets larger than the sampling distance itself, or, that is to say, when there is a break in the sampling sequence, the instrument function suffers a large distortion. A correction of the resulting distortion is generally impossible and no worthwhile spectral recovery can be achieved. Since the step intervals are obtained mechanically it is often difficult to choose the most suitable power level for the stepper motor. Too high a power level will cause vibrational stepping noise and too low a power level will lead to erratic stepping and even breaks in the sampling sequence. The system also requires a temperature stabiliser in order to reduce the differential thermal expansion or contraction between the two arms due to ambient temperature changes.

Furthermore, an interferometer equipped with a stepper motor and a phase sensitive detector is not designed to operate in a fast scanning mode. Normally, it takes about a day to obtain ten interferograms with low S/N ratio. During this long scanning period, fluctuations in the power supplies especially to the detector and the source lamp will effect the quality of the output spectra. The use of long recording periods and the need to store interferograms one by one in a computer demand additional manual hours.

In order to obtain a required spectral region, a dielectric beamsplitter of a particular thickness has to be selected and placed inside the interferometer. To realign the interferometer again can be a slow task since the reference surface of the slot for the beamsplitter only

acts as a rough guide to the previously aligned position. This is discussed further in section 3.2.8.

All the limitations described above are inherent in an interferometer that uses a stepper motor to drive the moving mirror. Therefore, radical improvements have to be made in order to dispel the above mentioned setbacks.

3.2.2 THE HYDRAULIC MOVING MIRROR DRIVE

A pneumatically controlled moving mirror drive has been constructed in place of the stepper motor and the micrometer drive. The mirror is mounted on a precision linear slide and a hydraulic piston is used to drive the slide. This hydraulic drive unit provides continuous and smooth mirror motion and therefore, if a subsidiary laser control channel is used, the sampling points of the interferogram can be determined with very high precision, as described in section 3.2.6. Furthermore, since the mirror is now driven linearly the ghostlines do not occur anymore.

The hydraulic drive was first introduced by Burton and Parker (1984) into the field of Fourier transform spectroscopy. A comprehensive account of the operation and performance of the hydraulic drive unit can be found in their publication.

Essentially, hydraulic pressure is used to drive a piston in either a forward or reverse direction when a solenoid-operated valve is actuated with a +12 volts signal. The hydraulic pressure is derived from a cylinder of compressed oxygen-free nitrogen and the drive unit

requires a minimum pressure of 45 psi in order to operate. All hydraulic components were obtained from Activ-Air Automation Ltd.

The speed at which the mirror is moving can be selected by adjusting the settings of two micrometer flow control valves. These valves control the rate of oil flow to the piston cylinder and incorporate a sensitive poppet type mechanism which allows full flow in one direction but, when the flow is reversed, seals tight to divert the flow past a fine metering needle. The unit also contains pilot valves which prevent any drift in piston position. This drift is sufficient to move the mirror through several microns making it impossible to locate the starting and stopping positions of the piston to within a few fringes. The elimination of this drift is essential, as will be discussed later, to avoid ambiguities in choosing a prominent feature which can be either the maximum or minimum point of an interferogram of poor S/N ratio.

This system allows a scan speed to be chosen between 1μm and 10mm per second. The speed is selected to match the dynamic response of the infrared detector as explained in section 3.3.

The moving mirror translation unit is housed in a cylindrical chamber module in the moving mirror arm of the interferometer. A stainless steel rod acting as a vacuum feedthrough connects the piston shaft to the translation unit.

The feedthrough rod is held in contact with the piston shaft by a pair of steel springs attached between the

translation unit and the cylindrical chamber module. The remaining hydraulic circuit elements are isolated from the optical table, the only communication between these and the piston cylinder being a pair of reinforced plastic pipes carrying hydraulic fluid.

The hydraulic control box which supplies the +12V power line is activated when it receives a control pulse generated using the computer software. In other words, the acquisition of data is controlled by the computer.

3.2.3 ROOFTOP REFLECTORS

A pair of rooftop reflectors was obtained from SPECAC Ltd. which allows a maximum throughput beam of about 12 cm^2 in area and a tolerance of about 30 sec in the mirror angle. To preserve the quoted tolerance, each mirror was carefully mounted using only one half of the mirror, leaving the other half free from any physical contacts. A piece of paper was inserted in between the mount and the back of the mirror to prevent the possibility of the second half from crushing the mount while tightening the attachment screws.

Before the commercial rooftop reflectors were utilised, readily available rooftop mirrors in the laboratory were used. However it was found that the rooftop angles of the mirrors were 89° 58.1 min and 89° 45.5 min respectively, giving a difference of 12.6 min. This gives a deviation of 3.6 mm for every metre travelled after the reflection. With the length of each arm of the interferometer about 150 mm and the laser detector about 50 mm away from the

beamsplitter, the two laser spots are 0.7 mm apart, centre to centre. Therefore this discrepancy produced very poor quality fringes since the diameter of the laser spot is approximately 1.5 mm. Though the mirrors are optically flat, their poor perpendicularity is incurable since there is no alignment system to correct for it.

To configure the interferometer in a single pass dispersive mode, a module is added after the collimator unit to displace the infrared beam laterally by 12.7 mm with respect to the input optical axis. This causes the infrared beam to be reflected on the central area of one of the rooftop mirrors after it has undergone the division of its amplitude at the beamsplitter. A second identical module is attached at the output port before the detector to restore the continuity of the optical path. This arrangement was first used by Parker et al (1978).

3.2.4 ALIGNMENT OF THE FIXED ARM

The complete assembly of the rooftop reflector that has been constructed at the fixed mirror arm is shown in figure 3.4. The rooftop reflector was mounted on a precision rotator unit which can be rotated smoothly about a horizontal axis. The rotator unit was attached to a precision gimbal mount so that the mirror can be tilted in the horizontal plane over a range of 3° by turning the tangential micrometer of the gimbal. The gimbal was then fixed onto a micrometer driven linear stage which allows the height of the mirror to be adjusted. The gimbal and the stage were obtained from Ealing-Beck Ltd. The alignment to

the mirror can be done from outside the interferometer by having the appropriate vacuum feedthrough rods.

3.2.5 ALIGNMENT OF THE LASER BEAM

The commercial rooftop reflectors acquired for this work were designed mainly for use with submillimetre wavelength radiation. With a quoted tolerance of two or three visible fringes over the central area, they can be considered optically flat for far infrared radiation. However, it was found that the mirror was not optically flat over the whole area and a small amount of roll-off was observed near the edges. Because of this it was found that the laser and the infrared fringes could not be simultaneously aligned and an additional independent alignment mechanism was required for the laser beam. Accurate alignment of the laser beam is then carried out after the infrared beam has been fully aligned. This is done by using two small pieces of glass each of 5mm thickness, sufficient to allow the beam to be moved sensitively. This is shown in figure 3.5. They are situated inside the moving mirror arm of the interferometer; one across the incoming beam and the other one across the outgoing beam. The glass pieces provide two orthogonal axes of tilt to the laser beam. The alignment can be carried out from outside the interferometer.

3.2.6 LASER CONTROL CHANNEL

The laser channel is constructed to provide an accurate method of measuring the path difference. Monochromatic

radiation from a He-Ne laser produces the interference fringes for monitoring the position of the moving mirror. Since the sampling is now done internally, any differential thermal expansion between the two arms of the interferometer during a scan is automatically corrected.

The input port of the laser channel is situated immediately after the collimator unit. The laser housing is located away from the warm infrared lamp housing and its power supply box is isolated from the optical table. The infrared beam path is carefully avoided by installing a small reflecting mirror at 45° to the incoming laser beam beside the infrared path. At the input port, a quarter-wave plate is placed perpendicular to the beam in order to prevent feedback from the interferometer into the laser. This improves the stability of the laser beam. The He-Ne laser was obtained from Scientifica-Cook Ltd.

The electronic circuit for the laser channel is shown in figure 3.6. The signal derived from the laser fringes incident on the photodiode (type BPX 65) is passed from the detector through low noise operational amplifiers (type 038) in the laser sampling unit. The Schmidd trigger converts the sinusoidal signal to a square wave signal and the signal is then passed through a monostable. The output pulses are then used to trigger the analogue-to-digital converter (ADC).

The sampling unit also allows the size of the sampling interval to be chosen in terms of the number of laser fringes; i.e 2^n fringes per step where n=0,1,2,3,4. This facility can be utilised when a longer scan is needed so

that the large number of data points can still be stored in the limited computer memory size, bearing in mind also the respective aliasing zone. The sampling technique will be discussed later.

3.2.7 INFRARED SIGNAL CHANNEL

The broad band submillimetre radiation beam is provided by a high pressure mercury lamp (Philips 125-HPK) encapsulated in a quartz envelope. The lamp is enclosed inside a hollow copper cylinder with an aperture of about 7mm centred on the optical axis of the collimator unit. The lamp mount is cooled by the water circulated around it and is kept at constant temperature by using a temperature controller fitted inside the circulator. The radiation from the source is collimated before arriving at the beam divider by using a parabolic mirror and a plane mirror as shown in figure 3.1

At the output port, the signal is received by a Golay detector. The DC level of ≐17V present in the "null interferogram" is first reduced to ≐1V by a 22pF capacitor held in series before the signal can be amplified conveniently by the low noise operational amplifiers. The span of the amplified signal is then set to within a 0 to +10V range before entering the analogue input port of the ADC.

Golay detectors have been used throughout this work. One advantage of using a Golay detector is that it operates at room temperature. A choice of window materials enables different regions of the infrared spectrum to be studied.

The three window materials used in this work are diamond, quartz and CsI. Usually, a piece of dyed black polyethylene of an appropriate thickness is used to filter out any high frequency components beyond ≈800 cm^{-1}. A KI blank of ≈2 mm thickness could also be used to remove any low frequency components below ≈200 cm^{-1}. Filtering also protects the Golay from being overloaded. Figure 3.7 shows the transmission curves of the above mentioned windows. A power supply unit for the Golay has been built which uses three 12V car batteries connected in series. The unit gives very low noise DC output lines of +24V and +2.2V required by the Golay. The circuit diagram of the power supply unit is shown in figure 3.8

To provide a quick change in the amplifier gain from a background run to a sample run, a dual sensitivity amplifier has been designed. Each working range can be selected at the touch of a toggle switch. The ratio of amplification between the two runs which is required for later use, can then be easily measured. The electronic circuit diagram of the amplifier is shown in figure 3.9.

The Golay housing is wrapped with a piece of cloth during a scan. This is to eliminate any fluctuations in the DC level of the recorded interferogram due to ambient temperature changes.

Due to high water vapour absorption in the far infrared region, the instrument has to be evacuated to $\simeq 10^{-1}$ torr or lower before carrying out any room temperature measurement. This condition is obtained by connecting a rotary pump to the interferometer. For low temperature measurements, a

diffusion pump is used in order to attain a pressure of 10^{-6} torr so as to prevent the deposition of any ice on the specimen due to any small amount of moisture still present in the interferometer.

3.2.8 DIELECTRIC BEAM DIVIDERS

The dielectric beam dividers used in this work are made of mylar (polyethelene terephthalate) and are stretched taut on a metal frame. The frame is located in a slot cut across the diagonal of the central cube and is held securely with minimum force acting on it to avoid any deformation.

Since the beam divider is parallel sided, multiple internal reflections occur. Therefore not only primary reflected and transmitted beams must be considered but also all the other beams produced by internal reflection. The mylar beamsplitter is held at 45° to the incident radiation for ease of construction. At this angle, as shown by Bell (1972), the primary transmitted beam contains 83% of the unpolarised incident flux whereas the secondary transmitted beam contributes only 0.7%. The first, second and third order reflected beams contain 8.9, 7.4 and 0.07% of the incident intensity respectively. This is calculated on the assumption that the dielectric film is non-absorbing. Therefore, only the primary transmitted, and primary and secondary transmitted beams are important. The refractive index, n was taken to be 1.85. Due to multiple beam effects, the net reflectivity of the mylar film approaches zero when the optical path difference is an integral

multiple of wavelengths λ. Therefore, the condition for interference is

$$m\lambda = 2d\nu/[n^2-1/2]$$

where d is the thickness of the film. For constructive interference, m = 1/2, 3/2, 5/2... and for destructive interference, m = 0, 1, 2, 3 .... The above equation essentially governs the efficiency of the beam divider. The efficiency at $\nu = 1/\lambda = 0$ is zero as one reflected component has a phase shift of π with respect to the other and they thus interfere destructively. Figure 3.10 depicts the relative intensity in arbitrary units as a function of ν for various thicknesses of the dividers. Therefore, the right thickness of the film must be chosen in order to optimise the throughput energy in the spectral region under investigation. Below about 20 cm^{-1}, where the output energy from the lamp is very low, mylar beam dividers are not practical for use with Golay detectors since the S/N ratio obtained rapidly deteriorates.

The interferometer has to be re-aligned when the beam divider is changed from one thickness to another. With the help of the laser control channel, this can be carried out fairly quickly by locating the new beam splitter at the position where the largest laser signal is observed on the oscilloscope. In this way, the laser control channel is acting as a reference to the previously aligned position.

3.2.9 SPECIMEN CHAMBER

The specimen chamber is situated on the fixed mirror arm. The specimen to be studied can be inserted into the

beam without breaking the vacuum inside the interferometer, thus avoiding the introduction of systematic errors in the final output and removing the requirement for a stabilisation period (Birch,1980).

To perform low temperature measurements, a cold finger (dewar) was installed on the sample chamber. A flexible copper braid is used to provide good thermal contact between the copper mount holding the specimen and the copper base of the liquid nitrogen cold finger. The sample chamber has been re-designed to provide a larger internal volume so that the thickest possible copper braid could be used without it touching the wall of the interferometer. An intermediate nylon rod is fixed between the sample mount and the vacuum feedthrough rod to isolate the specimen thermally.

3.2.10 VIBRATION ISOLATION SYSTEM

The components that require isolation from any mechanical vibrational noise are placed on the optical table. The table top is a stack of three heavy slate slabs with a sheet of steel on the top. Screw thread holes can be tapped on the steel sheet for holding any interferometer components. Pipes connecting the interferometer and the rotary pump are padded with soft sponges placed between heavy lead blocks to eliminate any vibration which can be transmitted to the interferometer.

The vibration isolation stands (called MICRO-g) were obtained from Backer-Loring Corp. A continuous source of compressed nitrogen is used to maintain the operational

level although the flow rate is negligible once the isolator has been pressurised and raised to this level.

An earlier attempt to isolate the table from floor vibrations by using four solid steel cones fixed onto the base of wooden table legs was not successful.

3.3 SELECTING SCAN SPEEDS

The speed of the hydraulic drive is set such that the Fourier components in the chosen spectral region are modulated in the frequency band which matches the dynamic response of the detector. Figure 3.11 shows a selection of modulation frequencies of the far infrared spectral components at given laser fringe frequencies. To illustrate this, spectral response curves for several scan speeds are plotted, as shown in figure 3.12 using a Golay detector. It can be observed from figure 3.12 that the peak response of the Golay moves towards the lower wavenumber region as the scan speed is increased. Since the response of the Golay is between about 0.2 and 20 Hz, as can be seen in figure 3.13, any spectral components modulated outside this frequency band will be filtered out by the Golay. Thus the unwanted high frequency components can be removed in this way.

3.4 SAMPLING THE INTERFEROGRAM

This section explains aspects of sampling in a continuously driven interferometer. Since there is no reference to the starting position of a scan, the height of the maximum point and also its position in the recorded interferogram varies from one scan to another.

Figure 3.14 illustrates how 3 scans with 3 different starting points give rise to 3 different maximum positions. In this case, each interferogram is sampled at every 8 laser fringes by counting the fringes electronically before the signal reaches the ADC. Because of the variation in the positions of the maximum signal, the coherence of the shorter wavelength components in the interferograms will be degraded when the interferograms are co-added. It can be shown that in the worst case, where the positions of the maxima of 2 interferograms differ by $1/4\nu_{max}$, where ν_{max} is the aliasing frequency as defined in chapter 2, the average spectrum is the original spectrum modified by a cosine term

$$M(\nu) = |\cos(\pi\nu/4\nu_{max})|.$$

$M(\nu)$ is a smooth function as shown in figure 3.15 (Guangzhao, 1981).

To eliminate this problem, the interferogram is sampled at the interval equivalent to one fringe spacing of the monochromatic control channel. In this way, the height of the maximum signal and consequently its position varies only if the S/N ratio is poor. Once the maximum point has been established, the computer then selects the signal at intervals of every 8 laser fringes on both sides of the maximum point so that the sampling interval is still maintained at 8 laser fringes. However, with a limited memory space available, this method has the disadvantage that the computer arrays cannot hold large numbers of points and this limits the resolution. For a given number of points that can be stored in the arrays, the computer

can record 8 times longer optical path lengths if the interferogram is sampled electronically at every 8 laser fringes.

By comparing the stability of the laser fringes with the oscilloscope time base it was found that random fluctuations of the order of 1 or 2% of the wavelength occurred. This corresponds to a sampling accuracy of about 6 nm. This proves the superiority of the laser sampling technique over the mechanical stepping method.

An ADC interface board has been built for this work. The electronics layout is similar to that of Mok et al (1982) and detailed explanations of the hardware aspects of the design can be found in the publication. Essentially, a 12-bit ADC chip has been used on an 8-bit microcomputer, therefore requiring two input ports to read the digitised interferogram signal. The communication protocols that have been set up control the incoming analogue signal so that a particular A-D conversion is initiated only after the previous conversion has been completed. A computer program has been written to control this ADC interface circuit so that the data can be recorded correctly.

3.5 DATA ACQUISITION

The software that has been written for data acquisition is shown in figure 3.16. The specimen is placed in the fixed mirror arm and the interferograms are recorded by scanning the moving mirror away from the beam divider.

The procedure to record an interferogram is as follows. The hydraulic control box is first switched on to manual.

Since the piston travels some distance before it attains a constant speed, an allowance of about 1000 laser fringes (≈0.3 mm) is made before the actual starting position of the interferogram is reached. The control box is then switched on to automatic mode. The hydraulic drive is activated when a pulse from the microcomputer (Tuscan S100) is sent to the control box requesting a +12V supply line to be sent to the hydraulic solenoid. After the scan has been completed another pulse is sent to stop the drive. The computer then searches for a prominent point to act as a reference position. Once this point has been located, the data is trimmed to the required size. The time in searching for this prominent point is further reduced by selecting the data to be read only within the small region where it is situated. When the above process has been completed, the Tuscan once again sends another pulse to the hydraulic control box to request the drive to move in the forward direction. When it reaches the position where it has previously started, another pulse is sent so that the piston stops momentarily while waiting for the next order to start the reverse scan again. This cycle is repeated until the required number of scans has been completed.

When the S/N ratio in the specimen interferogram is poor causing ambiguity in the choice of a reference point, an extra subroutine is introduced in the program to tell the computer whether to accept or to reject that particular run. Once the acceptable specimen interferogram is established in the first run, then the rest of the interferograms scanned afterwards will only be accepted if

their prominent positions are less than 20 points from the first one. This is the situation where the pilot valves in the hydraulic unit become useful because they provide precise starting and stopping positions.

Therefore, once the hydraulic drive is switched on to the automatic multiple-scanning mode, no more manual work is needed.

3.6 THE PARTIAL INSERTION TECHNIQUE

An experimental technique known as the partial insertion technique is introduced in this DFTS work so that the gross phase shift associated with the shift of the interferogram due to the specimen can be recorded in a single continuous scan.

To obtain the phase shift with this technique, the sample is partially inserted into the beam so that the background and the sample interferograms are recorded in the same scan. Then the separation between the two maximum (or minimum) points is measured in terms of the number of laser fringes. Therefore, the phase shift can now be obtained to an accuracy of one laser fringe provided that sampling is carried out at every laser fringe.

The technique can also be used for co-adding noisy specimen interferograms (typically with the S/N ratio of about 3). This can be done by partially withdrawing the sample from the beam so as to produce a very small "blip" of a background interferogram to act as a reference position for the process of co-adding. This small reference signal is later removed from the averaged interferogram.

3.7 INSTRUMENT TEST RESULTS

As a prerequisite to carrying out further work, the interferometer system was tested by choosing water vapour as a test sample. Since water vapour spectral lines are already well established, comparisons can then be made with confidence.

The interferometer was partially filled with atmospheric air and a high resolution run of 0.25 cm^{-1} was taken. The water vapour and the background spectra are shown in figures 3.17(a),(b) and the ratio spectrum is depicted in figure 3.18. The spectral components obtained are in excellent agreement with the data of Rao et al (1966). A section of the ratio spectrum is picked out as shown in figure 3.19 and the spectral lines from this figure are listed in table 3.1

The dramatic improvement in the performance of the laser-controlled interferometer compared with the original step-driven interferometer is illustrated in figures 3.20(a) and (b). The amplitude spectrum of a single crystal of GaP obtained with the step-driven interferometer is shown in figure 3.20(a) and a spectrum obtained with the laser-controlled interferometer is shown in figure 3.20(b). It is quite obvious that the spectral reproducibility of figure 3.20(b) is far superior to that of figure 3.20(a) even though the time taken to record the interferograms for figure 3.20(a) is about 20 times longer. (Two GaP crystals with thicknesses differing by about 20μm were used for these measurements). Details of the analytical procedures required to obtain these results are given in chapter 5.

References to chapter 3

Activ-Air Automation Ltd., Belmont, Sutton, Surrey.

Backer-Loring Corp., Peabody, Massachussetts, USA.

Bell R J; "Introductory Fourier transform spectroscopy", Academic Press, New York (1972).

Birch J R; J. Phys. E: Sci. Instrum. 13, 716 (1980).

Burton N J and Parker T J; Int. J. Infrared and Millimeter Waves 5, 803 (1984).

Ealing-Beck Ltd., Watford, England.

Guangzhao Z; internal reports, Westfield College (1981).

Martin D H and Puplett E; Infrared Phys. 10, 105 (1970).

Mok C L, Burton N J and Parker T J; Int. J. Infrared and Millimeter Waves 3, 331 (1982).

Parker T J, Chambers W G, Ford J E and Mok C L; Infrared Phys. 18, 571 (1978).

Rao K N, Humphreys C J and Rank D H; "Wavelength standards in the infrared", Academic Press, New York (1966).

Scientifica-Cook Ltd., Acton, London.

SPECAC Ltd., St. Mary Cray, Orpington, Kent.

Steeg M J H, Jongbloets H W H M, Stoelinga J H M, Heijden R W, Van Vucht R J M and Wyder P; Infrared Phys. 20, 121 (1980).

Zachor A S; Appl. Optics 16, 1412 (1977).

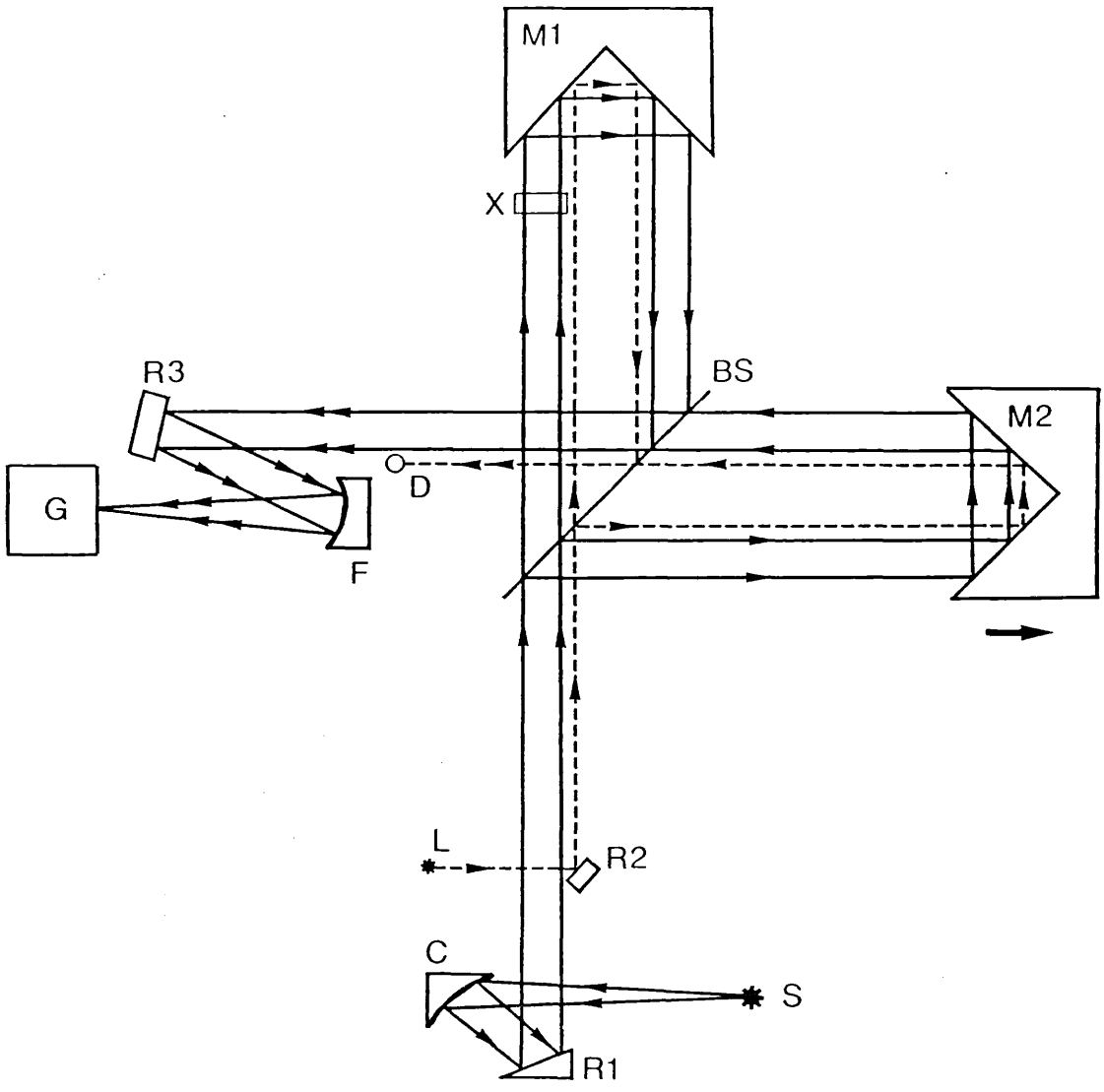

Figure 3.1 Schematic diagram of the single pass transmission interferometer. Continuous lines represent the infrared channel and broken lines represent the monochromatic control channel.

Key: S infrared source (Hg lamp), L monochromatic source (laser), M1 fixed mirror, M2 moving mirror, BS beam splitter, C collimating mirror, F focussing mirror, R1, R2 and R3 plane mirrors, G Golay detector, D photodiode detector, X specimen.

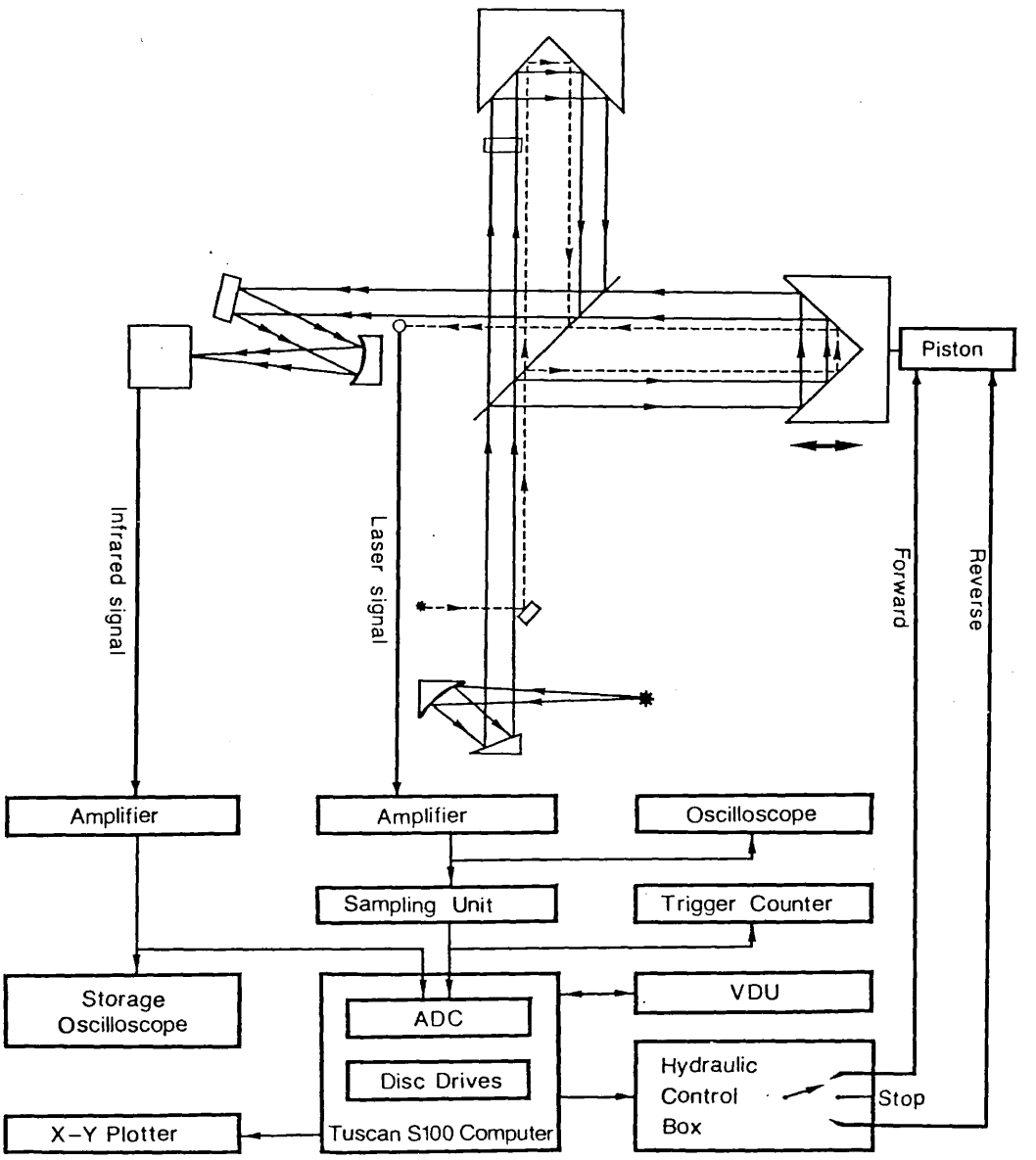

Figure 3.2 Block diagram of the interferometer and data acquisition system

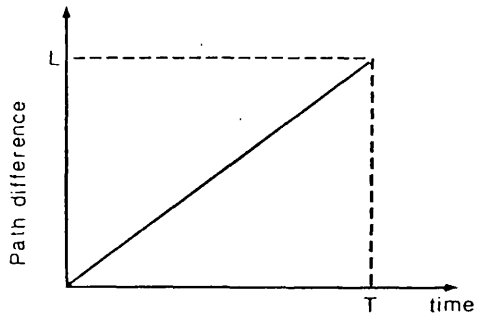

(a)

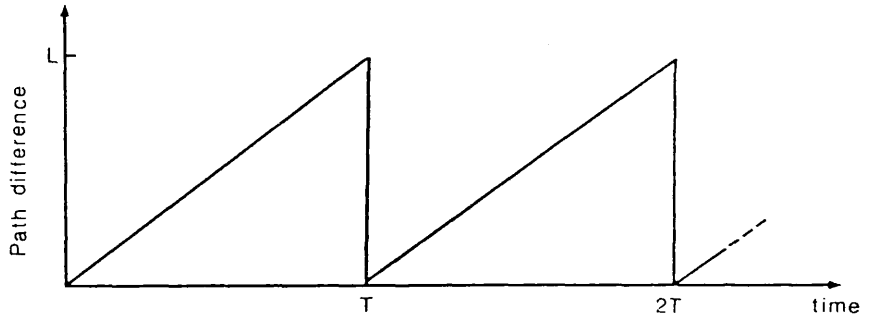

(b)

Figure 3.3 (a) The variation of path difference as a function of time in a continuous scanning interferometer. (b) The implicit repetition that develops from one-directional multiple scanning.

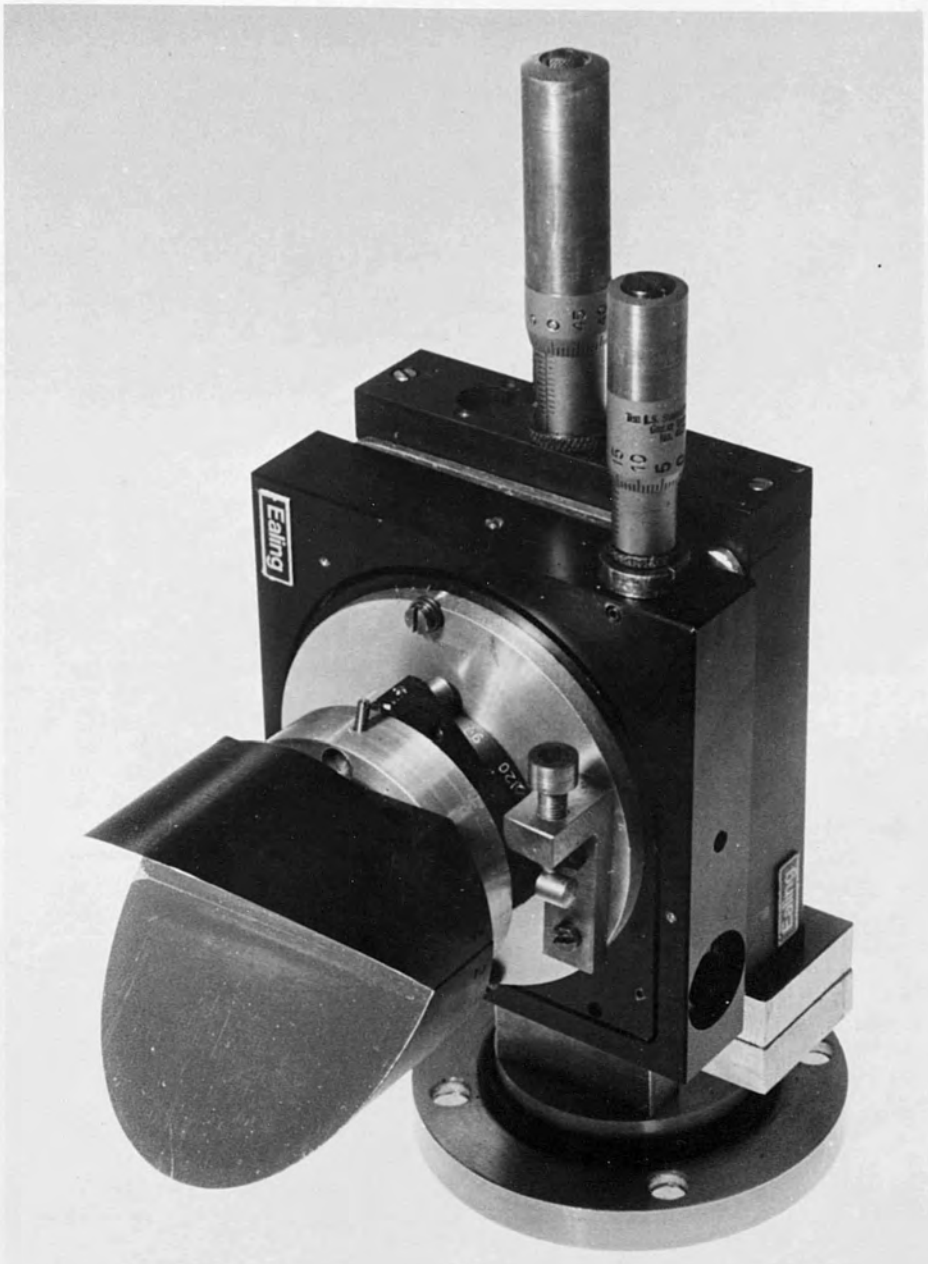

Figure 3.4 Picture of the complete assembly of the rooftop reflector at the fixed mirror arm.

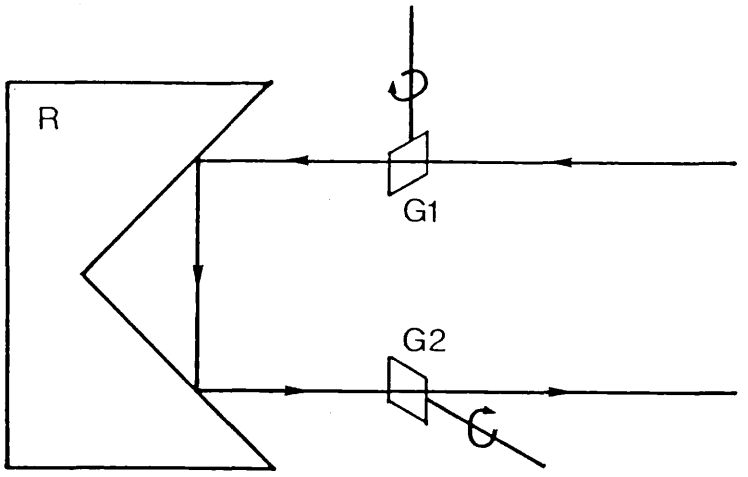

Figure 3.5 The mechanism for the alignment of the laser beam.

Key: G1 and G2 small glass plates

R rooftop reflector.

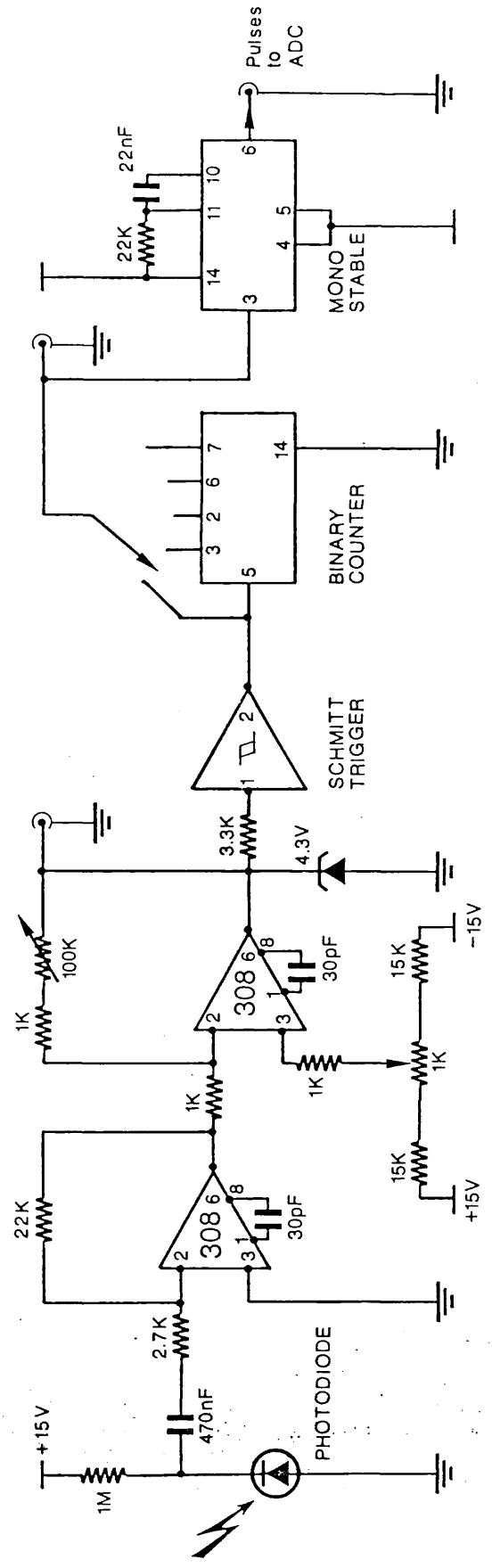

Figure 3.6 Circuit diagram for the laser fringe amplifier and counter.

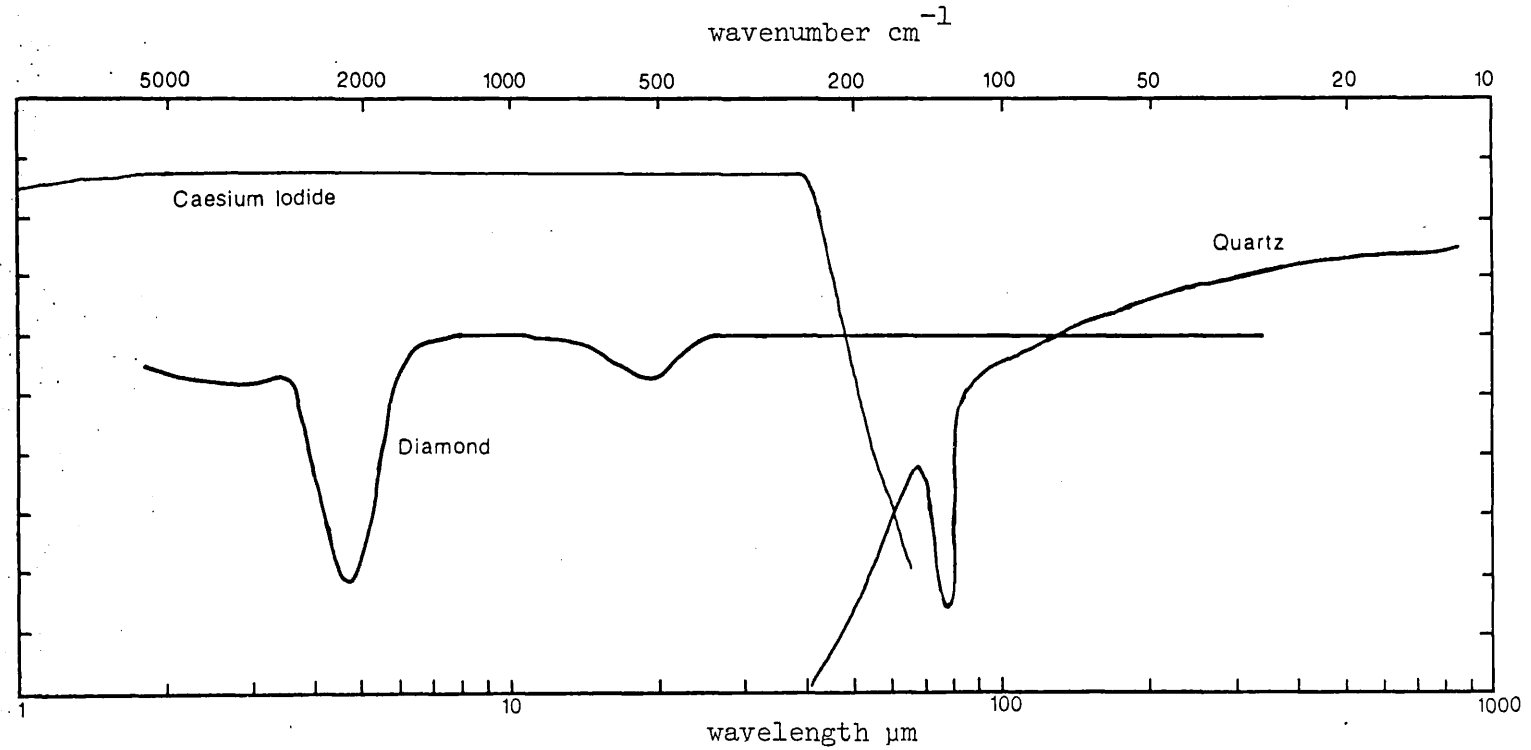

Figure 3.7 Transmission curves for various Golay windows.

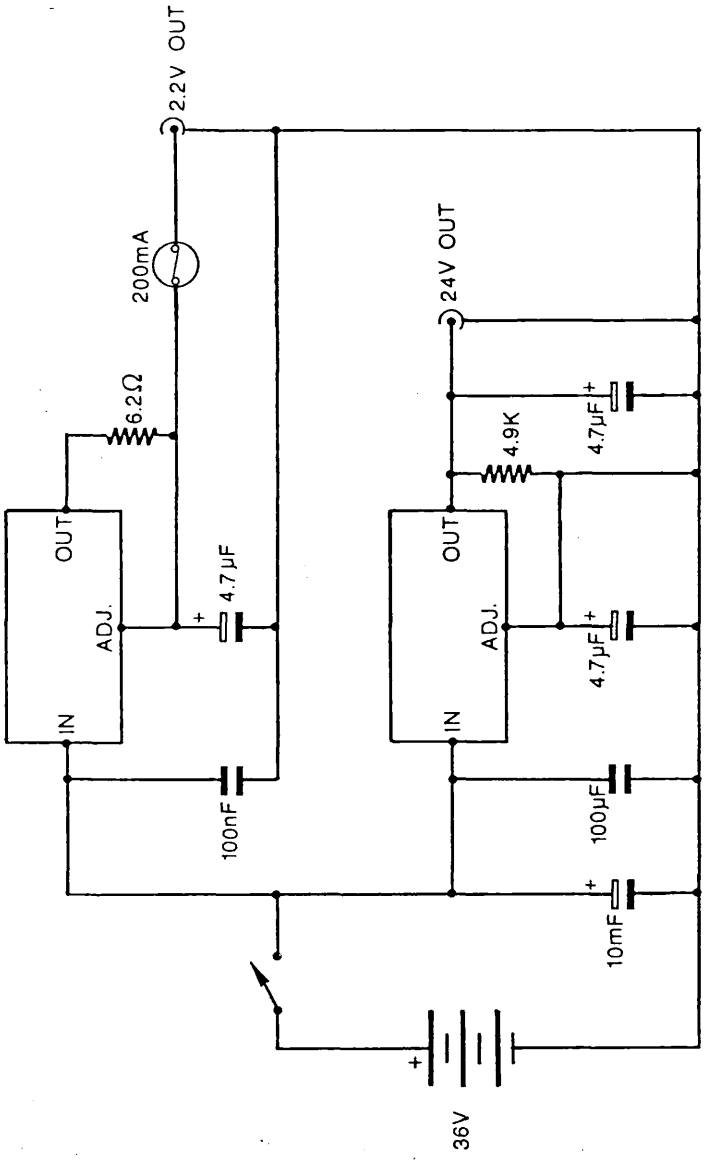

Figure 3.8 Circuit diagram for the Golay power supply.

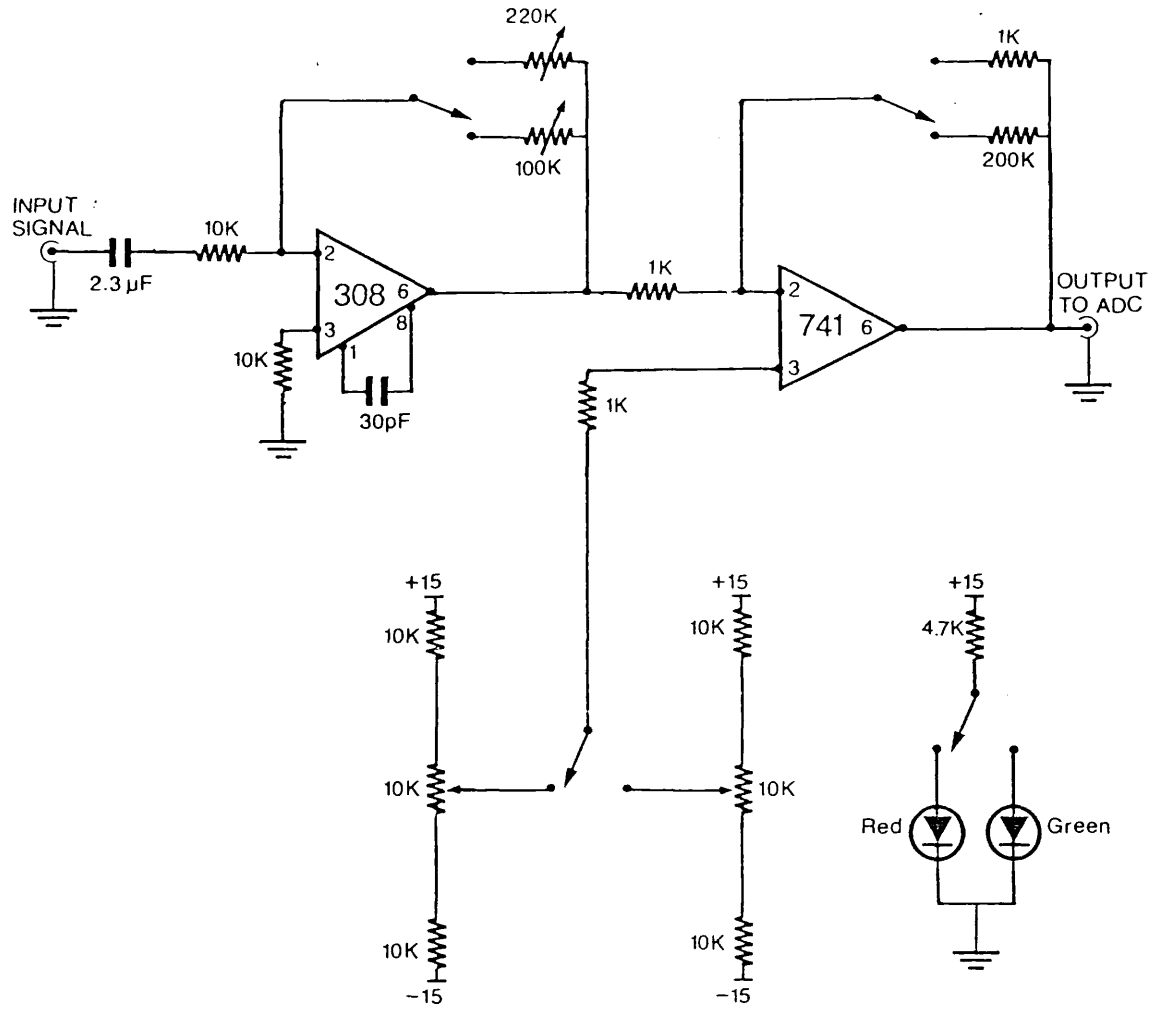

Figure 3.9 Circuit diagram for dual sensitivity infrared signal amplifier.

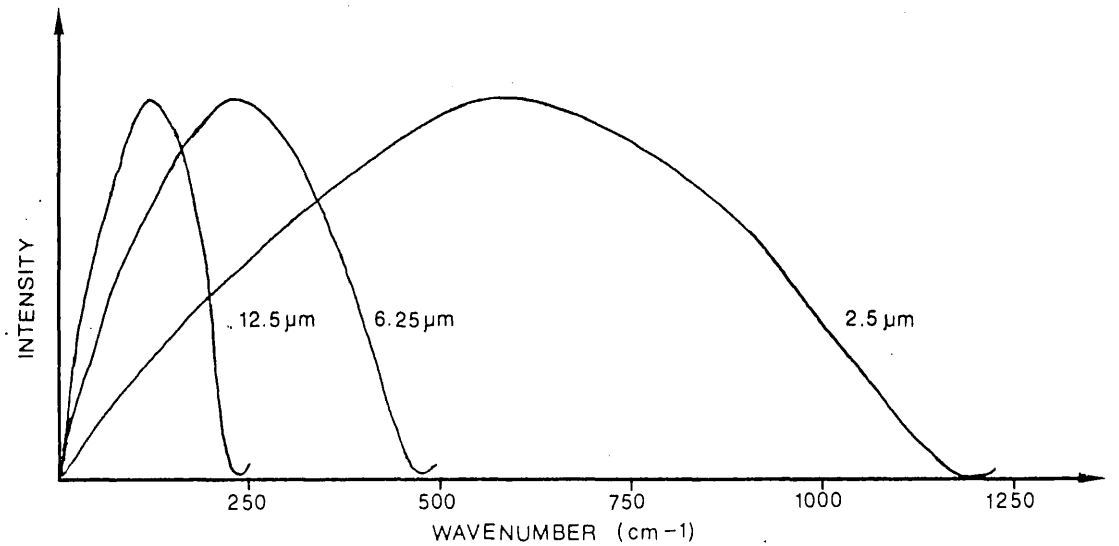

Figure 3.10 First order interference fringes produced by a mylar beam divider.

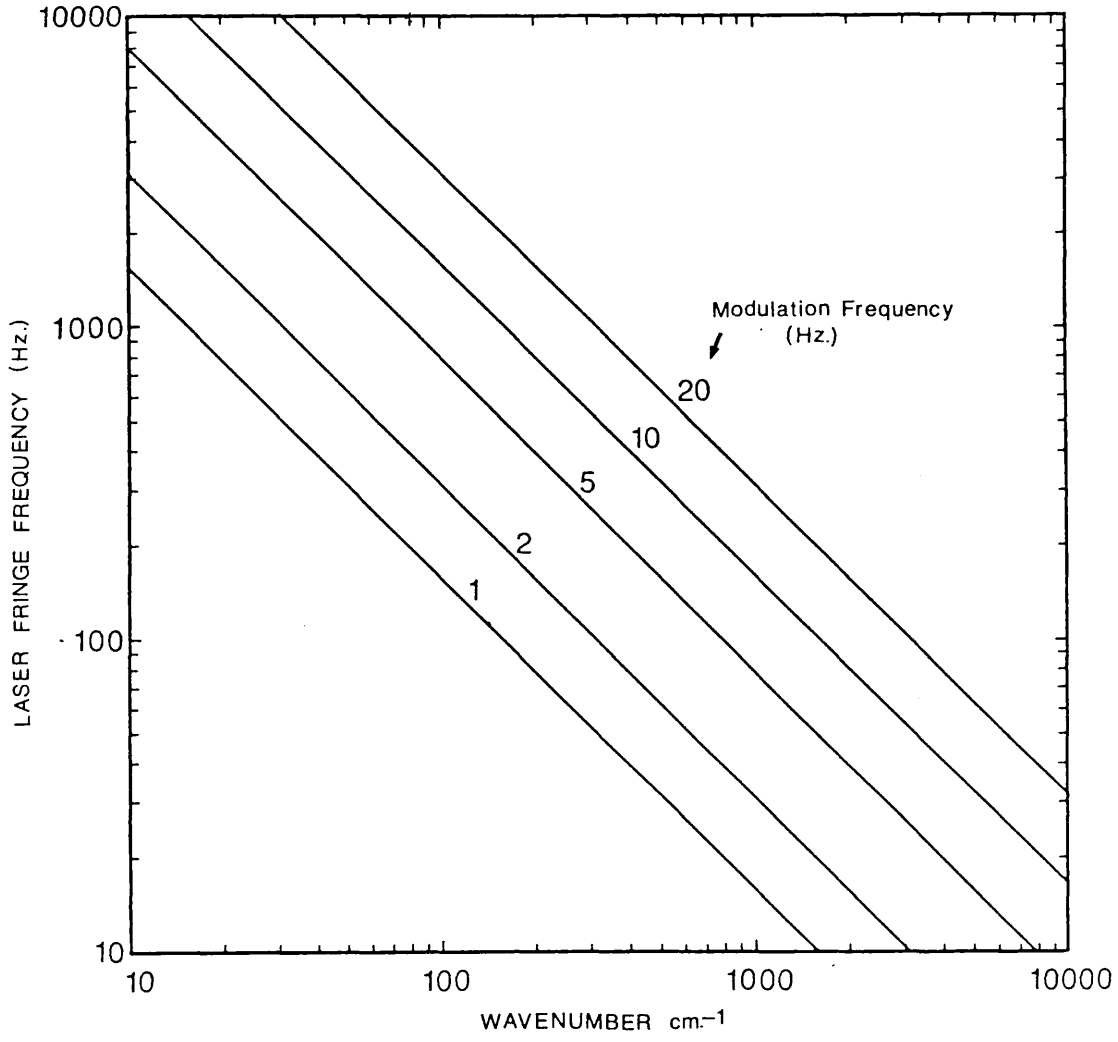

Figure 3.11 Plot of laser fringe frequency versus wavenumber for a selection of modulation frequencies.

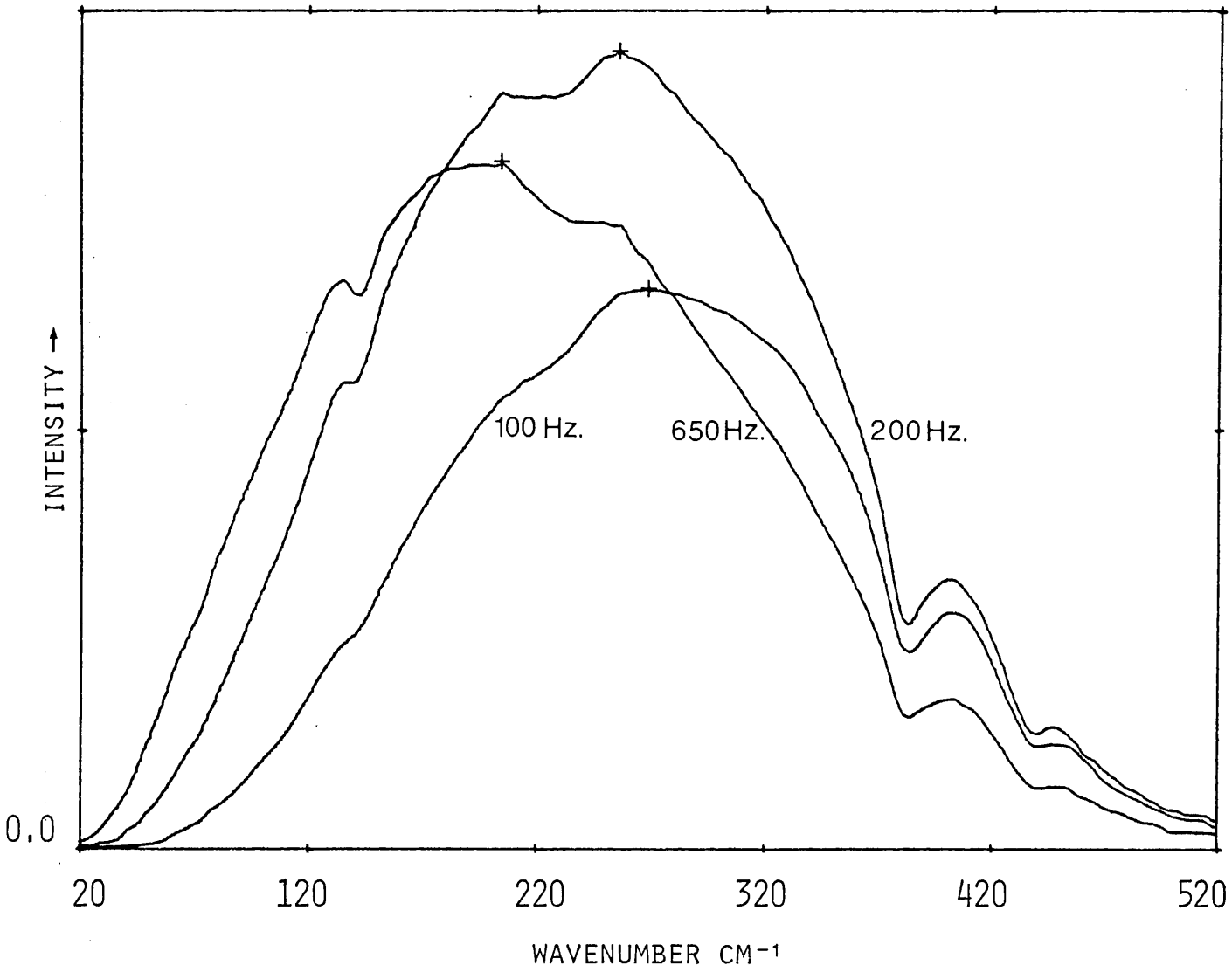

Figure 3.12 Spectral response of the Golay at various laser fringe frequencies.

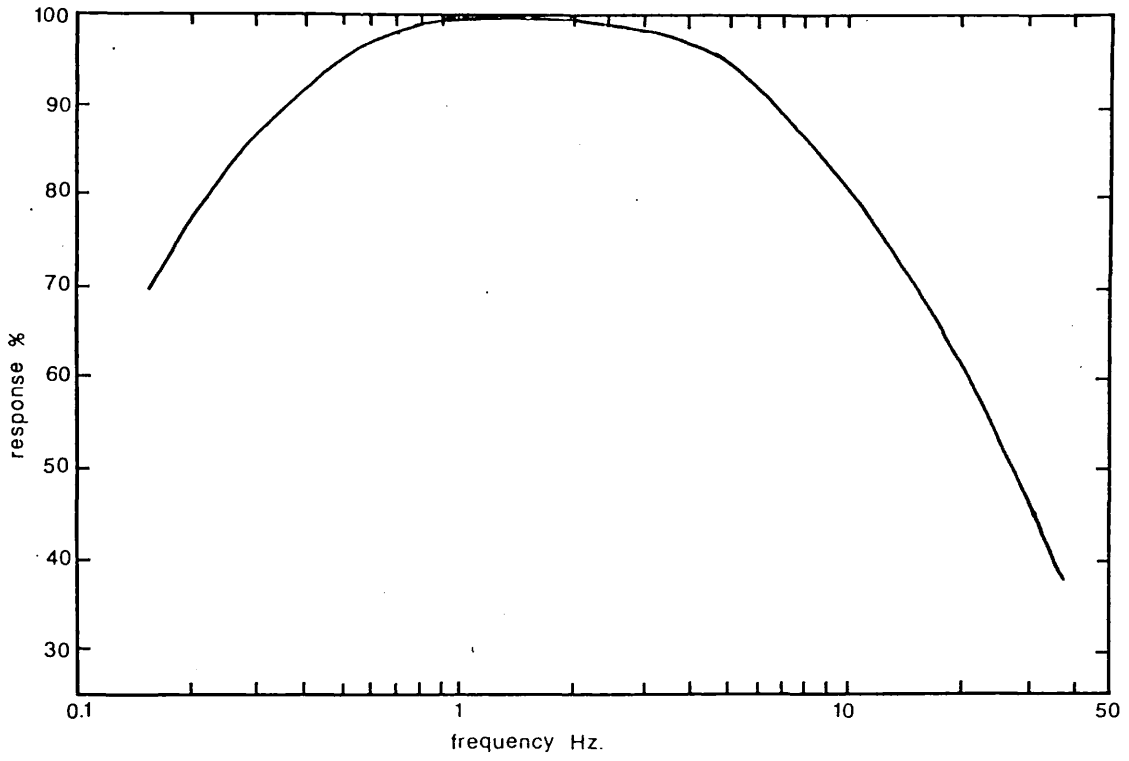

Figure 3.13 Plot of the Golay response versus frequency of modulated infrared signal.

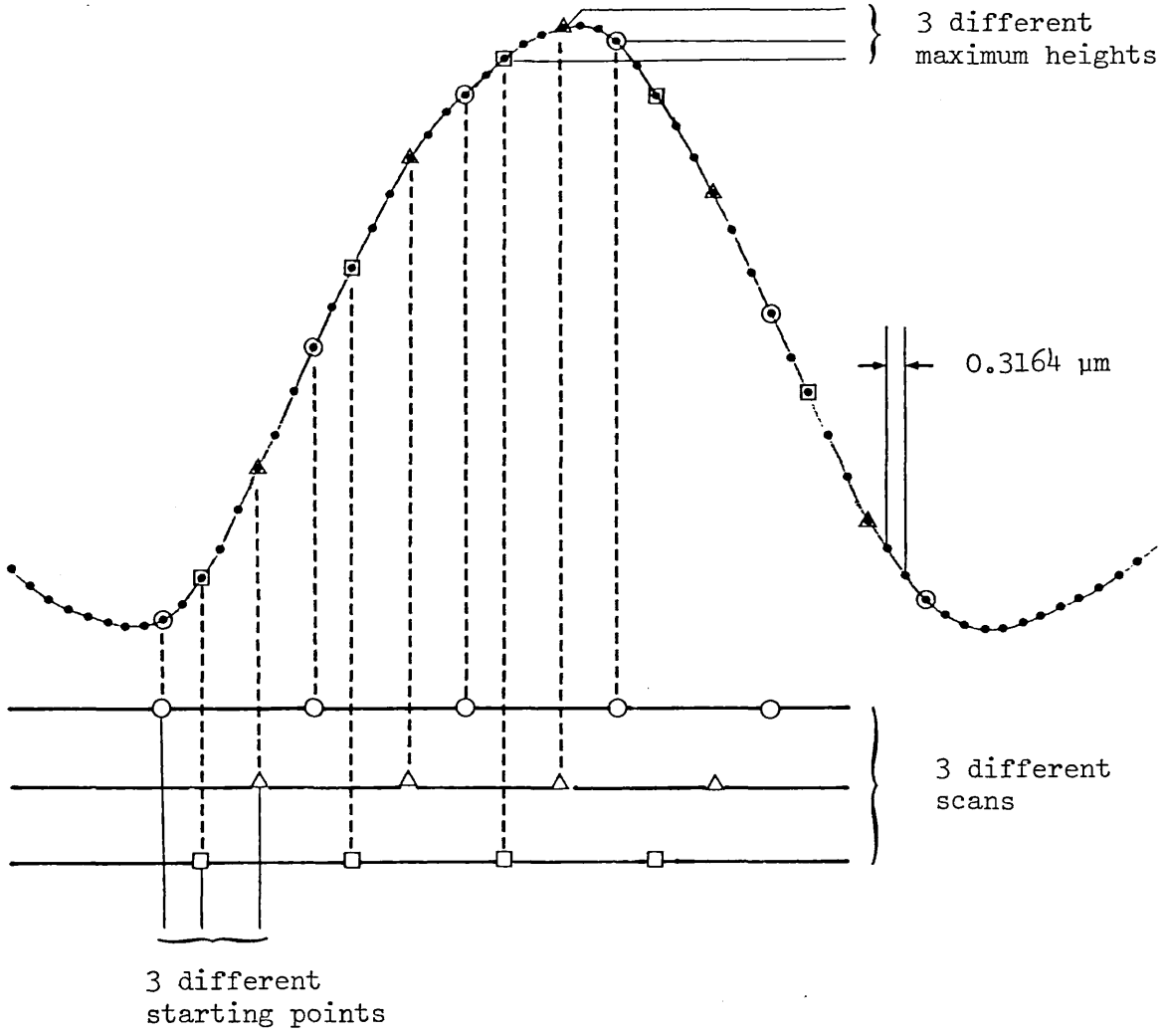

Figure 3.14 Diagram showing the effect of electronic sampling at every 8th. laser fringe.

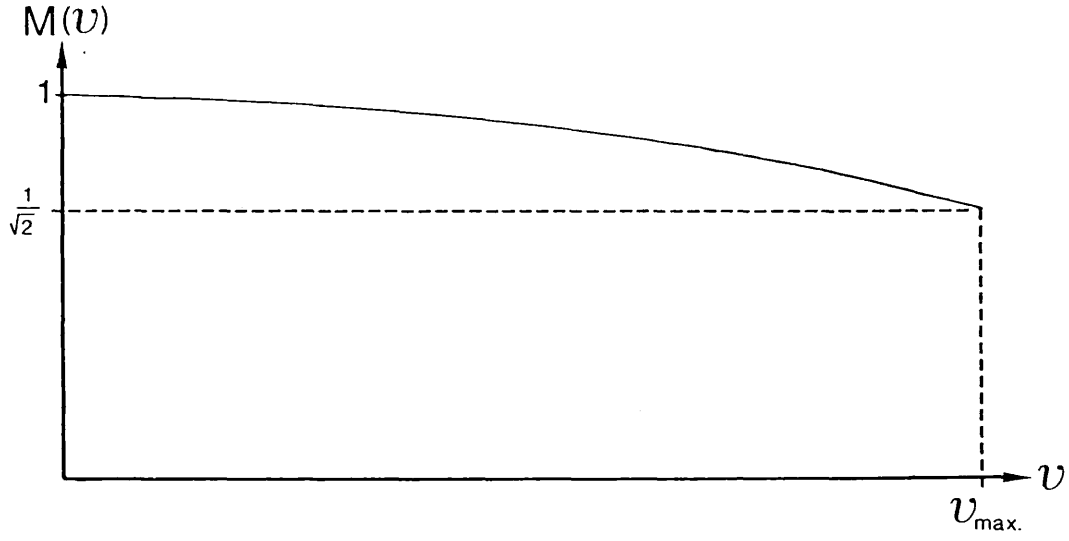

Figure 3.15 Diagram showing the spectral decay curve which results from co-averaging two interferograms when the maximum positions differ by $1/4\nu_{max}$.

Figure 3.16(a) Pascal program for data acquisition.

```
program scan(input,output);
label 1,2,4;
type    twobyte= 0..32000;
        intarray = array [1..16000] of twobyte;
var     nend : twobyte;
        bal : intarray;
        ba : array [1..2048] of real;
        y,pos,ref : string[2];
        fname1: string[14];
        st,fi,p,q,l,i,j,k,a,b,c,d,from,stara: integer;
        shift,z,max,min,imin,noof,nsave,nscan: integer;
procedure rscan(var bal : intarray;nend : twobyte);external;
procedure tscan(nend : twobyte):external;
procedure store;
var i: integer;
f: file of twobyte;
begin
        assign(f,fname1);rewrite(f);
        for i:=1 to nsave do write(f,trunc((ba[i]/nscan)+0.5));
end;

                        (* main program *)
begin
1: writeln;
  writeln('Multiple-scanning and sampling every laser fringe');
  writeln('then dividing by no. of fringes per point');
  writeln('& set the start point from prominent position.');
  writeln('Locate range to search for prominent position.');
  writeln;
  write('Filename to be stored: '); readln(fname1);
  write('Press either s for min. or b for max. position: ');
  readln(pos);
  write('Press either w for with ref. or t for without: ');
  readln(ref);
  write('Number of data points : ');readln(nend);
  write('Laser fringes per point : '); readln(noof);
  write('No. of points to save : '); readln(nsave);
  write('No. of points to start from zpp.: '); readln(from);
  write('Start searching for prominent pt.at: '); readln(st);
  write('Stop searching at: '); readln(fi);
  write('No. of scans : '); readln(nscan);
  for i:=1 to nend do bal[i]:=0; (* clears integer buffer *)
  for i:=1 to nsave do ba[i]:=0; (* clears real buffer *)
  imin:=1;
2:for z:=1 to  nscan do
  begin
    shift:=imin;
    rscan(bal,nend);
max:=bal[1]; min:=bal[1];
```

```
for i:=st to fi do
  begin
    if (pos='s') then
    begin
    if max<bal[i] then max:=bal[i];
    if min>bal[i] then begin min:=bal[i]; imin:=i; end;
    end
    else
    begin
    if max<bal[i] then begin max:=bal[i]; imin:=i; end;
    if min>bal[i] then min:=bal[i];
    end;
  end;
if z=1 then begin
                writeln('Prominent pt. was at ',imin);
                write('Want this first run data: ');readln(v);
                 if (v='n') then begin z:=0; goto 4; end;
                 shift:=imin;
              end;
 if (imin-shift=0) then shift:=imin-1;
 if (ref='w') then
 begin
 if (sqr(imin-shift) > 400) then
         begin z:=z-1; imin:=shift; goto 4; end;
 end;
 stara:=imin - (from * noof);
 if (stara+(nsave*noof) > nend) or (imin-from <0)
 then    begin
         writeln('Points to be saved exceeds ifq. points');
         goto 1; (* re-run *)
         end;
 for i:=1 to nsave do
   begin
     if nscan = 1 then ba[i]:=0;
     ba[i]:=bal[stara-noof+j*noof] + ba[i];
   end;
 for i:=1 to nend do bal[i]:=0;
 writeln('Reverse scan ',z,' completed');
 writeln('ADC range is ',max - min,' with ZP at ',imin);
 4:  fscan(nend);
   for p:=1 to 2000 do q:=10*p; (* pause loop *)
   if z=0 then goto 2;
 end;
 store;
 write('Another run ? '); readln(v);
 if (v='y') then goto 1;
 end.
```

Figure 3.16(b) Z-80 assembly language subroutine.

```
            .Z80
            .radix 10
            ENTRY rscan,fscan

porta       EQU 71H
portb       EQU 70H
delval      EQU 100

rscan:      POP IY              ;remove link
            POP HL              ;setup
            POP DE
            LD BC,1

            CALL pulse                  ;reverse scan

            XOR A
rloop1:                         ;loop test
            SBC HL,BC
            JP M,rexit

rloop2:     IN A,(porta)        ;wait until ADC is ready
            AND 10H
            JR Z,rloop2

            CALL delay          ;delay for program to work

            IN A,(portb)        ;get lower byte from ADC
            LD (DE),A
            INC DE

            IN A,(porta)        ;get upper byte
            AND 0FH
            LD (DE),A
            INC DE
            JR rloop1

rexit:      CALL pulse                  ;stop scanning
            OUT (6H),A
            PUSH IY
            RET


fscan:      POP IY
            POP HL                      ;setup
            LD BC,1

            CALL pulse                  ;forward scan

            XOR A
floop1:                         ;loop test
            SBC HL,BC
            JP M,fexit
```

```
floop2: IN A,(porta)     ;wait for ADC
        AND 10H
        JR Z,floop2

        CALL delay

        IN A,(portb)

        JR floop1

fexit:  CALL pulse              ;stop scanning
        PUSH IY
        RET

pulse:  LD A,1
        OUT (6H),A
        CALL delay
        LD A,0
        OUT (6H),A
        RET


delay:  EXX
        LD B,delval
dloop:  DJNZ dloop
        EXX

        RET


        END
```

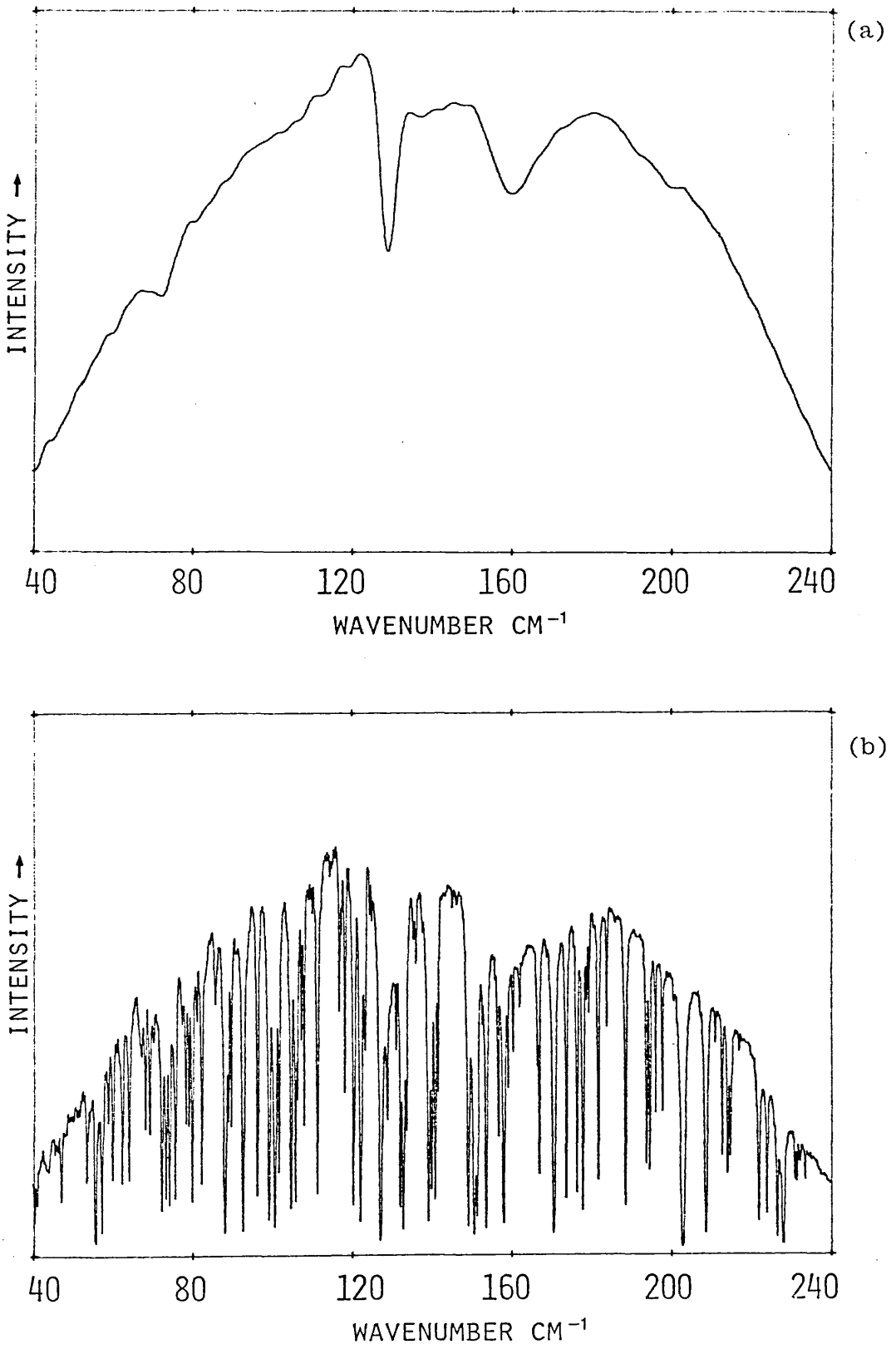

Figure 3.17 (a) Background spectrum between 40 and 240 cm^{-1}

(b) Water vapour spectrum between 40 and 240 cm^{-1}.

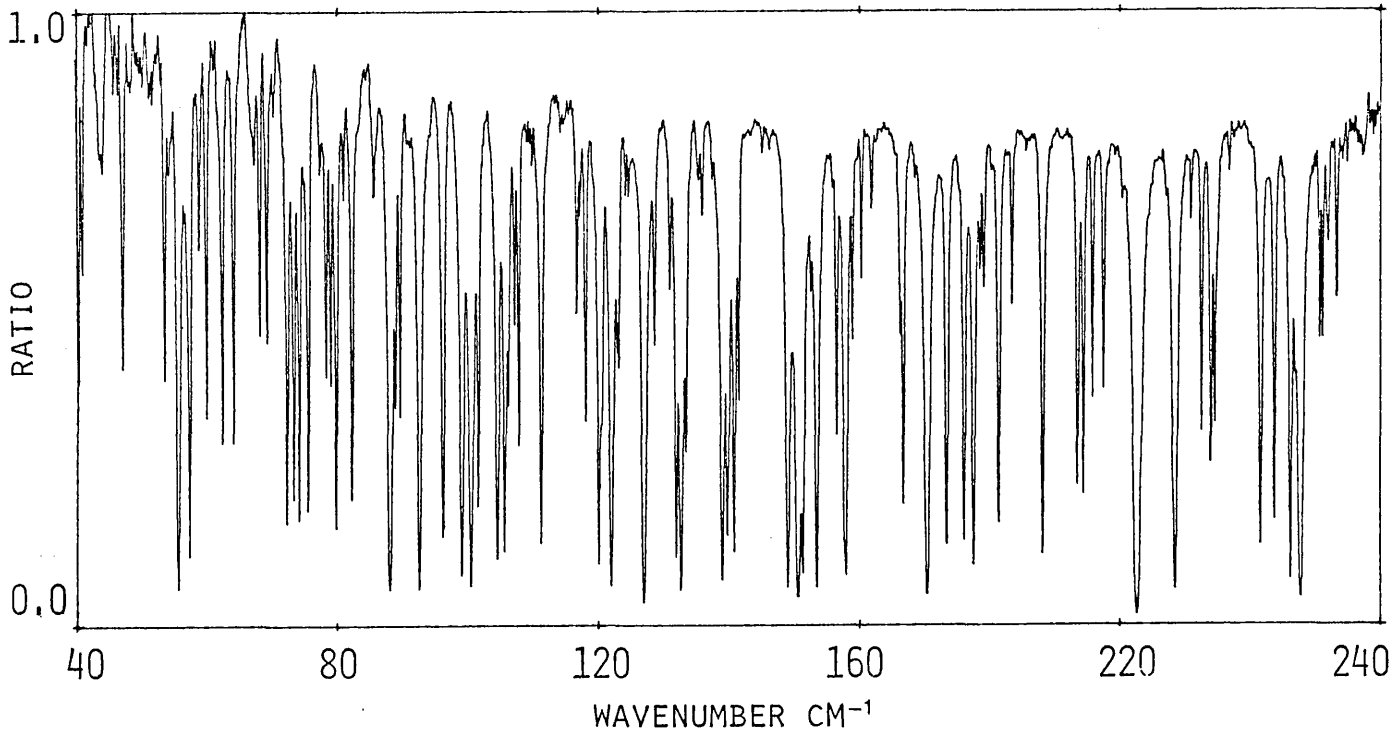

Figure 3.18 High resolution (0.25 cm^{-1}) spectrum of water vapour obtained by ratioing the two spectra shown in figure 3.17.

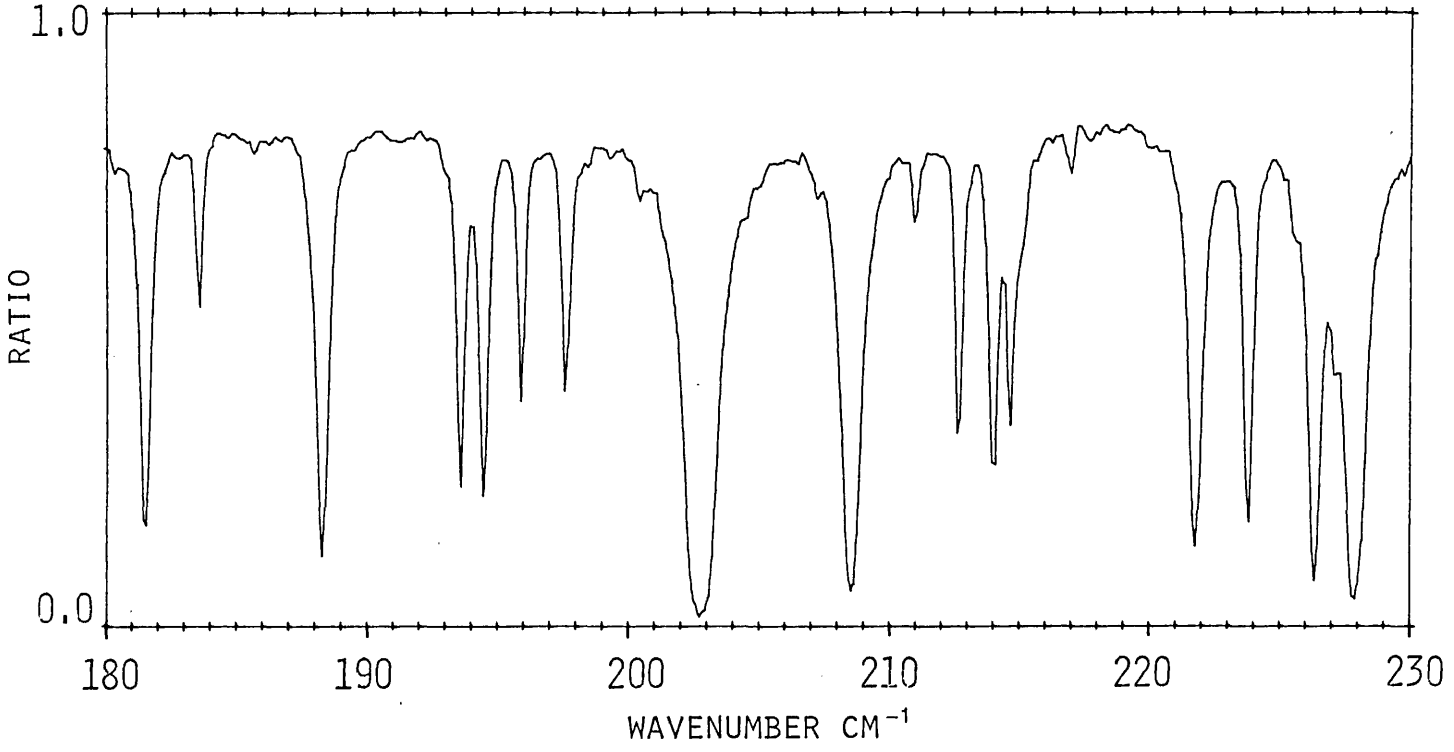

Figure 3.19 Spectrum showing the water vapour spectral lines between 180 and 230 cm^{-1}.

This work (cm^{-1})	Rao et al.(cm^{-1})
181.4	181.4
183.5	183.46
188.2	188.21
193.5	193.45
194.4	194.37
195.9	195.83
197.5	197.45
202.6	202.6
208.5	208.46
212.6	212.59
214.0	213.95
214.6	214.59
221.7	221.67
223.8	223.72
226.3	226.27
227.8	227.83

Table 3.1 Water vapour spectral lines between 180 and 230 cm^{-1}

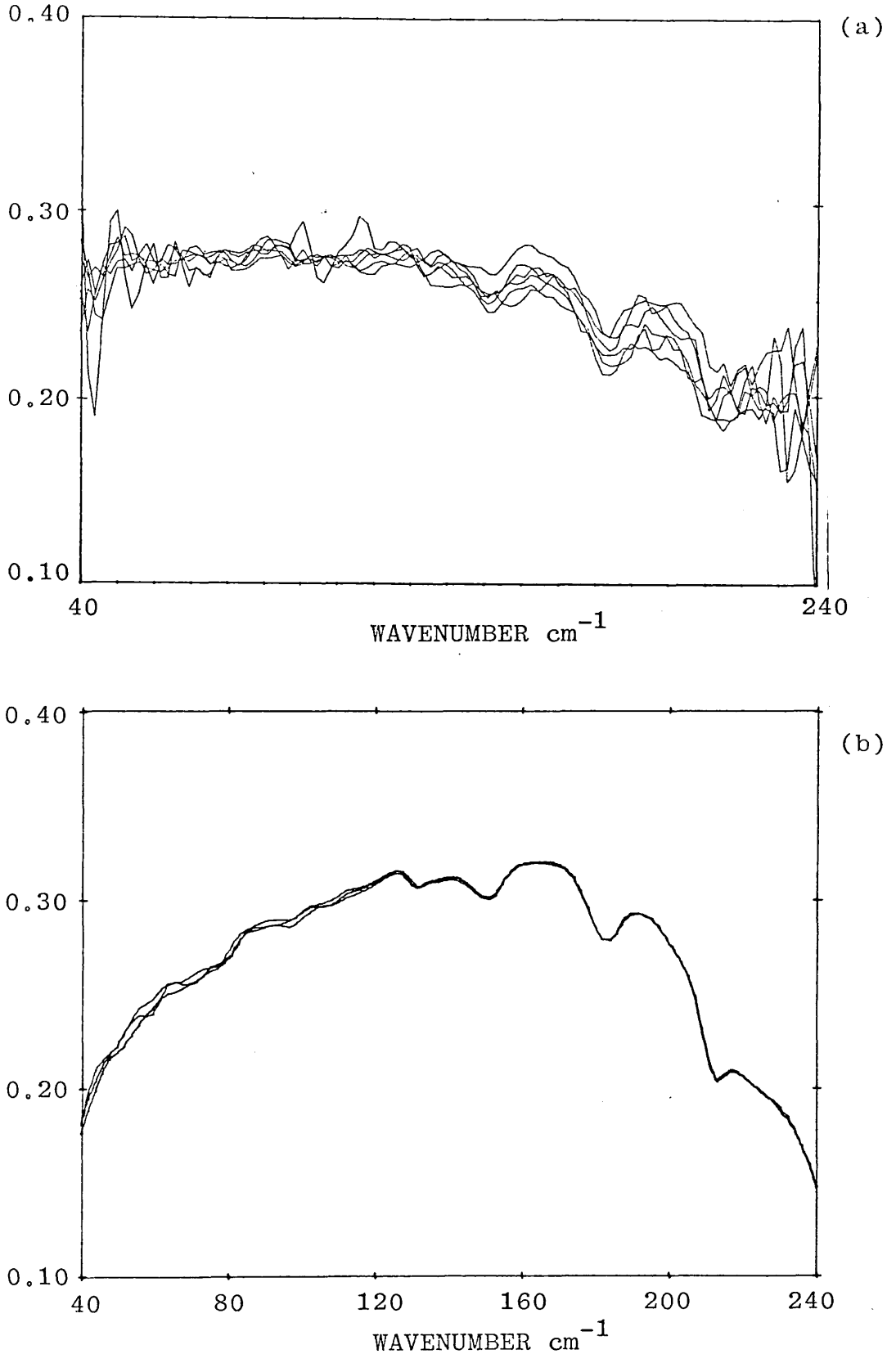

Figure 3.20 Comparison of the amplitude transmission spectra of GaP obtained with (a) step driven interferometer and (b) laser-controlled interferometer.

Chapter 4

FAR INFRARED PROPERTIES OF BINARY CRYSTALS

4.1 INTRODUCTION

In this chapter, the theoretical aspects of the optical and dielectric properties of ionic crystals in the far infrared will be discussed. The classical description of the dielectric response of a simple harmonic oscillator can lead to a fairly satisfactory phenomenological description of the main features of the lattice response of an ionic crystal. However, this theory is insufficient to explain the finer details of the observed spectra of real crystals because it neglects the contributions from the non linear dipole moment and anharmonic terms in the interatomic displacements. A modified form of dielectric response is obtained by taking into account the lattice anharmonicity present in real crystals. The expressions for the anharmonic self-energy of the transverse optic mode at the wave vector $q \approx 0$ will be shown. The importance of non linear dipole absorption in zinc blende structure crystals will also be discussed.

The temperature dependence of two-phonon combination bands will be discussed by considering the net number of phonons created or annihilated in two-phonon processes. At the end of the chapter, the selection rules for the interactions of light with phonons will be pointed out.

4.2 DISPERSION RELATION IN BINARY LATTICES

It is well-known that the Born-Von Karman model of the vibration of a diatomic linear chain gives rise to two branches of the phonon dispersion curves called the acoustic and optical branches (Dekker, 1975). The difference between these two branches can be observed in the plot of angular frequency $\underline{\omega}$ versus wave vector $\underline{q}$ where the acoustic branch is identified by the fact that $\underline{\omega}(\underline{q})\rightarrow 0$ as $\underline{q}\rightarrow 0$ whereas the optic branch has a finite value as $\underline{q}\rightarrow 0$. In an optical branch at zero wavevector the motion of two atoms of opposite charges gives rise to a net oscillatory dipole moment which is totally absent in the acoustic branch where the opposite charges move in unison. Because of the presence of a dipole moment in the long wavelength limit of the optical branch, the electric vector associated with the electromagnetic radiation which passes through the crystal can couple directly with the $\underline{q}\approx 0$ optical phonon under the condition in which the frequencies and wavevectors of the participating photons and phonons are equal. In general, for a crystal with N atoms per unit cell, there are (3N-3) optical branches and 3 acoustic branches. The numerology of the branches follows from the number of degrees of freedom of the atoms. Hence, for binary crystals there are 3 optical and 3 acoustic branches.

The essential ideas underlying the dielectric response involve the interaction of lattice vibrations and electromagnetic radiation. In first order, the only lattice

vibrations which contribute to the dielectric constant are those for which $\underline{q} \approx 0$ (Donovan and Angress, 1971). The propagation of electromagnetic waves and lattice vibrations is not independent and the modified wave is a combination of electromagnetic and mechanical vibrations (Born and Huang, 1954).

For diatomic ionic crystals having cubic symmetry, the theory of optical vibrations with $\underline{q} \approx 0$ can be explained phenomenologically in terms of the macroscopic electric field and the relative displacement of the two ions in a unit cell. The theory is fully embodied in the following pair of equations of motion (Born and Huang, 1954) :

$$\ddot{\underline{w}} = b_1 \underline{w} + b_2 \underline{E} \qquad (4.1)$$

$$\underline{P} = b_2 \underline{w} + b_3 \underline{E} \qquad (4.2)$$

where $\underline{w}$ is the macroscopic sublattice displacement which can be written as

$$\underline{w} = \left[\frac{M^*}{V} \right]^{1/2} (\underline{u}_+ - \underline{u}_-) \qquad (4.3)$$

and $(\underline{u}_+ - \underline{u}_-)$ is the relative displacement of the ions, M^* is the reduced mass of the ions, b_1, b_2 and b_3 are the scalar coefficients and V is the volume of the unit cell. $\underline{P}$ and $\underline{E}$ are the dielectric polarisation and macroscopic electric field respectively and they are related by

$$\underline{E} + 4\pi \underline{P} = \epsilon \underline{E} \qquad (4.4)$$

where ϵ is defined here as the real part of the dielectric constant of the crystal.

If $\underline{w}$, $\underline{E}$, and $\underline{P}$ are assumed to vary with time as

$$(\underline{w}, \underline{E}, \underline{P}) = (w_0, E_0, P_0)\, e^{-i\nu t} \qquad (4.5)$$

then the polarisation $\underline{P}$ can now be written as

$$\underline{P} = \left[b_3 - \frac{b_2^2}{b_1 + \nu^2} \right] \underline{E} \qquad (4.6)$$

By comparing Eq.(4.6) with Eq.(4.4) a simple type of dielectric response can then be obtained in the following form:

$$\epsilon = 1 + 4\pi b_3 - \frac{4\pi b_2^2}{b_1 + \nu^2} \qquad (4.7)$$

which is more generally written as

$$\epsilon = \epsilon_\infty + \frac{(\epsilon_0 - \epsilon_\infty)\, \nu_0^2}{(\nu_0^2 - \nu^2)} \,. \qquad (4.8)$$

In this expression ν_0 is the infrared dispersion frequency, at which the dielectric constant and refractive index become infinitely large, and ϵ_∞ and ϵ_0 are the limiting high frequency and static values of the dielectric constant respectively. By comparing Eq.(4.7) with Eq. (4.8), the scalar coefficients can now be obtained in terms of measurable quantities i.e,

$$b_1 = -\nu_0^2,\ b_2 = (\epsilon_0 - \epsilon_\infty)^{1/2} \text{ and } b_3 = (\epsilon_\infty - 1)/4\pi \qquad (4.9)$$

The type of response function given by Eq.(4.8) can be used to interpret the response of the crystal to the radiation of frequency ν in terms of the lattice vibrations.

When Eqs.(4.1) and (4.2) are solved simultaneously with Maxwell's equations assuming that $\underline{w}$, $\underline{P}$, $\underline{E}$ and the associated magnetic field $\underline{H}$ all vary as $e^{i(\underline{q}.\underline{r} - \nu t)}$ then the following expressions are obtained:

$$\underline{q} \,.\, (\underline{E} + 4\pi\underline{P}) = 0 \qquad (4.10)$$

$$\underline{q} \,.\, \underline{H} = 0 \qquad (4.11)$$

$$\underline{q} \times \underline{E} = \frac{\nu}{c}\, \underline{H} \qquad (4.12)$$

$$\text{and } \underline{q} \times \underline{H} = \frac{-\nu}{c}\, (\underline{E} + 4\pi\underline{P}) \qquad (4.13)$$

By recognising that $\underline{E}$ cannot vanish as this gives the trivial case $\underline{E}=\underline{H}=\underline{P}=\underline{w}=0$, Eqs.(4.4) and (4.10) yield

$$\epsilon(\nu)[\underline{q} \cdot \underline{E}] = 0 \qquad (4.14)$$

where $\epsilon(\nu)$ is given by Eq.(4.7).

Two alternative possibilities are admitted in the solution of (4.14) namely, either $\epsilon(\nu)=0$ or $(\underline{q}.\underline{E})=0$. First, in the case where $\epsilon(\nu)=0$, it follows from Eqs. (4.11) and (4.13) that $\underline{H}=0$. Then, since $\underline{E}\neq 0$, Eq. (4.12) gives the condition that $\underline{w}\|\underline{P}\|\underline{E}\|\underline{q}$, which specifies longitudinal waves. Then, using the identities in Eq. (4.9), Eq. (4.7) leads to the well-known Lyddane-Sachs-Teller (LST) relation

$$\nu_L = (\epsilon_0/\epsilon_\infty)^{1/2}\ \nu_0 \qquad (4.15)$$

where ν_L is the frequency of the longitudinal mode as given in their publication (Lyddane et al, 1941). In the second case where $(\underline{q}.\underline{E})=0$ and $\underline{E}$ is non-zero, $\underline{E}$ must be perpendicular to $\underline{q}$. It follows from (4.12) that $\underline{q}$, $\underline{E}$ and $\underline{H}$ form a right-handed orthogonal system of vectors. It can be seen from Eqs. (4.1) and (4.2) that $\underline{w}$ and $\underline{P}$ are both parallel to $\underline{q}$ and thus the resulting modes are transverse and are described by

$$\left[\frac{qc}{\nu}\right]^2 = 1 + 4\pi b_3 + \frac{4\pi b_2{}^2}{\nu_T - \nu^2} \qquad (4.16)$$

where ν_T is the frequency of the transverse mode.

Substituting the scalar constants into Eq.(4.16) and remembering that the refractive index n is the ratio of the velocity of light to the phase velocity, Eq.(4.16) reduces to

$$n(\nu)^2 = \epsilon(\nu) = \epsilon_\infty + \frac{(\epsilon_0 - \epsilon_\infty)}{1 - (\nu/\nu_T)^2} \qquad (4.17)$$

With the inclusion of the LST relation Eq.(4.17) becomes

$$\epsilon(\nu) = \epsilon_\infty \left[\frac{\nu_L^2 - \nu^2}{\nu_T^2 - \nu^2}\right] \qquad (4.18)$$

It is well known that in the plot of ϵ versus ν, the dielectric constant is negative in the region bounded by ν_L and ν_T which implies that the refractive index is imaginary and the crystal is therefore perfectly reflecting. This region is known as the reststrahlen region.

The theory of lattice vibrations as discussed above has been limited in the potential energy to terms quadratic in the interatomic displacement and no damping has been included. This situation is depicted in the observed linearity of the equations of motion (4.1) and (4.2). This leads to the conclusions that lattice waves do not interact and to the unphysical consequences that the lattice spectra would consist of sharp, undamped temperature resonances and that the crystal would have no thermal expansion.

4.3 DAMPING IN REAL CRYSTALS

For the purpose of analysing the empirical data in the neighbourhood of ν_0, a damping term is included in the equation of motion (4.1) which takes account of the energy dissipation so that it now becomes:

$$\ddot{\underline{w}} = b_1 - \gamma\dot{\underline{w}} + b_2\underline{E} \qquad (4.19)$$

where γ is a frequency independent damping constant. This leads to a new dispersion formula

$$\hat{\epsilon}(\nu) = \epsilon_\infty + \frac{(\epsilon_0 - \epsilon_\infty)\,\nu_T^2}{\nu_T^2 - \nu^2 - i\gamma\nu} \qquad (4.20)$$

However, since Eq. (4.20) is only an ad hoc formula

designed to reproduce energy absorption in the simplest manner (Born and Huang,1954), the failure of this model to account for detailed structure in the measured spectra is hardly surprising. This is so because it neglects the details of the interactions between the normal modes.

There are two well-known mechanisms that can cause the observed side-band structure.

The first mechanism, which is due to higher order moments in the dipole expansion (Lax and Burstein, 1955) in which the second order term leads directly to two-phonon processes was put forward as the principal mechanism in diamond-type semiconductors. These are shown diagrammatically in figures 4.1(a) and (b) where (a) represents the creation of two phonons giving rise to a summation band and (b) the creation of one and annihilation of another which gives rise to a difference band.

The second mechanism, which was first suggested by Kleinman (1960) was put forward as the principal mechanism in GaP. Basically, the theory is that in zinc blende structure crystals light can couple very strongly with the TO mode at $\underline{q}\approx 0$. The TO phonon serves as an intermediate virtual state which then decays into two phonons under the perturbing influence of cubic anharmonic terms in the crystal potential. Processes of this type are illustrated in figures 4.1(c) and (d) which represent two-phonon combination and difference bands, respectively. Obviously this mechanism would be inoperative in diamond type semiconductors since there is no coupling between light and the $\underline{q}\approx 0$ TO mode.

Szigeti (1959) has used ordinary perturbation methods to describe the dielectric response with the perturbing term being the anharmonic contribution of the electric transition moment and potential function. Szigeti (1959) suggested that the widening of the main band is, in general, due to the third order potential and the absorption far from the main band to the second order moment. However, because the interaction between the first and second order moments contributes to the third order potential, a large second order moment may result in a wide band as well as in a strong side band. The application of ordinary perturbation methods by Szigeti is by no means straightforward [Wallis and Maradudin (1962), Donovan and Angress (1971)].

Wallis and Maradudin (1962) and Cowley (1963) have also studied anharmonic phonon interactions in crystals possessing cubic symmetry. It has been shown by Cowley (1963) that, if non-linear contributions to the dipole moment are neglected, the frequency dependent dielectric response can be written in the modified form:

$$\hat{\epsilon}(\nu) = \epsilon_\infty + \frac{(\epsilon_0 - \epsilon_\infty)\,\nu(0j)^2}{\nu(0j)^2 - \nu^2 + 2\nu(0j)[\Delta(0j,\nu) - i\Gamma(0j,\nu)]} \qquad (4.21)$$

where $\nu(0j)$ is the harmonic frequency of the transverse optic (TO) mode at wave vector $\underline{q} \approx 0$, and $\Delta(0j,\nu)$ and $\Gamma(0j,\nu)$ are, respectively, the real and imaginary parts of the irreducible self-energy of the TO phonon.

The real part, $\Delta(0j,\nu)$, of the self-energy can be written as the sum of two parts,

$$\Delta(0j,\nu) = \Delta^E(0j) + \Delta^A(0j,\nu) \qquad (4.22)$$

where $\Delta^E(0j)$ is a frequency-independent contribution which arises from the thermal expansion of the crystal and $\Delta^A(0j,\nu)$ is frequency-dependent and arises from the anharmonic interactions.

Cowley (1963) has expressed $\Delta^A(0j,\nu)$ and $\Gamma(0j,\nu)$ in terms of the cubic coupling coefficient which connects the $q\approx 0$ TO mode with the lattice modes in the two-phonon final state via cubic anharmonicity in the following way:

$$\Delta^A(0j,\nu) = -(18/\hbar^2) \sum_{q_1 j_1 q_2 j_2} \sum |V(0j,q_1 j_1,q_2 j_2)|^2 R(\nu) \quad (4.23)$$

and $$\Gamma(0j,\nu) = 18\pi/\hbar^2 \sum_{q_1 j_1 q_2 j_2} \sum |V(0j,q_1 j_1,q_2 j_2)|^2 S(\nu) \quad (4.24)$$

where

$$R(\nu) = (n_1+n_2+1)[(\nu_1+\nu_2+\nu)^{-1} + (\nu_1+\nu_2-\nu)^{-1}]_p + (n_2-n_1)[(\nu_1-\nu_2-\nu)^{-1} + (\nu_1-\nu_2+\nu)^{-1}]_p \quad (4.25)$$

and $$S(\nu) = (n_1+n_2+1)[\delta(\nu-\nu_1-\nu_2) - \delta(\nu_1+\nu_2+\nu)] + (n_2-n_1)[\delta(\nu_2-\nu_1+\nu) - \delta(\nu_1-\nu_2+\nu)] \quad (4.26)$$

In Eqs. (4.23) and (4.24) $V(0j,q_1 j_1,q_2 j_2)$ is the cubic coupling coefficient and in Eqs. (4.25) and (4.26) $n_i=n_i(q_i j_i)$ with i=1,2. Here $R(\nu)$ and $S(\nu)$ are also functions of temperature resulting from the transition probabilities for phonon creation and annihilation. The first part in Eqs. (4.25) and (4.26) describes the summation process where two phonons are created and the second part represents the difference process in which one phonon is created and another destroyed.

If in fact non linear contributions to the dipole moment can be safely neglected then it follows from Eq. (4.21) that the real and imaginary parts of the anharmonic self-energy of the TO mode can be written as

$$\Delta(0j,\nu) = \frac{1}{2}\left[\nu(0j)\left[\frac{[\epsilon_0-\epsilon_\infty][\epsilon'(\nu)-\epsilon_\infty]}{[\epsilon'(\nu)-\epsilon_\infty]^2+\epsilon''(\nu)^2} - 1\right] + \frac{\nu^2}{\nu(0j)}\right] \quad (4.27)$$

$$\Gamma(0j,\nu) = \frac{1}{2}\left[\frac{\nu(0j)[\epsilon_0-\epsilon_\infty]\epsilon''(\nu)}{[\epsilon'(\nu)-\epsilon_\infty]^2 + \epsilon''(\nu)^2}\right] \quad (4.28)$$

and determined from the measured values of the dielectric response functions $\epsilon'(\nu)$ and $\epsilon''(\nu)$.

It was found from the literature survey that several authors have generally accepted the anharmonic mechanism to be the dominant mechanism in alkali halide crystals and thus have used the above expressions to determine the frequency dependence of the anharmonic self energies of the TO modes in their investigations. [Johnson and Bell (1969), Eldridge and Staal (1977), Rastogi et al (1978), Mok et al.(1980), Memon and Parker (1981)]. Experimental results obtained by the above authors as well as theoretical studies by Hardy and Karo (1979) have shown that the self-energy function $\Gamma(0j,\nu)$ converges near the two-phonon cut-off wavenumber and in the low wavenumber region. Furthermore, in all of the experimental investigations the results are in excellent quantitative agreement with calculations based on lattice anharmonicity in which the higher order dipole contributions are completely neglected. This establishes clearly that the anharmonic model can be safely used for alkali halide crystals.

In the case of zinc blende structure crystals, where the ionicity is weaker than in rock salt structure crystals, there has been considerable evidence that both the non-linear dipole moment and anharmonicity should be important in the region of two-phonon and three-phonon

summation bands. [Borik (1970) and Geick (1965)].

It is shown by Geick (1965) that in the imaginary part of the dielectric function of GaAs, lattice anharmonicity dominates at frequencies near the resonance frequency ν_{TO}, while the nonlinear dipole moment dominates in the three-phonon summation band region where $(\nu^2/\nu_{TO}^2 - 1) \gg 1$. It is shown in the paper that if the second order dipole moment is neglected, the calculated form of the damping function required to account in full for the observed absorption increases by an order of magnitude in the two-phonon region and fails to decay as expected at higher frequencies. On the other hand, when the second order dipole moment is included in the calculation the damping function required to account for the remaining absorption converges at the two-phonon cut-off as expected. This provides a useful indication of whether the higher order dipole moment is significant in multiphonon processes for zinc blende structure crystals even though a number of approximations were used in the calculation. Thus, if Eq. (4.28) is used to estimate the contribution from the anharmonic mechanism required to account for the observed structure, any divergence in the calculated value of $\Gamma(\nu)$ would indicate that the contribution from the non-linear dipole moment has become significant. In the following chapter, this simple guide will be used to interpret the self-energy spectra determined in this way. Measurements of the absorption as a function of temperature give no information on the solution to this problem since the expressions for temperature dependence are the same for the

two absorption mechanisms.

4.4 TEMPERATURE DEPENDENCE OF TWO-PHONON PROCESSES

Since phonons are bosons, the occupation number for the mode $(\underline{q}_i j_i)$ at thermal equilibrium is given by the well-known Bose-Einstein statistics:

$$n(\underline{q}_i, j_i) = [e^{h\nu(\underline{q}_i, j_i)/KT} - 1]^{-1} \qquad (4.29)$$

where $\nu(\underline{q}_i j_i)$ is the frequency of the mode in the harmonic approximation and K is the Boltzmann constant.

As can be seen from Eq. (4.28), the temperature dependence of the net absorption for the summation band is proportional to

$$n_1+n_2+1 \qquad (4.30)$$

and in the case of the difference band, the temperature dependence of the net absorption of the participating phonons is proportional to

$$n_2-n_1 \qquad (4.31)$$

Therefore, from Eqs. (4.30) and (4.31) it can be observed that the phonon occupation number of a difference band tends to vanish as the absolute temperature tends to zero whereas the expression containing n_i for the summation band remains finite.

Thus, the observed features in an infrared spectrum can be classified into summation and difference bands by observing the change in the intensity of the features at two different temperatures.

4.5 SELECTION RULES

The selection rules for the interactions of

electromagnetic radiation with phonons are based on the requirements of conservation of energy and crystal momentum. There must also be an electric dipole moment associated with the phonons involved. In referring to figure 4.1, momentum is conserved at each vertex and energy is conserved overall. The processes must therefore satisfy the following conditions:

$$\underline{k} = \underline{q} = \pm \underline{q}_1 \pm \underline{q}_2 = 0, \tag{4.32}$$

and

$$\nu_{\underline{k}} = \pm \nu_{\underline{q}_1 j_1} \pm \nu_{\underline{q}_2 j_2} \tag{4.33}$$

where $\underline{k}$ is the photon wavevector and j is the branch index of the participating phonons, and the positive and negative signs correspond to phonon creation and annihilation respectively. The simultaneous annihilation of two phonons cannot occur, since it would violate the energy conservation rule in Eq. (4.33). Also, the two phonons must have the same value $|\underline{q}|$ and the branches, signified by j_1, j_2 may be either optical or acoustic.

The contribution to the absorption from either the anharmonic or the second order dipole moment mechanism involves the two-phonon density of states. The two-phonon absorption spectrum is in general continuous. However, peaks occur in the regions where there is a high density of phonon states per unit wavenumber interval. Therefore, any structure in the infrared spectrum as a consequence reflects structure in the two-phonon density of states curve. The regions where the phonon concentration is large in the dispersion curves are known as critical points. A

critical point is a point where the gradient $\nabla_q \nu(q)$ is either zero or changes sign discontinuously. Figure 4.2 shows the locations of critical points denoted by Γ, X, L and W in the first Brillouin zone of zinc blende type crystals. In a few cases in the work described in the next chapter it has been necessary to account for observed bands in terms of unidentified peaks in the two-phonon density of states. Such peaks, which are not due to phonon pairs at the critical points, can occur in the density of combined states when (Patel et al.,1984)

$$\frac{d\nu_1}{dq} = \pm \frac{d\nu_2}{dq}, \text{ for then } \frac{d(\nu_1 \mp \nu_2)}{dq} \to 0 \qquad (4.34)$$

These peaks are not usually associated with singularities in the one-phonon density of states.

Birman (1963) has used group theoretical methods to deduce selection rules for determining the optical activity of two-phonon processes in crystals with the diamond and zinc blende structure. The selection rules for infrared-active two-phonon processes in crystals with the zinc blende structure are listed in table 4.1. It can be deduced from the table that there are only two dipole-forbidden combinations [i.e. 2LA(X) and 2LO(X)] out of a possible 36 combinations from the major symmetry points Γ, X and L. Furthermore, since the symmetry of diamond structure crystals is higher than that of zinc blende type crystals, it also follows that there are fewer infrared active combination bands in crystals of the diamond structure. This is apparent from the list of combination bands reported by Birman (1963).

References to chapter 4

Birman J L; Phys. Rev. 131, 1489 (1963).

Borik H; Phys. Stat. Sol. 39, 145 (1970).

Born M and Huang K; "Dynamical theory of crystal lattices", Clarendon Press, Oxford (1954).

Cowley R A; Advances in Physics 12, 421 (1963).

Dekker A J; "Solid State Physics", Macmillan Press (1975).

Donovan B and Angress J F; "Lattice vibrations", Chapman and Hall, London (1971).

Eldridge J E and Staal P R; Phys. Rev. 16B, 4608 (1977).

Geick R; Phys. Rev. 138, 1495 (1965).

Hardy J R and Karo A M; "The Lattice Dynamics and Statics of Alkali Halide Crystals", Plenum Press, New York (1979).

Johnson K W and Bell E E; Phys. Rev. 187, 1044 (1969).

Kleinman D A; Phys. Rev. 118, 118 (1960).

Lax M and Burstein E, Phys. Rev. 97, 39 (1955).

Lyddane R H, Sachs R G and Teller E; Phys. Rev. 59, 673 (1941).

Memon A and Parker T J; Int. J. Infrared and Millimeter Waves 2, 839 (1981).

Mok C L, Parker T J and Chambers T J; Sol. St. Comm., 34, 567 (1980).

Rastogi A, Pai K F, Parker T J, Lowndes R P; Proc. Int. Conf. on Lattice Dynamics, Paris, p.142 (1977).

Patel C, Parker T J, Jamshidi H and Sherman W F; Phys. Stat. Sol.(b) 122, 461 (1984).

Szigeti B; Proc. Roy. Soc. (London), A 252, 217 (1959).

Wallis R F and Maradudin A A; Proc. Int. Conf. on the Physics of Semiconductors, Exeter, p.490 (1962).

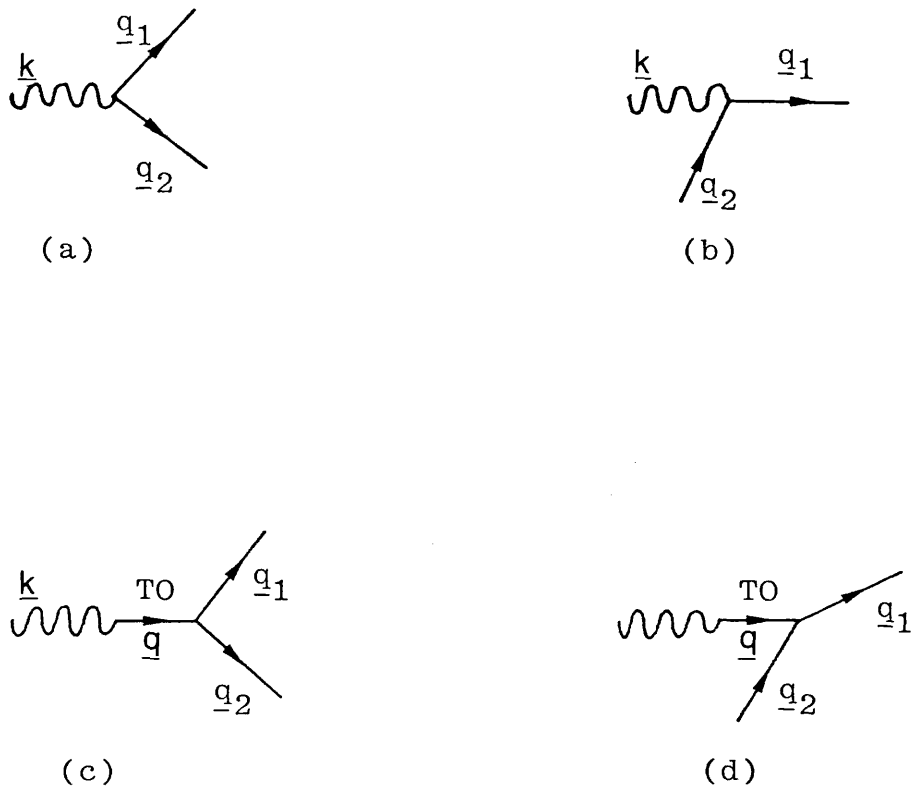

Figure 4.1 Photon-phonon interactions:
(a) and (b) two-phonon processes due to higher order dipole moments,
(c) and (d) two-phonon processes due to cubic anharmonic influence.
Wavy lines represent photons and straight lines represent phonons.

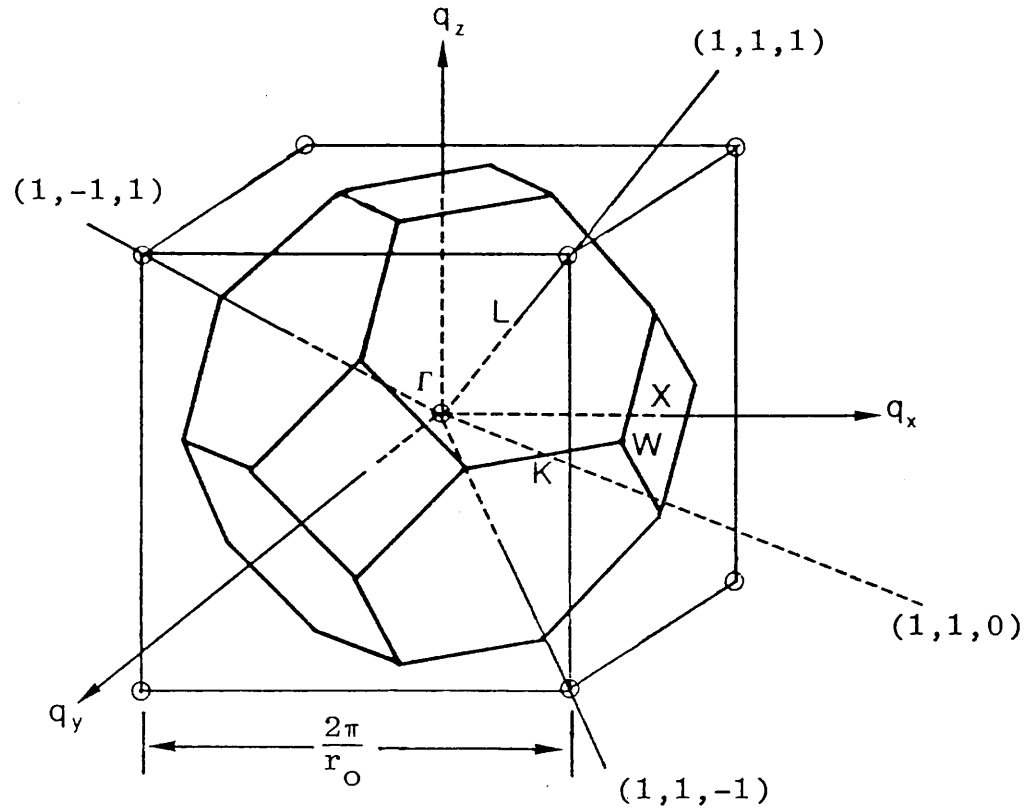

Figure 4.2 The reciprocal lattice and the first Brillouin zone for a zinc blende type structure.
$\Gamma = (0,0,0)$; $K = \frac{\pi}{r_o}(\frac{3}{4},\frac{3}{4},0)$; $W = \frac{\pi}{r_o}(1,\frac{1}{2},0)$;
$X = \frac{\pi}{r_o}(1,0,0)$ and $L = \frac{\pi}{r_o}(\frac{1}{2},\frac{1}{2},\frac{1}{2})$.

$2LO(\Gamma)$, $LO(\Gamma) + TO(\Gamma)$, $2TO(\Gamma)$
$2TO(X)$, $TO(X) + LO(X)$, $TO(X) + LA(X)$, $TO(X) + TA(X)$
$LO(X) + LA(X)$, $LO(X) + TA(X)$
$LA(X) + TA(X)$
$2TA(X)$
$2TO(L)$, $TO(L) + LO(L)$, $TO(L) + LA(L)$, $TO(L) + TA(L)$
$2LO(L)$, $LO(L) + LA(L)$, $LO(L) + TA(L)$
$2LA(L)$, $LA(L) + TA(L)$
$2TA(L)$
$TO_1(W) + LO(W)$, $TO_1(W) + LA(W)$
$TO_2(W) + LO(W)$, $TO_2(W) + LA(W)$
$LO(W) + LA(W)$, $LO(W) + TA_1(W)$, $LO(W) + TA_2(W)$
$LA(W) + TA_1(W)$, $LA(W) + TA_2(W)$

Table 4.1 Infrared-allowed two-phonon processes in the zinc blende structure at the critical points Γ, X, L and W.

Chapter 5

OPTICAL CONSTANTS RESULTS

5.1 INTRODUCTION

The far infrared optical constants of five binary semiconductors with the zinc blende structure have been measured at 300 and 100K. They are GaP, GaAs, InSb, InAs and ZnSe. All the crystals are undoped single crystals.

Precise data for the optical constants of these materials in the far infrared have been found to be rather limited. Most probably this is due to difficulties encountered as a result of not having suitable experimental techniques. Therefore, the apparatus and experimental methods that have been developed were specifically aimed at fulfilling the needs of obtaining accurate data for these semiconductors. In many cases, new optical constants results have been obtained for the first time.

Features observed in the spectra are interpreted as either two- or three-phonon combination bands by using critical point analysis. The selection rules worked out by Birman (1963) for two-phonon processes in zincblende type crystals have been explicitly used in the analysis. Whenever the observed features could not be assigned in terms of two-phonon processes then the possibility of assigning them in terms of three phonon processes has been considered. Where possible, comparisons have been made between the results obtained with other published

experimental data and the theoretical predictions based on an 11-parameter rigid ion model (RIM) developed by Patel (1982).

The temperature dependence of the intensities of two-phonon combination bands at 100 and 300K in the present work was also obtained. Comparisons have been made between the present results and those calculated from Bose-Einstein statistics using phonon frequencies taken from the 11-parameter RIM. The expression shown in Eq. (4.30) in the previous chapter was used in the calculation. Since free carrier absorption was found to be present in the low wavenumber region and the theory does not take this absorption into account, only the region above the reststrahlen band has been analysed in detail.

For each sample the contribution from the anharmonic self-energy function, $\Gamma(\nu)$, which would be required to account in full for the observed absorption has been estimated from Eq. (4.28). As stated in the previous chapter, this assumes that non linear contributions to the dipole moment are negligible. The values of ν_{TO}, ϵ_0 and ϵ_∞ used to obtain $\Gamma(\nu)$ were obtained from Kunc et al (1975).

The major obstacle in obtaining high resolution transmission spectra below the reststrahlen band is the presence of signatures in the interferograms which are associated with the quartz window of the Golay. They occur on each side of the main interferogram as shown in figures 5.1(a) and (b). [The interferogram in figure 5.1(b) was obtained from a GaP sample]. They give spurious features in the ratioed spectrum because a dispersive specimen

interferogram produces a dispersive signature which will be different from that of a background interferogram. To exclude these signatures from the interferogram, a shorter path length is recorded and this limits the resolution. However, it was found that the resolution of about 4 cm^{-1} obtained by excluding these signatures was sufficient for most of this work since two-phonon combination bands are fairly broad.

A Golay fitted with a thick CsI window has been used to obtain spectra above 180 cm^{-1} and the type of restriction to the resolution described above is removed. In this case an interferogram is recorded in which the optical path length is sufficiently large to include almost all features in the strongly dispersed sample interferogram. This means that the number of points in the interferogram is not symmetrical about the position of the maximum signal. A typical specimen interferogram recorded in this way is shown in figure 5.2. (In this case an InSb specimen was used). The above experimental procedure, which must be accompanied by an appropriate apodising procedure has been described by Parker and Chambers (1976).

The procedures that have been used to obtain the optical constants of the five specimens will be described in detail using the GaP results. Table 5.1 shows information which is relevant to the work described in this chapter. The thickness of various specimens shown in the table was measured using an overhead Nikon projector which gives an accuracy of about 2.5μm. per reading. The measurements were confirmed with a micrometer.

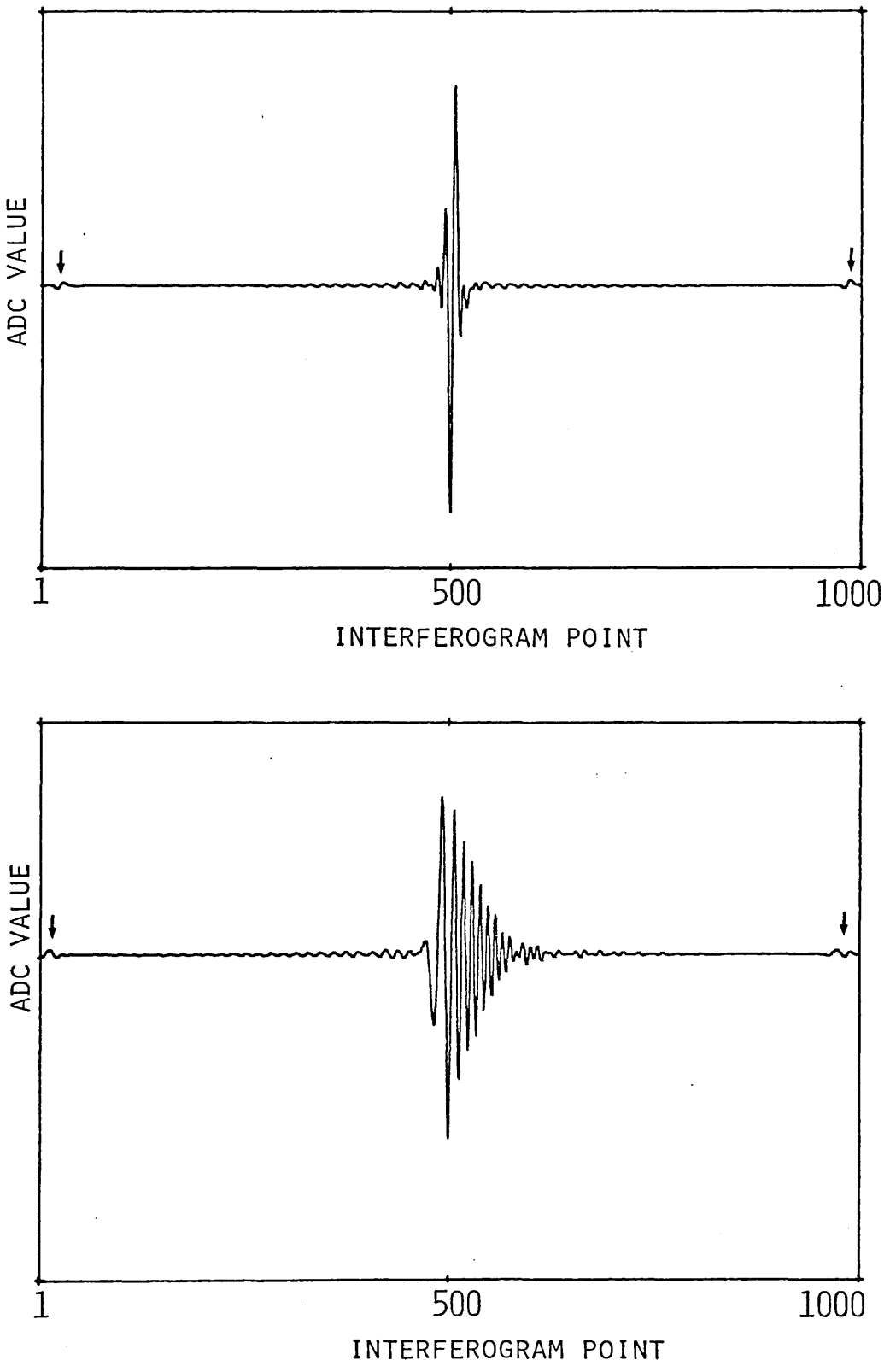

Figure 5.1 shows the presence of signatures as indicated by the arrows. (a) background interferogram (b) sample interferograms.

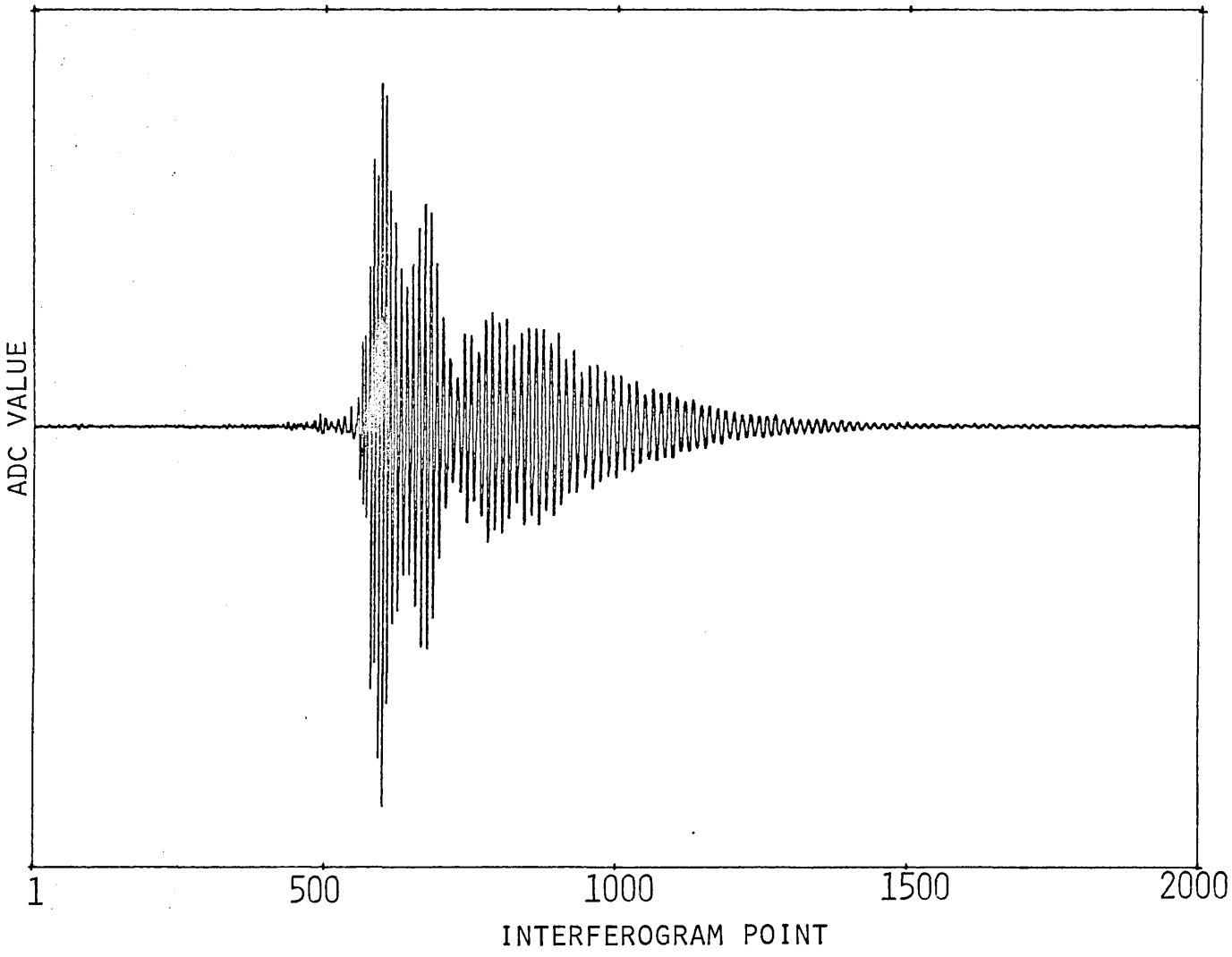

Figure 5.2 Sample interferogram recorded with a CsI window Golay.

Table 5.1

Experimental parameters for the transmission data

Material		GaP	GaAs	InSb	InAs	ZnSe
Thickness (mm ± 1.5μm)		0.508	0.523	0.824	0.500	0.431
Golay window	Below reststrahl band	Quartz,CsI	Quartz	Quartz	Quartz	Quartz
	Above reststrahl band	CsI	CsI	CsI	CsI	CsI,Diamond
Beam splitter thickness (μm)	Below reststrahl band	12.5, 2.5	12.5	12.5	12.5	12.5
	Above reststrahl band	2.5	2.5	2.5	2.5	2.5, 6.25
Scan speed in terms of laser fringe frequency (Hz)	Below reststrahl band	400, 180	400	400	400	400
	Above reststrahl band	180	180	180	180	180
Resolution (cm^{-1})		4	4	4	4	4
Average value of linear expansion coefficient between 100 and 300K ($10^{-6}K^{-1}$)		3.0	4.0	4.0	3.4	5.0

5.2 RESULTS AND DISCUSSION FOR GaP

The optical constants of GaP have been measured above and below the reststrahlen band which occurs in the region between 380 and 420 cm^{-1}. To obtain these data the following experimental procedures are used. The background interferograms are first recorded and they are shown in figure 5.3 for the spectral region below the reststrahl band. The specimen is then inserted into the partial beam in the fixed arm of the interferometer and the specimen interferograms as shown in figure 5.4 are recorded. A number of runs are co-added until an acceptable signal-to-noise (S/N) ratio has been achieved. The power parts of the Fourier transforms of the background and the sample interferograms are shown separately in figures 5.5 and 5.6 respectively. These two figures also give a good indication of the reproducibility of the measured spectra.

The measured spectra of the amplitude transmission coefficient t and the principle values of the phase ϕ below the reststrahlen band obtained by ratioing the complex Fourier transforms of the averaged background and sample interferograms are given in figure 5.7(a). The branches in the computed phase must then be shifted by $\pm 2m\pi$ where m = 0,1,2 etc. to give a continuous spectrum as shown in figure 5.7(b).

The gross phase shift associated with the shift of the interferogram due to the specimen is obtained by using the partial insertion technique as described in chapter 3. This is shown in figure 5.8. The interferogram is sampled at each laser fringe so that the shift, 2B, can be measured to

the nearest laser fringe. A phase shift $4\pi\nu B$ (as defined in chapter 2 section 2.2.4) is then added to the phase spectrum in figure 5.7(b), but before calculating the optical constants over the whole spectral region a further correction to the phase spectrum above the reststrahlen band is needed as described in the following paragraph.

To obtain the correct value of phase above the reststrahlen band by transmission DFTS, it is necessary to have a predetermined value of n near this region of intense absorption obtained through other means. For this purpose, data obtained in the same laboratory by Maslin (1986) who used the technique of reflection DFTS were available. The region where there is the best overlap between the reflection and transmission data is first established then followed by adding the correct number of π's to the phase data until the recomputed value of n matches the reflection data in this region. This region is shown figure 5.9. It has already been pointed out in chapter one that the complex reflection data is becoming less accurate in the region further away from the reststrahlen band as the phase response becomes nearly zero. Likewise, no transmission data can be obtained from the thick sample in the vicinity of the reststrahlen band. The two techniques are thus complementary to each other.

The complete amplitude and phase spectra of GaP at 300K determined by the above procedure are shown in figure 5.10 and the resulting values of the optical constants are given in figure 5.11. In order to demonstrate the sensitivity of the technique of DFTS in the measurement of the refractive

index, a small part of the spectrum in figure 5.11 is picked out as shown in figure 5.12. It can be seen from figure 5.12 that the dispersion in the refractive index curve in the regions where the strong absorption bands occur is clearly revealed. The dielectric response curves ϵ' and ϵ'' at 300K are shown in figure 5.13.

Kleinman and Spitzer (1960) have reported the optical constants at 300K in the region from 330 to 625 cm^{-1} which includes the reststrahlen band and their results were found to be approximately 1% higher than the present data. Parsons and Coleman (1971) have measured the values of n and the absorption coefficient α between 25 and about 320 cm^{-1}. Their refractive index data in this spectral range were about 0.3% smaller than the present results. The value of α measured by them is much lower than the present results. This difference is most probably due to a high concentration of free carriers in the specimen used in this work. No other reported value of n has been found between 185 and 320 cm^{-1}.

Table 5.2 shows the critical point phonon (cpp) frequencies at 300K. These were obtained from the calculations based on an 11-parameter RIM by Patel et al (1982) who used the neutron scattering data of Borcherds et al (1979) to determine the model parameters. Patel et al have also obtained another set of phonon dispersion curves to fit the neutron scattering data of Yarnell et al (1968). Both sets of neutron data are given in the table in order to show the difference between them especially in the measurement of the LO frequency at the L point. Several

authors [Kleinman and Spitzer (1960), Koteles and Datars (1976a), Hoff and Irwin (1973) and Ulrici and Jahne (1978)] have investigated two-phonon processes in GaP. Table 5.3 shows the list of assignments made on the observed combination bands and they are compared with the results of other authors. They are assigned using the cpp frequencies shown in table 5.2.

The amplitude and phase spectra at 100K are shown in figure 5.14. It can be seen from the figure that the transmission amplitude signal has increased by a factor of about 2 compared with that at 300K. As expected, the difference bands reduce in intensity and above the reststrahlen region the combination bands become more enhanced as the transmission amplitude signal increases at this temperature. As can be seen from table 5.3, the bands above the restrahlen region have been shifted by about 4 cm^{-1} compared with those observed at 300K.

The minimum signal in the specimen interferogram in figure 5.8 is shown in figure 5.15 for the purpose of comparison with the one obtained at 100K. As can be observed from this figure, the position of the maximum signal of the specimen interferogram obtained at 100K has been shifted by a distance of about 16 laser fringes ($\simeq$5.062 μm) from the signal obtained at 300K. This corresponds to a reduction of about 0.8% in the gross phase shift compared with the value obtained at 300K. The average value of the coefficient of linear expansion of GaP between 100 and 300K is 2.5×10^{-6} K^{-1} [Deus et al,(1983)] and this gives a calculated contraction of 0.3 μm in the thickness

of the specimen at 100K. This contraction is too small to cause any significant effect in the calculation of n. Thus the overall change in the refractive index is determined almost entirely by the value of 2B, giving n_{100K}/n_{300K} = 0.994 or $\delta n \approx 0.6\%$ at 100 cm^{-1}. It should be noted that the reduction of 0.8% in the gross phase shift differs from the 0.6% change in δn because only the part n-1 contributes to 2B. An important conclusion which can be drawn here is that the phase branch does not change as the specimen is cooled down since a change of 2π at 100 cm^{-1} corresponds to $\delta n \approx$ 6% which is very large compared to the value calculated above. It was found that this simple deduction also applies in the determination of the value of n at 100K above the reststrahlen band. Thus, the value of n at 100K can be determined even in the absence of any data measured at 100K above the reststrahlen region to act as a reference.

The resulting values of the optical constants of GaP at 100K are shown in figure 5.16 and the real and imaginary parts of the dielectric response at this temperature are shown in figure 5.17. It seems from the literature that no other data for the optical constants at 100K in this spectral region have been reported.

The absorption coefficient ($\alpha=4\pi k\nu$) at 300 and 100K above the reststrahlen band is given in figure 5.18. The overall value of α at 300K was found to be slightly higher than the results obtained by Kleinman and Spitzer (1960).

The temperature dependence of the intensities of two-phonon combination bands in GaP is shown in table 5.4. Comparisons have been made between the present results and

those calculated from Bose-Einstein statistics using phonon frequencies taken from the 11-parameter RIM.

The contribution from the anharmonic self-energy $\Gamma(\nu)$ which would be required to account in full for the measured absorption has been estimated at 300 and 100K. This is shown in figures 5.19 and 5.20 respectively. These are the first reported results. The fact that $\Gamma(\nu)$ diverges with increasing wavenumber is an indication that non linear terms in the dipole moment are contributing significantly to the lattice absorption. It can also be seen from the two figures that the self-energy function also diverges at low wavenumbers. In this region there is a contribution from the free carrier absorption which has also been neglected.

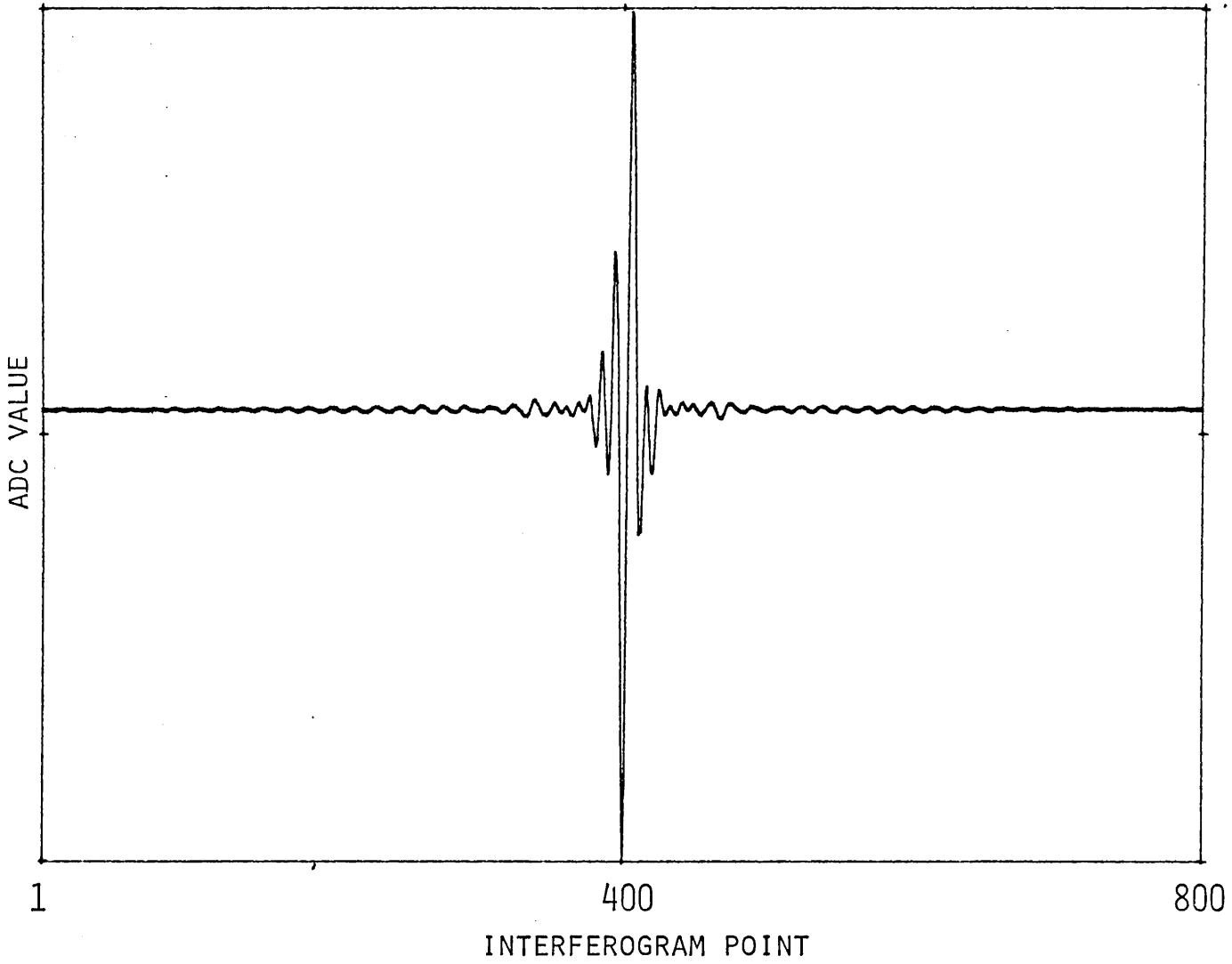

Figure 5.3 Three background interferograms superimposed on each other.

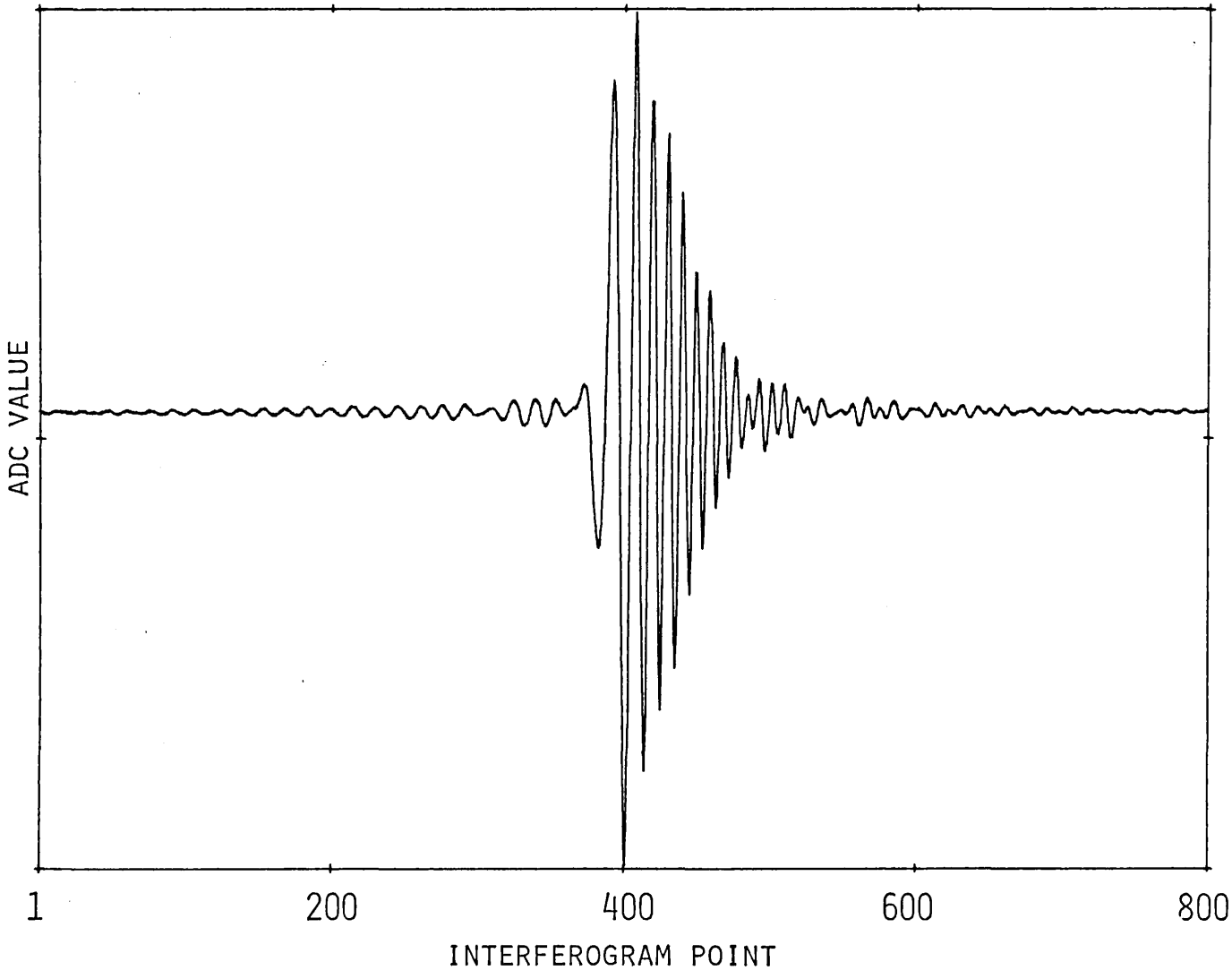

Figure 5.4 Three GaP sample interferograms superimposed on each other.

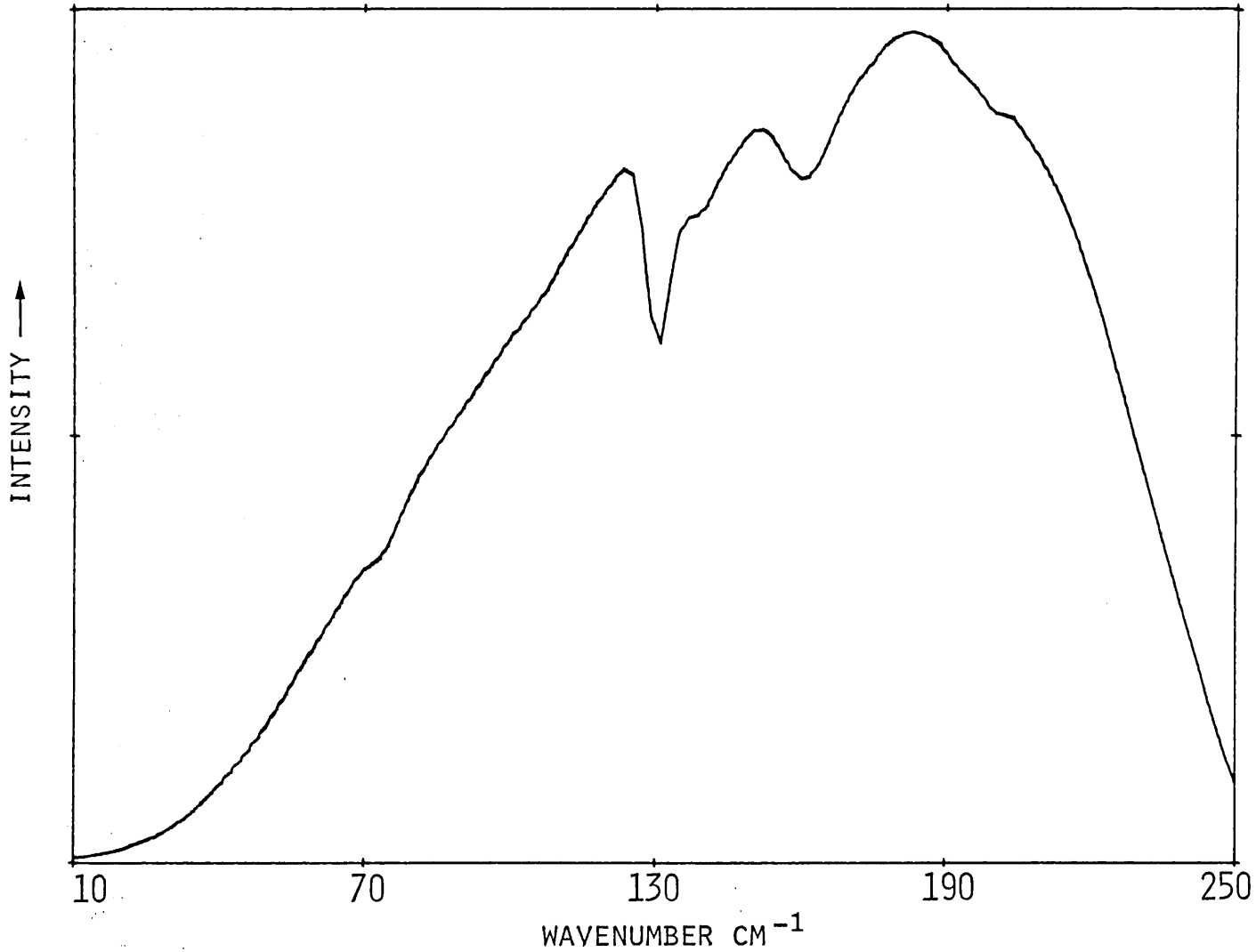

Figure 5.5 Three background spectra superimposed on each other.

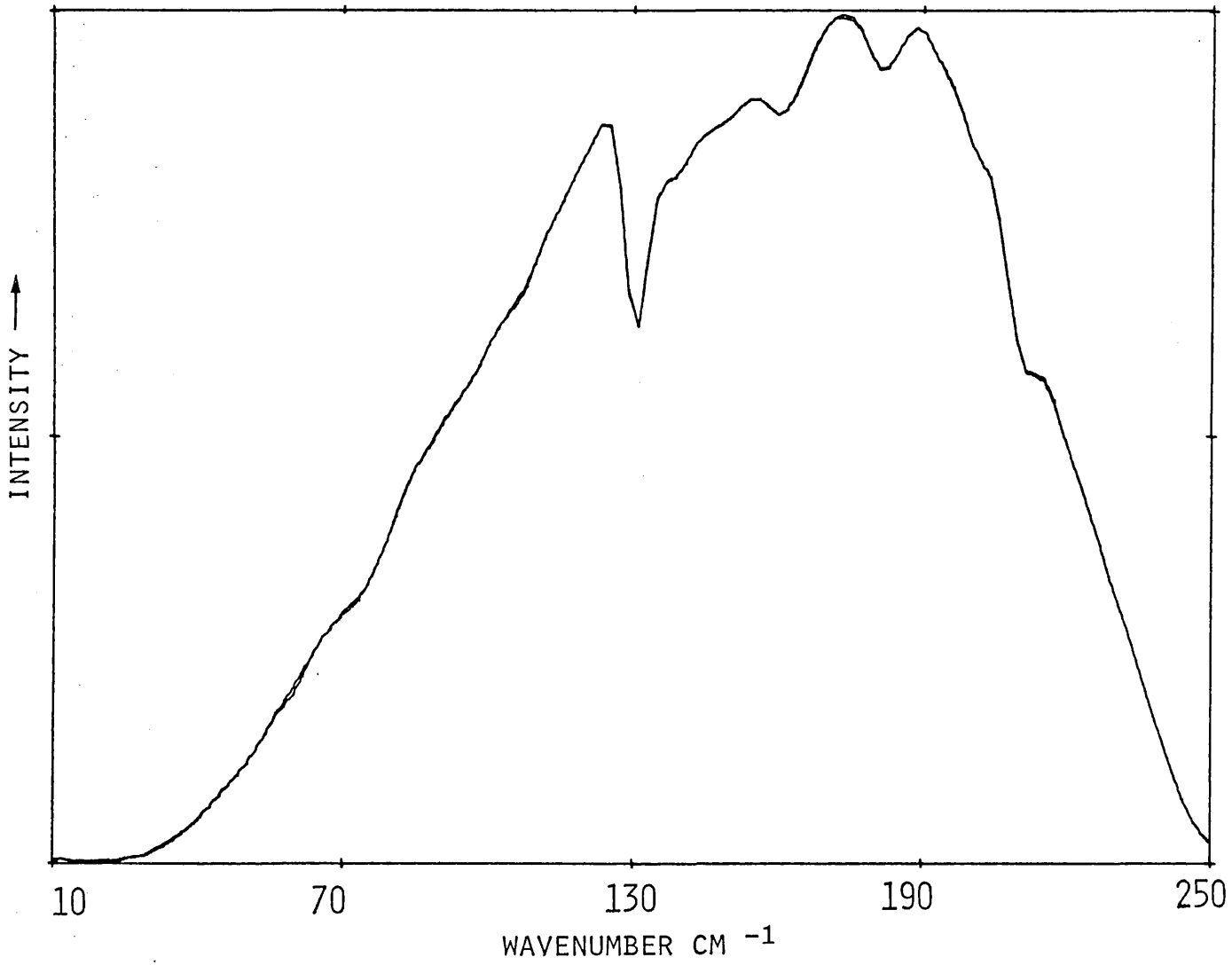

Figure 5.6 Three GaP sample spectra superimposed on each other.

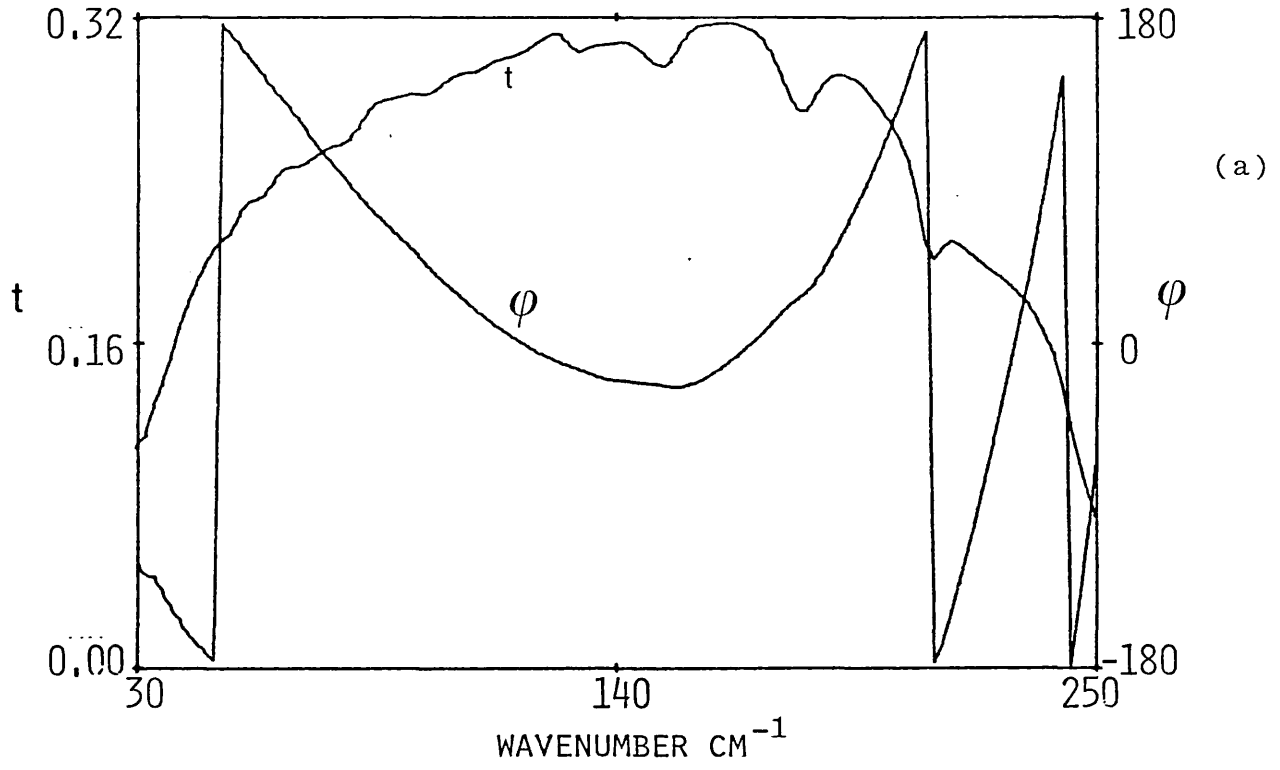

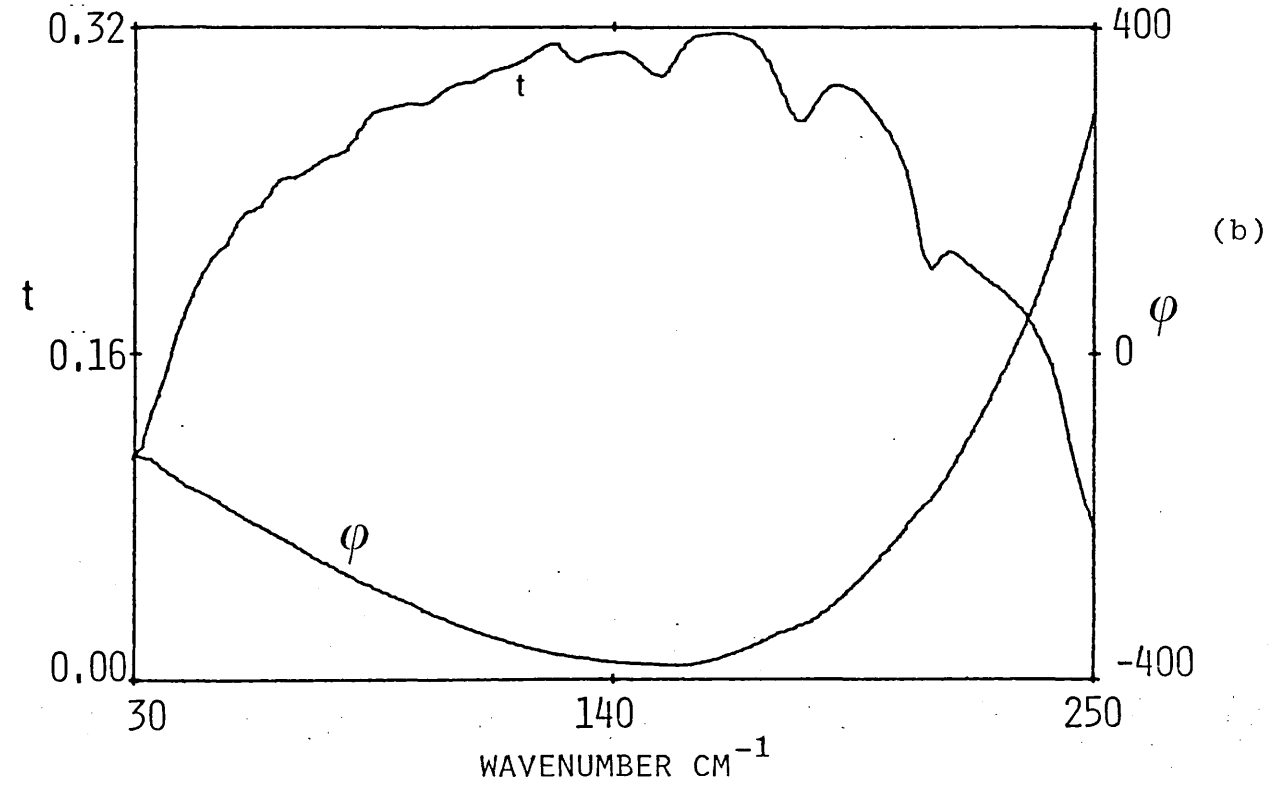

Figure 5.7 (a) Amplitude and phase spectra of GaP at 300K showing the principle values of the phase.

(b) Amplitude and phase spectra of GaP at 300K showing the continuous phase before adding a phase shift of $4\pi\nu B$.

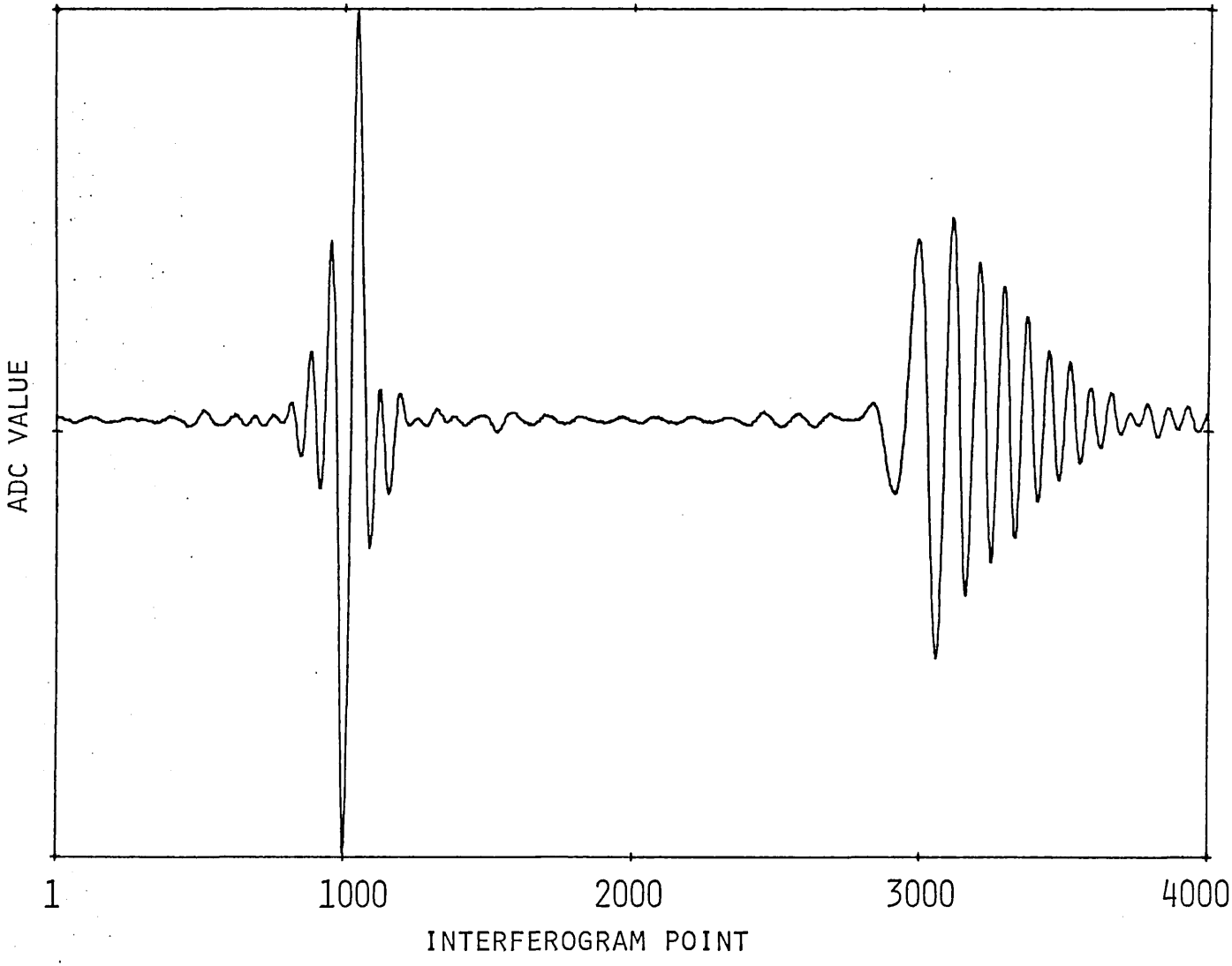

Figure 5.8 An interferogram showing the gross shift in the path difference due to the GaP sample.

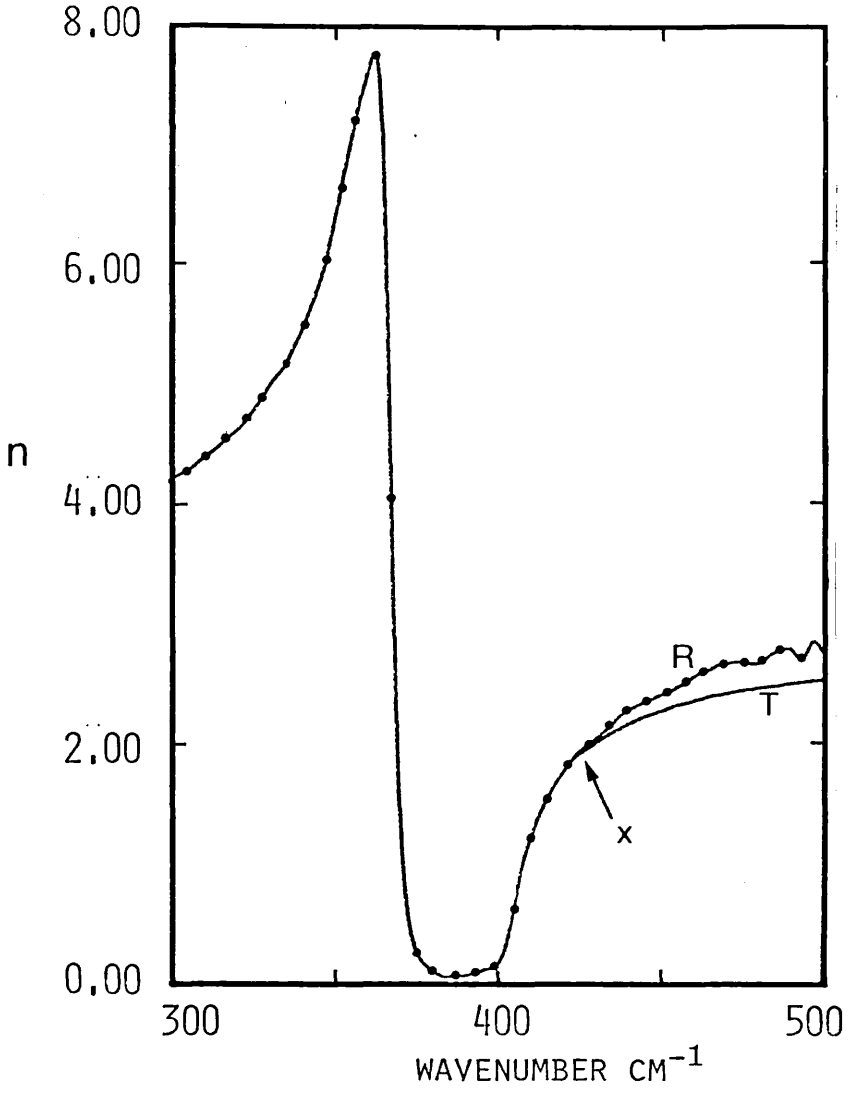

Figure 5.9 Refractive index of GaP at 300K showing the region of overlap, X obtained using the reflection and transmission DFTS techniques.

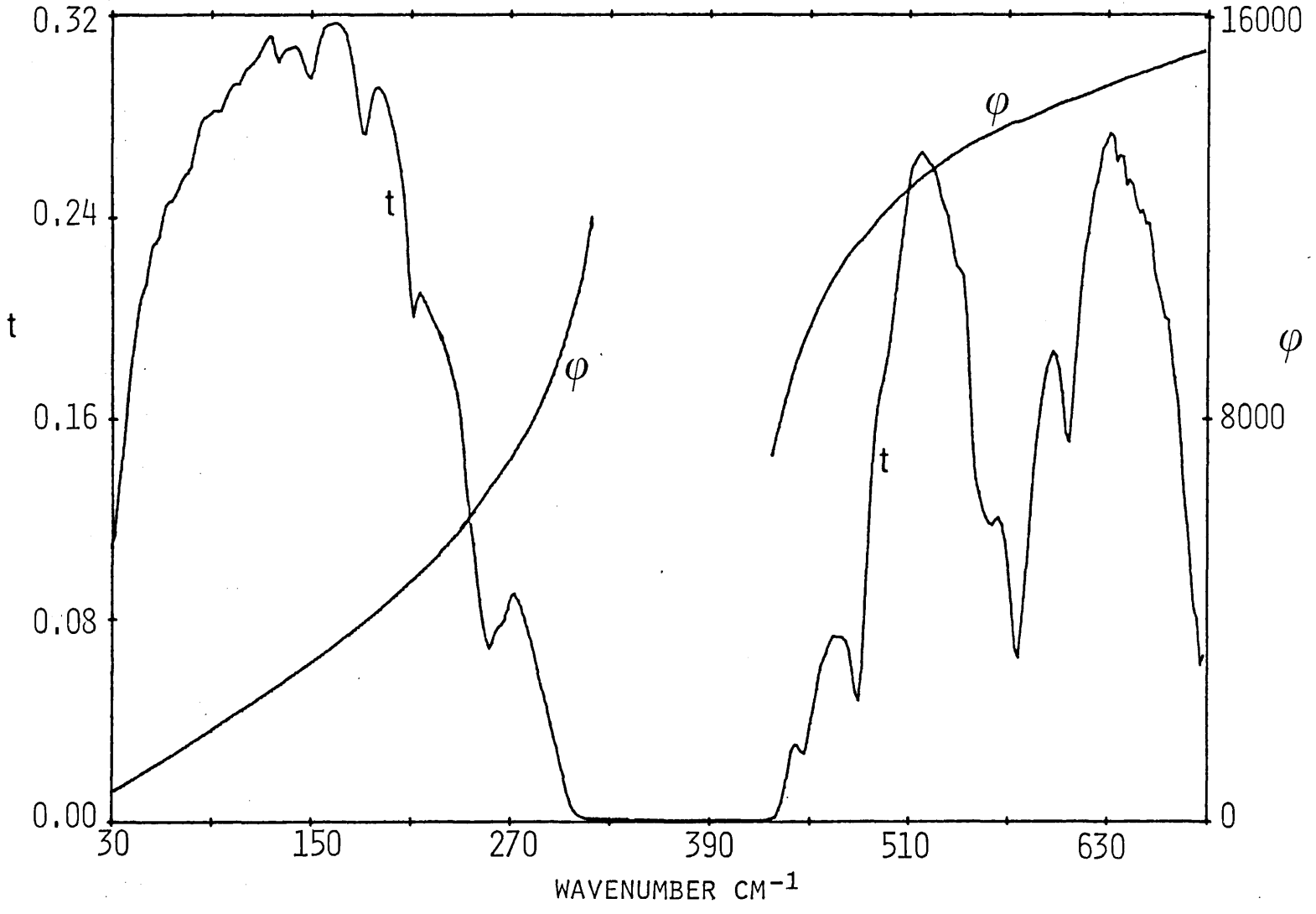

Figure 5.10 Complex transmission amplitude t and phase ϕ of GaP at 300K.

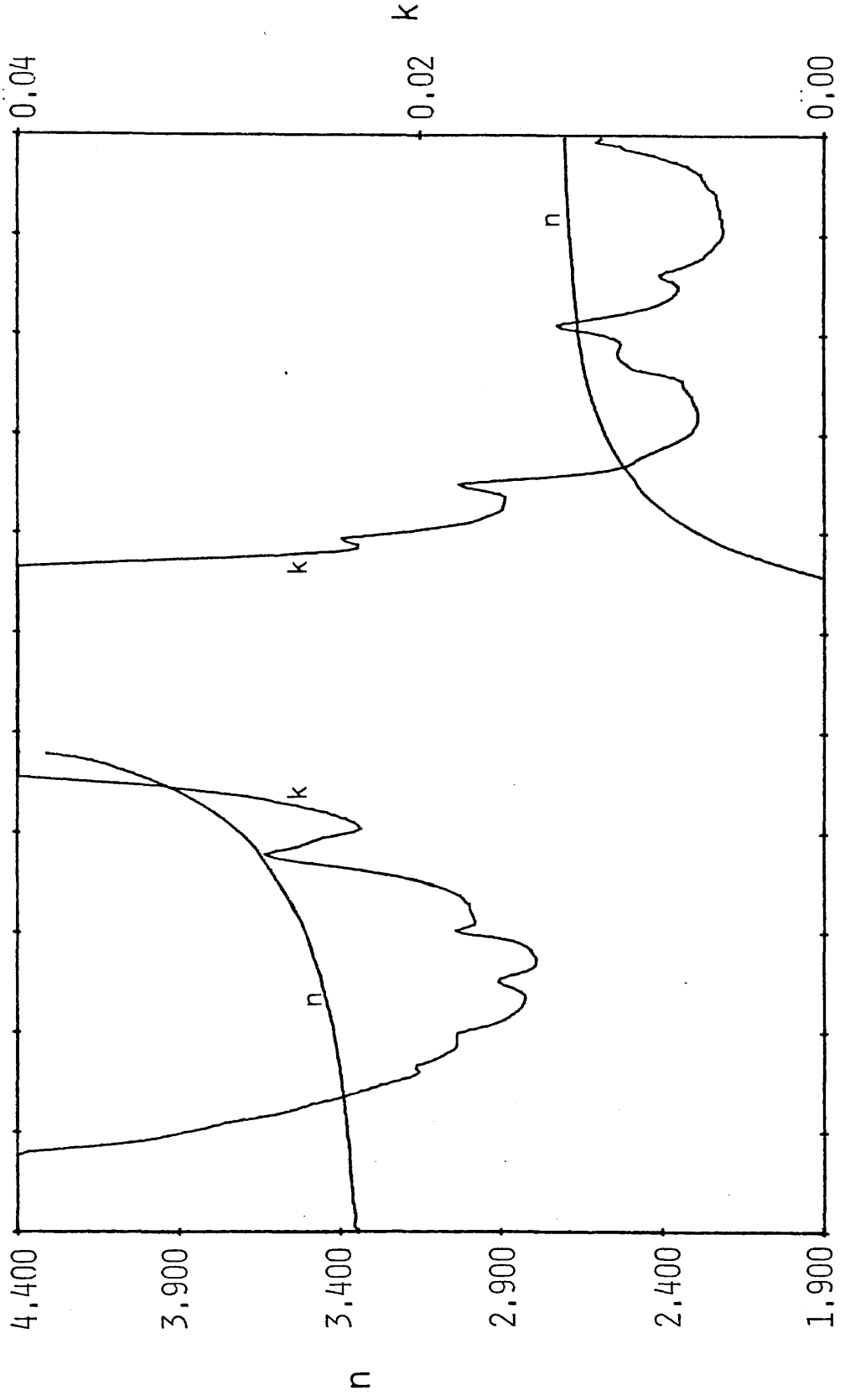

Figure 5.11 Refractive index n and extinction coefficient k of GaP at 300K.

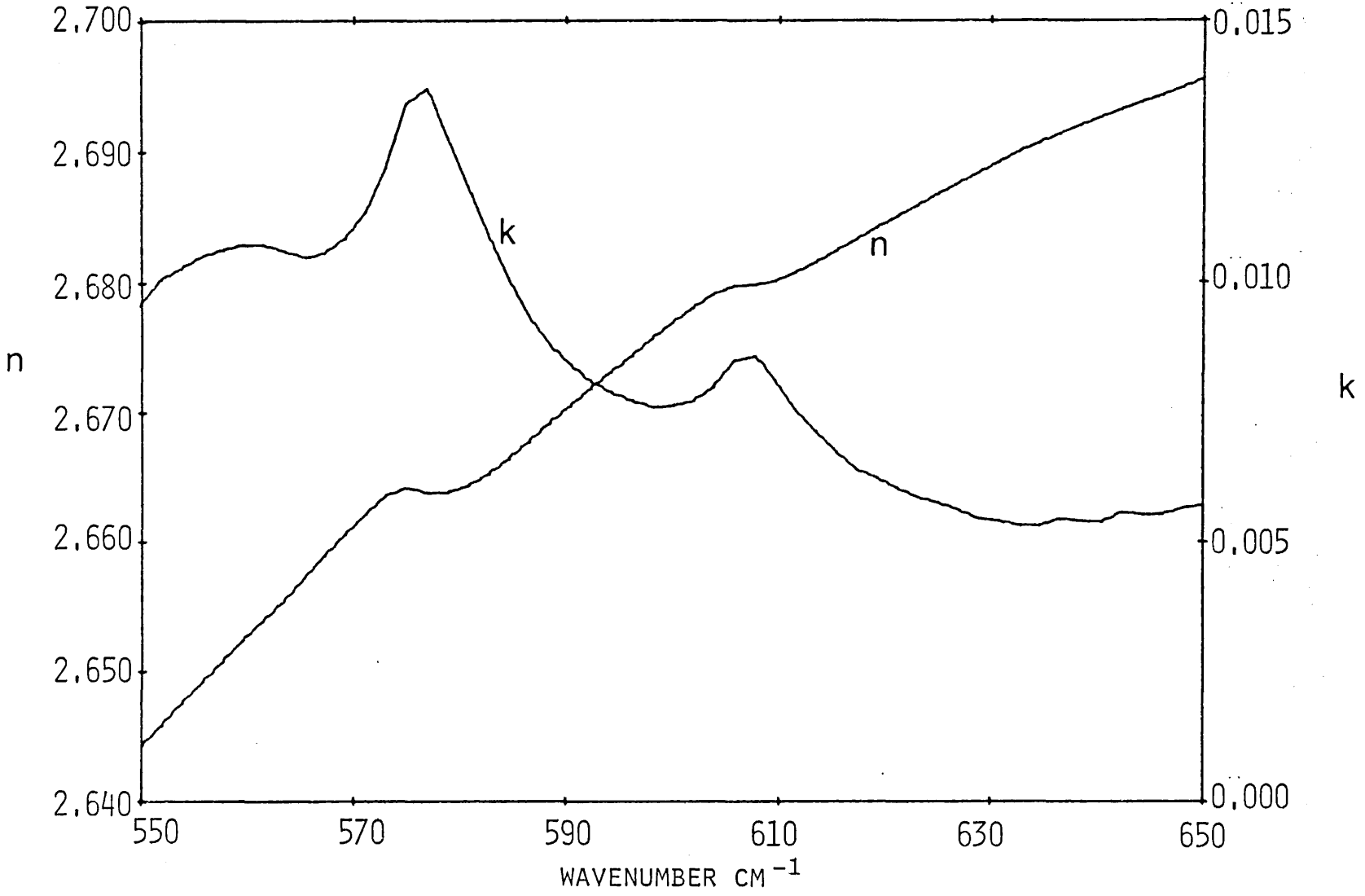

Figure 5.12 Refractive index n of GaP at 300K showing the detailed dispersion.

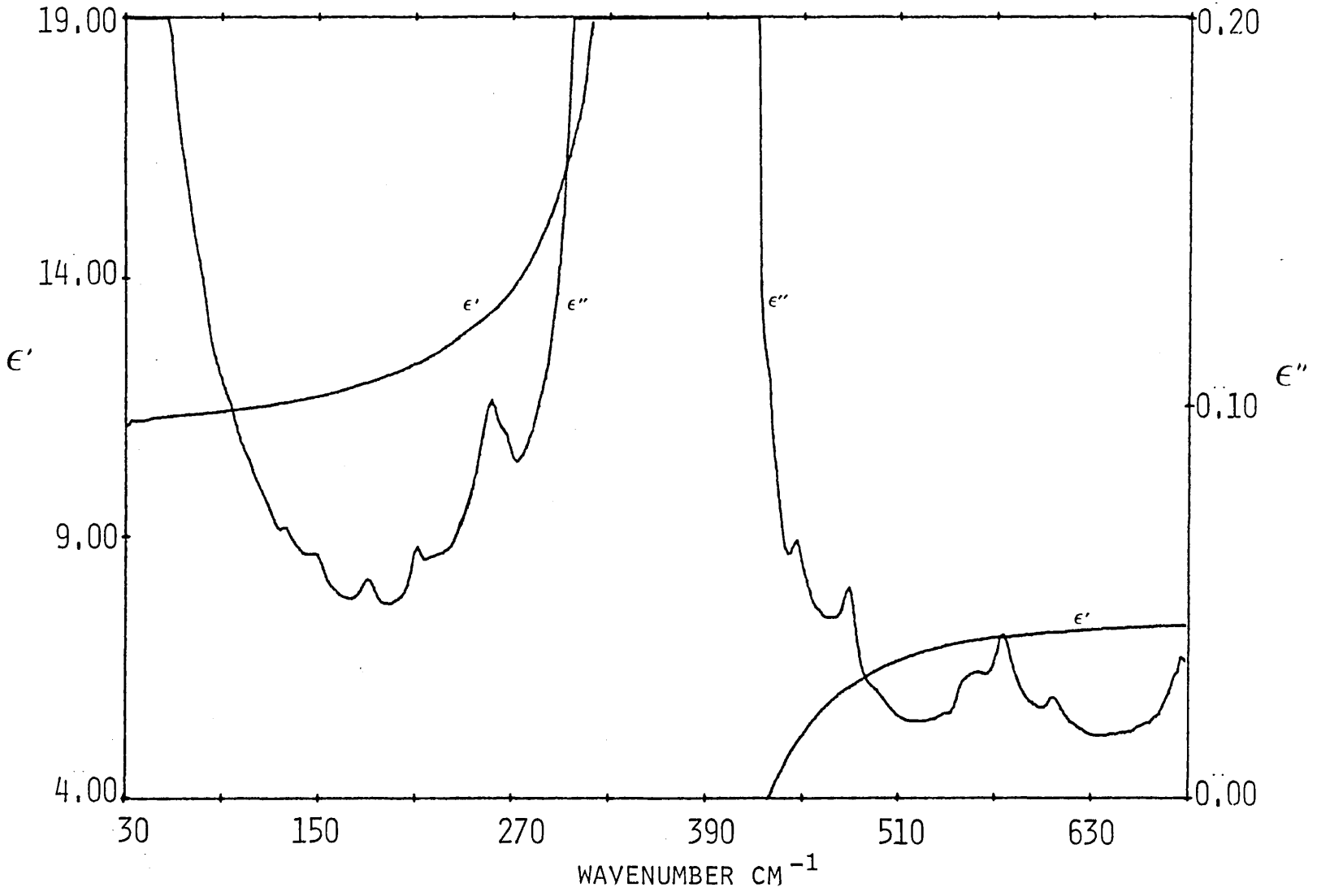

Figure 5.13 Real ϵ' and imaginary ϵ'' parts of the dielectric response of GaP at 300K.

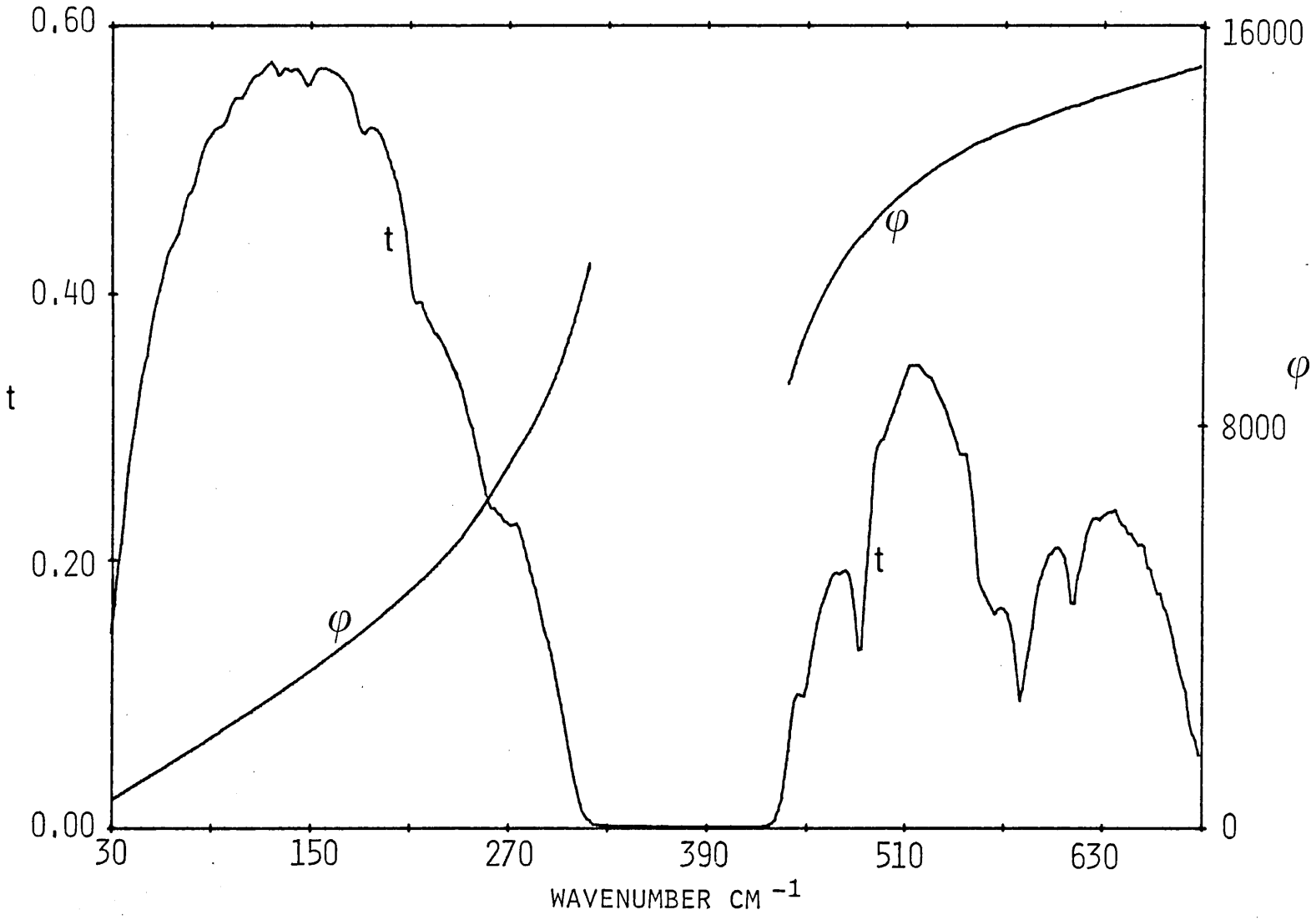

Figure 5.14 Complex transmission amplitude t and phase ϕ of GaP at 100K.

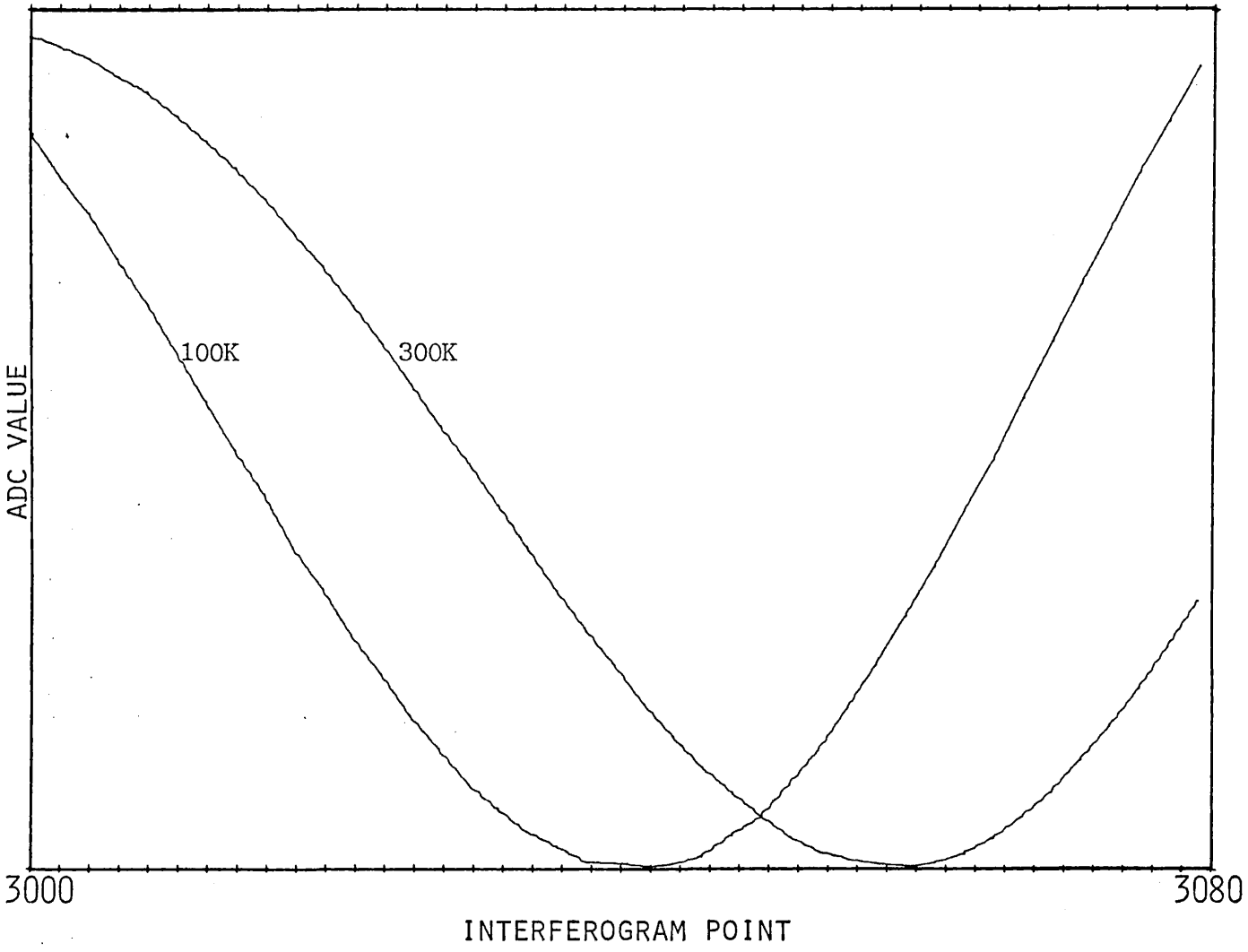

Figure 5.15 showing the positions of the minimum signal of GaP interferograms at 300 and 100K with respect to the position of the background interferogram.

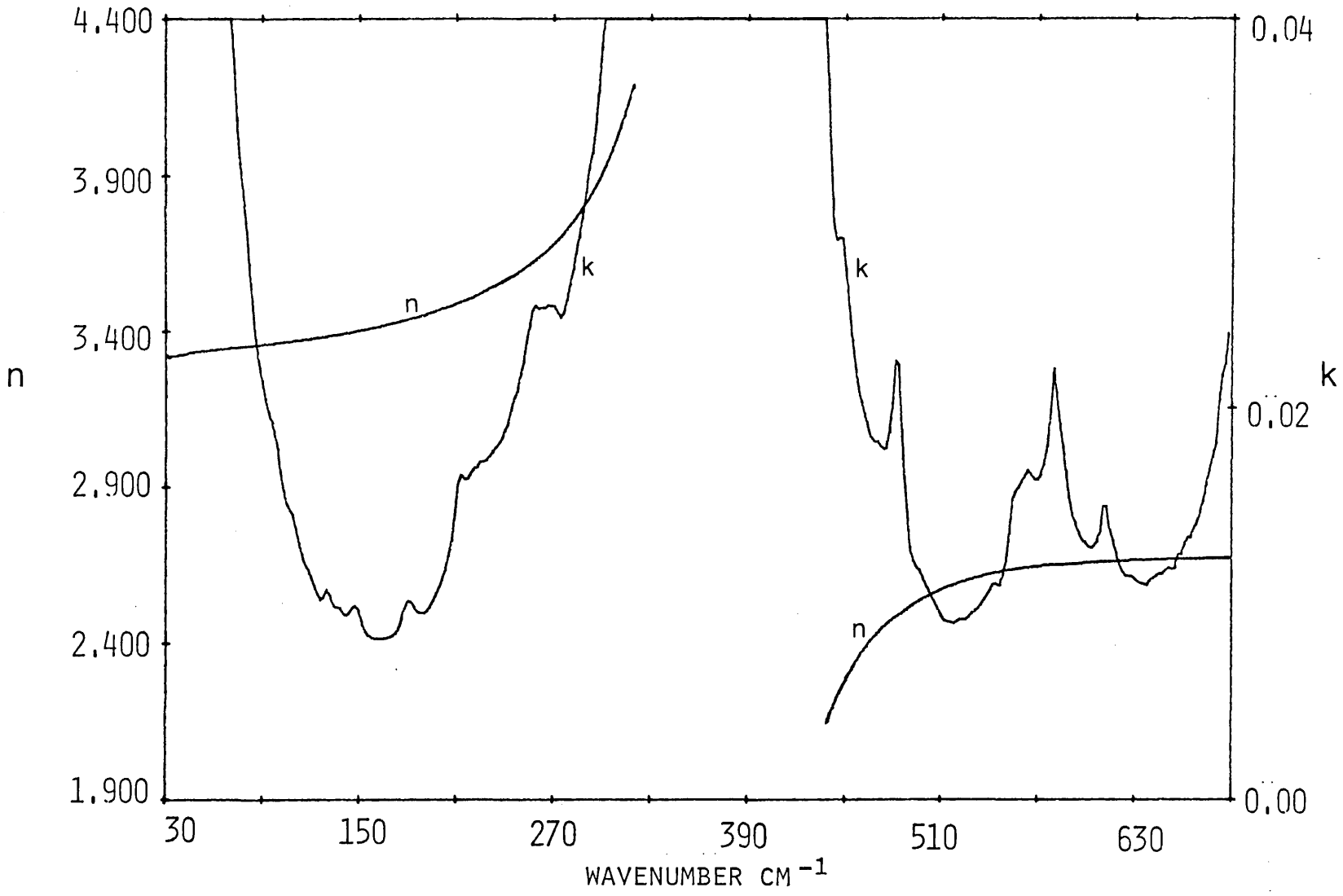

Figure 5.16 Refractive index n and extinction coefficient of GaP at 100K.

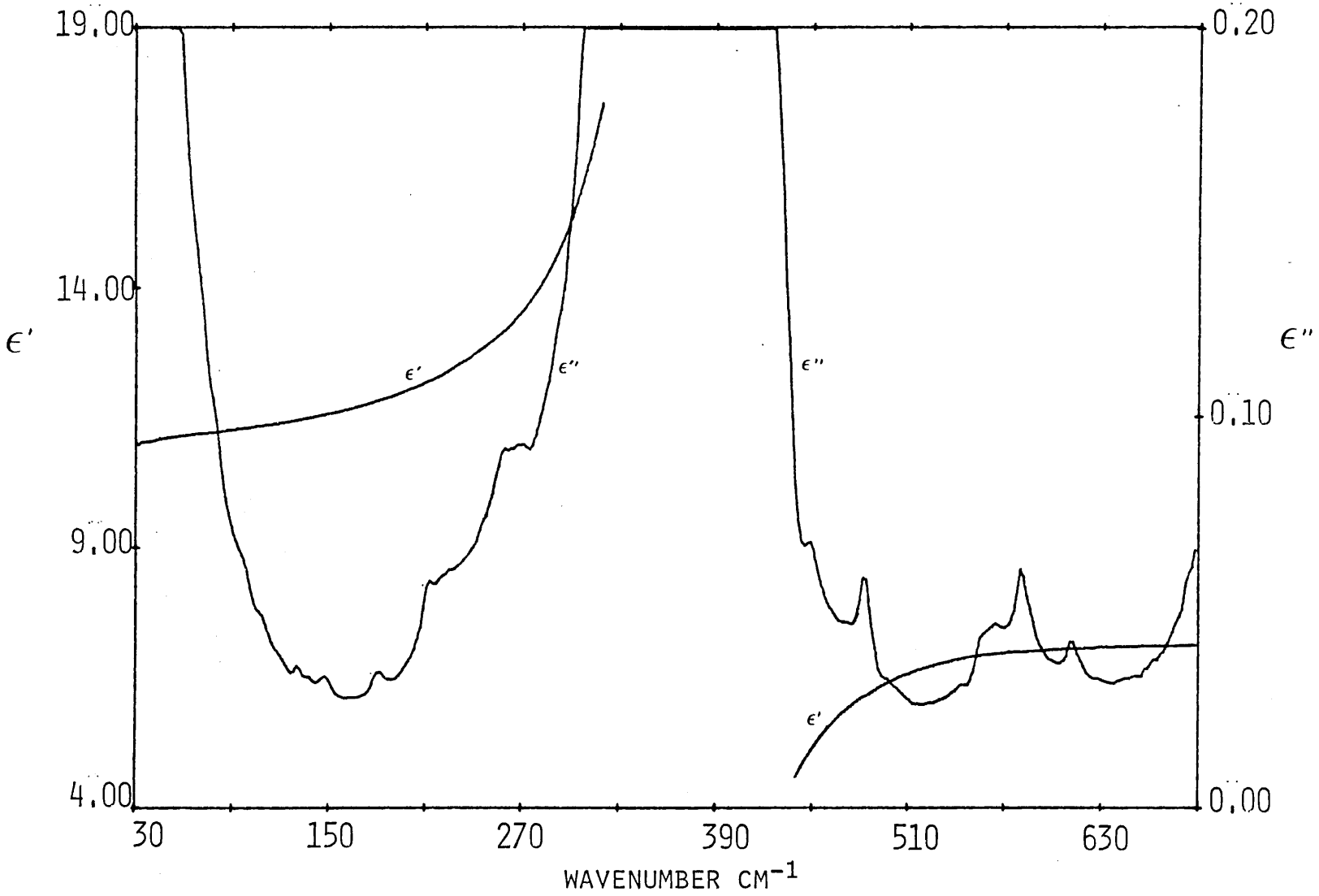

Figure 5.17 Real ϵ' and imaginary ϵ'' parts of the dielectric response of GaP at 100K.

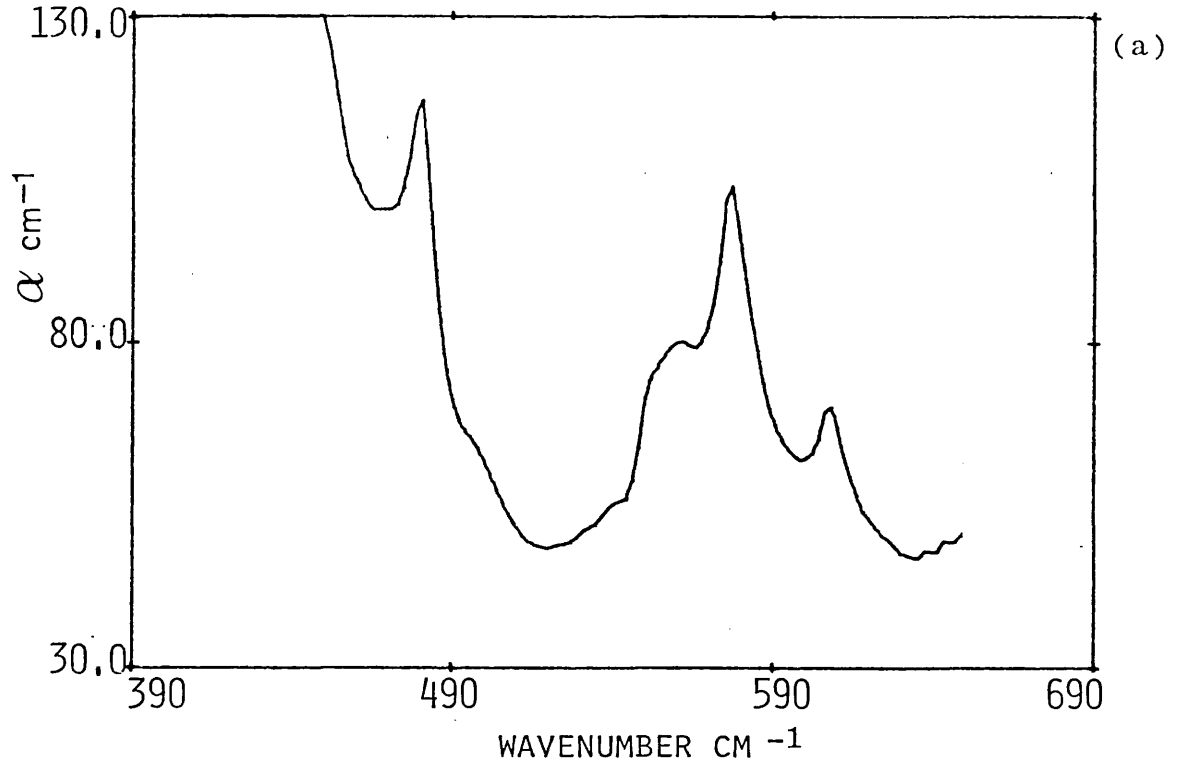

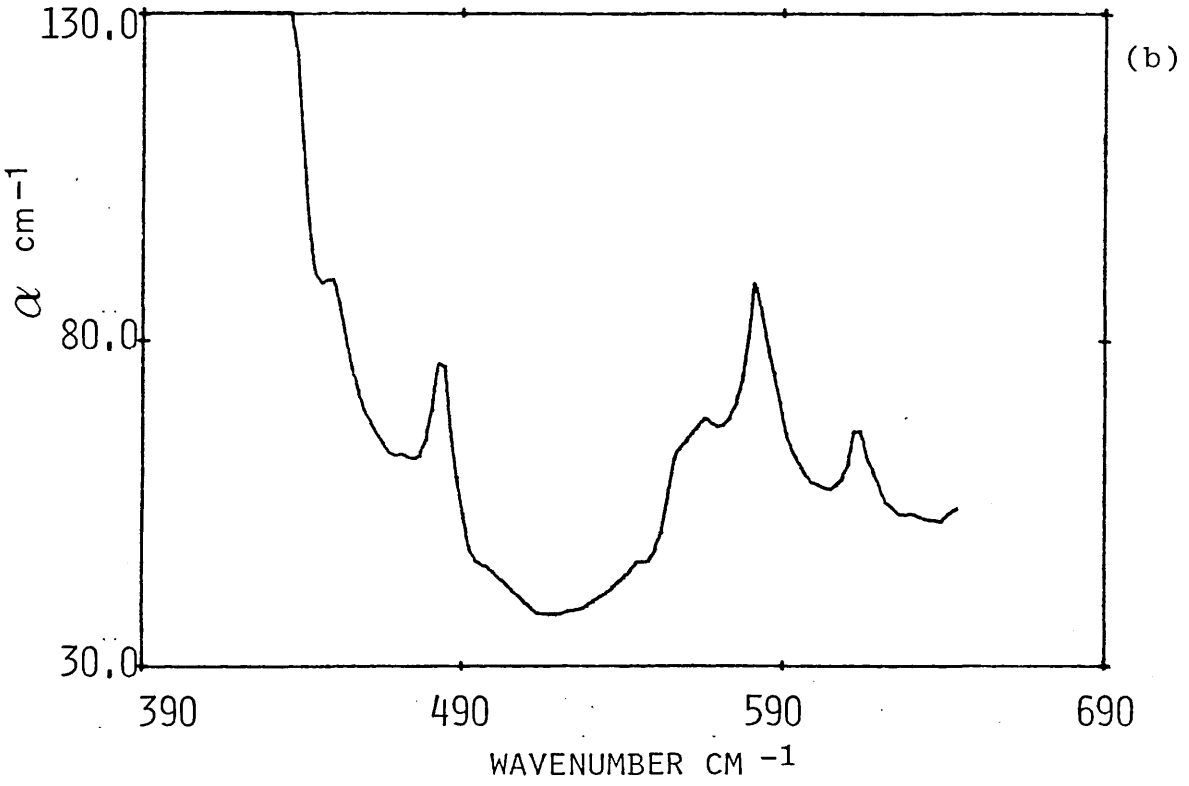

Figure 5.18 Power absorption coefficient α of GaP at (a) 300K and (b) 100K.

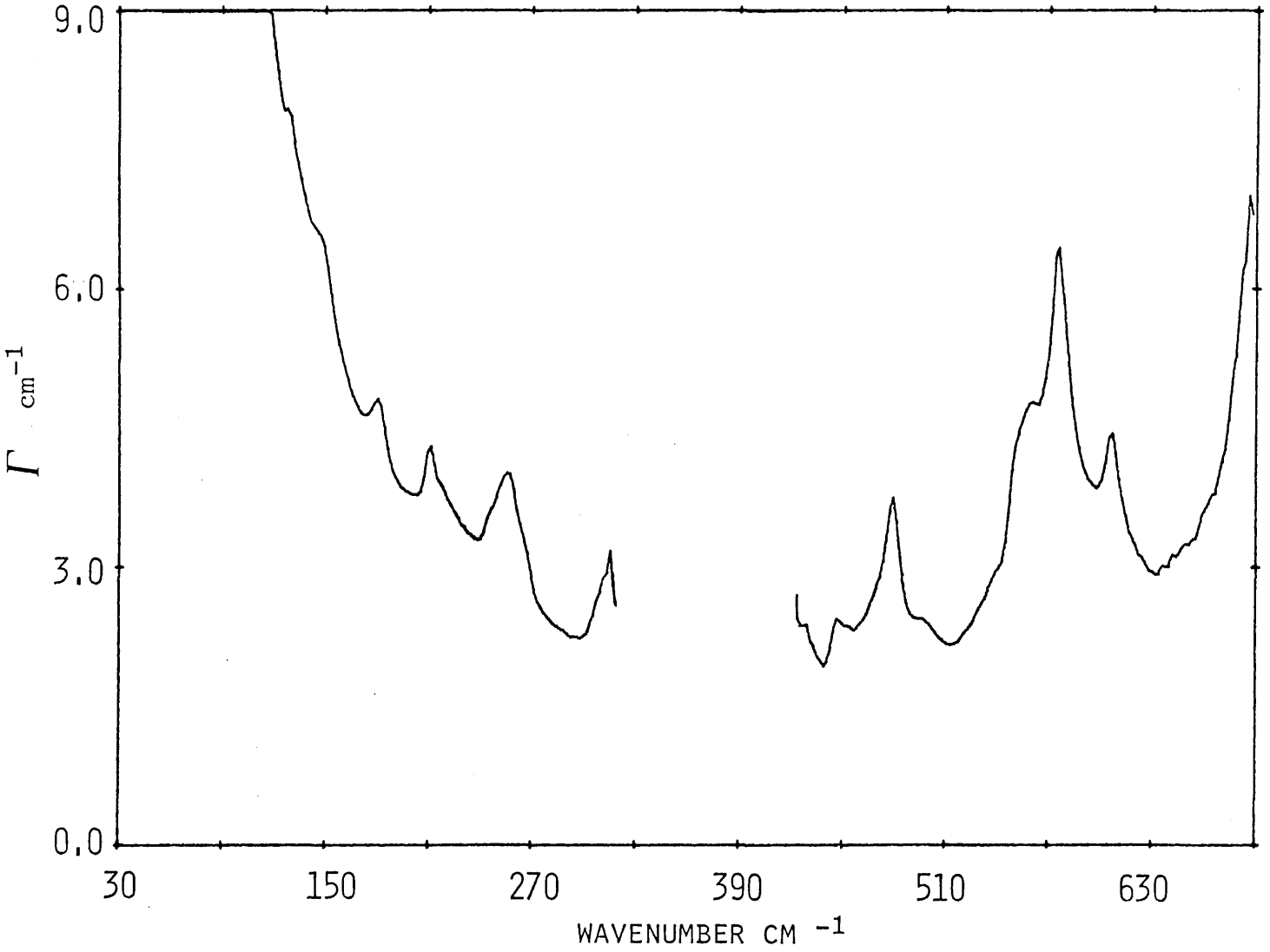

Figure 5.19 Frequency dependence of Γ required to account fully for the observed absorption in GaP at 300K if the non linear dipole contribution is neglected.

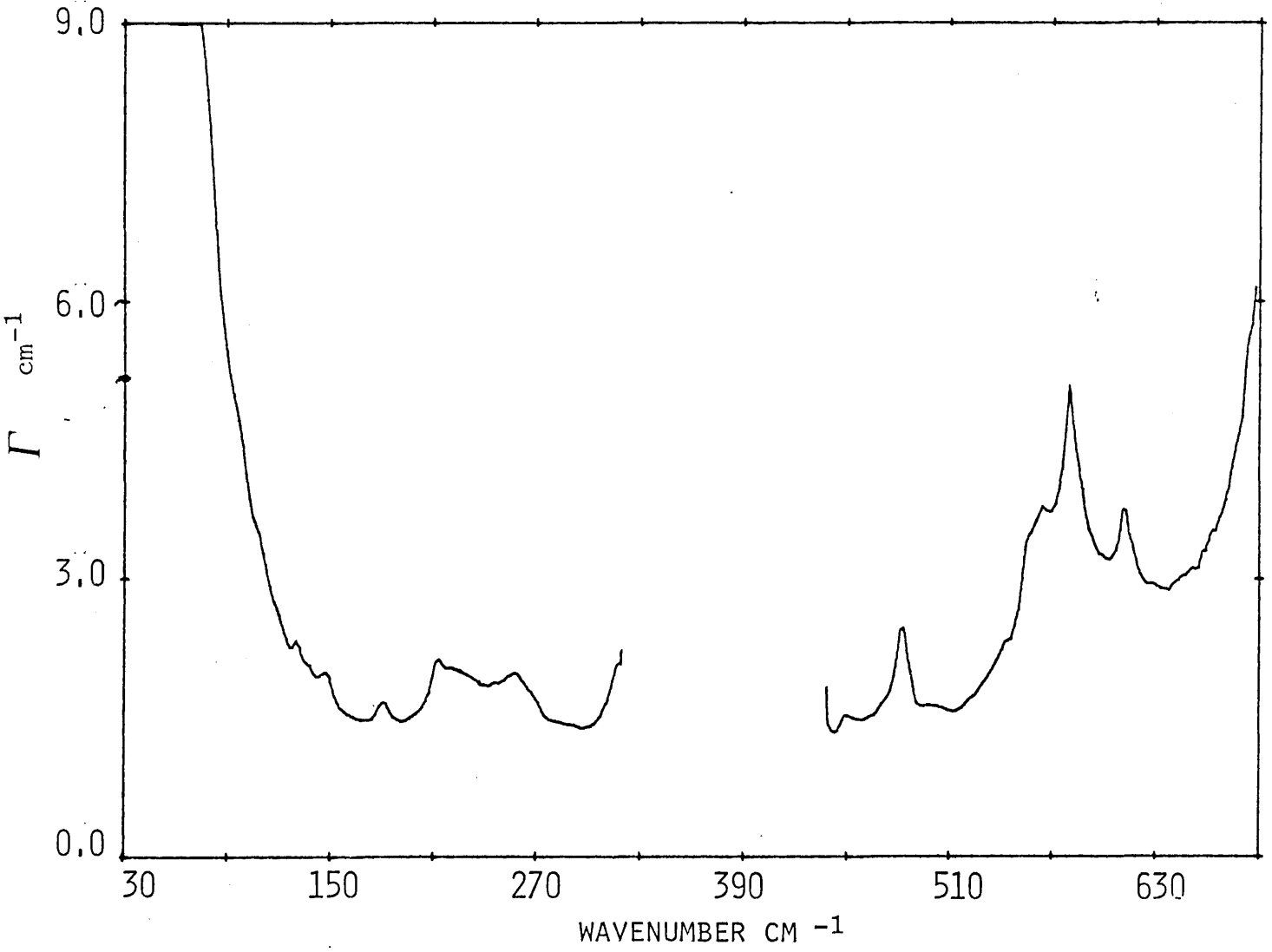

Figure 5.20 Frequency dependence of Γ required to account fully for the observed absorption in GaP at 100K if the non linear dipole contribution is neglected.

Table 5.2 Critical point phonon frequencies of GaP

Critical point		11-parameter RIM	Neutron data	
		ref 1	ref 2	ref 3
Γ	LO	402.8	408.3±1.7	402.0±13
	TO	368.3	-	367.0±11
X	LO	368.3	366.7±10	366.1±12
	LA	254.2	250.0±13	249.3±4
	TO	362.7	355.0±17	353.3±8
	TA	106.1	104.3±5	106.6±3
L	LO	405.3	405.3±1.7	373.5±8
	LA	214.2	-	212.2±8
	TO	352.8	353.3±7	357.6±8
	TA	83.3	83.3±1.7	85.4±2
W	W1	366.9	-	
	W2	365.0	-	
	W3	363.5	-	
	W4	224.7	-	
	W5	155.8	153.3±3.3	
	W6	106.4	123.3±3.3	
K	$IIO\Sigma_1$	372.1	-	
	$IIA\Sigma_1$	231.2	-	
	$IO\Sigma_1$	366.4	350.0±10	
	$TO\Sigma_2$	358.2	-	
	$IA\Sigma_1$	143.1	-	
	$TA\Sigma_2$	97.8	105.0±6.7	

ref 1 Patel et al, (1982)
ref 2 Borcherds et al, (1979)
ref 3 Yarnell et al, (1968)

Table 5.3 GaP assignments

This work		11-parameter RIM	Neutron data		Infrared data 20K	Assignments
300K	100K	ref 1	ref 2	ref 3	ref 4	
51	-	52.5	52	16		LO(L) - TO(L)
97	97	108.5	105	104		TO(X) - LA(X)
130	130	130.9	-	127		LA(L) - TA(L)
152	152	148.1	146	143		LA(X) - TA(X)
182	182	186.1	191	161	180	LO(L) - LA(L)
212	213	212.2	209	212	213	2TA(X)
258	260	256.6	251	247	258	TO(X) - TA(X)
		257.1	-	-		W3 - W6
		258.6	-	-		W2 - W6
268	272	268.6	245	-	274	$IO\Sigma_1$ - $TA\Sigma_2$
		269.5	270	273		TO(L) - TA(L)
447	452	436.1	437	443	448	TO(L) + TA(L)
480	485	474.0	471	472	483	LO(X) + TA(X)
491	496	488.6	489	458	503	LO(L) + TA(L)
542	546	-	-	-	544	3-phonon ?
555	560	-	-	-	554	3-phonon ?
562	565	567.0	-	570	564	TO(L) + LA(L)
580	585	619.5	-	586	584	LO(L) + LA(L)
608	612	603.3	-	-	609	$IIO\Sigma_1$ + $IIA\Sigma_1$

ref 1 Patel et al (1982)
ref 2 Borcherds et al (1979)
ref 3 Yarnell et al (1968)
ref 4 Koteles et al (1976a)

Table 5.4

Temperature dependence of the intensities of two-phonon summation bands in GaP

Summation bands	Calculated $\frac{(1+n_1+n_2)_{100K}}{(1+n_1+n_2)_{300K}}$	Measured $\frac{\alpha_{100K}}{\alpha_{300K}}$
TO(L) + TA(L)	0.44	0.55
LO(X) + TA(X)	0.47	0.52
LO(L) + TA(L)	0.45	0.47
TO(L) + LA(L)	0.59	0.70
LO(L) + LA(L)	0.61	0.80
$IIO\Sigma_1$ + $IIA\Sigma_1$	0.62	0.83

5.3 RESULTS AND DISCUSSION FOR GaAs

The optical constants of GaAs have been measured at 300 and 100K on either side of the reststrahlen band. The crystal was obtained from MCP Electronic Materials Ltd and its quoted carrier concentration is 2.4×10^{16} per cm^3.

Unlike the GaP specimen, the GaAs crystal used in this work is very absorbing throughout the spectral region under investigation. Thus, to obtain an average value of the specimen interferogram, the partial insertion technique was employed where the specimen was slightly withdrawn from the beam to obtain a small blip of the background interferogram to use as a reference for co-adding. This method has been described in chapter 3. Figures 5.21(a),(b),(c) show the GaAs interferograms below the reststrahl obtained by using the above technique. A single scan of the specimen interferogram [figure 5.21(a)] gives a S/N ratio of about 4 and this increases to about 70 after averaging 300 runs. Figure 5.21(c) is the final interferogram stored after the reference signal has been exluded. These are typical results obtained by using the partial insertion technique. It is unlikely that these results could have been obtained in any other way.

The amplitude and phase spectra of GaAs at 300K are shown in figure 5.22. Below the reststrahlen band the maximum transmission amplitude is only about 3.5%. This is probably why no other transmission data from a thick crystal of GaAs at room temperature have been found in the literature. The optical constants results are shown in figure 5.23 and the real and imaginary parts of the

dielectric response at 300K are given in figure 5.24. The crystal was then cooled to approximately 100K and the transmission and phase spectra obtained at this temperature are shown in figure 5.25. It can be observed from figure 5.25 that the difference bands have reduced in intensity compared to the room temperature results. The linear expansion coefficient between 100 and 300K was obtained from Soma et al (1982) and this gives a calculated reduction of 0.42μm in the thickness of the specimen at 100K, which is negligible. Values of the optical constants and dielectric parameters calculated from the amplitude and phase obtained at 100K are shown in figures 5.26 and 5.27.

There have been many determinations of the absorption coefficient in the infrared on either side of the reststrahlen band by power transmission spectroscopy [Spitzer and Whelan (1959), Cochran et al (1961), Iwasa et al (1964), Johnson et al (1969), Sobotta (1970), Perkowitz (1971), Koteles and Datars (1976)] and the published data covers a selection of differently doped samples and a wide range of carrier concentration. Afsar and Button (1983) have recently used the technique of transmission DFTS to make high precision measurements of the optical constants and dielectric functions of high resistivity GaAs at room temperature in the millimetre wave region.

The cpp frequencies used in this work are taken from values calculated by Patel et al (1984) using the 11-parameter RIM and these are shown in table 5.5 together with other reported values [Waugh and Dolling (1963), Dolling and Waugh (1965), Mooradian and Wright (1966)]. It

should be noted that no neutron data are available to provide a check on frequencies calculated from the RIM at the W critical point. Spectral features at 100 and 300K obtained from the present work are assigned in terms of combinations of critical point phonons using the frequencies derived from the RIM. These assignments are given in table 5.6.

Recently Patel et al (1984) have assigned the reported two-phonon infrared spectra and second order Raman spectrum in GaAs on the basis of the RIM and good agreement has been obtained. Some of their calculated phonon frequencies at room temperature were compared with the features obtained at 15K by Koteles and Datars (1976). Since the data at 300K is now available, some of these assignments can now be made directly to the observed features obtained at 300K.

Johnson et al (1969) have measured the real refractive index n at 300K and 8K from about 33 to 800 cm^{-1} and the present measurements at 300K above the reststrahlen region agree very well with their room temperature results. Their calculated values of n above the reststrahlen region at 100K were predicted to be nearly coincident with their experimental data obtained at 300K. The calculation was made using the single oscillator model as described in their publication. However, in the present work, by careful analysis of the gross phase shift associated with the shift of the interferogram at 100K, it was found that the value of n above the reststrahl band was about 1% lower than that at 300K. (At 500 cm^{-1}, n_{300K}= 3.175 and n_{100K}=3.145). There seem to be no other reported values of n and k at 100K.

Figures 5.28(a),(b) show the plot of absorption coefficient of GaAs at 300 and 100K above the reststrahlen region. A reasonable agreement has been found between the present data obtained at 300K and the data of Spitzer and Whelan (1959) who used a crystal with a free electron concentration of 1.3×10^{17} per cm^3 as one of their specimens. It was not possible to compare the present data of α with the results of Cochran et al (1961) since their results were found to depend on the sample thickness.

Table 5.7 shows the temperature dependence of the intensities of two-phonon combination bands in GaAs where comparisons have been made between the measured values and theoretical predictions.

The frequency dependence of $\Gamma(\nu)$ required to account fully for the observed absorption at 300K and 100K if the non linear dipole contribution is neglected is shown in figures 5.29 and 5.30, respectively. The self energy in the reststrahlen region has been determined by Jamshidi et al (1984) at 300 and 6K and by Maslin (1986) at 300K using the technique of reflection DFTS. The values of $\Gamma(\nu)$ measured by Jamshidi et al are generally higher than the present results. Near the edge of the reststrahl band the results of Maslin (1986) are in good agreement with the present data. It can be seen from figures 5.29 and 5.30 that in the higher wavenumber region the self-energy function diverges. This indicates that the non linear dipole moment has contributed significantly to the absorption. The divergence in $\Gamma(\nu)$ below the reststrahlen band is dominated by free carrier effects which have not been subtracted out.

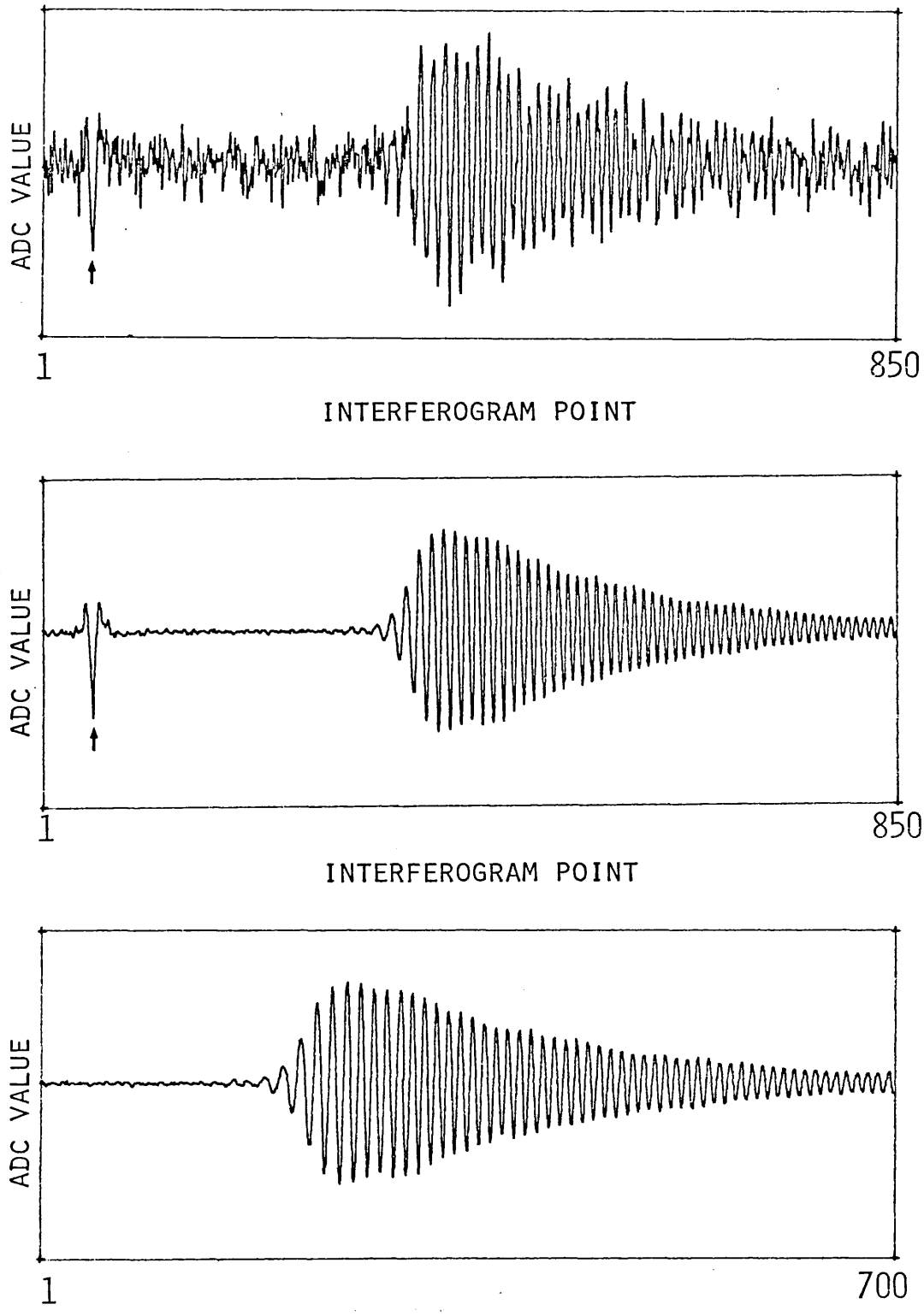

Figure 5.21 Interferograms of GaAs obtained using the partial insertion technique. (a) 1 scan (b) an average of 300 scans (c) after removing the reference signal. The arrow indicates the reference signal.

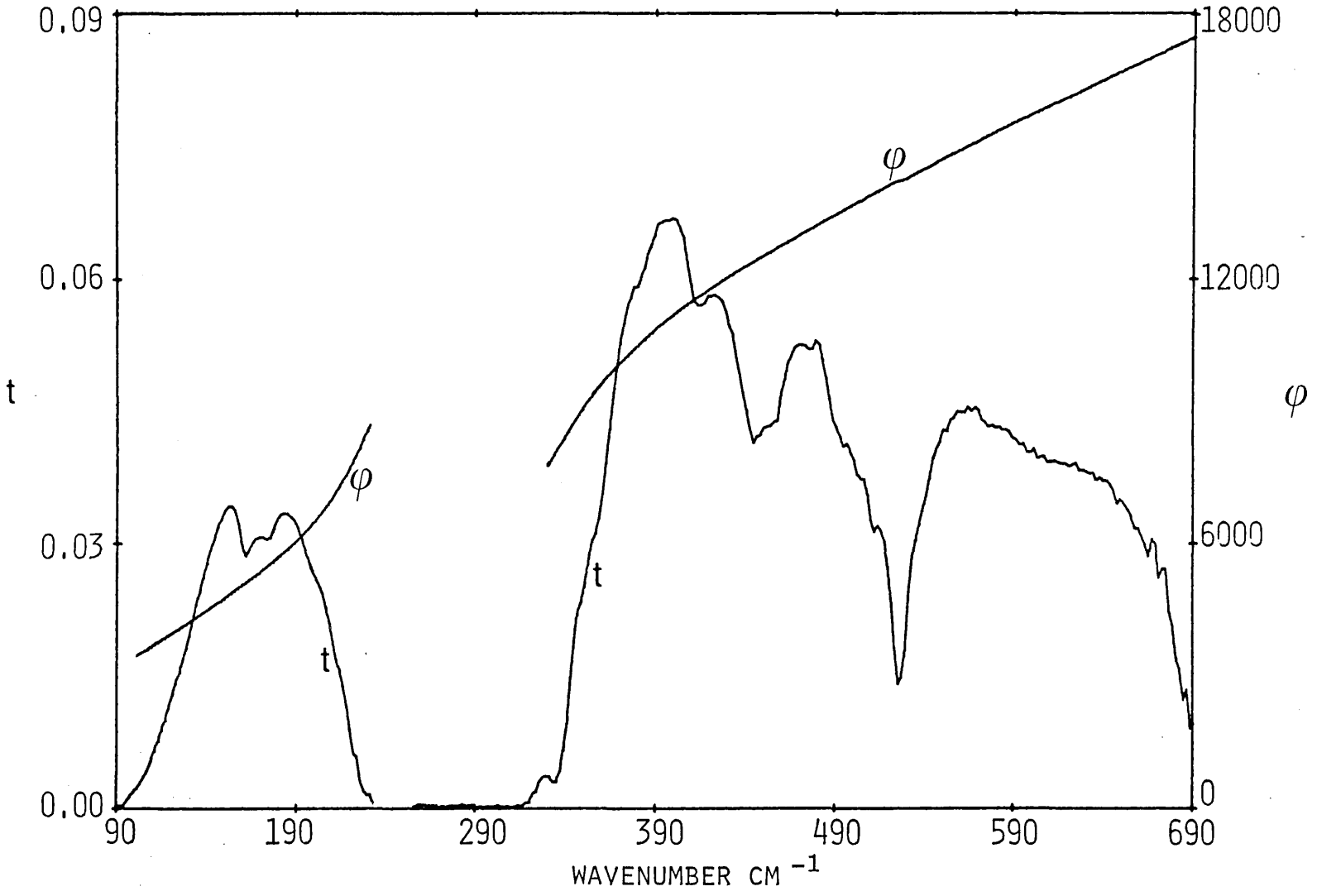

Figure 5.22 Complex transmission amplitude t and phase ϕ of GaAs at 300K.

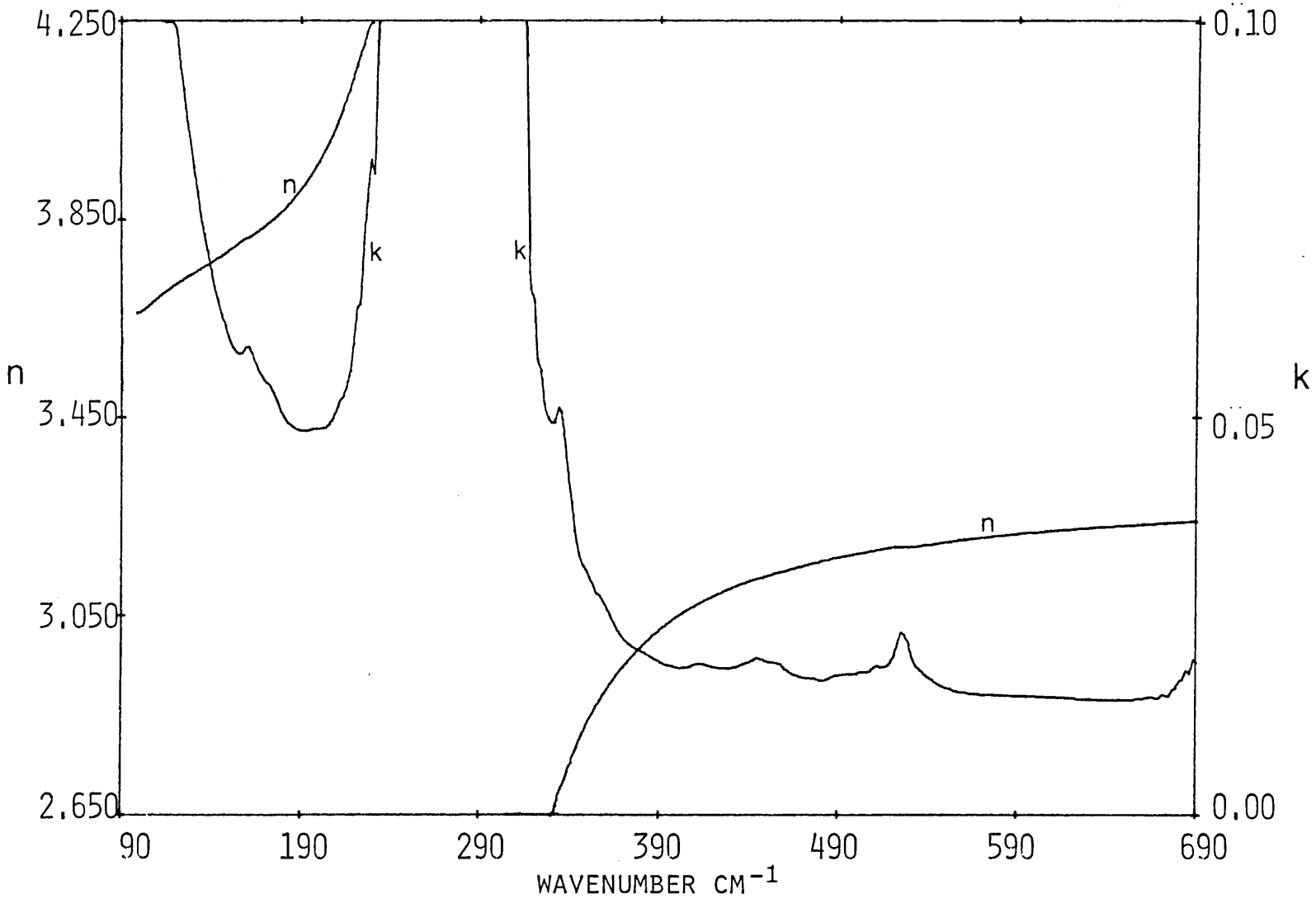

Figure 5.23 Refractive index n and extinction coefficient k of GaAs at 300K.

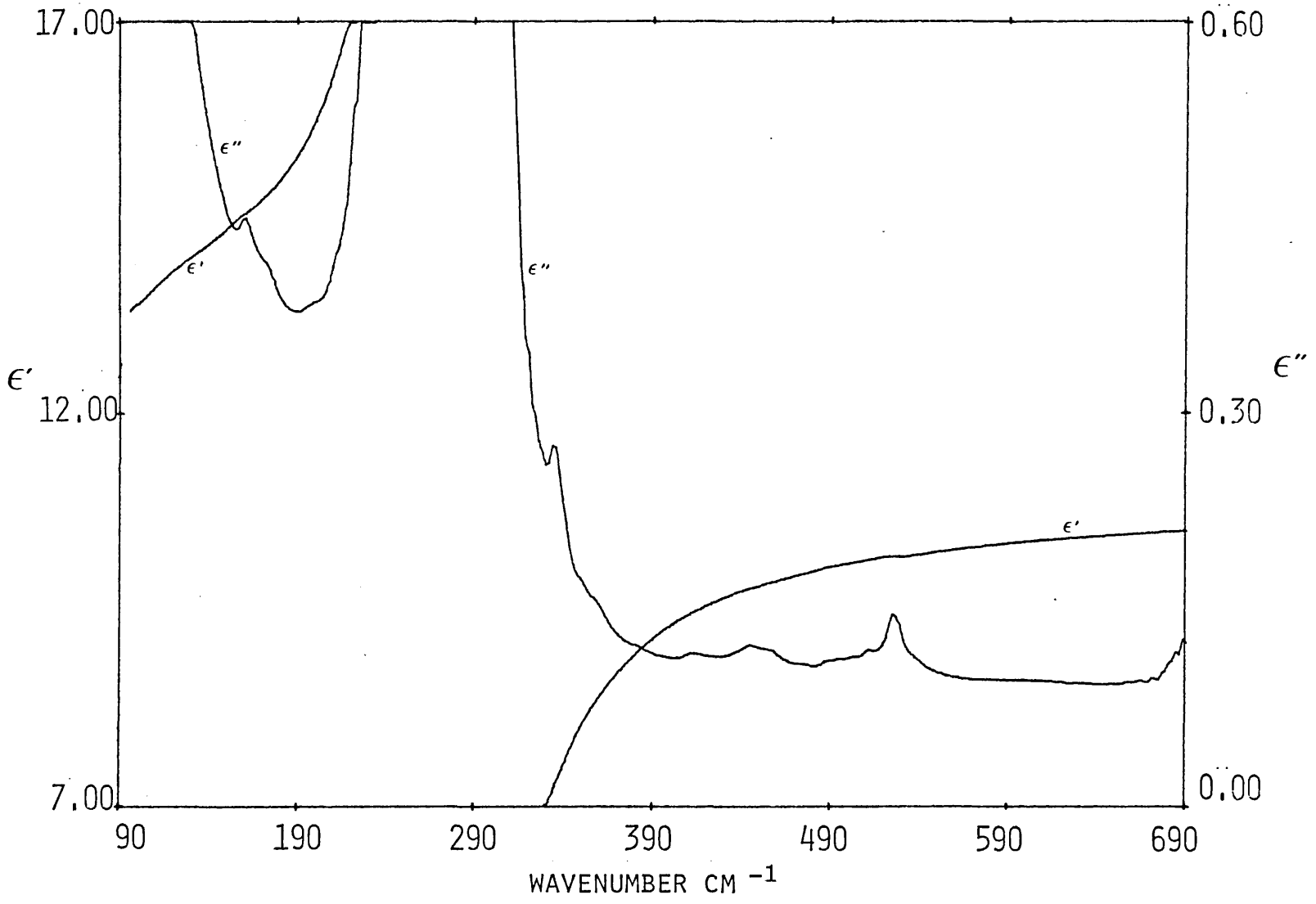

Figure 5.24 Real ϵ' and imaginary ϵ'' parts of the dielectric response of GaAs at 300K.

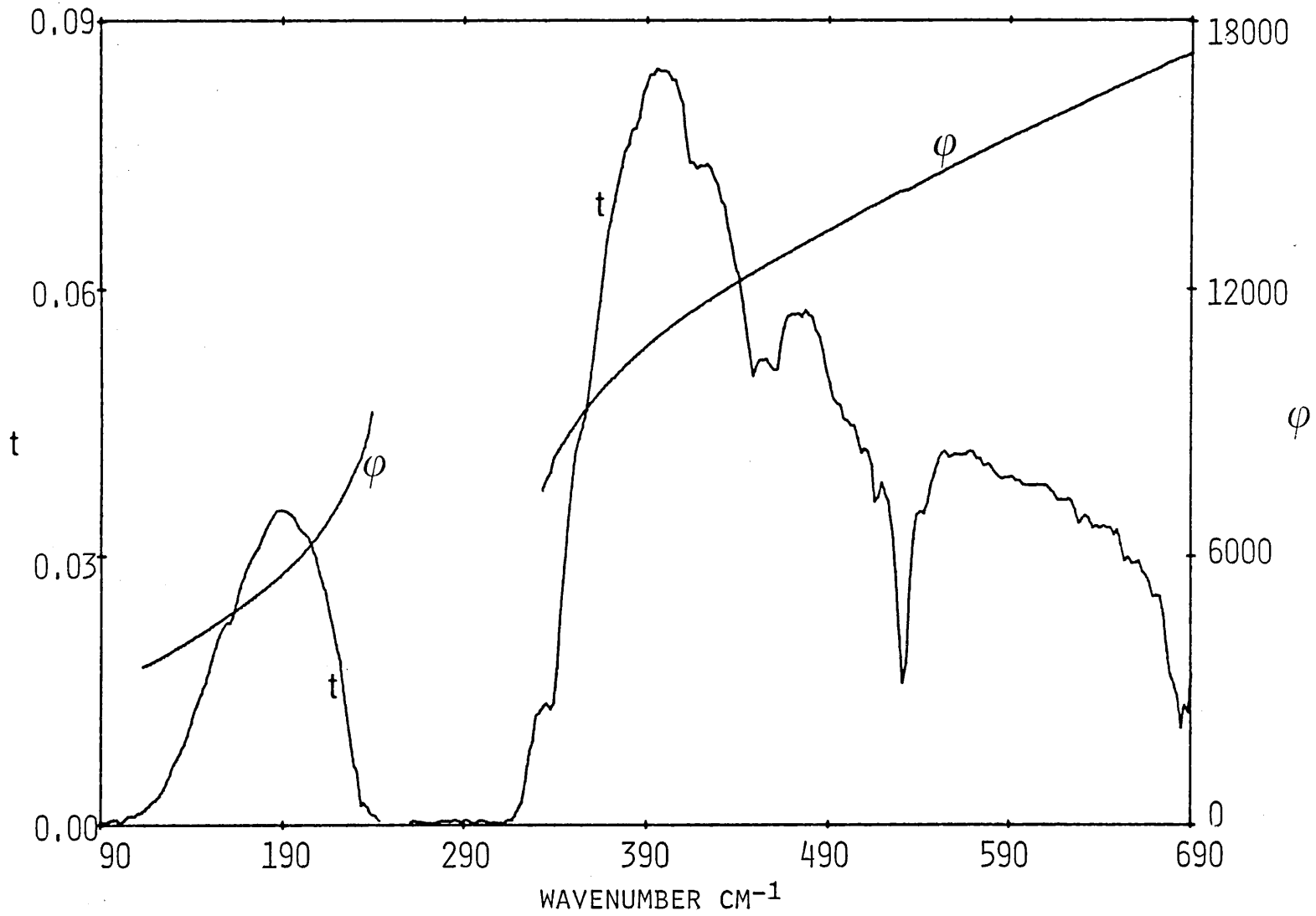

Figure 5.25 Complex transmission amplitude t and phase ϕ of GaAs at 100K.

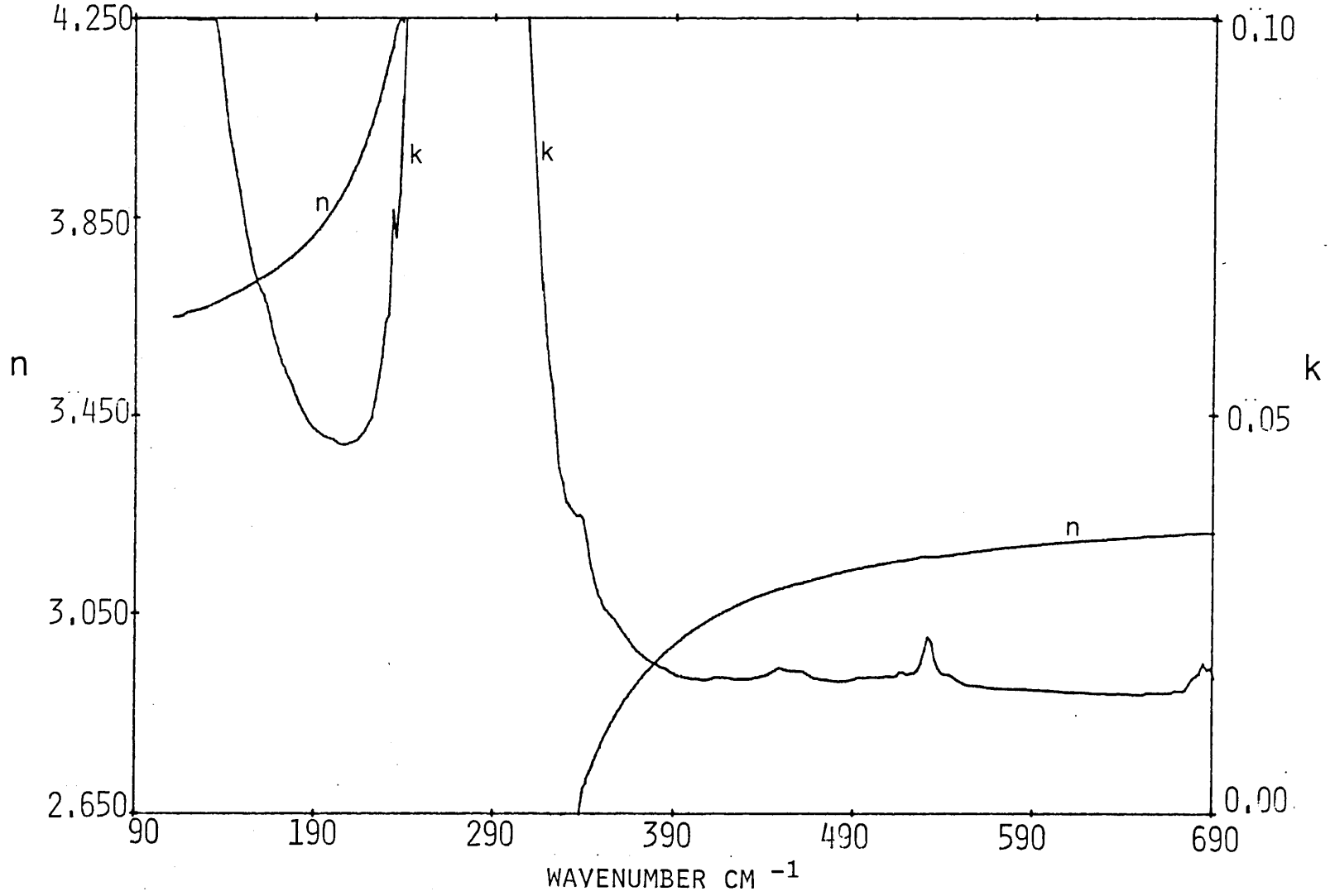

Figure 5.26 Refractive index n and extinction coefficient k of GaAs at 100K.

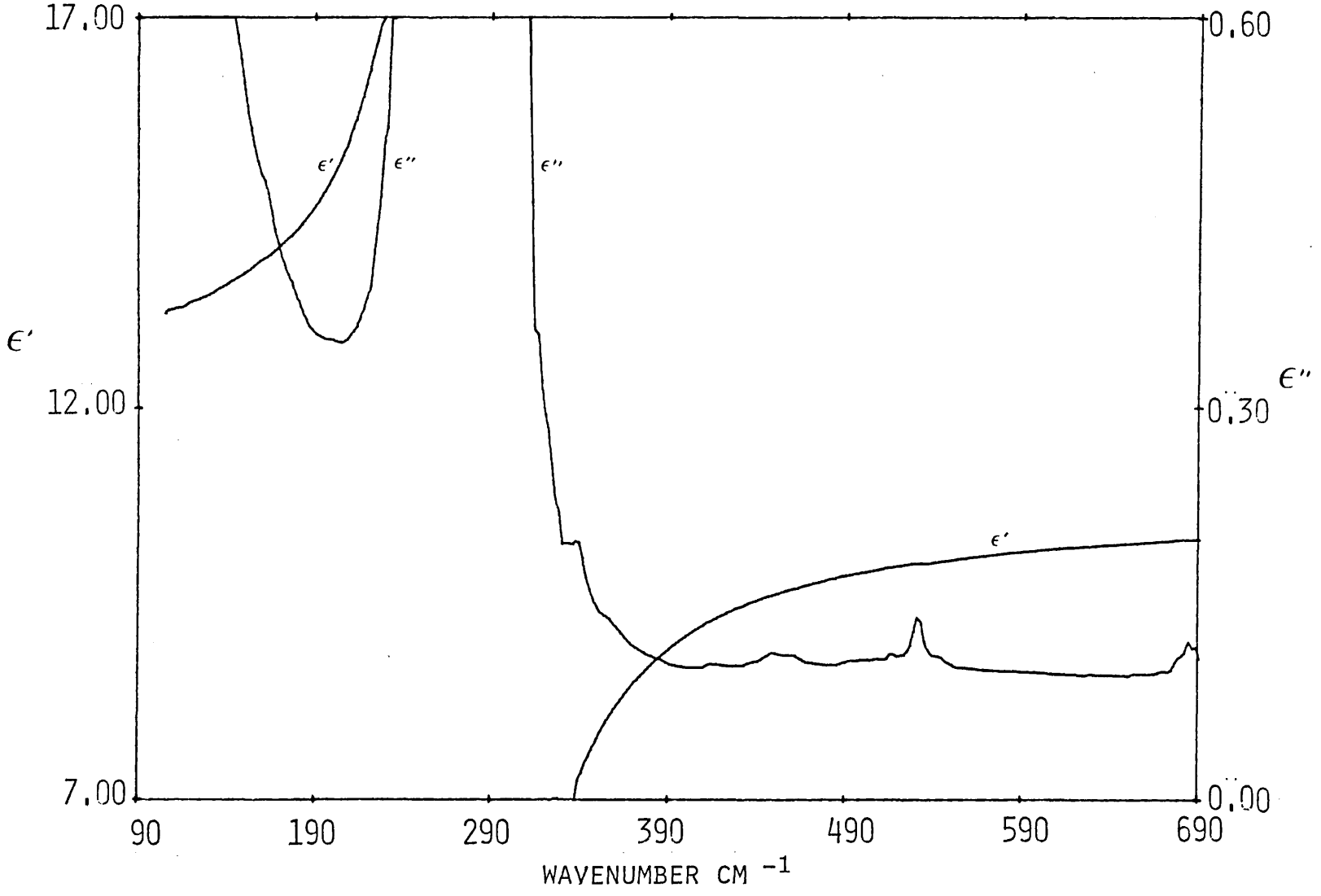

Figure 5.27 Real ϵ' and imaginary ϵ'' parts of the dielectric response of GaAs at 100K.

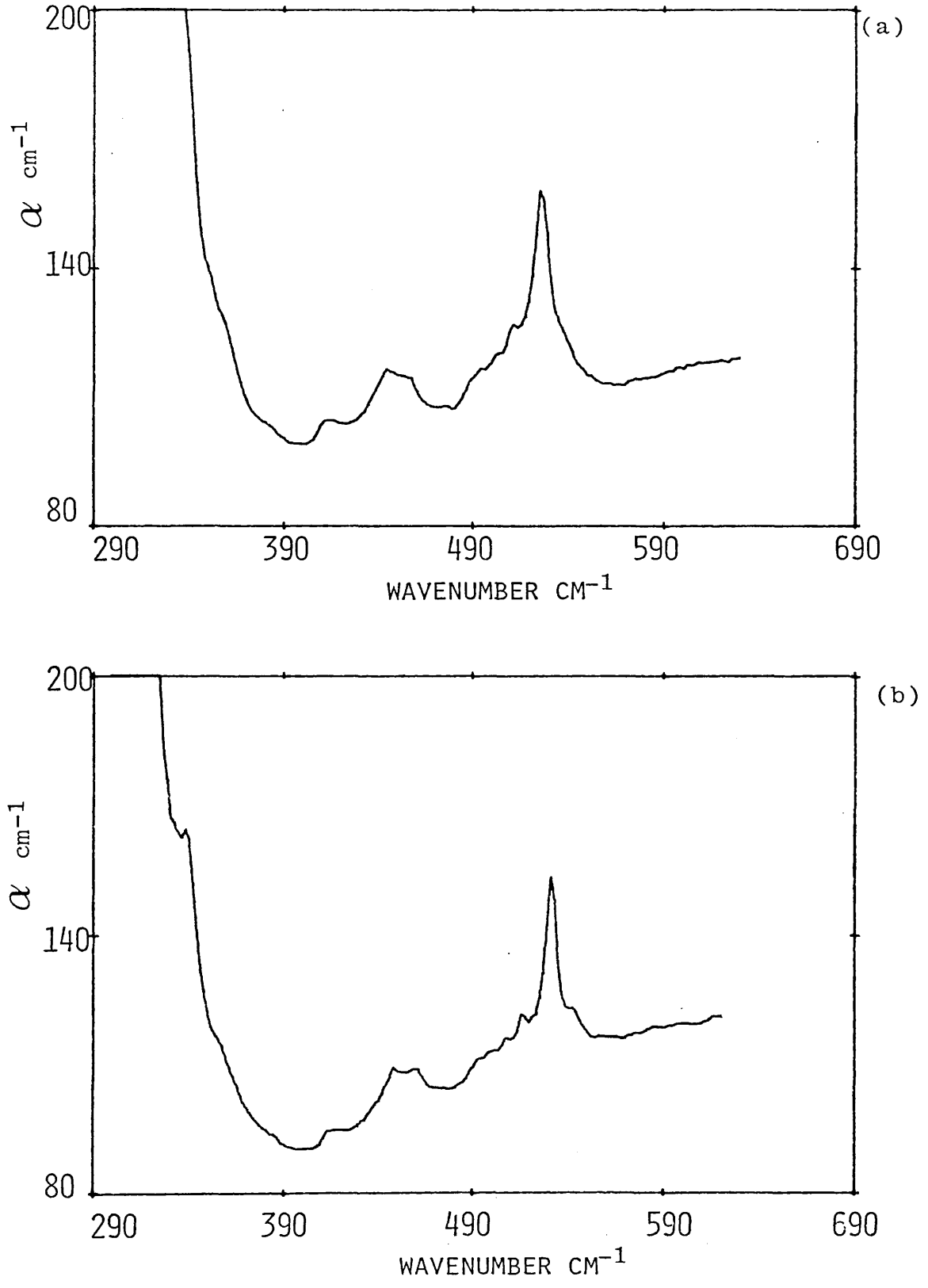

Figure 5.28 Power absorption coefficient α of GaAs at (a) 300K and (b) 100K.

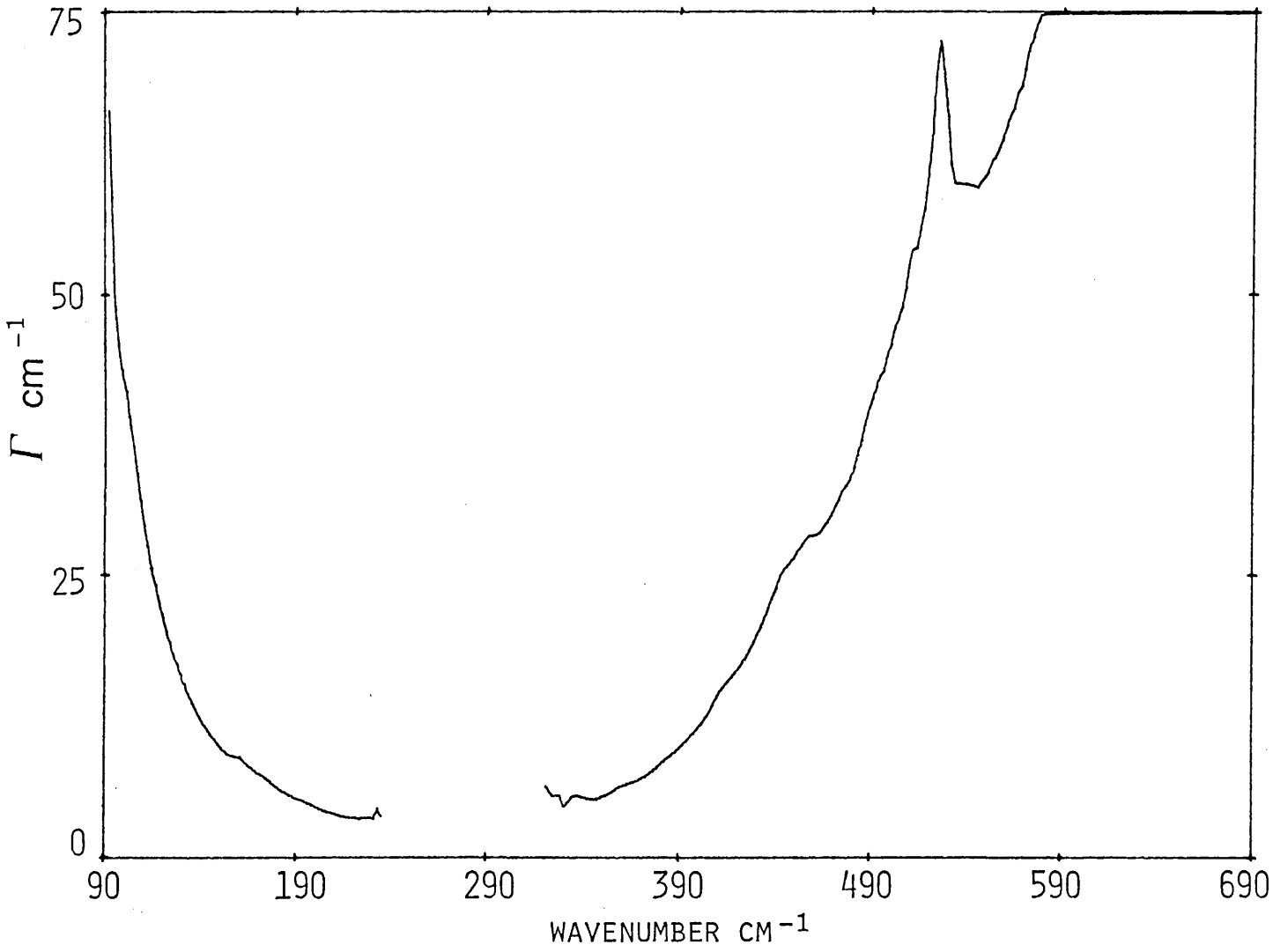

Figure 5.29 Frequency dependence Γ required to account fully for the observed absorption in GaAs at 300K if the non linear dipole contribution is neglected.

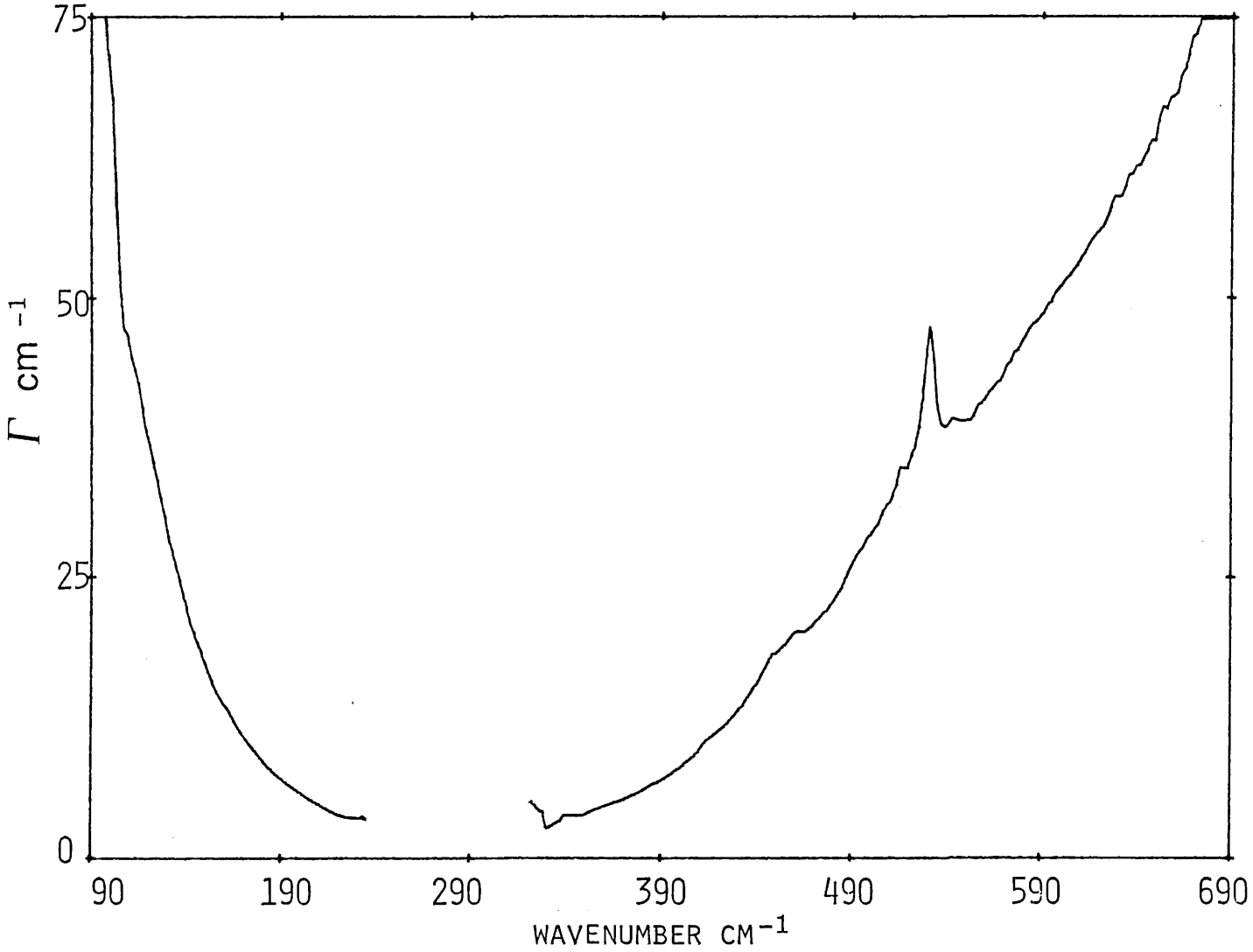

Figure 5.30 Frequency dependence Γ required to account fully for the observed absorption in GaAs at 100K if the non linear dipole contribution is neglected.

Table 5.5 Critical point phonon frequencies of GaAs

Critical point		11-parameter RIM ref 1	Neutron data ref 2,3	Raman ref 4
Γ	LO	292	285.0±6.7	291.9±0.3
	TO	269	267.3±2.7	268.6±0.3
X	LO	234	240.7±5.0	
	LA	224	226.7±2.0	
	TO	254	252.0±3.0	
	TA	79	78.7±0.5	
L	LO	241	238.3±2.3	
	LA	206	208.7±3.3	
	TO	259	261.3±4.0	
	TA	62	62.0±0.7	
W	W1	271		
	W2	255		
	W3	216		
	W4	206		
	W5	117		
	W6	73		
K	$IIO\Sigma_1$	224	217.3±4.0	
	$IIA\Sigma_1$	205	198.7±3.7	
	$IO\Sigma_1$	267	264.7±4.0	
	$TO\Sigma_2$	256	-	
	$IA\Sigma_1$	107	111.3±2.3	
	$TA\Sigma_2$	71	79.3±1.3	

ref 1 Patel et al (1984)
ref 2 Waugh and Dolling (1963)
ref 3 Dolling and Waugh (1965)
ref 4 Mooradian and Wright (1966)

Table 5.6 GaAs assignments

This work		11-parameter RIM	Neutron	Infrared 15K	Raman	Assignments
300K	100K	ref 1	ref 2,3	ref 4	ref 5	
163	163	165		161	163	S*
176	176	176	173	176	-	TO(X) - TA(X)
198	198	197	199	195	-	TO(L) - TA(L)
213	213	215	223	214	212	$2IA\Sigma_1$
223	223	225		-	228	S*
234	234	-		235	236	3-phonon ?
335	338	333	-			W3 + W5
		338	331	338	338	TO(X) + TA(X)
357	357	357	-	-	-	S*
380	383	388	-	385	390	W1 + W5
410	412	412	417	414	-	2LA(L)
443	448	447	447	447	-	LO(L) + LA(L)
456	460	458	467	460	-	LO(X) + LA(X)
488	492	488	493	490	-	LO(X) + TO(X)
493	498	491	482	498	-	$IIO\Sigma_1 + IO\Sigma_1$
502	507	500	500	507	498	LO(L) + TO(L)
510	515	509	504	516	510	2TO(X)
525	530	526	-	531	-	W1 + W2
-	540	538	535	538	537	2TO(Γ)

ref 1 Patel et al (1984)
ref 2 Waugh and Dolling (1963)
ref 3 Dolling and Waugh (1965)
ref 4 Koteles et al (1976)
ref 5 Sekine et al (1977)

* S = summation band (unassigned) see ref 1.

Table 5.7

Temperature dependence of the intensities of two-phonon summation bands in GaAs

Summation bands	Calculated $\frac{(1+n_1+n_2)_{100K}}{(1+n_1+n_2)_{300K}}$	Measured $\frac{\alpha_{100K}}{\alpha_{300K}}$
TO(X) + TA(X)	0.42	0.60
W1 + W5	0.46	0.52
2LA(L)	0.51	0.55
LO(L) + LA(L)	0.53	0.73
LO(X) + LA(X)	0.54	0.75
LO(X) + TO(X)	0.56	0.79
$II O\Sigma_1$ + $IO\Sigma_1$	0.56	0.81
LO(L) + TO(L)	0.57	0.84
2TO(X)	0.57	0.87
W1 + W2	0.59	0.88

5.4 RESULTS AND DISCUSSION FOR InSb

The optical constants of InSb have been measured at 300 and 100K in the regions where the crystal is transparent in the far infrared.

The sample was obtained from MCP Electronic Materials Ltd. The quoted carrier concentration was 7×10^{15} per cm^3. At room temperature the transmission below the reststrahl band is zero. This can be observed in the Fourier transform of the sample interferogram shown in figure 5.31 [A diamond window golay was used. Since this is not a ratio spectrum some of the bands shown are due to the thick polyethylene blank which was used as a filter]. Fray et al (1960) have also observed the null transmission between 120 and 230 cm^{-1} at room temperature.

The amplitude and phase spectra at higher wavenumbers measured at 300K are shown in figure 5.32 which includes the region beyond the 2-phonon cut-off. The values of the optical constants obtained from the data in figure 5.32 are given in figure 5.33 and the dielectric response curves can be seen in figure 5.34.

When the specimen was cooled to 100K a maximum transmission amplitude of about 42% was obtained below the reststrahl band. The complete amplitude and phase spectra at 100K are shown in figure 5.35. Thus the optical constants below the reststrahl band can now be determined and the results obtained over the whole spectrum are given in figure 5.36. Free carrier plasma effects are quite prominent at low frequencies judging by the profile of the n and k curves in this region. Figure 5.37 shows the real

and imaginary parts of the dielectric constant computed from the optical constant data. The value of the coefficient of linear thermal expansion required to calculate the thickness of the specimen at 100K was obtained from the results of Novikova (1960). The calculated reduction in the thickness was 0.33 μm.

The first reported observation of some of the combination bands of InSb was made by Spitzer and Fan (1955). Since then several authors [Fray et al (1960), Koteles and Datars (1976)] have reported detailed measurements at low temperatures and assigned the spectral features in terms of cpp frequencies. No assignments have been made before to the features observed in the infrared spectrum at room temperature.

Table 5.8 shows the cpp frequencies calculated by using the 11-parameter RIM (Patel, 1982) and they are compared with the neutron scattering data obtained by Price et al (1977). The assignments of the observed features obtained from the present work at room temperature and 100K are shown in table 5.9. Comparisons are also made with the results of Kiefer et al (1975) who measured the second order Raman spectrum at 300K and the infrared transmission data obtained at 15K by Koteles and Datars (1976).

A few authors have obtained the optical constants of InSb in the infrared from power reflectivity measurements [Hass and Henvis (1962), Sanderson (1965)], a combination of power reflectivity and transmission methods [Yoshinaga and Oetjen (1956)] and by using the technique of reflection DFTS [Gast and Genzel (1973), Afsar et al (1975)].

Sanderson (1965) has calculated the conductivity ($2nk\nu$) of InSb by using a Kramers-Kronig analysis of the power reflection spectrum and attributed the structures obtained between 100 and 170 cm^{-1} as due to errors in the reflectivity. However, it was found from the present work that the weak features obtained at 100K below 170 cm^{-1} are in fact phonon combination bands. The values of n at room temperature obtained from this work between 250 and 350 cm^{-1} are found to be in excellent agreement with the results of Maslin (1986) who used the technique of reflection DFTS in the same laboratory. The data of Yoshinaga and Oetjen (1956) obtained at room temperature are found to be generally higher than the present results. Moss et al (1957) have also measured the refractive index from 500 to 1400 cm^{-1} but no mention has been made of the temperature at which the data were taken.

Figures 5.38(a) and (b) show the plots of absorption coefficient above the reststrahl band obtained at 100 and 300K. It can be observed that at low temperature thermal broadening of the lattice absorption lines is reduced.

Table 5.10 shows the temperature dependence of the intensities of the absorption bands observed in InSb above the reststrahlen region.

The form of $\Gamma(\nu)$ required to account fully for the observed absorption was calculated at 100 and 300K by neglecting the contribution from the non linear dipole moment. These are the first reported results for InSb and are shown in figure 5.39. The divergence in the high wavenumber region is quite clear.

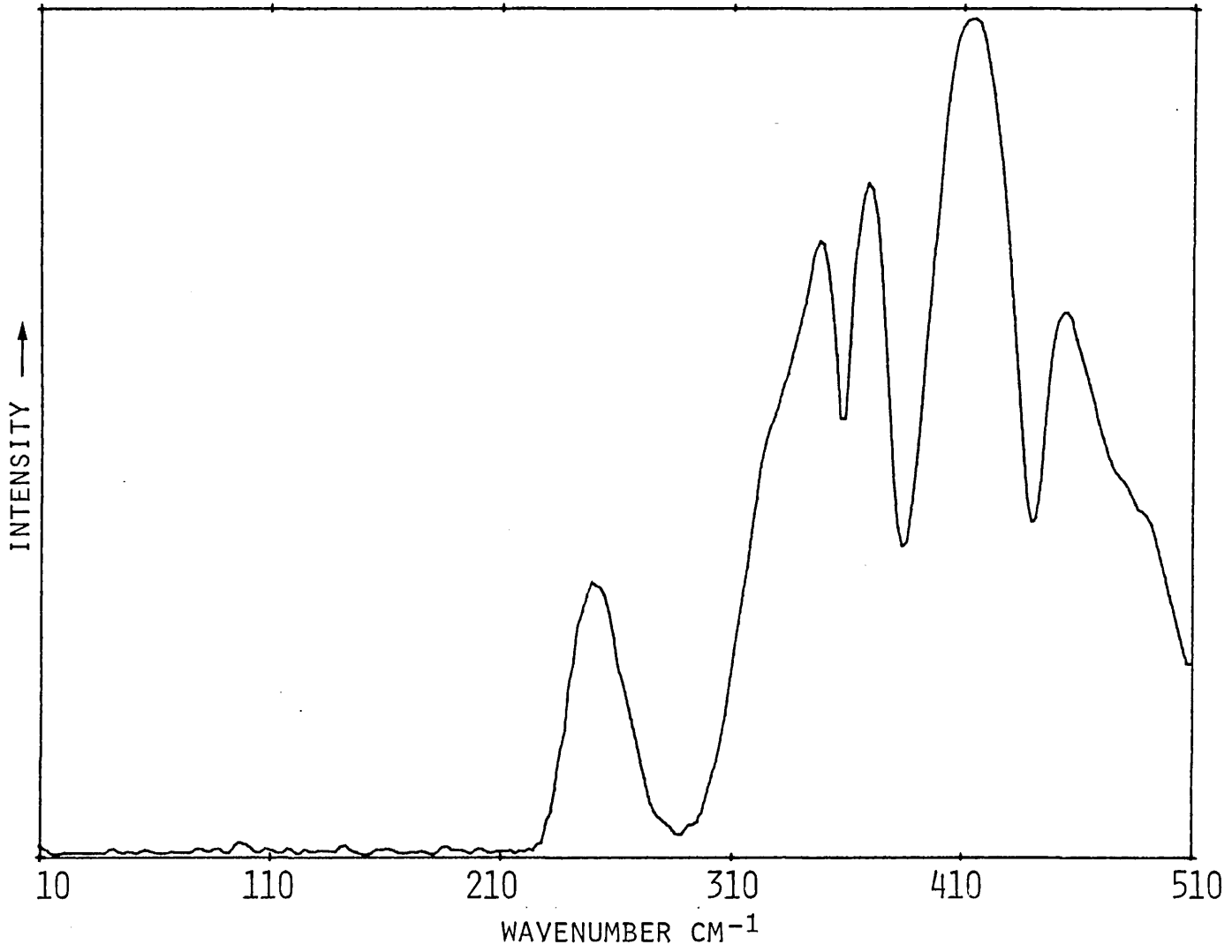

Figure 5.31 An InSb power transmission spectrum at 300K.

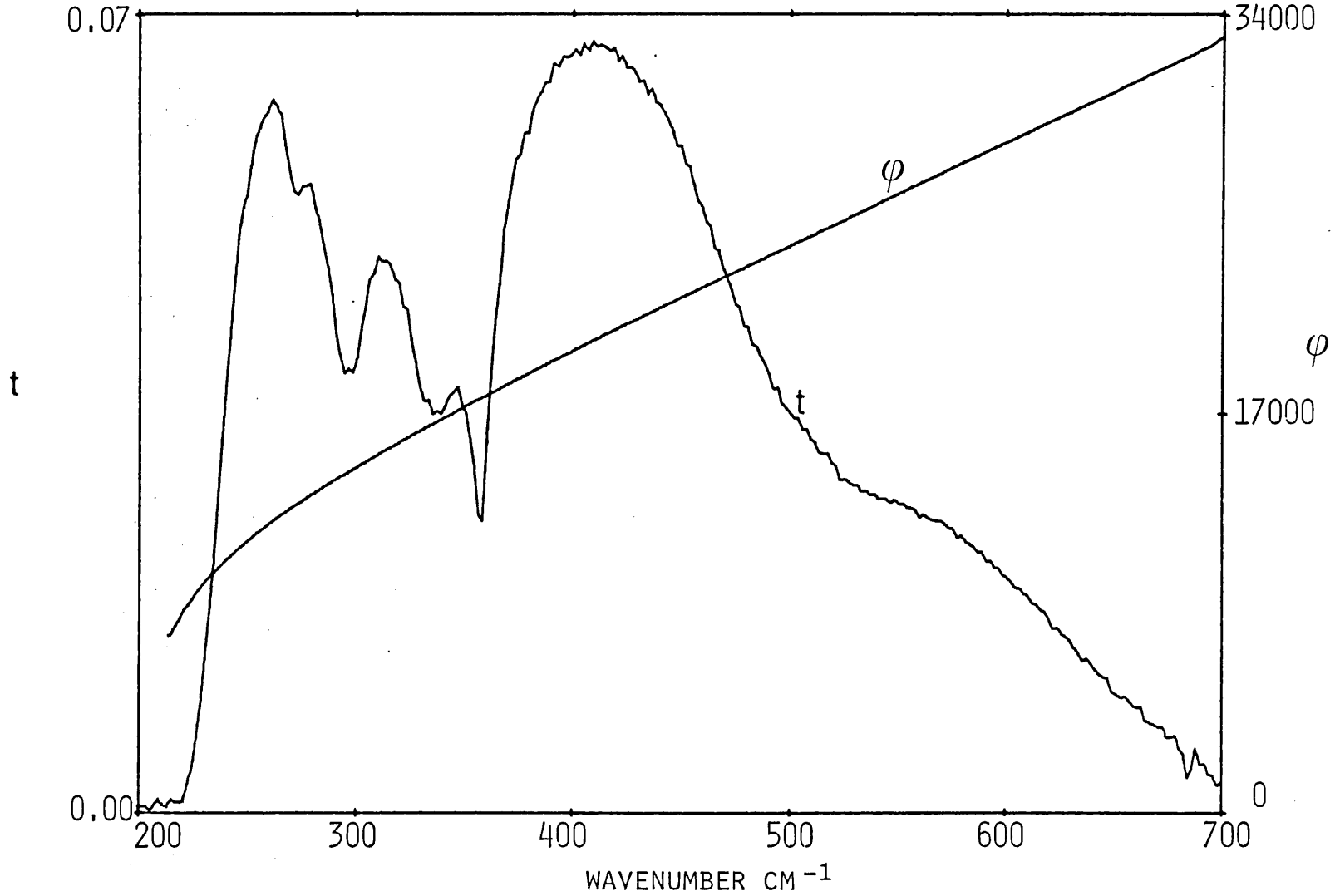

Figure 5.32 Complex transmission amplitude t and phase ϕ of InSb at 300K.

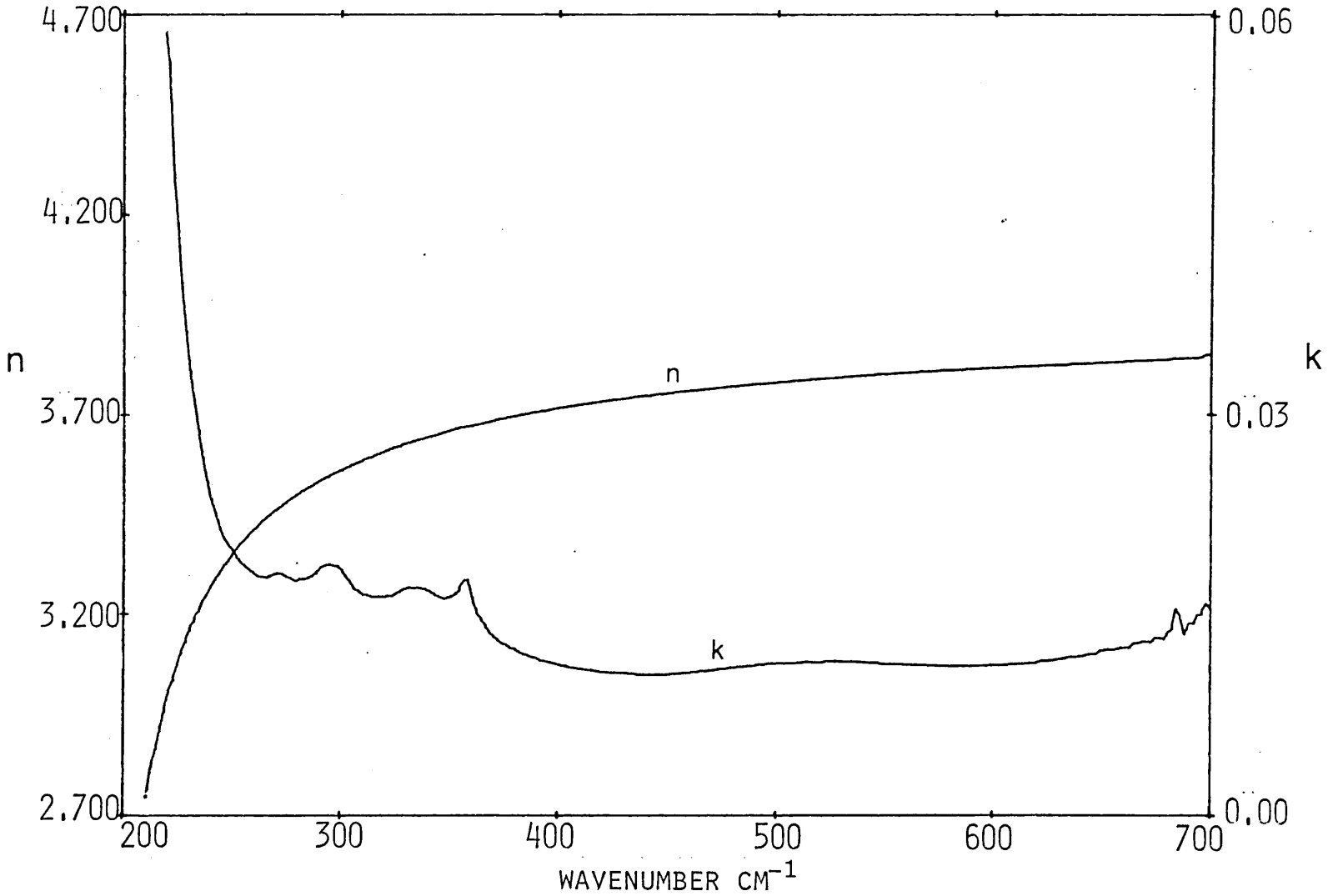

Figure 5.33 Refractive index n and extinction coefficient of k InSb at 300K.

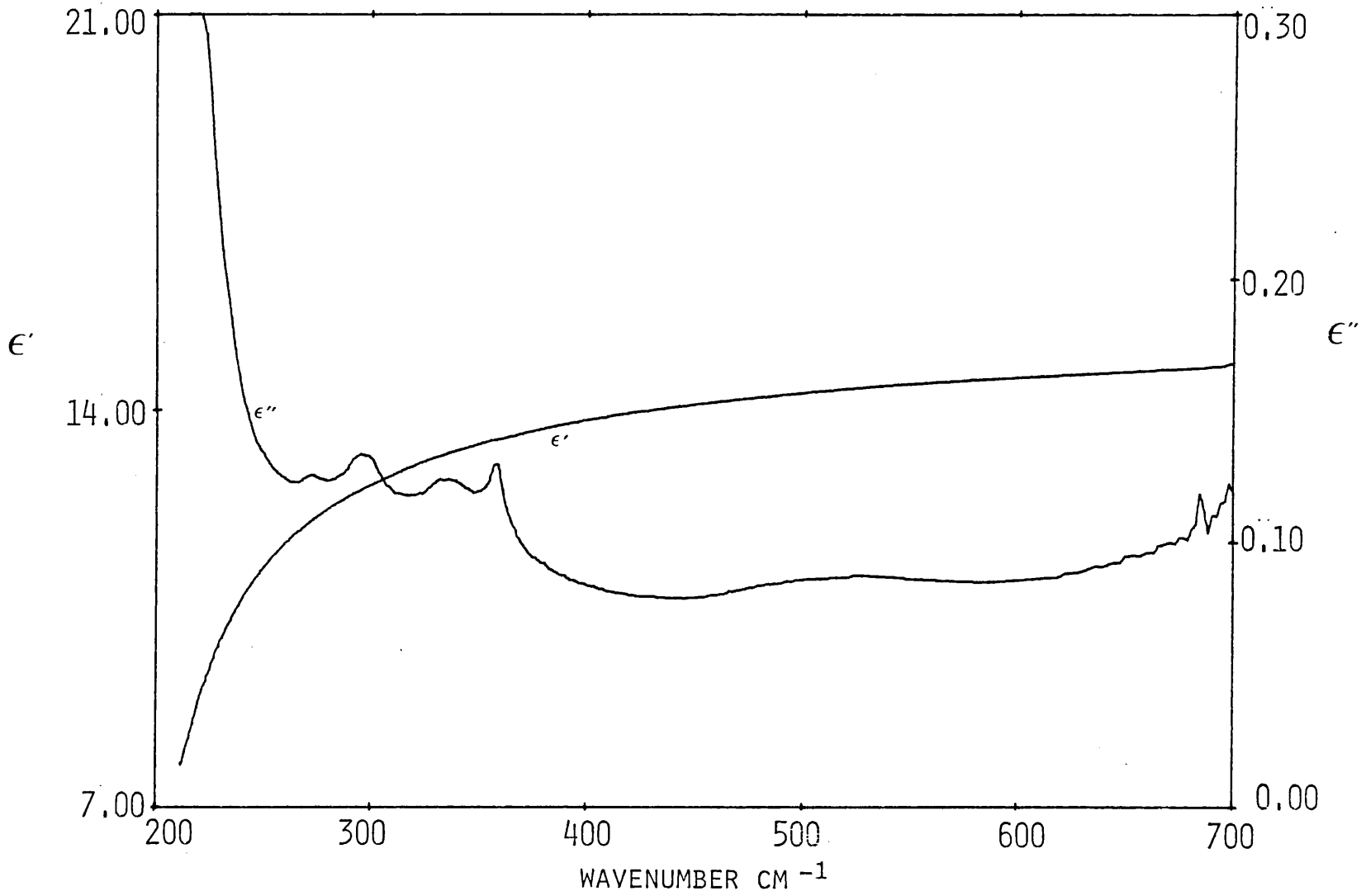

Figure 5.34 Real ϵ' and imaginary ϵ'' parts of the dielectric response of InSb at 300K.

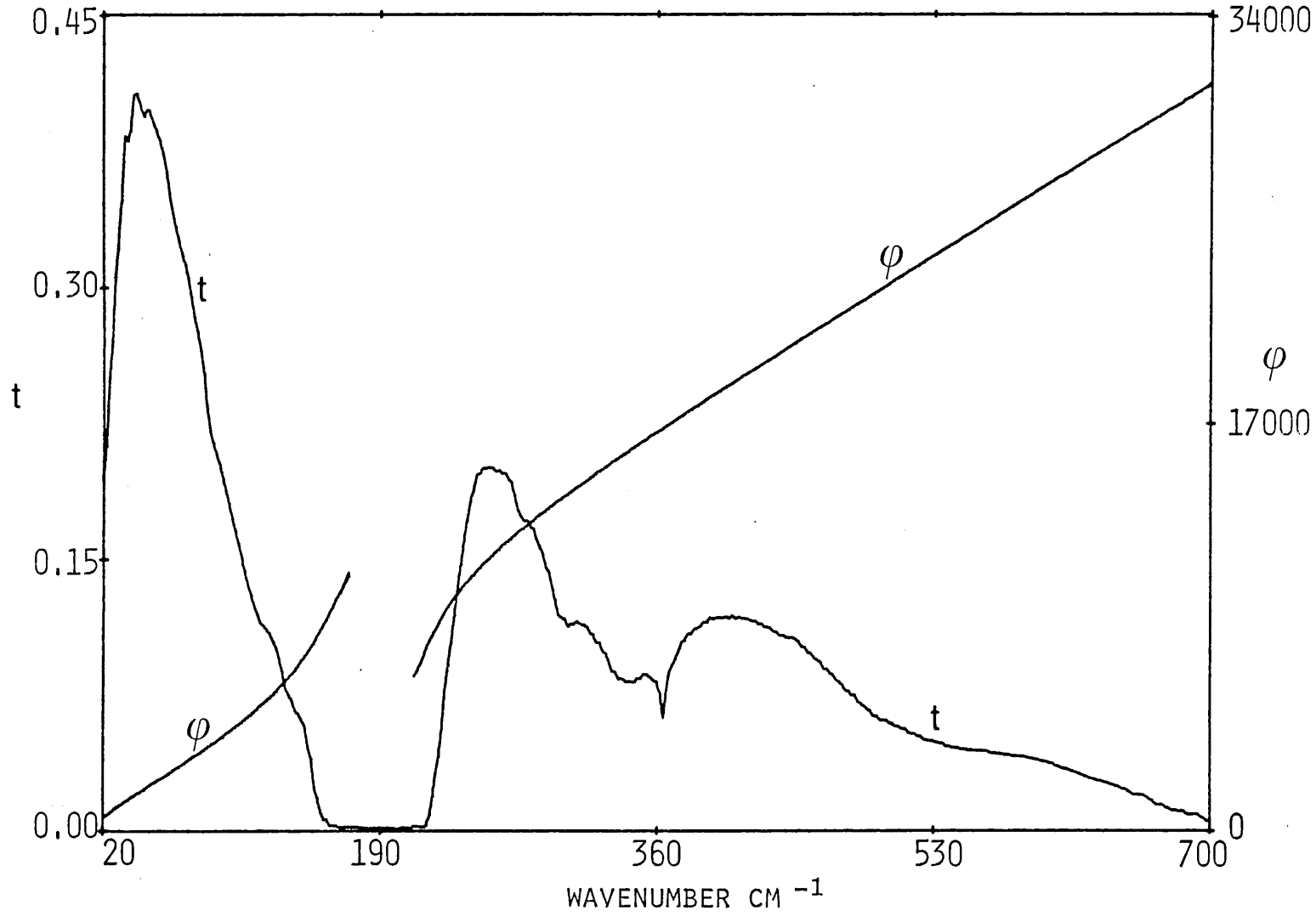

Figure 5.35 Complex transmission amplitude t and phase ϕ of InSb at 100K.

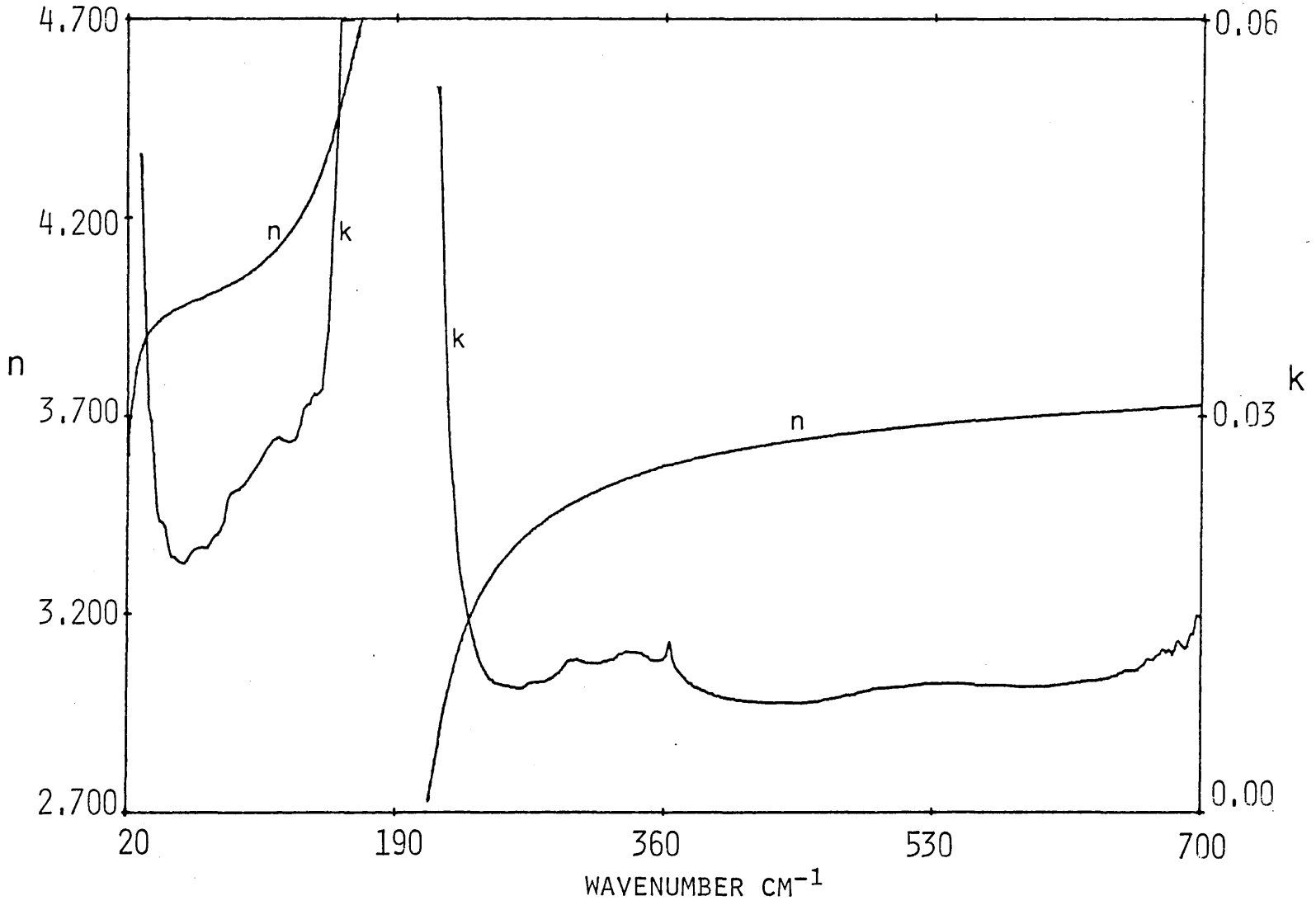

Figure 5.36 Refractive index n and extinction coefficient k of InSb at 100K.

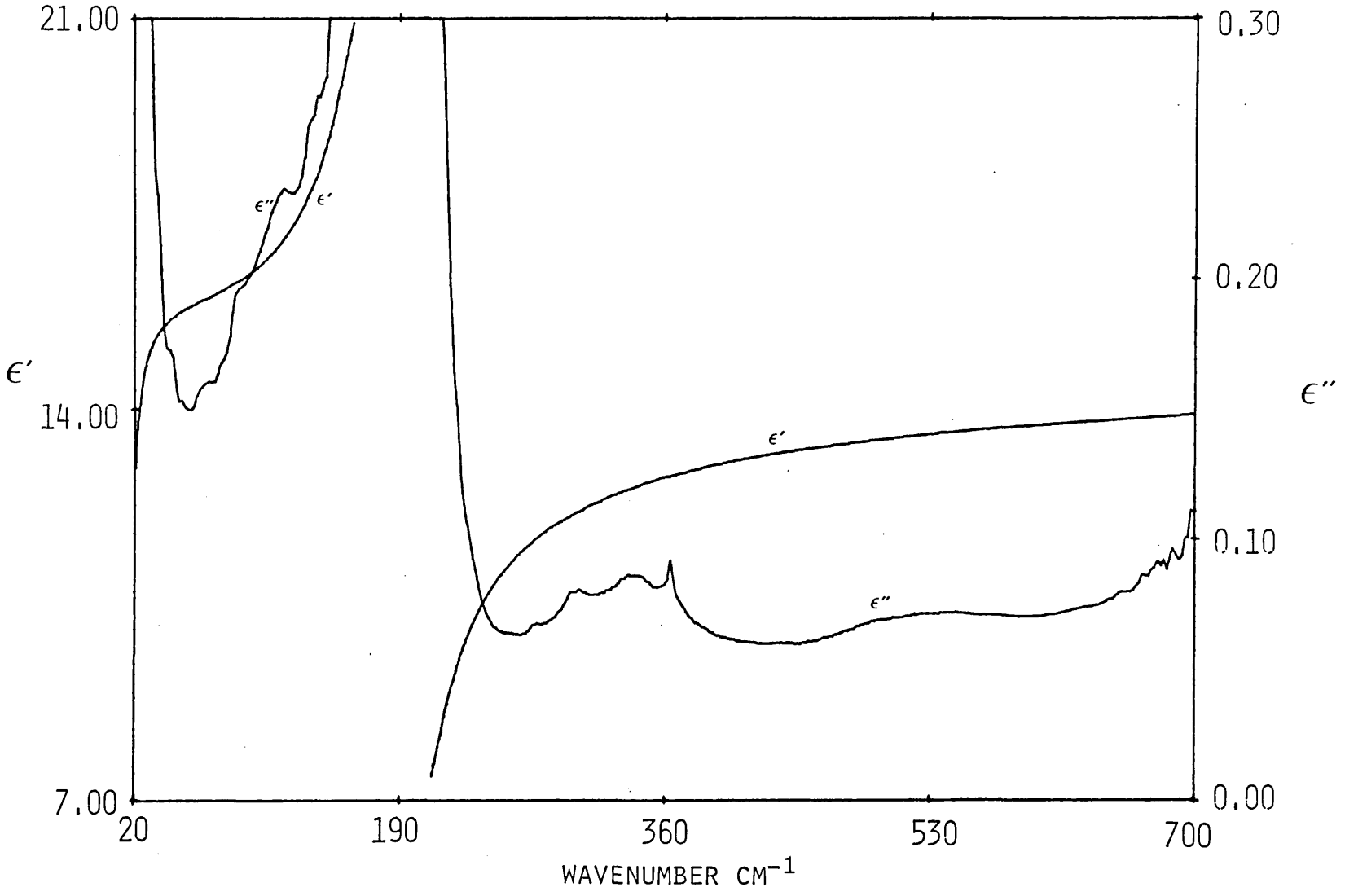

Figure 5.37 Real ϵ' and imaginary ϵ'' parts of the dielectric response of InSb at 100K.

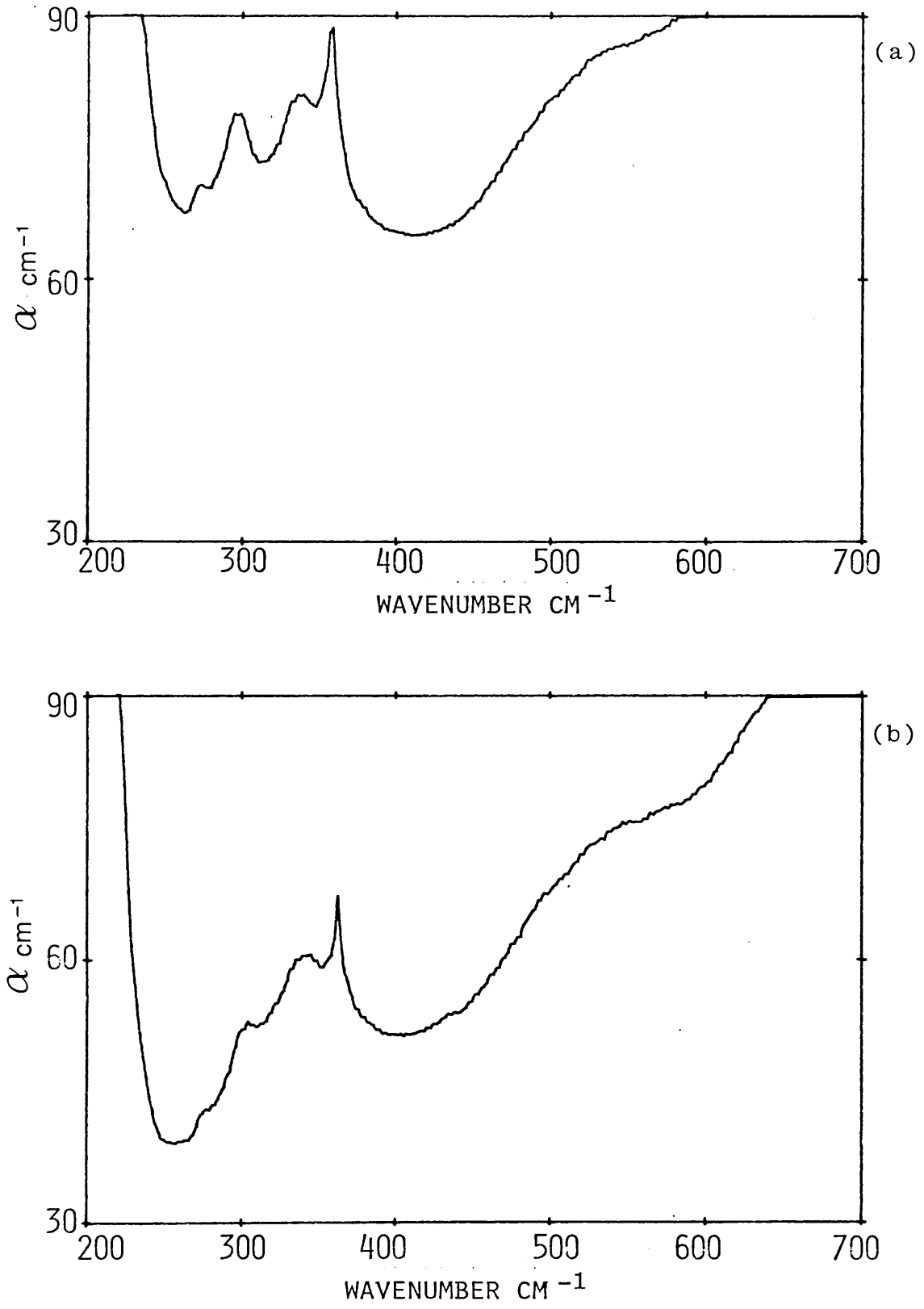

Figure 5.38 Power absorption coefficient α of InSb at (a) 300K and (b) 100K.

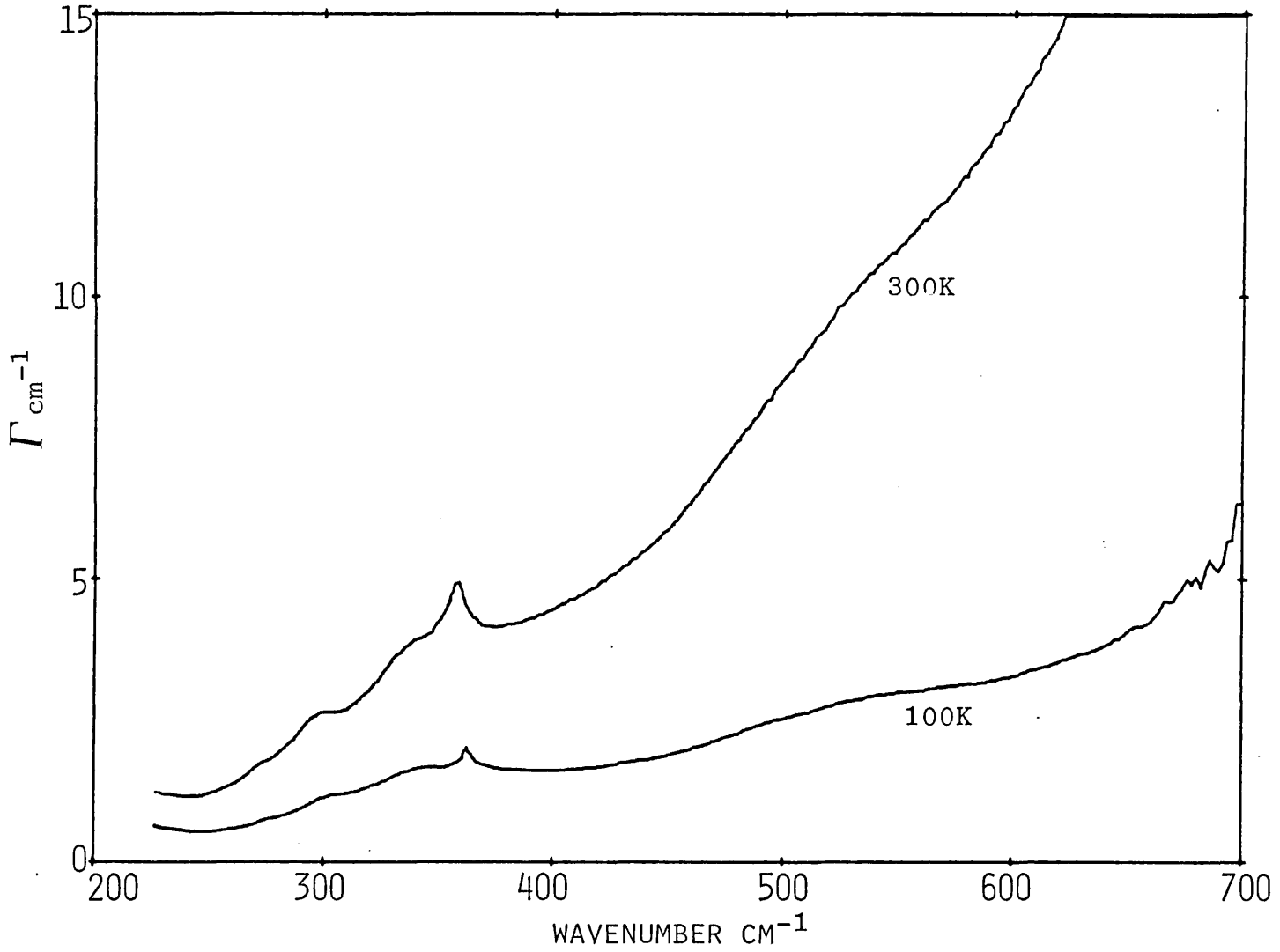

Figure 5.39 Frequency dependence of Γ required to account fully for the observed absorption in InSb at 300 and 100K if the non linear dipole contribution is neglected.

Table 5.8 Critical point phonon frequencies of InSb

Critical point		11-parameter RIM ref 1	Neutron data ref 2
Γ	LO	190.5	197±8.0
	TO	179.2	185±2.0
X	LO	154.2	158±6.7
	LA	139.1	143±3.3
	TO	177.3	180±5.7
	TA	32.8	37±1.7
L	LO	160.8	161±3.3
	LA	127.1	127±2.0
	TO	177.1	177±2.0
	TA	32.8	33±1.7
W	W1	194.6	
	W2	177.4	
	W3	136.7	
	W4	126.3	
	W5	53.9	
	W6	46.6	
K	$IIO\Sigma_1$	191.0	
	$IIA\Sigma_1$	129.0	
	$IO\Sigma_1$	177.3	
	$TO\Sigma_2$	140.6	
	$IA\Sigma_1$	55.9	
	$TA\Sigma_2$	37.0	

ref 1 Patel (1982)

ref 2 Price et al (1977)

Table 5.9 InSb assignments

This work		11-parameter RIM ref 1	Neutron ref 2	Infrared ref 3	Raman ref 4		Assignments
300K	100K			15K	77K	300K	
-	35	33.7	34	-	-	-	LO(L) - LA(L)
		36.7	-				$IO\Sigma_1$ - $TO\Sigma_2$
-	45	48.3	-	-	-	-	$IIA\Sigma_1$ - $IO\Sigma_1$
-	64	62.0	-	62	69		$IIO\Sigma_1$ - $IIA\Sigma_1$
		65.6	65				2TA(L)
-	85	84.7	-	85	84	82	$TO\Sigma_2$ - $IA\Sigma_1$
-	115	115.2	121	115	-	-	LO(X) - TA(X)
-	132	130.8	-	136	137	134	W2 - W6
272	275	269.6	-	273	-	-	$IIA\Sigma_1$ + $TO\Sigma_2$
298	305	304.2	304	305	306	-	TO(L) + LA(L)
		306.3					$IIA\Sigma_1$ + $IO\Sigma_1$
336	340	337.9	338	345	-	-	LO(L) + TO(L)
359	362	358.4	370	363	362	361	2TO(Γ)

ref 1 Patel (1982)
ref 2 Price et al (1977)
ref 3 Koteles et al (1976)
ref 4 Kiefer et al (1975)

Table 5.10

Temperature dependence of the intensities of two-phonon summation bands in InSb

Summation bands	Calculated $\frac{(1+n_1+n_2)100K}{(1+n_1+n_2)300K}$	Measured $\frac{\alpha 100K}{\alpha 300K}$
K2 + K4	0.42	0.33
TO(L) + LA(L)	0.43	0.47
LO(L) + TO(L)	0.46	0.59
2TOΓ	0.47	0.64

5.5 RESULTS AND DISCUSSION FOR InAs

A small crystal of InAs with a usable area of 1 cm^2 has been used to obtain the optical constants in the far infrared. Measurements were made at 100 and 300K.

The amplitude and phase spectra of InAs at 300K are shown in figure 5.40. At room temperature the transmission below the reststrahl band was zero and therefore only the spectral region above the reststrahl band is shown in the figure. The values of the optical constants obtained from the amplitude and phase data are shown in figure 5.41 and the dielectric response curves at 300K are shown in figure 5.42.

The observed features at room temperature agree very well with the infrared data obtained by Lorimor and Spitzer (1965) and the Raman spectrum obtained at 330K by Carles et al (1980).

The values for n obtained from this work were found to be slightly higher than the data tabulated by Seraphin and Bennet (1967) who analysed the transmission interference fringes measured in transmission by Lorimor and Spitzer (1965). The optical constants measured at room temperature in the reststrahl band have been reported by Gast and Genzel (1973) and Memon and Parker (1981) by using the technique of reflection DFTS.

When the sample was cooled to about 100K a very small transmission signal was detected below the reststrahl band. Since the signal-to-noise ratio per run was only about 2 the interferograms were co-averaged using the partial insertion technique described earlier.

The amplitude and phase spectra measured at 100K are shown in figure 5.43. The coefficient of linear thermal expansion of InAs between 100 and 300K was obtained from the data of Sirota and Pashintsev (1959) and this gives a calculated contraction of 0.34μm in the thickness of the crystal at 100K. The calculated values of n and k are given in figure 5.44 and the values of ϵ' and ϵ'' are shown in figure 5.45. The apparent rise in absorption at low frequencies is due to the onset of free carrier plasma effects. Koteles and Datars (1976) have also observed similar effects. Apparently no other optical constant data at 100K have been reported in the literature.

InAs absorbs neutrons heavily. As a result, very few neutron scattering measurements have been made on this compound. This has greatly inhibited the determination of reliable phonon dispersion curves. Several attempts have been made to establish the complete sets of cpp frequencies by interpreting the experimentally measured combination bands with the aid of lattice dynamical models [Stierwalt and Potter (1967), Talwar and Agrawal (1974), Koteles and Datars (1976), Carles et al (1980), Patel (1982)]. However, significant discrepancies exist between the different sets of the calculated phonon frequencies. In the present work the cpp frequencies (table 5.11) predicted by the 11-parameter RIM [Patel, (1982)] were used in the assignments of the observed bands. This should provide a good opportunity to test the viability of the model. The list of assignments is shown in table 5.12. It can be observed from the table that in many cases, a reasonable

agreement has been found.

The values of the absorption coefficient of InAs at 100 and 300K are shown in figures 5.46(a) and (b). The overall results at room temperature were found to be slightly higher than the data measured by Lorimor and Spitzer (1965).

The temperature dependence of the intensities of summation bands in InAs is shown in table 5.13.

Figure 5.47 shows the form of $\Gamma(0j,\nu)$ required to account fully for the observed absorption at 100K where the non linear dipole contribution has been neglected. This is the first measurement obtained at low temperature. Memon and Parker (1981) have determined the values of $\Gamma(0j,\nu)$ at room temperature from 140 to 290 cm^{-1} using the technique of reflection DFTS. As in the case of the previous materials, the value of Γ above the reststrahlen band increases with increasing frequency. Again, this is an indication that non linear terms in the dipole moment expansion have contributed significantly to the absorption.

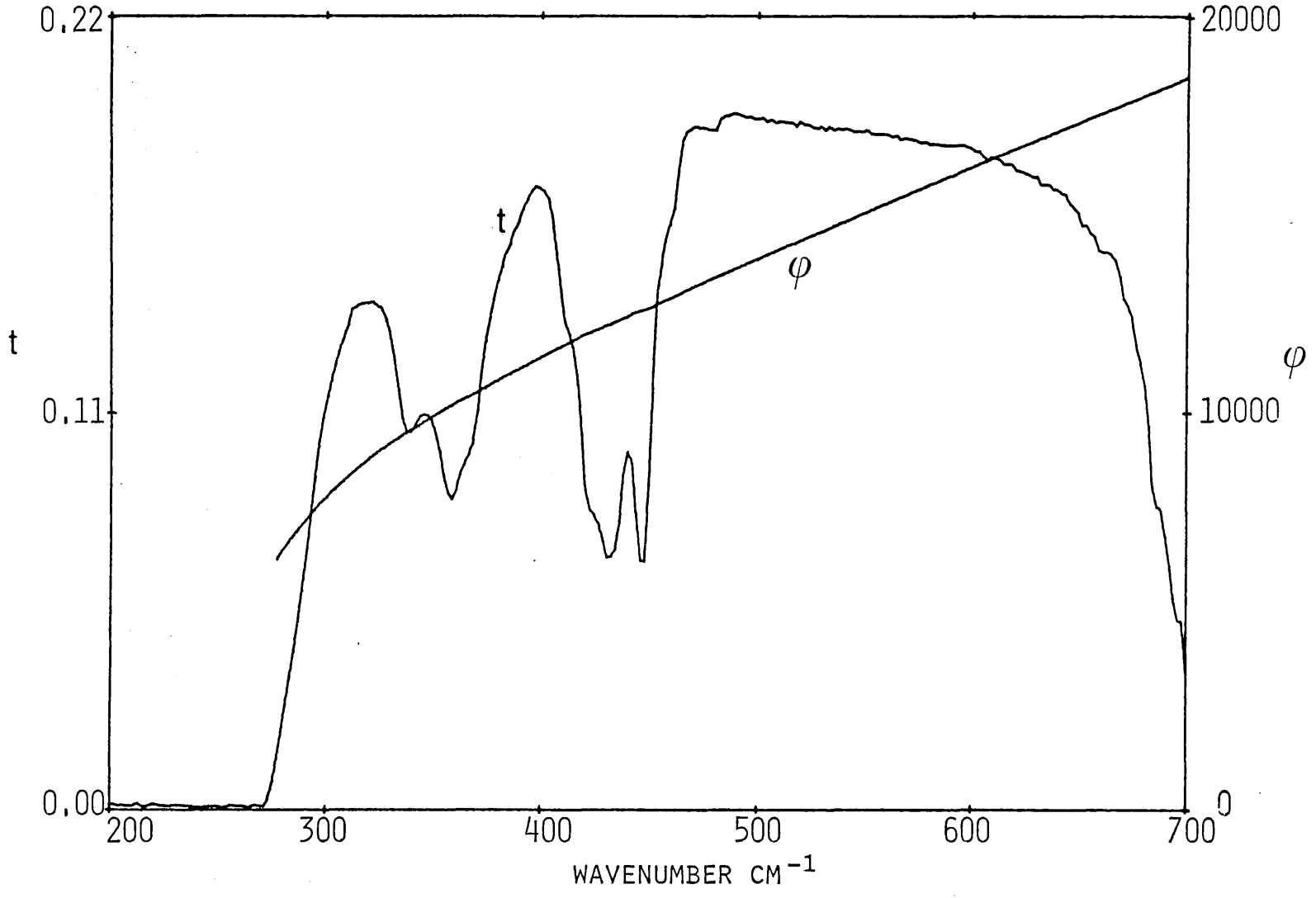

Figure 5.40 Complex transmission amplitude t and phase ϕ of InAs at 300K.

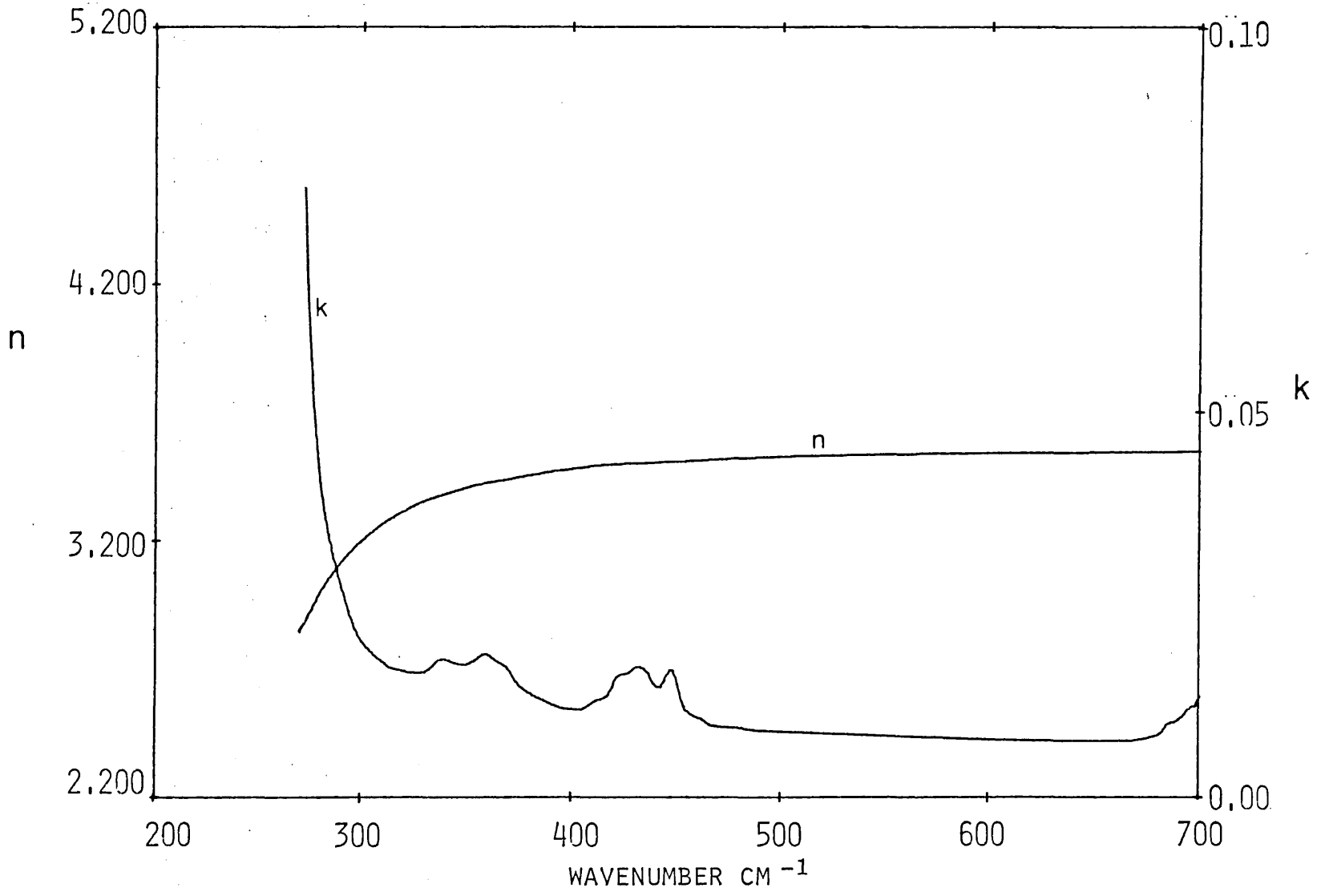

Figure 5.41 Refractive index n and extinction coefficient k of InAs at 300K.

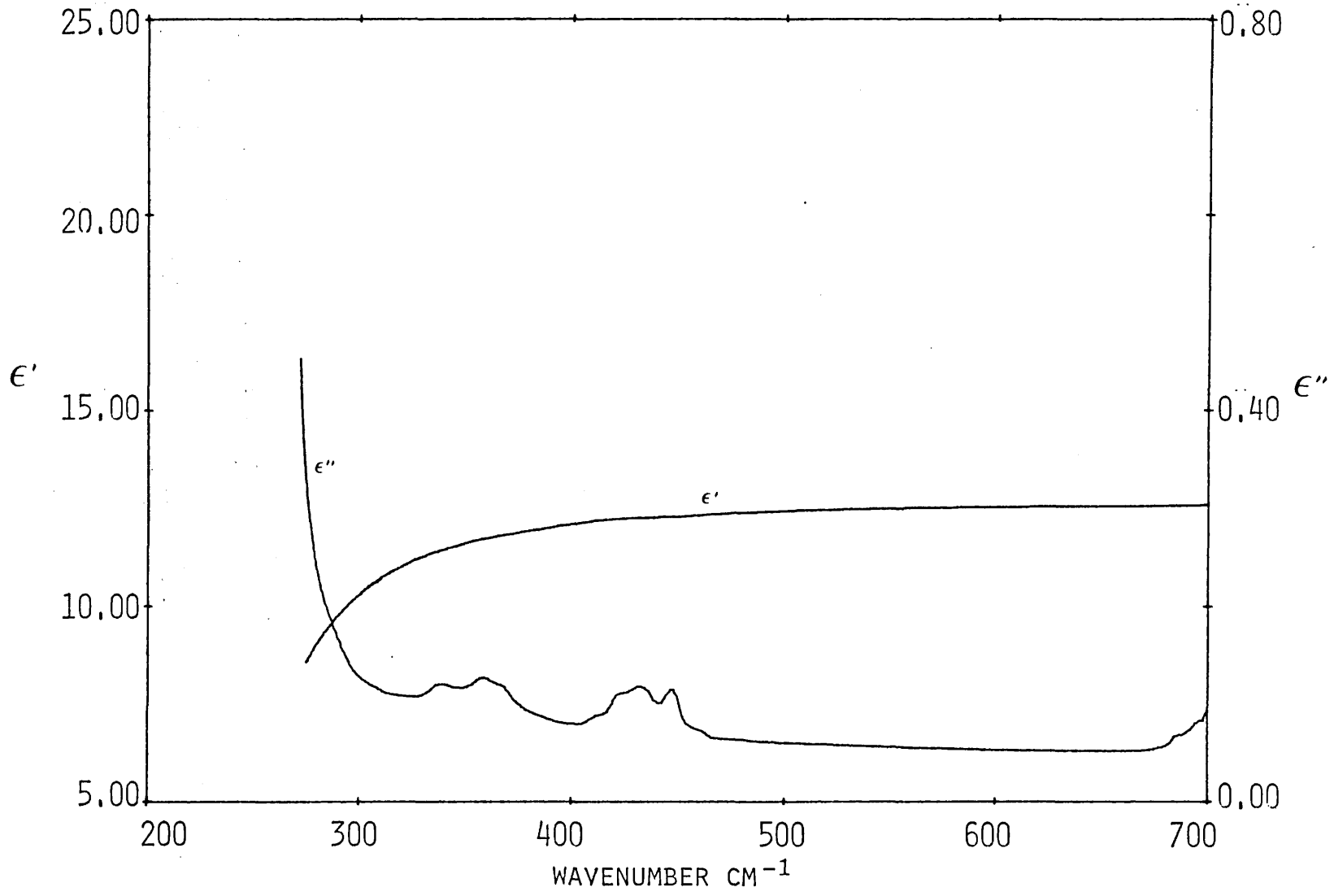

Figure 5.42 Real ϵ' and imaginary ϵ'' parts of the dielectric response of InAs at 300K.

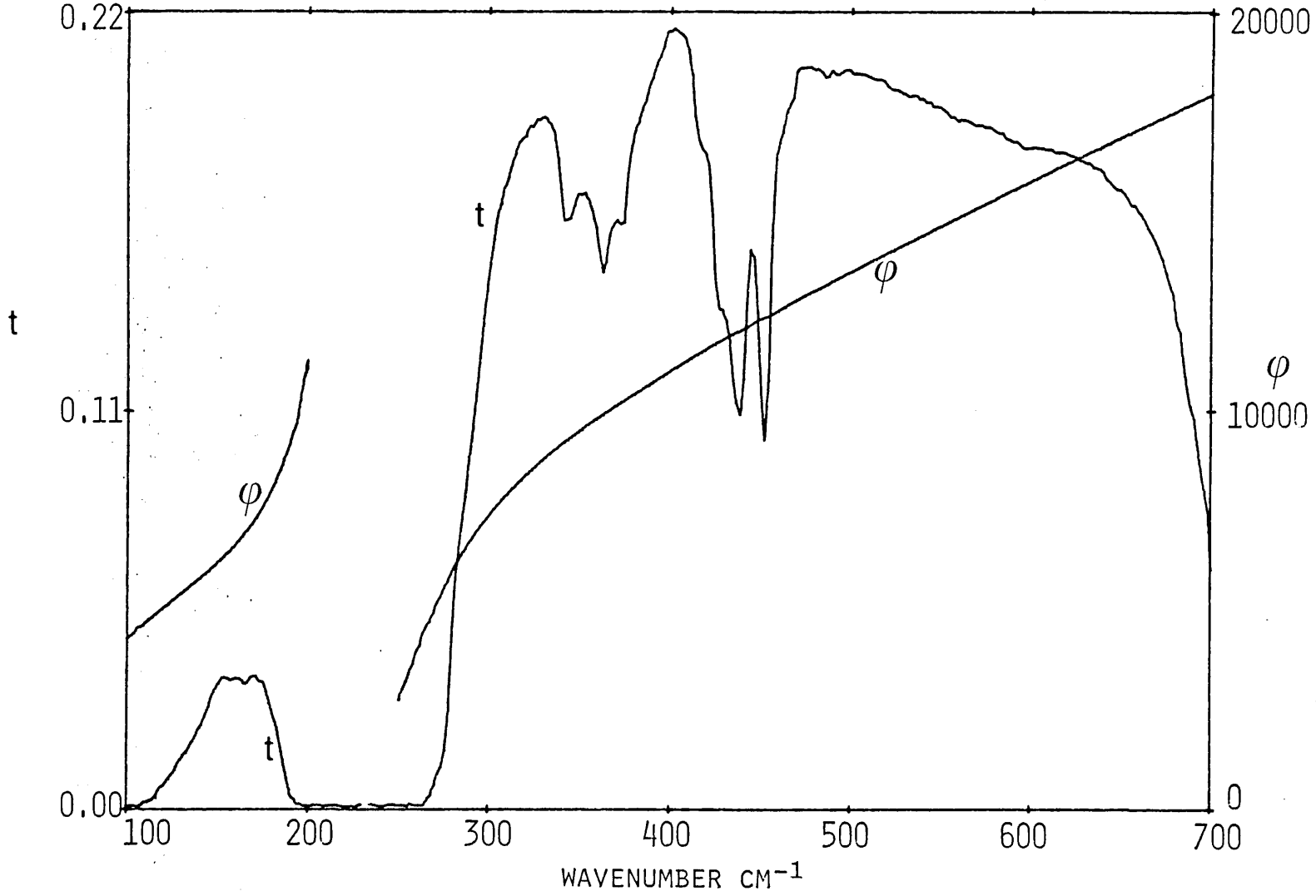

Figure 5.43 Complex transmission amplitude t and phase ϕ of InAs at 100K.

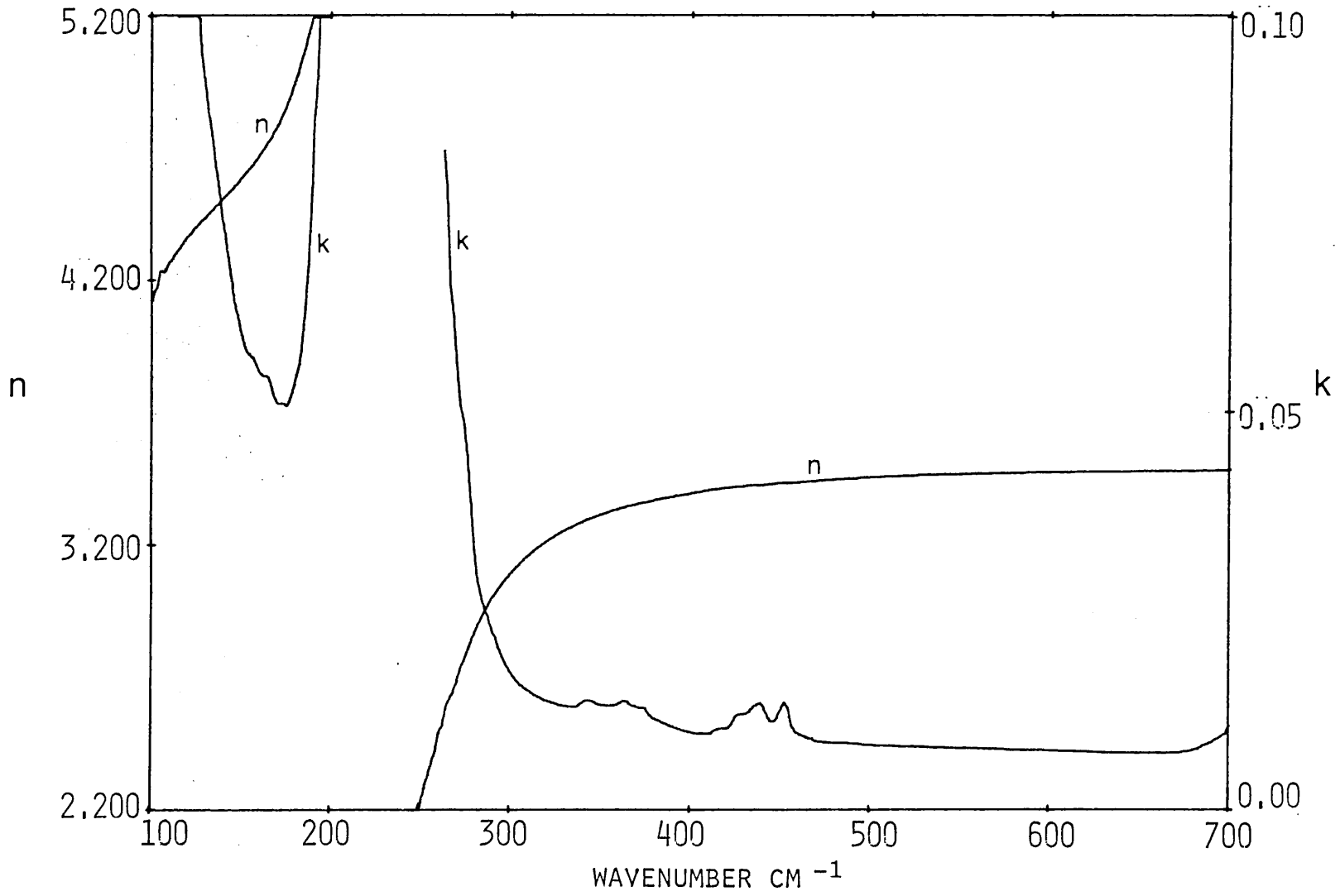

Figure 5.44 Refractive index n and extinction coefficient k of InAs at 100K.

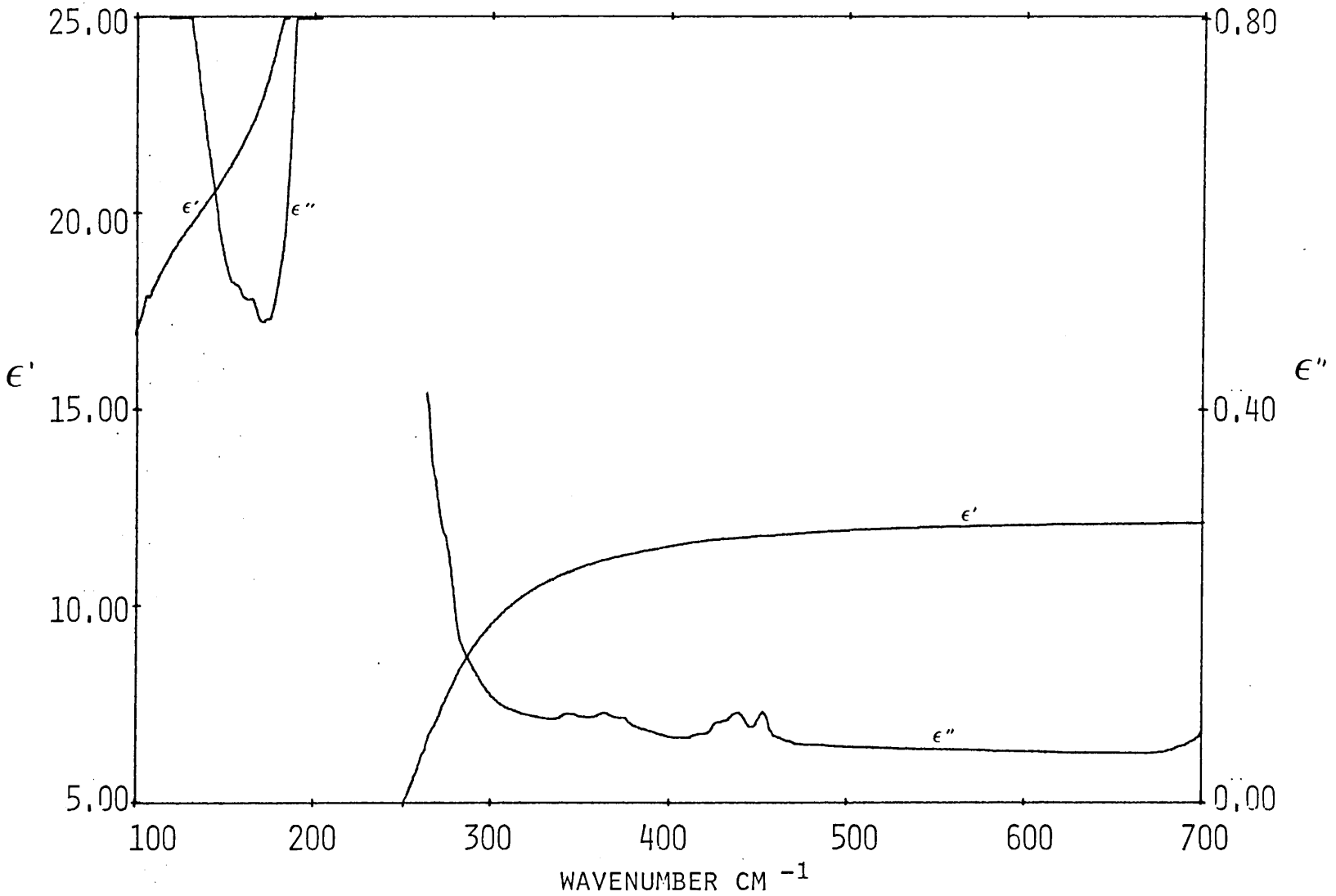

Figure 5.45 Real ϵ' and imaginary ϵ'' parts of the dielectric response of InAs at 100K.

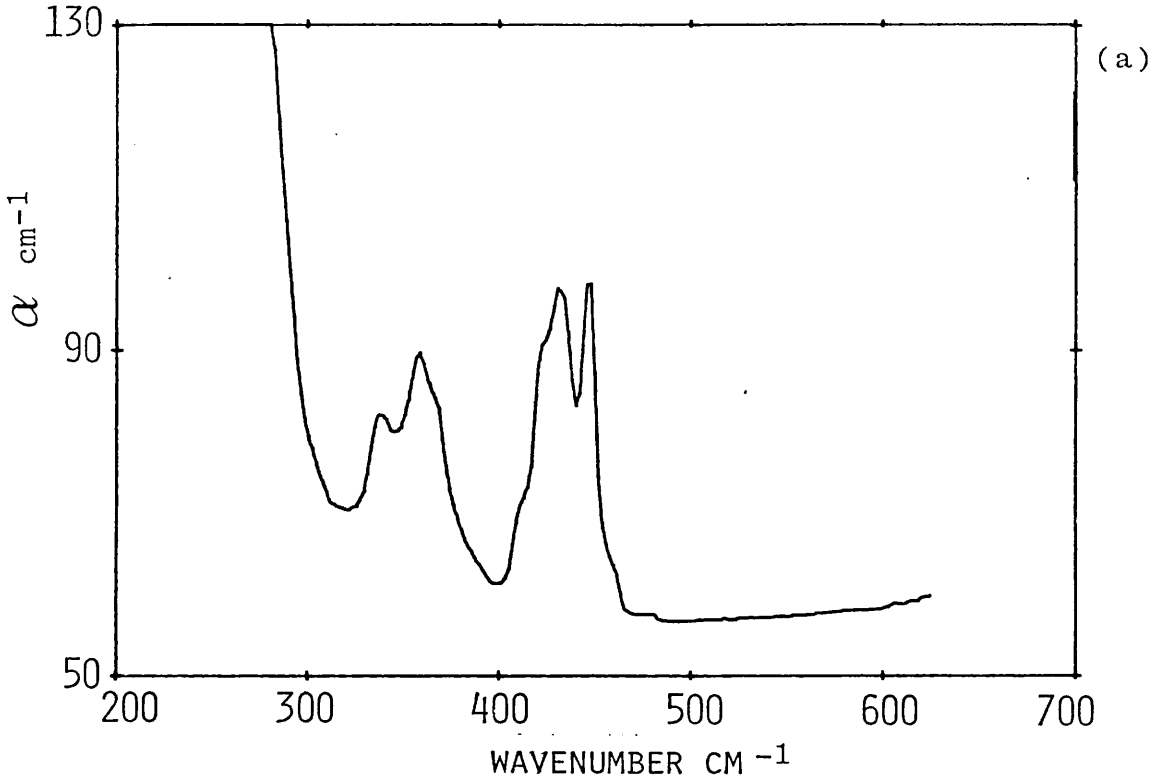

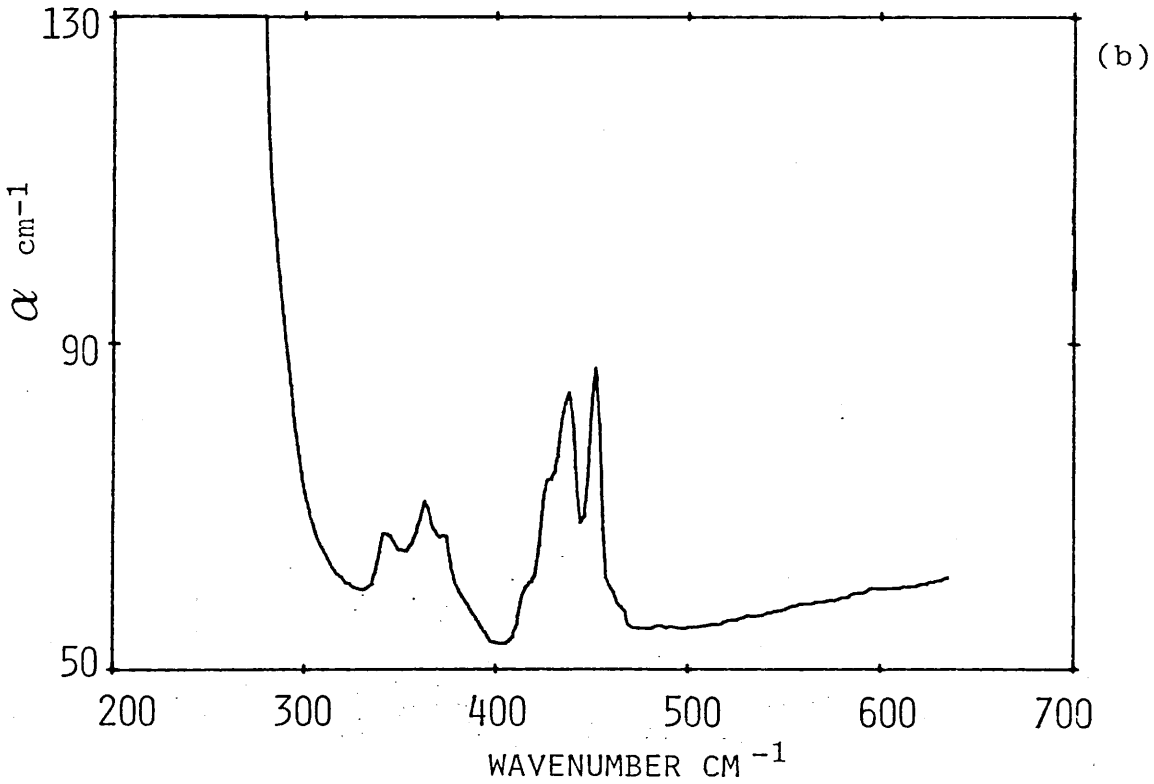

Figure 5.46 Power absorption coefficient α of InAs at (a) 300K and (b) 100K.

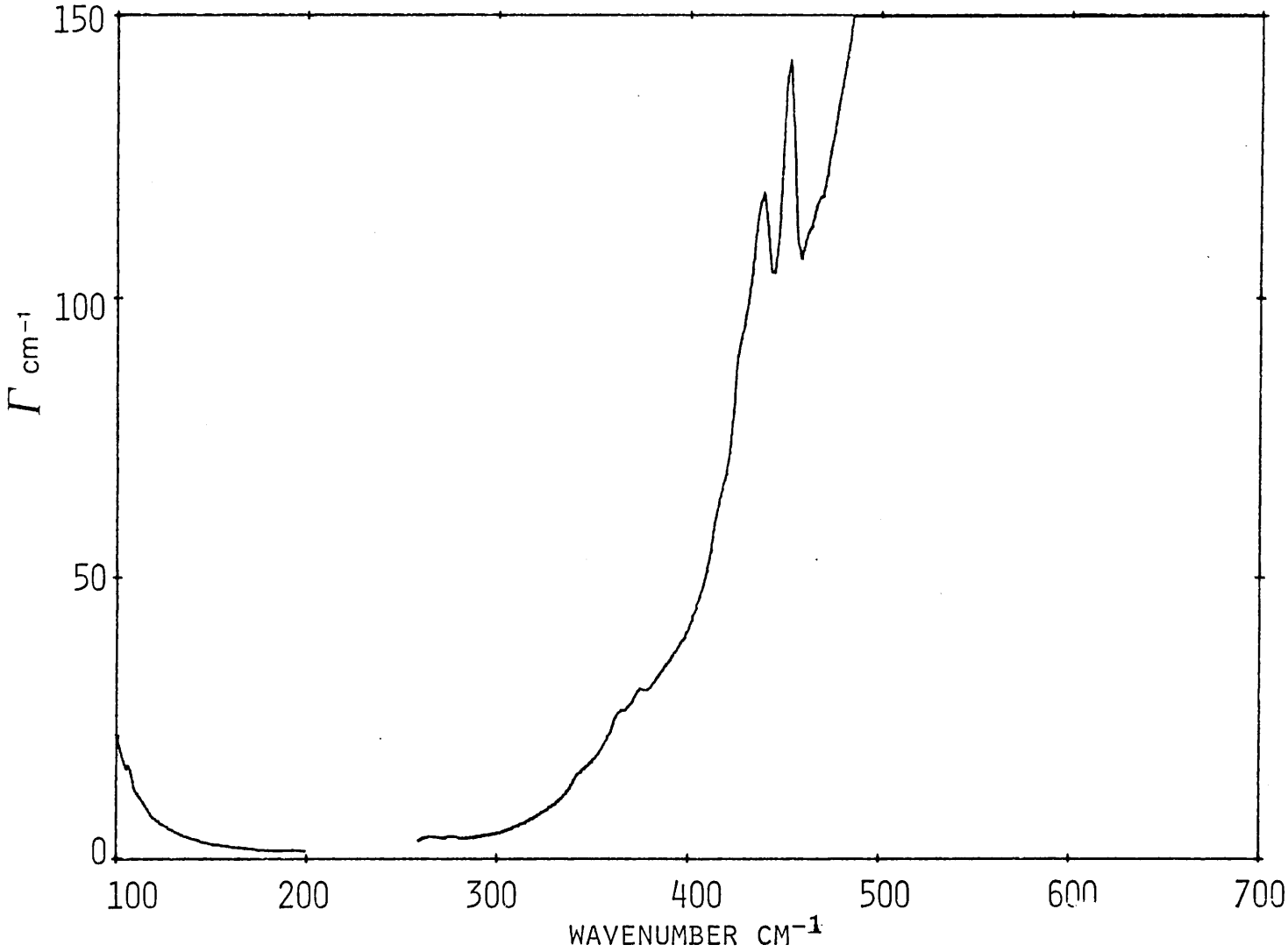

Figure 5.47 Frequency dependence of Γ required to account fully for the observed absorption in InAs at 100K if the non linear dipole contribution is neglected.

Table 5.11 Critical point phonon frequencies of InAs

Critical point		11-parameter RIM (Patel, 1982)
Γ	LO	238.8
	TO	216.5
X	LO	187.1
	LA	171.1
	TO	203.5
	TA	53.1
L	LO	193.1
	LA	148.1
	TO	211.1
	TA	44.0
W	W1	204.3
	W2	196.3
	W3	193.7
	W4	149.7
	W5	97.3
	W6	55.7
K	$IIO\Sigma_1$	198.0
	$IIA\Sigma_1$	154.4
	$IO\Sigma_1$	206.8
	$TO\Sigma_2$	191.6
	$IA\Sigma_1$	88.2
	$TA\Sigma_2$	48.5

Table 5.12 InAs assignments

This work		11-parameter RIM ref 1	Infrared ref 2	Raman ref 3	Assignments
300K	100K		15K	100K	
-	108	107.0	-	108	W1 - W5
		109.8			$II O\Sigma_1 - IA\Sigma_1$
-	115	118.0	-	115	LA(X) - TA(X)
		118.6			$IO\Sigma_1 - IA\Sigma_1$
-	134	134.0	-	-	LO(X) - TA(X)
-	157	158.3	158	160	$IO\Sigma_1 - TA\Sigma_2$
-	166	167.1	165	167	TO(L) - TA(L)
-	175	176.4	178	175	$2IA\Sigma_1$
338	342	341.2	340	343	LO(L) + LA(L)
358	362	358.2	362	363	LO(X) + LA(X)
		359.2			TO(L) + LA(L)
368	373	374.6	373	373	LA(X) + TO(X)
410	415	407.0	413	-	2TO(X)
420	425	422.2	424	425	2TO(L)
430	436	433.0	437	437	$2TO(\Gamma)$
445	450	455.3	451	451	$LO(\Gamma) + TO(\Gamma)$
460	466	-	468	464	3-phonon ?

ref 1 Patel (1982)
ref 2 Koteles et al (1976)
ref 3 Carles et al (1980)

Table 5.13

Temperature dependence of the intensities of two-phonon summation bands in InAs

Summation bands	Calculated $\frac{(1+n_1+n_2)100K}{(1+n_1+n_2)300K}$	Measured $\frac{\alpha 100K}{\alpha 300K}$
LO(L) + LA(L)	0.46	0.50
LO(X) + LA(X)	0.47	0.50
LA(X) + TO(X)	0.47	0.48
2TO(X)	0.50	0.50
2TO(L)	0.51	0.58
2TO(Γ)	0.52	0.68
LO(Γ) + TO(Γ)	0.54	0.70

5.6 RESULTS AND DISCUSSION FOR ZnSe

The far infrared optical constants of ZnSe have been measured at 100 and 300K. These are the first reported measurements on this material.

Figure 5.48 shows the amplitude and phase spectra measured at 300K and from these results, the values of n and k were obtained as shown in figure 5.49. The real and imaginary parts of the complex dielectric response of ZnSe are given in figure 5.50.

The amplitude and phase spectra obtained at 100K are shown in figure 5.51. More phase information has been obtained compared with the room temperature data in the region which lies close to the reststrahl as the sample becomes more transparent in this region at lower temperatures. The reduction in the thickness of the specimen at 100K was 0.43μm and in the calculation, the mean value of the coefficient of linear expansion measured by Soma (1980) was used. The optical constant data and the dielectric response curves at 100K are given in figures 5.52 and 5.53 respectively.

The phase dispersion in the regions where the strong absorption bands occur away from the reststrahl can be clearly seen in figures 5.48 and 5.51 and consequently, this dispersion can also be observed in the refractive index curves. As in the case of the other four binary semiconductors described earlier, these are the first direct measurements of the refractive index in this region. Thus the technique of DFTS has proved to be a very useful tool in obtaining detailed spectra of n and k.

The phonon frequencies at the critical points calculated with the 11-parameter RIM (Patel, 1982) are listed in table 5.14 and they are compared, where possible, with the results of Hennion et al (1971) who used neutron scattering techniques. The assignments to the spectral features obtained from the present work are listed in table 5.15. Comparisons have been made with the results of other authors.

Figures 5.54(a),(b) show the absorption coefficient of ZnSe measured at 100 and 300K. The overall room temperature results were in reasonable agreement with the data obtained by Aven et al (1961).

Table 5.16 shows the temperature dependence of the intensities two-phonon combination bands in ZnSe.

The form of $\Gamma(\nu)$ required to account fully for the observed absorption was calculated at 300 and 100K and is shown in figures 5.55 and 5.56 respectively. These results were obtained for the first time. The measurements at room temperature in the reststrahl region (from 175 to 300 cm^{-1}) were reported by Patel et al (1985) by using the technique of reflection DFTS. It is apparent from the figures that the self-energy function diverges at high wavenumbers although the rate of divergence is smaller than in the previous cases. This suggests that the contribution from the non linear dipole moment in II-VI semiconductors is smaller than in the case of III-V semiconductors. The divergence in $\Gamma(\nu)$ at low wavenumbers is dominated by free carrier effects which have not been subtracted out.

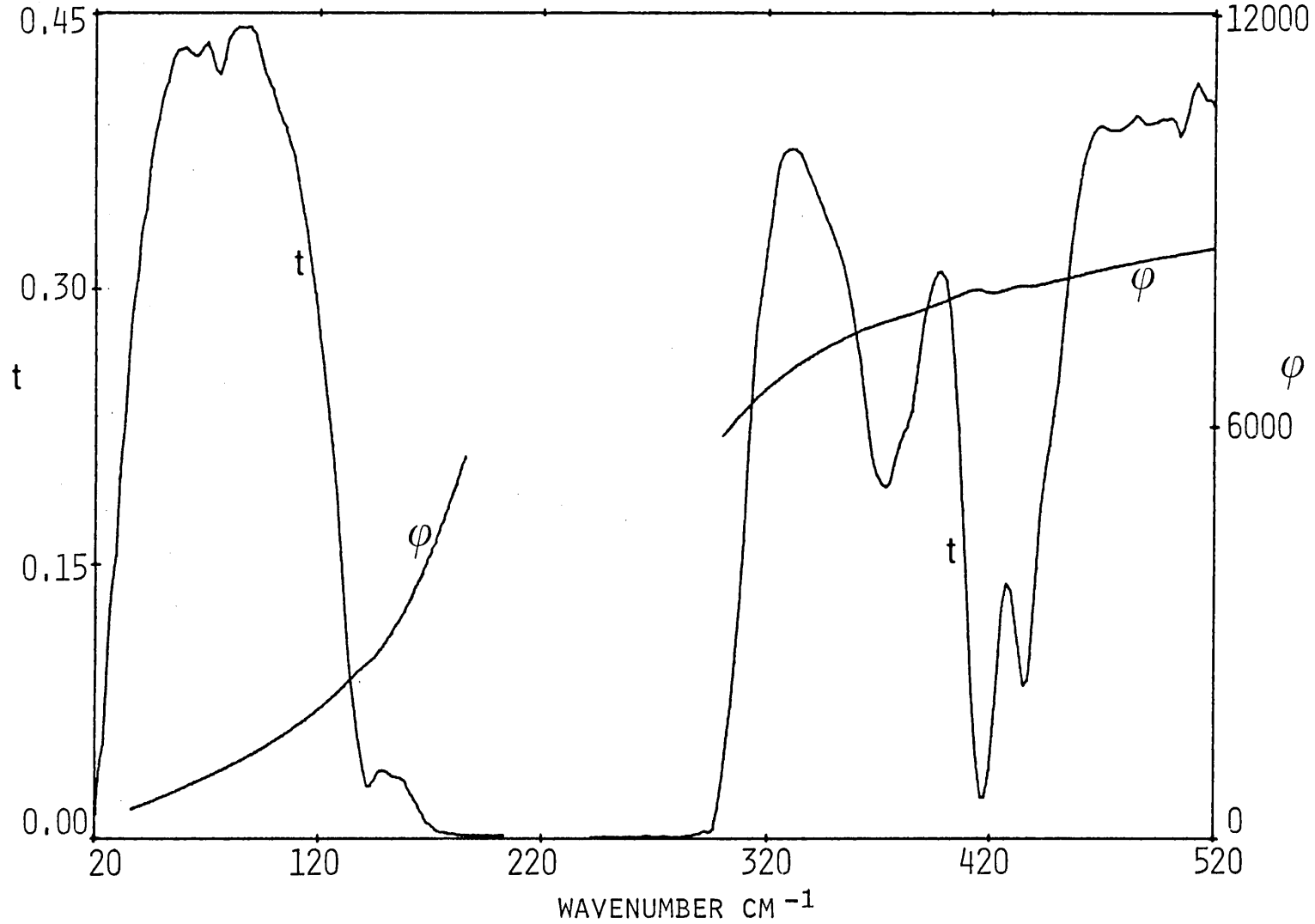

Figure 5.48 Complex transmission amplitude t and phase ϕ of ZnSe at 300K.

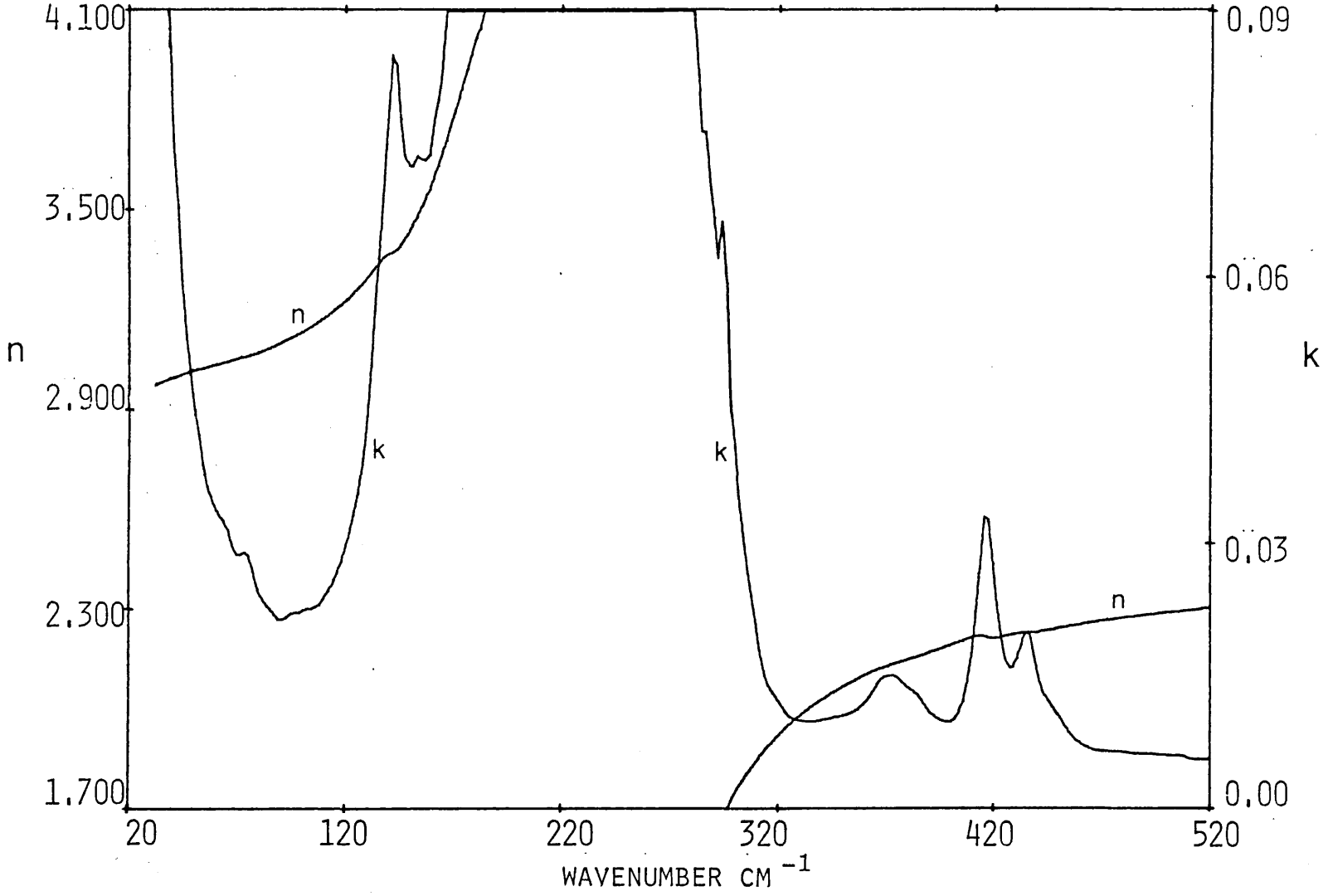

Figure 5.49 Refractive index n and extinction coefficient k of ZnSe at 300K.

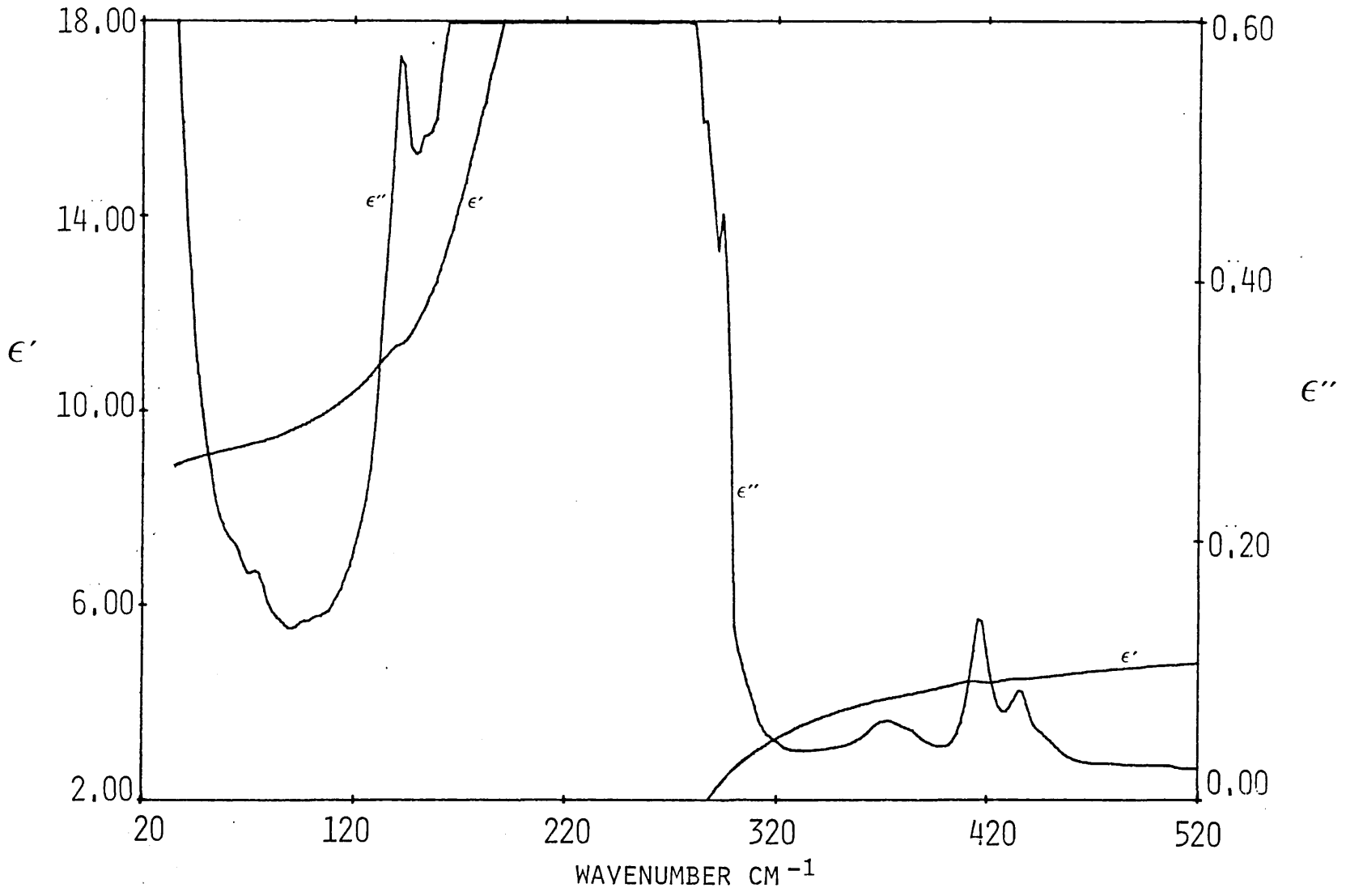

Figure 5.50 Real ϵ' and imaginary ϵ'' parts of the dielectric response of ZnSe at 300K.

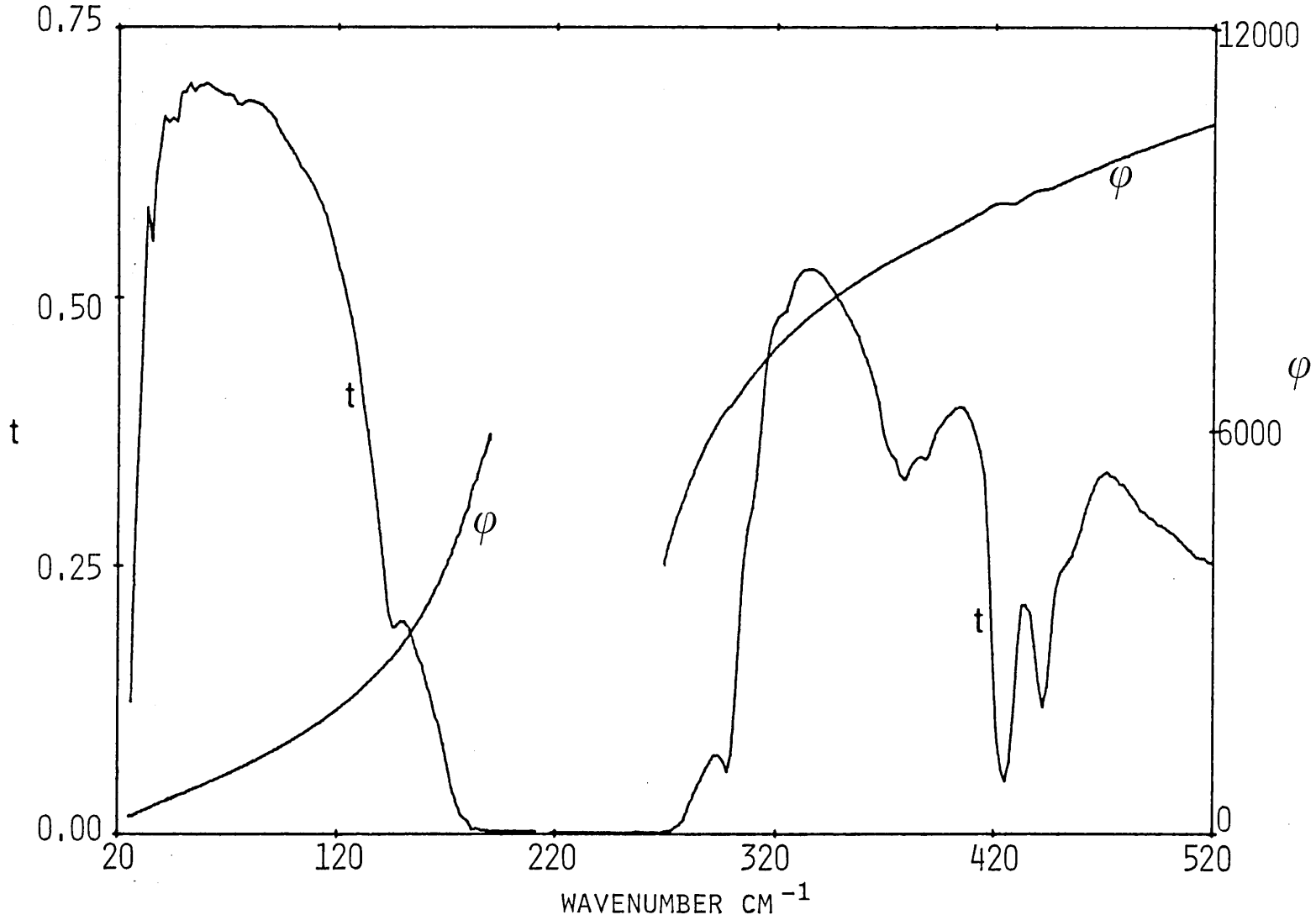

Figure 5.51 Complex transmission amplitude t and phase ϕ of ZnSe at 100K.

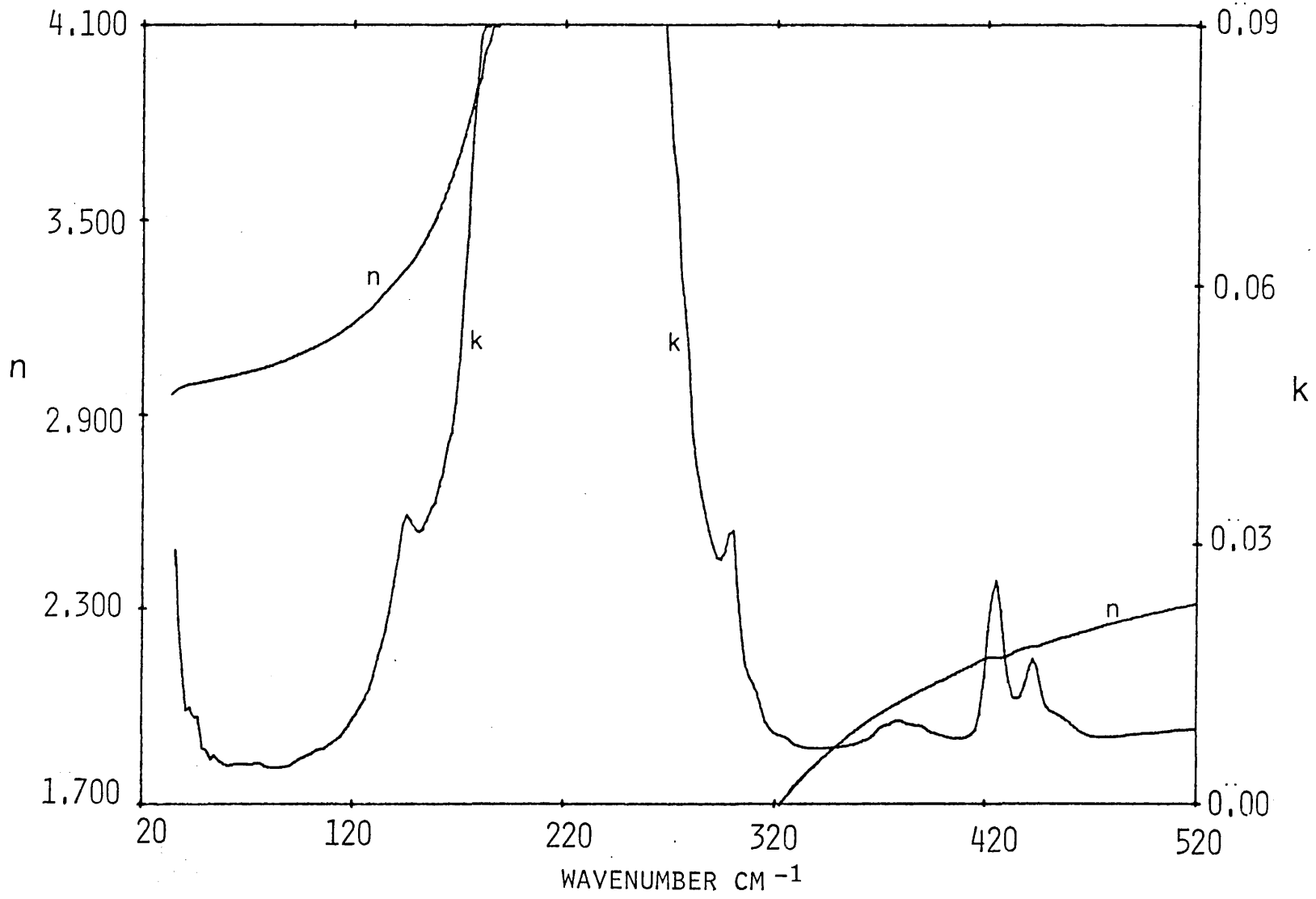

Figure 5.52 Refractive index n and extinction coefficient k of ZnSe at 100K.

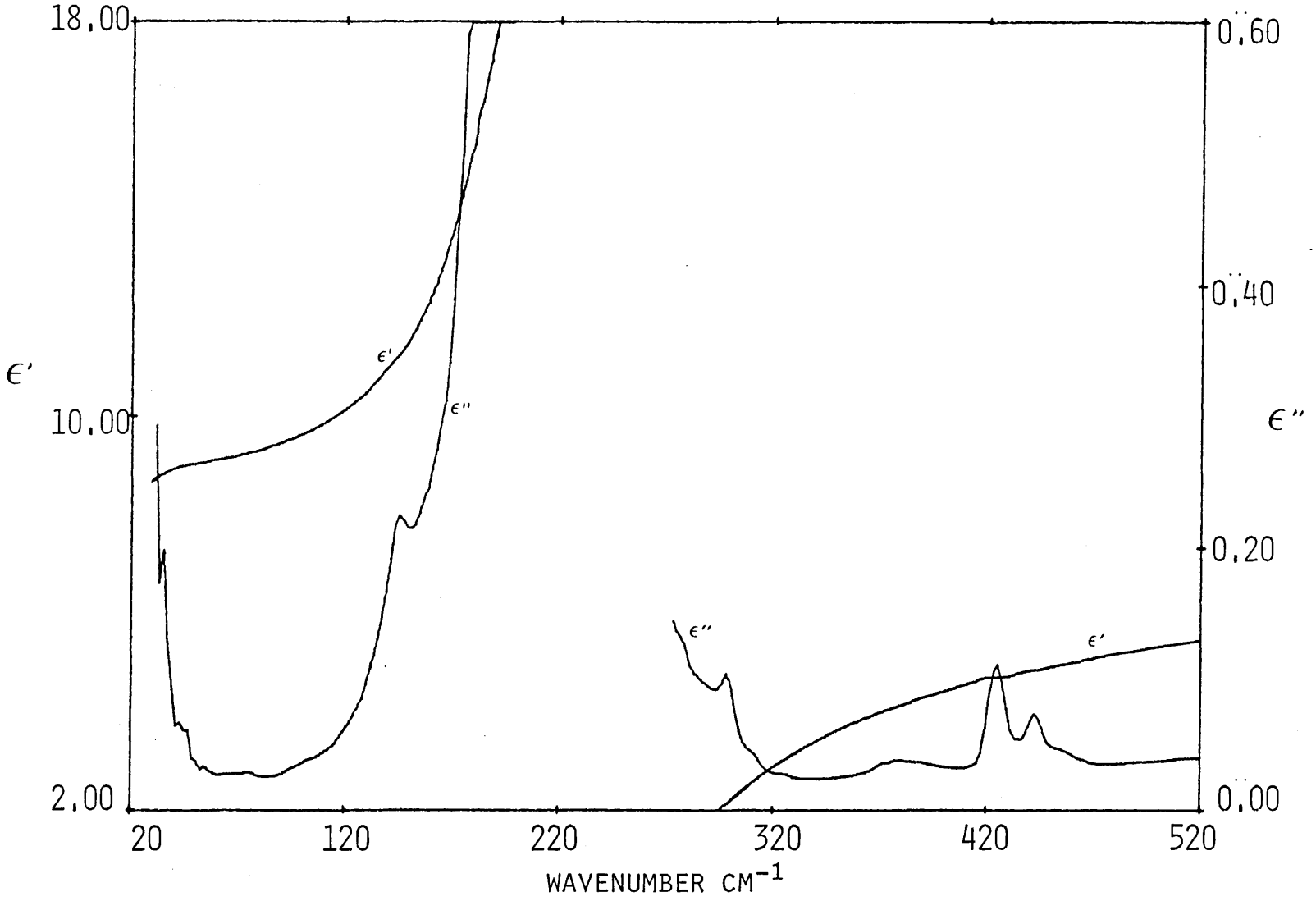

Figure 5.53 Real ϵ' and imaginary ϵ'' parts of the dielectric response of ZnSe at 100K.

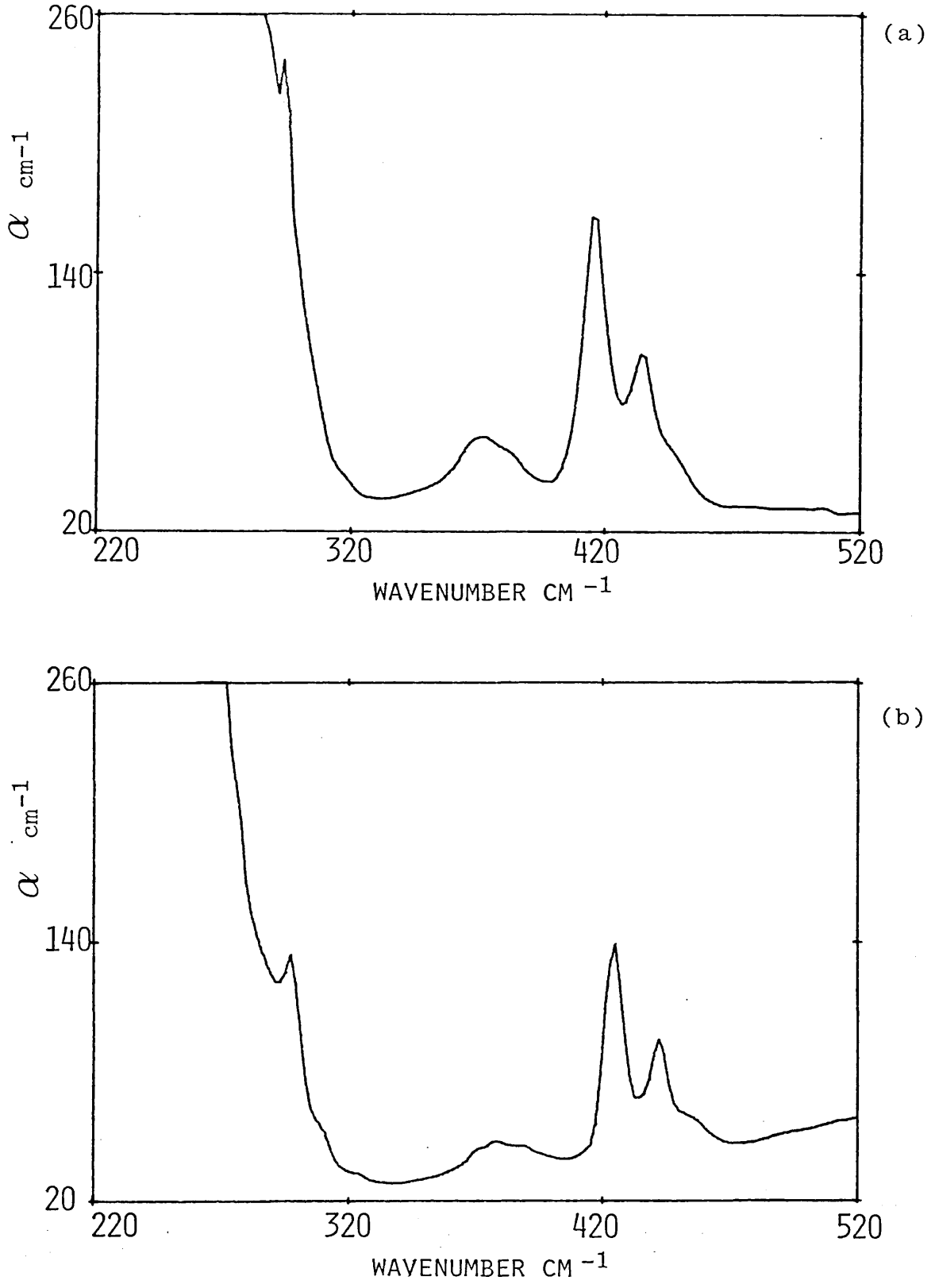

Figure 5.54 Power absorption coefficient α of ZnSe at (a) 300K and (b) 100K.

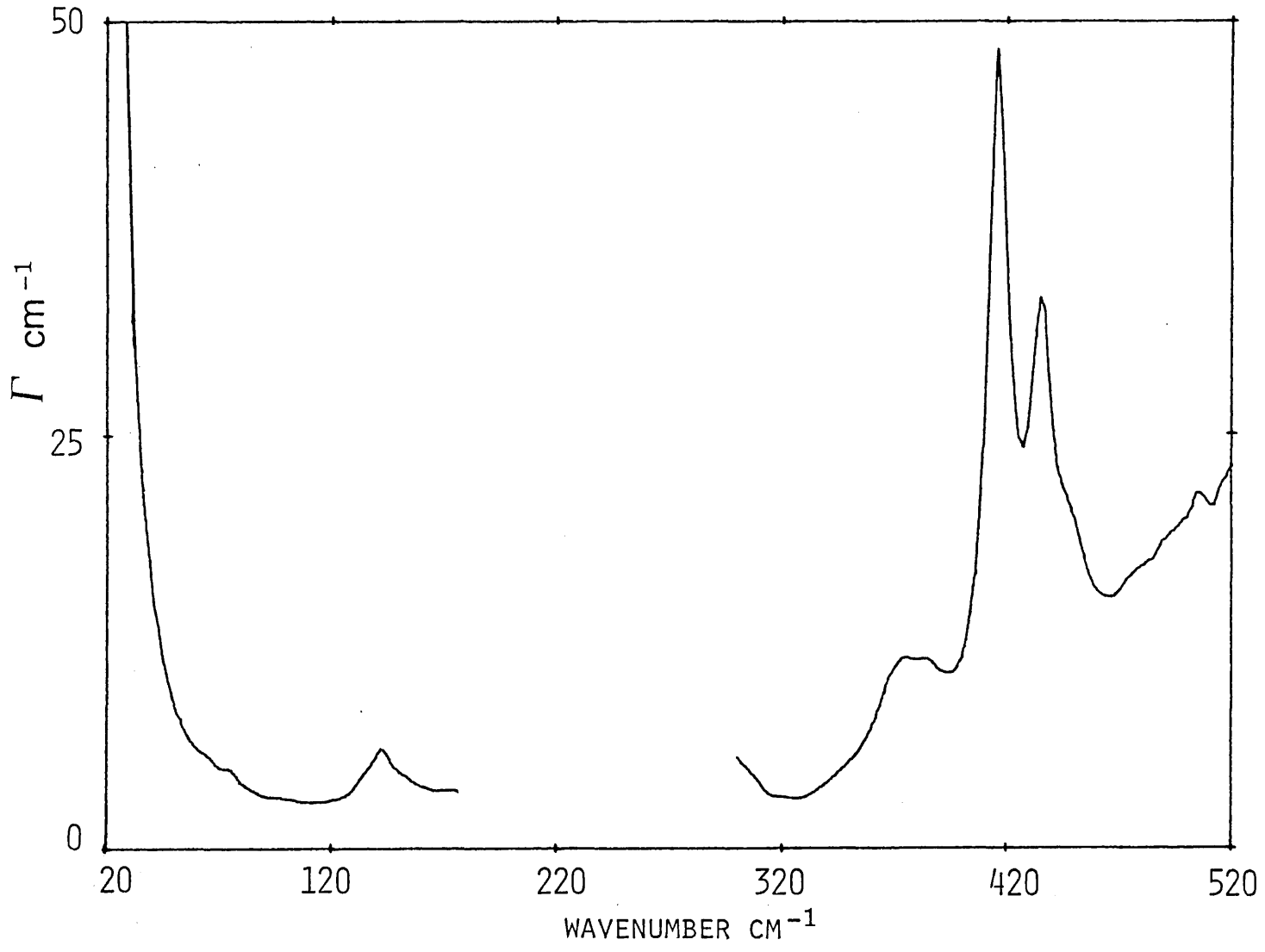

Figure 5.55 Frequency dependence of Γ required to account fully for the observed absorption in ZnSe at 300K if the non linear dipole contribution is neglected.

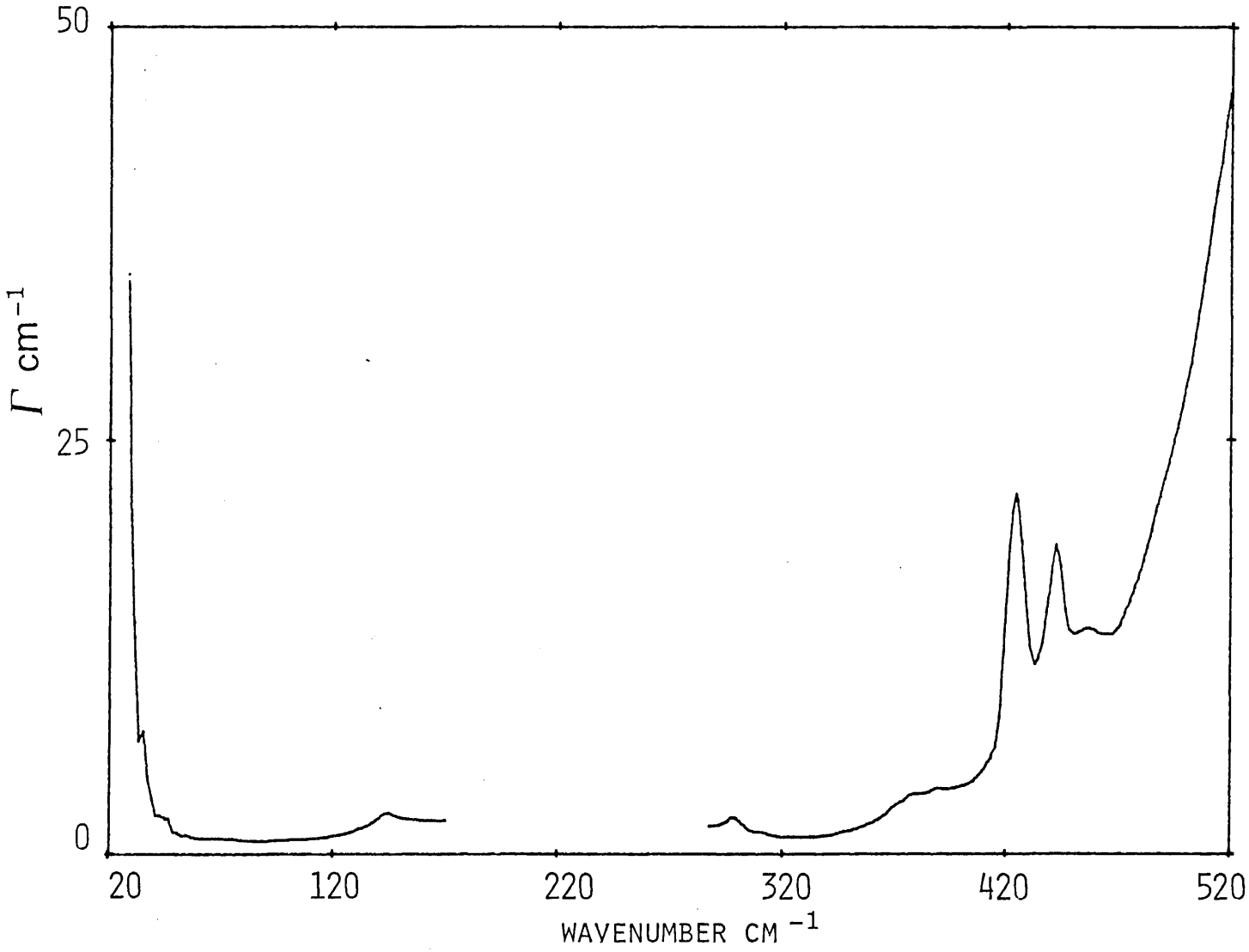

Figure 5.56 Frequency dependence of Γ required to account fully for the observed absorption in ZnSe at 100K if the non linear dipole contribution is neglected.

Table 5.14 Critical point phonon frequencies of ZnSe

Critical point		11-parameter RIM ref 1	Neutron data ref 2
Γ	LO	249.2	253.0
	TO	206.2	213.0
X	LO	206.2	213.0
	LA	187.2	194.0
	TO	216.6	219.0
	TA	70.1	70.0
L	LO	234.2	234.0
	LA	164.1	166.0
	TO	206.2	-
	TA	54.1	57.0
W	W1	235.5	
	W2	216.6	
	W3	179.8	
	W4	176.5	
	W5	87.7	
	W6	87.5	
K	$IIO\Sigma_1$	234.8	
	$IIA\Sigma_1$	177.0	
	$IO\Sigma_1$	211.8	
	$TO\Sigma_2$	189.3	
	$IA\Sigma_1$	92.7	
	$TA\Sigma_2$	68.6	

ref 1 Patel (1982)

ref 2 Hennion et al (1971)

Table 5.15 ZnSe assignments

This work		11-parameter RIM ref 1	Neutron ref 2	Raman ref 3	Assignments
300K	100K				
65	-	59.0	-	-	W1 - W4
75	75	70.1	68	-	LO(L) - LA(L)
141	141	140.2	140	139	2TA(X)
294	296	288.3	291	296	LO(L) + TA(L)
-	312	-	-	-	3-phonon ?
320	326	323.0	-	317	W1 + W6
		323.2			W1 + W5
-	372	366.3	-	368	$IIA\Sigma_1 + TO\Sigma_2$
373	379	370.3	-	-	TO(L) + LA(L)
385	392	388.8	-	381	$IIA\Sigma_1 + IO\Sigma_1$
417	426	415.3	-	414	W1 + W3
435	443	433.2	438	431	2TO(X)
450	458	452.1	-	448	W1 + W2

ref 1 Patel (1982)
ref 2 Hennion et al (1971)
ref 3 Irwin and LaCombe (1972)

Table 5.16

Temperature dependence of the intensities of two-phonon summation bands in ZnSe

Summation bands	Calculated $\frac{(1+n_1+n_2)_{100K}}{(1+n_1+n_2)_{300K}}$	Measured $\frac{\alpha_{100K}}{\alpha_{300K}}$
LO(L) + TA(L)	0.39	0.49
W1 + W6	0.42	0.44
TO(L) + LA(L)	0.48	0.56
$IIA\Sigma_1$ + $IO\Sigma_1$	0.49	0.69
W1 + W3	0.50	0.76
2TO(X)	0.52	0.85

References to chapter 5

Afsar M N and Button; IEEE Trans. MTT-31, 217 (1983).

Afsar M N, Birch J R and Chamberlain J; IEE Conf. Publ. 129, 131 (1975).

Aven M, Marple D T F and Segall B; J. Appl. Phys. 32, 2261 (1961).

Birman J L; Phys. Rev. 131, 1489 (1963).

Borcherds P H, Alfrey G F, Saunderson D H and Woods A D B; J. Phys. C 8, 2022 (1975)

Carles R, Saint-Cricq, Renucci J B, Renucci M A and Zwick A; Phys. Rev.B 22, 4804 (1980).

Cochran W, Fray S J, Johnson F A, Quarrington J E and Williams N; J. Appl. Phys. 32, 2102 (1961).

Deus P, Voland U and Schneider H A; Phys. Stat. Sol.(a) 80, K29 (1983).

Dolling G and Waugh J L T; Lattice Dynamics, Ed. Wallis R F, Pergamon Press, London, p.19 (1965).

Fray S J, Johnson F A and Jones R H; Proc. Phys. Soc. (London) 76, 939 (1960).

Gast J and Genzel L; Opt. Comm. 8, 26 (1973).

Hass M and Henvis B W; J. Phys. Chem. Solids 23, 1099 (1962).

Hoff R M and Irwin J C; Canad. J. Phys. 51, 63 (1973).

Irwin J C and La Combe J; Canad. J. Phys. 50, 2596 (1972).

Iwasa S, Balslev I and Burstein E; Proc. 7th. Int. Conf. on Physics of Semiconductors, Paris, p.1077 (1964).

Jamshidi H, Parker T J, Patel C and Sherman W F; J. Mol. Structure 113, 277 (1984).

Johnson C J, Sherman G H and Weil R; Appl. Optics 8, 1667 (1969).

Kiefer W, Richter W and Cardona M; Phys. Rev.B 12, 2346 (1975).

Kleinman D A and Spitzer W G; Phys. Rev. 118, 110 (1960).

Koteles E S and Datars W R; Sol. St. Comm. 19, 221 (1976a)

Koteles E S and Datars W R; Canad. J.Phys. 54, 1676 (1976)

Kunc K, Balkanski M and Nusimovici M A; Phys. Stat. Sol.(b) 71, 341 (1975); Phys. Stat. Sol.(b) 72, 229 (1975); Phys. Stat. Sol.(b) 72, 249 (1975).

Lorimor O G and Spitzer W G; J. Appl. Phys. 36, 1841 (1965)

Maslin K A; Ph.D thesis, University of London (1986).

MCP Electronic Materials Ltd., Middlesex, England.

Memon A and Parker T J; SPIE 289, 20 (1981).

Mooradian A and Wright G B; Sol. St. Comm. 4, 431 (1966).

Moss T S, Smith S D and Hawkins T D F; Proc. Phys. Soc. (London) B70, 776 (1957).

Novikova S I; Sov. Phys. (Solid State) 2, 2087 (1960).

Parker T J and Chambers W G; Infrared Phys. 16, 349 (1976).

Parsons D F and Coleman P D; Appl. Optics 10, 1683 (1971).

Patel C; Ph.D thesis, University of London (1982).

Patel C, Parker T J, Jamshidi H and Sherman W F; Phys. Stat. Sol.(b) 122, 461 (1984).

Patel C, Sherman W F and Wilkinson G R; Phys. Stat. Sol.(b) 111, 649 (1982).

Patel C, Maslin K A and Parker T J; Proc. 2nd. Int. Conf. on Phonon Physics, Budapest, 1985 (to be published).

Perkowitz S; J. Phys. Chem. Solids 32, 2267 (1971).

Price D, Rowe J and Nicklow R M; Phys. Rev.B 3, 1268 (1977)

Sanderson R B; J. Phys. Chem. Solids 26, 803 (1965).

Sekine T, Uchinokura K and Matsuura E; J. Phys. Chem. Solids 38, 1091 (1977).

Seraphin B O and H E Bennett; "Semiconductors and semimetals" Vol. 3, Eds. Willardson R K and Beer A C, Academic Press, New York, p.499 (1967).

Sirota N N and Pashintsev Y I; Dokl. Akad. Nauk SSSR 127, 627 (1959).

Sobotta H; Phys. Letts. 32A, 4 (1970).

Soma T; Sol. St. Comm. 34, 927 (1980).

Soma T, Sato J and Matsuo H; Sol. St. Comm. 42, 889 (1982).

Spitzer W G and Fan H Y; Phys. Rev. 99, 1893 (1955).

Spitzer W G and Whelan J M; Phys. Rev. 114, 59 (1959).

Stierwalt and Potter R F; "Semiconductors and semimetals" Vol. 3, Eds. Willardson R K and Beer A C, Academic Press, New York, p.71 (1967).

Talwar D N and Agrawal B K; Phys. Stat. Sol.(b) 63, 441 (1974).

Ulrici B and Jahne E; Phys. Stat. Sol.(b) 86, 517 (1978).

Waugh J L T and Dolling G; Phys. Rev. 132, 2410 (1963).

Yarnell J L, Warren J L, Wenzel R G and Dean P J; Neutron Inelastic Scattering 1, I.A.E.A., Vienna, p.301 (1968).

Yoshinaga H and Oetjen R A; Phys. Rev. 101, 526 (1956).

Chapter 6

CONCLUDING REMARKS

The performance of an NPL/Grubb Parsons modular Michelson interferometer has been substantially improved by replacing the mechanical step drive mechanism of the moving mirror with a high precision linear slide driven by a hydraulic piston. A secondary He-Ne laser channel has been constructed to provide an accurate method of measuring the path difference. The position of the moving mirror is determined by monitoring the interference fringes produced by the laser and a sampling accuracy of ± 6nm has been achieved. The hydraulic drive unit can be actuated with an electronic trigger pulse which provides an easy method for automating data collection using a microcomputer. To improve the signal-to-noise ratio of the output interferograms the interferometer can be set to operate in a multiple scanning mode and a simple technique has been developed to co-add interferograms.

The interferometer is constructed in a single pass dispersive mode to enable transmission studies of highly absorbing solids to be carried out conveniently using the technique of dispersive Fourier transform spectroscopy (DFTS). This configuration is also compatible with the design of a Martin-Puplett polarizing interferometer and thus provides the potential for making measurements by DFTS down to a few wavenumbers. The only modification required

for this is the replacement of the dielectric beam divider with a beam divider constructed by depositing wire grids on a thin film of mylar.

The far infrared optical and dielectric properties of five binary semiconductors have been studied using the technique of transmission DFTS. The amplitude and phase spectra on either side of the reststrahlen band have been obtained at 300 and 100K. In all cases the phase dispersion in the regions where the strong absorption bands occur has been revealed and consequently this dispersion can also be observed in the refractive index curves. These are the first direct measurements of the refractive index in these regions.

Spectral features observed in the transmission spectra have been interpreted as phonon combination bands with the aid of an 11-parameter rigid ion model described by Patel. In most cases very good agreement has been found between calculated and observed features. The model has enabled the analysis of critical point phonon frequencies to be made more accurately, especially when neutron scattering data on critical point phonon frequencies were not available.

The form of the imaginary part, $\Gamma(\nu)$, of the anharmonic self-energy of the zone centre transverse optical mode required to account fully for the observed absorption has been calculated from the measured dielectric response functions using the expression given by Cowley. It was found that in all cases, the calculated values of $\Gamma(\nu)$ diverge with increasing frequency in the two- and three-phonon region. These results indicate that in zinc

blende structure crystals there is a significant contribution to the lattice absorption in this region from the non linear dipole moment. This is contrary to the case in alkali halide crystals where earlier work has shown that the contribution from non linear terms in the dipole moment expansion can be safely neglected. This work therefore provides the first clear experimental evidence by which the contributions from lattice anharmonicity and non linear terms in the dipole moment can be distinguished in zinc blende structure crystals.